



HAL
open science

Complexes de coordination magnétiques adressables pour l'information quantique

Idris Tlemsani

► **To cite this version:**

Idris Tlemsani. Complexes de coordination magnétiques adressables pour l'information quantique. Coordination chemistry. Université Paris-Saclay, 2024. English. NNT : 2024UPASF043 . tel-04786815

HAL Id: tel-04786815

<https://theses.hal.science/tel-04786815v1>

Submitted on 16 Nov 2024

HAL is a multi-disciplinary open access archive for the deposit and dissemination of scientific research documents, whether they are published or not. The documents may come from teaching and research institutions in France or abroad, or from public or private research centers.

L'archive ouverte pluridisciplinaire **HAL**, est destinée au dépôt et à la diffusion de documents scientifiques de niveau recherche, publiés ou non, émanant des établissements d'enseignement et de recherche français ou étrangers, des laboratoires publics ou privés.

Magnetic coordination complexes for quantum information

*Complexes de coordination magnétiques adressables pour
l'information quantique*

Thèse de doctorat de l'université Paris-Saclay

École doctorale n°571 Sciences Chimiques :
Molécules, Matériaux, Instrumentation et Biosystèmes (2MIB)
Spécialité de doctorat : Chimie
Graduate School : Chimie. Référent : Faculté des sciences d'Orsay

Thèse préparée à l'**Institut de Chimie Moléculaire et des Matériaux d'Orsay**
(Université Paris-Saclay, CNRS) sous la direction de **TALAL MALLAH**, Professeur des
Universités

Thèse soutenue à Paris-Saclay, le 26 septembre 2024, par

Idris TLEMSANI

Composition du Jury

Membres du jury avec voix délibérative

Pierre MIALANE Professeur, Université Paris-Saclay	Président
Guillem AROMI Professeur, Université de Barcelone	Rapporteur & Examineur
Lorenzo SORACE Professeur associé, Université de Florence	Rapporteur & Examineur
Sylvie CHOUA Professeur, Université de Strasbourg	Examinatrice

Titre : Complexes de coordination magnétiques adressables pour l'information quantique

Mots clés : information quantique, RPE, molécule aimant, magnétisme moléculaire, chimie de coordination

Résumé : La quantité d'information générée chaque année ne cesse de croître tout comme la complexité des problèmes à résoudre. Ces nouveaux défis ont conduit au développement de nouveaux paradigmes, tels que l'information quantique, qui utilise des ordinateurs quantiques basés sur des bits quantiques (qubits). Les molécules magnétiques sont des candidats intéressants pour coder des qubits de spin. Parmi les défis de la recherche sur les molécules paramagnétiques en tant que qubit, se trouve l'obtention de longs temps de relaxation (T_1 et T_2) ainsi que le couplage de qubit entre eux.

Un qubit de spin est un système de deux niveaux quantiques qui peuvent être mis en superposition suffisamment longtemps pour être observé et manipulé. Ceci peut être réalisé avec des molécules ayant un électron célibataire (comme un radical organique) avec un spin $\frac{1}{2}$ ou en concevant des molécules avec un spin entier ($S = 1$ pour les complexes Ni(II)) pour lever la dégénérescence en champ nul (ZFS). La transition entre ces niveaux, connue sous le nom de transition d'horloge (CT), est protégée des fluctuations magnétiques, ce qui allonge le temps de relaxation T_2 .

Durant cette thèse, nous avons étudié divers composés de nickel et essayé de prédire le signe de l'anisotropie axiale à partir de leur structure. Nous avons mesuré les spectres RPE de ces composés pour accéder aux paramètres ZFS et

avons rationalisé les résultats par le calcul. La modulation de la sphère de coordination par des effets stériques et électroniques des complexes de Ni(II) a donné lieu à des composés avec des transitions d'horloge accessibles. L'étude RPE pulsée de ces complexes a mis en évidence différentes stratégies pour augmenter le T_1 et a démontré la robustesse d'un CT contre les fluctuations magnétiques.

Nous nous sommes également orientés vers l'étude de complexes avec une valeur de spin $S = 1/2$, qui possèdent des temps de relaxation relativement longs et ne dépendent pas du ZFS. Ceci garantit la possibilité d'obtenir un signal RPE permettant une étude détaillée des composés. Pour les complexes de Cu(II), les temps de relaxation relativement longs ($T_2 = 1 \mu\text{s}$ et $T_1(7.5\text{K}) = 1.8 \text{ ms}$) trouvés dans l'unité monomérique restent inchangés dans le complexe binucléaire. Nous avons essayé de préparer plusieurs complexes binucléaires de Cu(II) avec différentes distances Cu-Cu. Nous avons également mesuré le temps de cohérence des spins nucléaires d'un proton et d'un azote couplés par une interaction superhyperfine au spin électronique du Cu(II) et avons trouvé une valeur T_2 de plus de 500 μs pour le proton. Nous avons ainsi montré la capacité d'une seule molécule magnétique à porter plusieurs ressources pour réaliser les portes quantiques nécessaires à l'informatique quantique.

Title : Magnetic coordination complexes for quantum information

Keywords : quantum information, EPR, molecular magnets, molecular magnetism, coordination chemistry

Abstract: The exponential growth in information processing and the demand for solving new challenges have led to the development of new paradigms, such as quantum information, which uses quantum computers based on quantum bits (qubits). Magnetic molecules, are attractive candidates to encode spin qubits. Among the challenges in the molecular magnet as qubit research we found obtaining long phase memory relaxation times and coupling qubit among them.

A spin qubit is a system of two non-degenerated quantum levels that can be put into superposition long enough to allow measurements to be made. This can be achieved with molecules having an unpaired electron (such as an organic radical) with a $1/2$ spin or by designing molecules with an integer spin ($S=1$ for Ni(II) complexes) to lift degeneracy without a magnetic field (ZFS). The transition between these levels, known as the clock transition (CT), is protected from magnetic fluctuations, lengthening the T_2 relaxation time.

In these projects we studied various nickel compounds and tried to predict the sign of the axial anisotropy from their structure. We measured the EPR spectra of these compounds to access the ZFS parameters and rationalised the results by calculation. The modulation of the coordination sphere by steric, electronic and packing effects of Ni(II) complexes has resulted in compounds with accessible clock transitions. The pulsed EPR study of these complexes has pointed out a strategy to increase the T_1 and

demonstrated the robustness of a CT against magnetic fluctuations. We also switch our focus on the study of complexes with an $S = 1/2$ spin value, which have relatively long relaxation times and are not dependent on ZFS. This guarantees the possibility of obtaining an EPR signal so that a detailed study could be carried out. For Cu(II) complexes, the relatively long relaxation times ($T_2 = 1\mu\text{s}$ and $T_1(7.5\text{K}) = 1.8\text{ ms}$) found in the monomeric unit remain unchanged in the binuclear complex. We tried to prepare several binuclear Cu(II) complexes with different Cu-Cu distances. We also measured the coherence time of the nuclear spins of a proton and a nitrogen coupled via superhyperfine interaction to the Cu(II) electronic spin and found a T_2 value of more than $500\ \mu\text{s}$, demonstrating the ability of a single magnetic molecule to bear several resources to perform quantum gates that are required for quantum computation

TABLE OF CONTENT

Resumé	2	
Abstract	3	
Table of content	4	
Introduction and state-of-the-art	7	
I.1 Motivations, objectives and resume of the principal results.....	8	
I.2 Background.....	11	
I.3 A brief introduction to relaxation	14	
I.3.a Definition of relaxation times.....	14	
I.3.b. Measuring a relaxation time.....	15	
I.3.c Mechanism of relaxation.....	17	
I.4. Spin based qubits.....	22	
I.4.a NV- centers.....	22	
I.4.b Silicon based qubit.....	22	
I.5. Molecular-based qubit.....	24	
I.5.a Qubit embedded in a CT.....	25	
I.5.b Qubit non-embedded in a CT.....	28	
I.6 Conclusion.....	33	
I.7 References.....	35	
Chapter I: Electronic structure of mononuclear Ni(II) complexes as S = 1 spin qubits		39
I.1 Concept of clock transition ($S = 1$).....	40	
I.2 Introduction.....	41	
I.2 Introduction on Zero-Field Splitting.....	43	
I.2.a Origin of ZFS.....	44	
I.2.b Rationalisation of the sign of D	46	
I.2.c Introduction of High Field High Frequency EPR (HF-HFEPR)	49	
I.3 Study of mononuclear Ni(II) compound	52	
I.3.a Distorted octahedra.....	53	
I.3.b C_3 symmetry.....	66	
I.3.c Tuning of ZFS in trigonal Ni complexes.....	73	
I.3.d A tricky case: $[\text{Ni}(\text{imdipa})(\text{NCS})](\text{NCS})$	89	
I.4 Conclusion.....	96	
I.5 References.....	97	
Chapter II: Pulsed EPR study of mononuclear Ni(II) complexes	99	
II. Introduction.....	100	
II.1 Introduction of pulsed EPR spectroscopy	102	
II.1.a Nutation experiment.....	102	
II.1.b Echo Detected Field Sweep.....	102	
II.2 Study of the relaxation times of mononuclear Ni(II) compounds with $D < 0$	103	
III.2.a Influence of the matrix.....	103	
II.2.b Influence of the number of ligand.....	121	
II.2.c Efficiency of the clock transition	132	
II.3 Conclusion.....	150	
II.4 Experimental part.....	152	
II.5 References.....	153	
Chapter III: Synthetic strategies of binuclear complexes as molecular quantum gates		155
III.1 Introduction.....	156	

III.2 Rigid bridging ligand.....	158
III.2.a Synthesis.....	158
III.2.b Magnetometry SQUID and EPR measurement.....	163
III.3 Chelating bridging ligand.....	167
III.3.a Mononuclear study.....	168
III.3.b From mononuclear to binuclear complexes.....	169
III.4 Conclusion.....	173
III.5 Experimental part.....	174
III.6 References.....	179

Chapter IV: Quantum coherence of mono- and binuclear complexes based on the salophen ligand 181

IV.1 Introduction.....	182
IV.1. Advanced pulsed EPR method:.....	186
IV.1.a. ENDOR.....	186
IV.1.b DEER.....	189
IV.2. [Cu(salophen)].....	193
IV.2.a. Preliminary experiment.....	194
IV.2.b. ENDOR Experiment.....	202
IV.3 [VO(salophen)].....	208
IV.3.a Preliminary experiment.....	208
IV.3.b ENDOR experiment.....	215
IV.4 From mononuclear to dinuclear complexes.....	216
IV.4.a Synthesis.....	216
IV.4.b Pulsed EPR experiment.....	219
IV.5 Conclusion.....	228
IV.6 Experimental part.....	229
IV.7 References.....	238
Conclusion and perspectives.....	239
Résumé en français.....	244

INTRODUCTION AND STATE-OF-THE-ART

I.1 MOTIVATIONS, OBJECTIVES AND RESUME OF THE PRINCIPAL RESULTS

In the past few years, the amount of information that needs to be treated has been increasing. An emerging field is quantum information that postulates the use of quantum computers based on quantum information storage units called quantum bits (qubits). Magnetic molecules, due to their flexibility and their potential long coherence time, are attractive candidates to encode spin qubits. The main challenge for molecular magnets to play the role of efficient qubits is to obtain long phase memory relaxation times T_2 . It has been shown that a clock transition (CT) system is protected from magnetic fluctuations and may lead to long phase memory times T_2 .

A qubit is a system with at least two quantum levels that can be put in superposition for a time long enough to be able to perform measurements. A two-level system can be obtained for a molecule that possesses an unpaired electron (an organic radical for example) with a spin $1/2$. Upon the application of an external magnetic field, the two-fold degeneracy ($m_s = \pm 1/2$) of the spin state is lifted (Zeeman effect) leading to two levels with different energy i.e. a qubit. Another way to obtain a qubit is to engineer the electronic structure of a molecule with an integer spin value ($S = 1$ for Ni(II) complexes, for example) to lift the degeneracy of the spin state without applying a magnetic field (Zero-Field Splitting, ZFS, see Chapter II). In such a case, the two low-lying levels may play the role of a qubit (in zero field). The transition between these two levels is not sensitive to the fluctuations of the magnetic surrounding atoms and is therefore protected from magnetic fluctuations of the spin bath (electronic and nuclear), this transition is called a clock transition (CT) (see chapter II). The relaxation time T_2 is expected to be larger in this situation than for the previous case.

The objective of this thesis is to synthesize and fully characterize binuclear compounds that can be used as quantum logic gates. To reach this objective, we will study the relaxation times of mononuclear complexes (playing the role of qubits) with or without a CT, then couple them chemically, study their coupling and their resulting relaxation times.

Introduction and state-of-the-art

Clock transition can be obtained using complexes with an integer spin value ($S = 1$ and $S = 2$) if one is able to engineer the ZFS to lead to two low-lying level states. The energy difference (ΔE) between the two quantum levels must be equal (or very close) to the electromagnetic radiation ($h\nu$) used to achieve the state of superposition, necessary to address the qubit. Since the spins ΔE is in the microwave range, Electron Paramagnetic Resonance (EPR) spectroscopy is used. Unfortunately, such apparatus are built with a given $h\nu$ value for historical reasons (0.33 cm^{-1} , 1 cm^{-1} for X and Q bands machines, for example), and no commercial microwave tunable machine exists yet. If one is interested in studying the effect of CT on T_2 , it is necessary to tune the value of the energy difference of the two levels to fit the ones of the available apparatus, which is challenging. Indeed, ΔE is highly sensitive to the chemical environment of the metal ion bearing the spin. However, some Ni(II) complexes that meet this condition have been identified and new ones have been synthesized (Chapter II). The study of these compounds by pulsed EPR revealed that, despite the relatively short relaxation times measured, the CT effectively preserves the qubit against magnetic field fluctuations (Chapter III).

In Chapter IV, we set the strategy of transposing mononuclear Ni(II) complexes into binuclear ones, by tuning the distance between the metal ions with the objective of investigating the effect of magnetic coupling on the relaxation times. In the course of this study, we realized that the complexes must have an important chemical stability, because many experiments must be carried out on very diluted samples. The bridging ligands must, therefore, possess a strong chelating effect, in order for the complexes to be as stable as possible in solution (or when diluted in some material). We also concluded that the synthetic procedures had to be modular in order to achieve chemical tunability. These conclusions were fully exploited for the synthesis of the binuclear complexes presented in Chapter V.

Chapter V focuses on the study of complexes with a $S = 1/2$ spin value, which has relatively long relaxation times and are not dependent on ZFS. This guarantees the possibility of obtaining an EPR signal so that a detailed study could be carried out. For Cu(II) complexes, the relatively long relaxation times ($T_2 = 1 \text{ }\mu\text{s}$ and $T_1(7.5\text{K}) = 1.8 \text{ ms}$) found in the monomeric unit remain unchanged in the binuclear complex. We tried to prepare several binuclear Cu(II) complexes with different Cu-Cu distances but unfortunately, we were not able to measure

couplings in those complexes.

As stated above, long phase memory times are ultimately needed to perform quantum calculations. It is well known that nuclear spins, since they are more protected from the environment than electronic spins, are expected to have longer relaxation times T_2 . Therefore, we measured the coherence time of the nuclear spin of a proton coupled via superhyperfine interaction to the Cu(II) electronic spin and found a T_2 value of more than 500 μs , demonstrating the ability of a single magnetic molecule to bear several operations to perform quantum gates that are required for quantum computation.

Results obtained with copper have been compared with another $S = 1/2$ spin with V(IV)O. It was evidenced that T_1 ($T_1(7.5\text{K}) = 12 \text{ ms}$) is longer in the case of the V(IV)O complex. The superhyperfine interaction between V(IV)O and the nuclear spin of the proton have been observed but no coherence time has been measured.

I.2 BACKGROUND

In recent years, the amount of generated data has grown continuously, giving rise to increasingly complex issues that entail a growing need for storage and computational resources. However, this demand sometimes exceeds the capabilities of classical computers operating with classical algorithms. For instance, let's consider the challenge of searching for information within an unsorted database: depending on the size of the database, a search operation may take mere seconds when performed on a hard drive, or conversely, several months or even years when executed on a massive data center.

In response to these challenges, a new field of research has emerged: quantum computing. Unlike classical bits, which represent discrete values (0 or 1), qubits can exist in a quantum superposition of these states, that with the adapted algorithms are expected to solve problems not accessible to classical computers. The main reason stems from the ability of quantum computers to operate by treating large amount of information in a parallel way, providing one relies on the adequate algorithms.

Although the potential of such computers was initially envisioned by Feynman,[1] it was later demonstrated by Shor [2] and Grover [3], who proposed quantum algorithms that could be implemented in a quantum computer. Shor's algorithm illustrates how large numbers can be efficiently factorized, while Grover's algorithm demonstrates how a quantum algorithm can accelerate the search for specific data within an unsorted database.

The transition from a classical bit to a qubit involves a shift from traditional electronic components to quantum systems. In classical computing, transistors play a central role as fundamental components in electronic circuits. They are utilized to perform logical operations or switching functions, enabling computational tasks. Transistors play a crucial role in manipulating bits by receiving a voltage corresponding to the binary state of the bit. The voltage state controls the operation of the transistor, determining whether it allows the passage of electrical current or whether it does not, representing the logical state of the bit ($|0\rangle$ or $|1\rangle$). The applied voltage to transistors serves as a mean to represent and manipulate bits in classical electronic circuits.

Figure 0-1 illustrates the case of a NOT gate. The logic gate is represented by a transistor (blue). If the input voltage is low, corresponding to the scenario where the information is a bit with a value of $|1\rangle$, then this transistor, acting as a NOT gate, will produce a high output voltage, corresponding to a bit value of $|0\rangle$. If the input voltage is high (state $|0\rangle$), the output of the transistor will be $|1\rangle$. The gate behaves as an inverter.

The operation on qubits technically differs significantly from classical bits, as there is no equivalent of the transistor in the qubit realm, but the logic remains the same. Qubits, which can be a spin,[4] a photon polarization, [5] or atomic energy levels,[6] cannot be manipulated via transistors. To manipulate qubits, external stimuli such as microwave pulses, magnetic or electric fields, and other forms of interaction with the qubit's quantum environment are employed. These techniques enable the precise and controlled preparation, manipulation, and readout of the qubit's state, thereby facilitating quantum operations and computations.

In the case of a controlled-NOT (CNOT) gate, two entangled (coupled) qubits are required ($|a\rangle$ and $|b\rangle$ Figure 0-1). Two qubits are said to be entangled when the total state is not the product of the individual qubit states (the wavefunction cannot be factorized). In other words, the measurement of one of the qubits instantaneously affects the state of the other qubit, even if they are spatially separated.

It is possible to simulate the action of a quantum NOT gate using this system. Indeed, given the state of the two qubits at the input, it is feasible to apply a stimulus. If the energy brought by the stimulus matches an energy gap, a transition occurs and the state of the qubit is changed. At the end, as for a transistor, it is possible to change the state of the qubit. However, CNOT gate has several advantages compared to the NOT gate. First, a CNOT gate allows the modification of multiples qubits in one operation which means that one can perform several computations in parallel. Second, the quantum gates are reversible, meaning that it is possible to find the entry knowing the result. This is not possible for a classical gate.

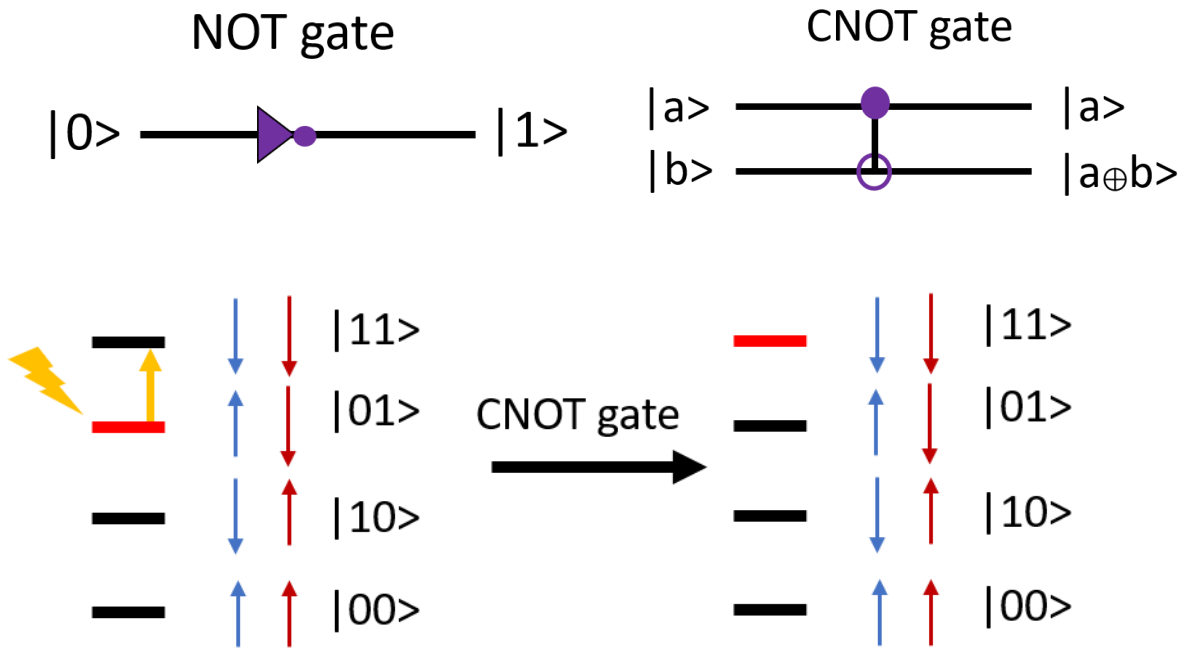


Figure 0-1. Schematic representation of the operation of a CNOT gate (right) and a NOT gate (left).

A quantum computer is composed of one or more quantum circuits, each one made up of one or more quantum logic gates themselves composed of multiple qubits. It should be noted that a system may be an excellent individual qubit, but if it cannot be coupled with other qubits, it cannot be implemented in a quantum circuit and is therefore useless. The entire challenge lies in finding qubits that perform well individually and that can be easily implemented in a circuit.

Di Vincenzo proposed a number of criteria for evaluating the potential of a qubit.[7] A qubit should have (i) a long coherence time, which is the lifetime of the superposition state, (ii) the ability to be initialized in a specific initial state, (iii) be well-defined and scalable, (iv) be individually measurable, and (v) be able to implement universal quantum gates.

Today, there are very few examples of quantum computers because qubits face a fundamental problem: the second law of thermodynamics. Indeed, the superposition of states generated corresponds to an excited quantum state and is therefore unstable over time, naturally tending to decay – this is known as decoherence. It is therefore necessary to be able to detect whether the information encoded in the qubit has deteriorated or not, which is referred to as error

correction. Indeed, finding a robust qubit system is crucial, meaning it must be well-isolated from its environment to ensure the integrity of information, i.e. a stable superposition state over time. The paradox lies in the fact that the same system must be able to interact with its environment (writing and reading from the macroscopic world), and isolated as much as possible.

Numerous physical systems have been proposed and studied, among which non-natural qubits like quantum dots and superconducting qubits stand out. The latter are currently at the forefront of development due to significant investments from major companies such as Rigetti, Microsoft, IBM, [8], [9], [10] and Google [11]. These investments have facilitated the creation of a quantum computer by Google, based on superconducting qubits. Despite those efforts, this quantum computer only works with relatively limited number of effective qubits, and to date there is no demonstration that it can be superior to classical computers.

Natural qubits, on the other hand, fall into two main categories: spin-based qubits, including NV centers [12], molecules, or cold atoms [13], and non-spin-based systems like photons, where polarization represents the states 0 or 1. In this thesis, our focus will be primarily on molecules playing the role of spin-based qubits.

I.3 A BRIEF INTRODUCTION TO RELAXATION

I.3.a Definition of relaxation times

Before going into details, we will briefly introduce the concept of relaxation time. The relaxation time is defined via two parameters T_1 and T_2 that correspond to the spin-lattice and the spin-spin relaxation times, respectively. The latter T_2 represents the coherence lifetime of the qubit or the phase memory time. Experimentally, it is possible to get access to those times using pulsed EPR spectroscopy. For example, when a spin is placed into a magnetic field applied along the z axis, the magnetic moment of the spin will precess around this axis. The net magnetization of the spin is represented by a vector M which contains three components M_x , M_y and M_z . In the absence of perturbation, the magnetization is aligned with the magnetic field leading to $M_z = 1$ and $M_x = M_y = 0$. When an electromagnetic impulsion is employed, it is

possible to flip the spin outside the magnetic axes thus changing the value of the magnetization. For example, an impulsion of $\frac{\pi_z}{2}$ moves the magnetization into the xy plane.

From a physical point of view; using the Bloch sphere formalism, T_1 corresponds to the return of magnetization along the z-axis and T_2 to its loss in xy plane (Figure 0-2). The question here is, how do we get access to those times?

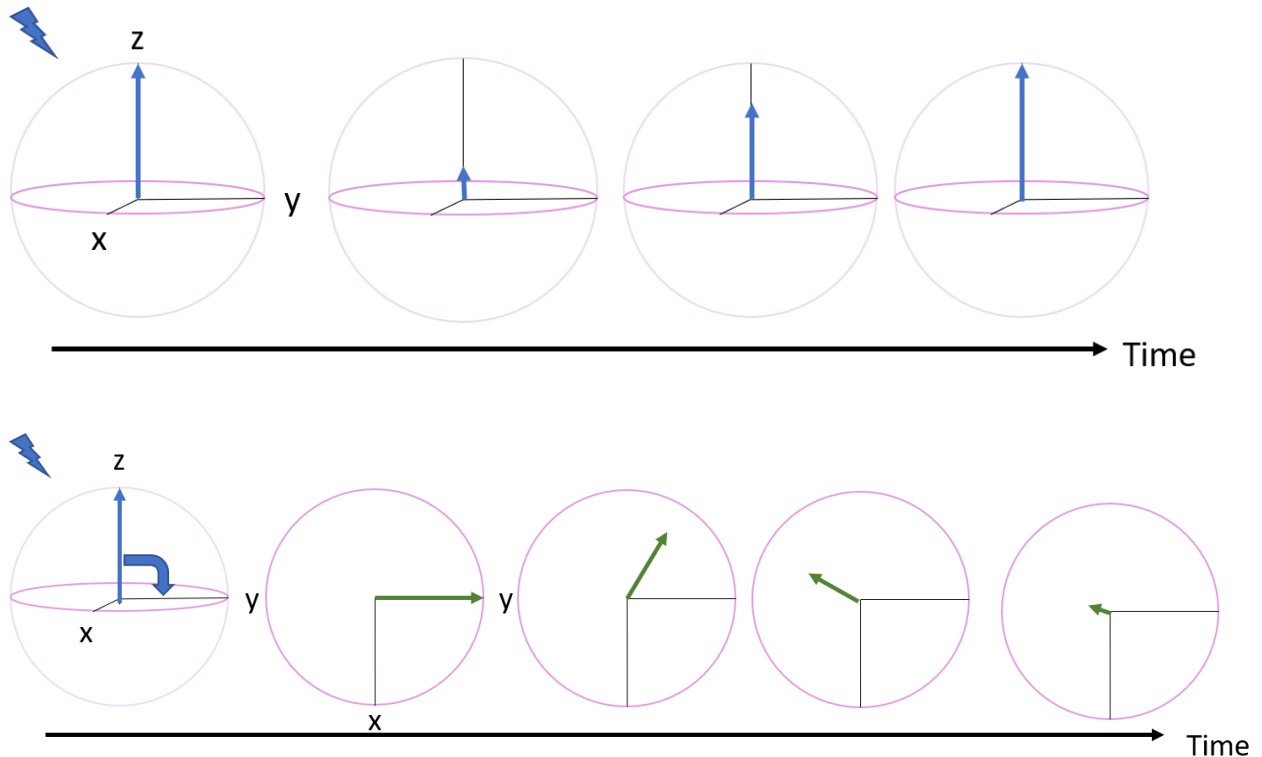


Figure 0-2. Representation of the spin-lattice relaxation (top) and the spin-spin relaxation (bottom) using the Bloch sphere model after an electromagnetic impulsion.

1.3.b. Measuring a relaxation time

1.3.b.i Coherence time

The Hahn echo is a fundamental technique used in pulsed EPR, that provides valuable insights into the interactions and motion experienced by nuclear and electronic spins throughout their lifetimes. This method relies on the formation of a magnetic echo induced by a series of pulses, which temporarily align the orientation of spins. During this time interval, the spins are free to experience the effects of their environment, such as dipolar interactions with neighbouring spins or fluctuations in the local magnetic field. When the spins return to their initial

orientation, they retain a trace of these interactions in the form of a phase shift, which is subsequently revealed upon detection of the echo. Thus, the Hahn echo not only allows for the measurement of T_2 relaxation times but also probes the dynamics and subtle interactions that govern spins behaviours in their environment. This technique provides a powerful tool for exploring and understanding the physical and chemical processes that influence spin relaxation in complex systems.

The Hahn echo sequence is reported below (Figure 0-3)

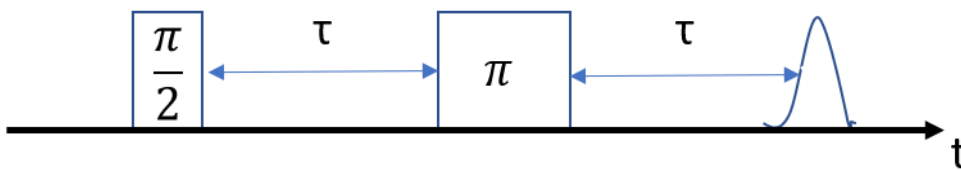


Figure 0-3. Hahn echo sequence

Initially the spins are aligned with the magnetic field induced by the magnet. This magnetic field corresponds to the static magnetic field. During the Hahn echo sequence, the initial magnetization is manipulated to lie in the xy plane (Figure 0-4.b), with a $\pi/2$ pulse, representing a superposition of states. Subsequently, during the free induction decay period, the spins precess along the magnetic z axis at different rates because their local magnetic environments are different (Figure 0-4-c), (red and blue spins). After a time τ , a π pulse is applied to refocus all spins (Figure 0-4-d). Subsequently, after another τ interval, the spins that remain in phase generate an echo (Figure 0-4-e). The echo is due to the emission of photons at the Larmor frequency of the spins that rotate in the laboratory frame and that have been refocused. The intensity of the echo depends of the numbers of refocused spins. Therefore, the experiment is repeated with increasingly longer τ values. Because of relaxation (interaction of the spins with their local environment, yellow spin in Figure 0-4), the intensity of the echo signal decays, and T_2 is extracted from this decay.

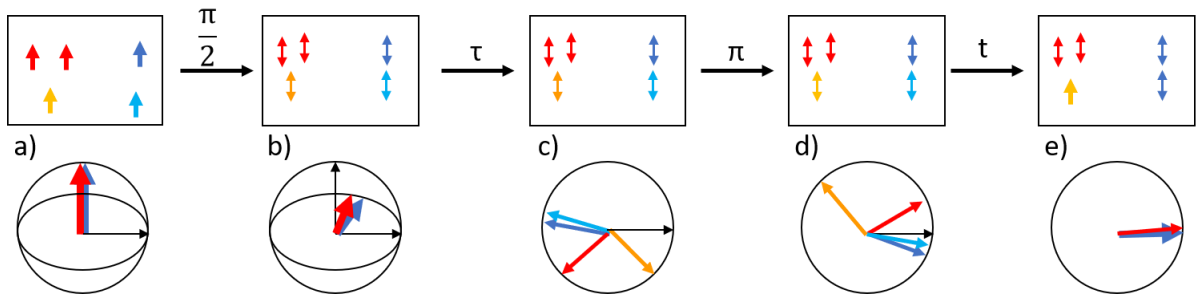


Figure 0-4. Schematic representation of the life of electron during Hahn echo sequence

An important image to keep in mind is that during such experiment, we always deal with a bath of spins in a matrix. This means that we always observe an average effect and in one sample the same individual spins can have completely different behaviours depending on their local environment.

1.3.b.ii Spin-lattice relaxation

A simple experiment to measure T_1 is called inversion recovery. The sequence involves applying a π pulse to reverse the magnetization, followed by a period during which the magnetization gradually returns to the z-axis (equilibrium). To discriminate the spins that have not yet fully returned to the z-axis after a time interval τ_1 , a Hahn echo sequence is performed. Consequently, this enables the following of the relaxation process associated with spin-lattice relaxation.

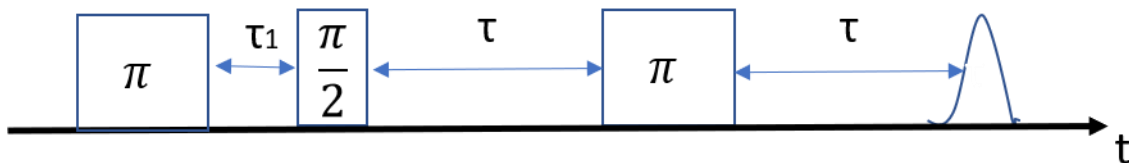


Figure 0-5. Inversion recovery sequence

1.3.c Mechanism of relaxation

Now we will briefly introduce the mechanism responsible for the relaxations.

1.3.c.i Spin-lattice relaxation

The spin-lattice (or longitudinal) relaxation time T_1 is a quantitative measurement of the rate at which energy is transferred from the system to the neighbouring molecules (the lattice). This is the z direction relaxation and leads to the restoration of the Boltzmann equilibrium (Figure

0-2 top). Here we suppose that the higher M_S corresponds to the ground state and that $M_S = 0$ corresponds to the highest energy.

There are four types of spin-lattice relaxation mechanism (Figure 0-6) [14]:

- (i) Direct process (red) involves relaxations from M_S to $-M_S$ with emission of a single lattice phonon.
- (ii) The Orbach process (yellow) involves absorption of a phonon followed by phonon emission and relaxation from an excited state.
- (iii) The Raman process (grey) is analogous to the Orbach mechanism with the exception that the relaxation occurs from a virtual state.
- (iv) Quantum tunnelling (green) corresponds to the case where the magnetization goes directly from $-M_S$ to $+M_S$ levels without going through any intermediate levels. The mechanism occurs if there is transverse anisotropy in the system – which is introduced by distortions from purely axial symmetry.

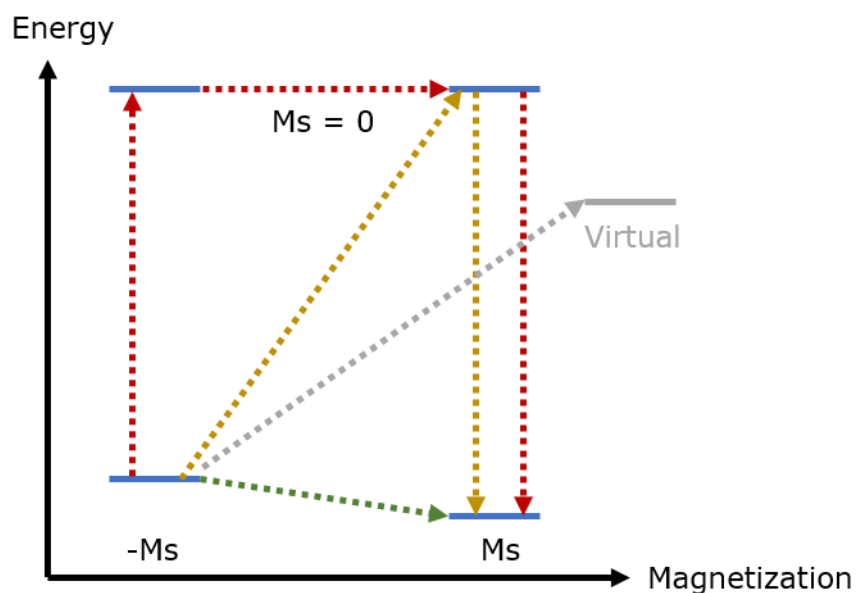


Figure 0-6. Schematic representation of relaxation pathways. Blue lines represent spin states. The grey line represents a virtual state by which Raman relaxation proceeds. The different processes are: direct process (green), thermally assisted quantum tunnelling, Orbach relaxation (yellow), Raman relaxation (grey).

The overall spin-lattice relaxation is described by the following equation:

$$\frac{1}{T_1(T,H)} = AH^2T + \frac{B_1}{1+B_2H^2} + CT^n + \tau_0^{-1}\exp\left(\frac{-U_{eff}}{KT}\right) \quad (1-1)$$

T: temperature in K; H: magnetic field in Oe; A, B: adjustable parameters; C: constant parameter U_{eff} : activation barrier. The different term correspond respectively to direct process, thermally assisted quantum tunnelling, Raman relaxation and Orbach relaxation.

All mechanisms can be discriminated by varying the temperature and the magnetic field and plotting $\log(T_1)$ vs. $\log(y)$.

1.3.c.ii Spin-spin relaxation

The spin-spin relaxation time (or transverse relaxation time, T_2) is a quantitative measurement of the decay rate (or decoherence) of magnetization within the xy plane. Following a $\pi/2$ pulse, spins (electronic or nuclear) are aligned in a single direction, forming a coherent state. However, this arrangement is gradually lost, for instance, as a result of field inhomogeneities and/or direct interactions between spins without energy transfer to the lattice (Figure 0-7).

In practice, it is nearly impossible to deal with one spin, we always deal with an ensemble of spins in a matrix: the spins of the material may interact with phonons, electric and magnetic field fluctuations or other environmental defects. These interactions result in temporal variations in the energy levels of the spins, which consequently modify their resonance frequency. The impact of these interactions on decoherence is as follows: fluctuating resonance frequencies result in a phase shift between the different spins within the system. As the frequencies shift incoherently, the quantum superposition loses its coherence, which in turn leads to decoherence of the overall system. A more precise description can be found in reference.[15]

The main mechanisms responsible for decoherence are described below.

Flip-Flop (Figure 0-7-b): This mechanism involves interactions between two neighbouring spins. If one of the spins changes its orientation (from the $|0\rangle$ state to the $|1\rangle$ state or vice versa), the other spin does the same in a coupled fashion, hence the term "flip-flop". In a system of spins, flip-flop can occur due to dipolar or exchange interactions. It is worth noticing that this

phenomenon is energy conservative, meaning that it happens only with qubit possessing the same energy, thus resonant spins affected by microwave excitation.

Instantaneous diffusion: This mechanism describes the decoherence of observed spins caused by flips of neighboring dipole-coupled electron spins in the bath. With the exception of a crystal, the spatial arrangement of each spin is different (distance with other species and angle with the magnetic field). The first consequence is that each spin feels a different local field. Therefore, spins with the same resonance frequency before the microwave pulse can have different resonance frequencies after the pulse, leading to decoherence.

Spectral diffusion: The term spectral diffusion is used to refer to indirect flip-flop or to refer to T_1 -induced flips of neighboring spins. Both processes are related to random fluctuations of the dipole field of neighboring donor spins, which decohere the observed spin. In the case of T_1 drive diffusion, the flip of the neighboring donor is completely random, whereas in the case of indirect flip it is correlated to the dipole-dipole interaction.

- i. **T_1 Flip** (Figure 0-7-a and 0-7-d): If $T_1 < T_2$ then the decoherence is due to a dissipation of the qubit energy which occurs before the dephasing of the qubit. The phenomenon can happen for neighbours spins too and create a magnetic field fluctuation thus decoherence for the observed spin.
- ii. **Indirect Flip-Flop** (Figure 0-7-c): This mechanism involves three spins, a resonant spin called A, and two off-resonant spins of the same species. Flip-Flop occurs between the two off resonant spins which results in a magnetic fluctuation in the environment off spin A.

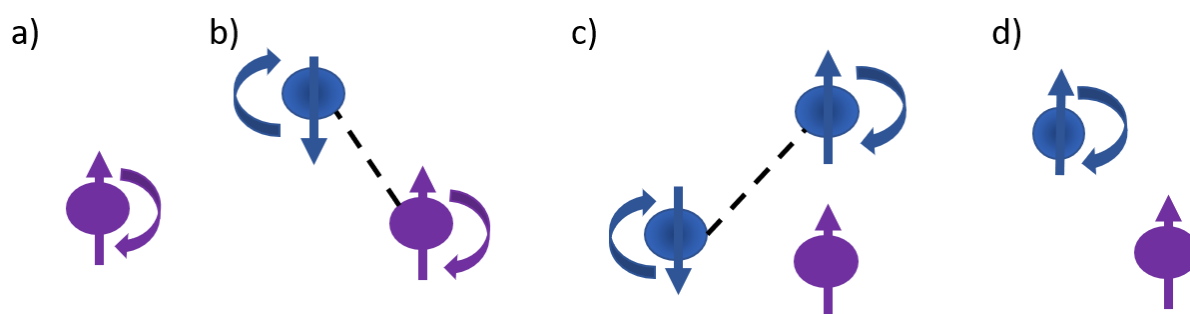


Figure 0-7. Relaxation mechanism. a) T_1 flip of donor. b) Flip-flop. c) Indirect Flip-Flop. d) T_1 flip of neighbours

1.3.c.iii Evaluating the potential of a qubit

The quality of a qubit can be evaluated through the figure of merit $\Omega = T_2/T_1$ which corresponds to the gate speed, in other words the number of operations that it is possible to perform during a sequence. For molecules, T_1 depends on the rigidity of the structure thus the vibration modes of the molecule. More generally, T_1 mostly depends on the temperature and can be pushed to the second time scale or longer while working at mK. From an experimental point of view, reaching such temperature is not so difficult this is why the only important point is to have $T_1 \gg T_2$. When this condition is respected T_2 does not show any temperature dependence this is why the temperature does not really matter. T_2 can be increased by isolating the qubit in order to diminish the interactions among them. This may lead to detection or coupling issue. One of the major challenges is to push T_2 to the ms range without destroying entanglement among the qubits. A small comparison among the different qubit system is proposed in Table 0-1. It is worth noting here that compared to other systems the limitation of employing molecules as qubit is more technical than fundamental.

System	Coherence time	Advantages	Inconvenients
Supraconductor	μs -ms	Coupling	Increasing T_2
Semi conductor	ms	Coupling Technology already developed	T_2 is difficult to increase
Photon	μs	Adressability	Detection

			Coupling Scalability
NV center	μs	Adressability	Tunability Coupling
Cold atom	μs -ms	Coupling	Scalability
Molecule (electronic spin)	ns-ms	Scalability Coupling	Detection
Molecule (nuclear spin)	μs -s	Scalability Coupling	Adressability Detection

Table 0-1. Advantages and inconvenients of different qubits

I.4. SPIN BASED QUBITS

I.4.a NV- centers

NV (N for nitrogen and V for vacancy)centers in diamonds are a relevant example of isolated qubits. In these systems, a NV center is formed by the substitution of a carbon atom by a nitrogen atom which creates a vacancy in the diamond's crystalline structure. This configuration creates an electron spin on the nitrogen atom and a spin on the vacant site leading to a $S = 1$ system. Extensive studies on NV centers in diamonds have revealed coherence times of up to T_2 (nuclear) = 0.9 ms at room temperature.[16] However, these systems have limitations in terms of modularity, and it is very difficult to control the coupling among the centers. Therefore, they are not considered relevant for the realization of a quantum computer, although they show other exciting properties such as ultrasensitive magnetic field detectors.[17]

I.4.b Silicon based qubit

The second example corresponds to the case of phosphorus atoms diluted in ultra-pure silica

which has been a very fruitful system to understand the decoherence mechanisms.

Nuclear spins of neutral donor impurities (D^0) in silicon have been proposed by Kane,[18] as promising qubit candidate due to their long T_2 . This resilience against decoherence is due to two properties of silicon:

- (i) A small spin-orbit coupling
- (ii) The absence of nuclear spins in ^{28}Si , [19], [20] so that no spin bath magnetic fluctuations occur

These advantages had led to $T_{2N}(^{31}\text{P}) \approx 1.3$ s at 1.8 K for a concentration of 1.2×10^{14} spins/cm³. Additionally, T_1 for phosphorus donors approaches an hour at 1.2 K and 0.35 T, exhibiting a strong temperature dependence at higher temperatures.[21]. It was also shown using this system that T_2 (T_{2e}) was found to be inversely proportional to the donor density (for densities ranging from 10^{14} to 10^{16} atoms/cm³) evidencing here the main mechanism of decoherence: dipolar interaction.[22] The reduction of spin density could be a good strategy to increase the coherence time but distancing the spins mean distance, weakening their coupling, which is deleterious for the realization of a quantum logic gate.

Later, a new system was proposed involving the replacement of phosphorus by bismuth.[23], [24]. Bismuth has a nuclear spin $I = 9/2$, leading to hyperfine interactions. Fortunately, the hyperfine coupling between the electronic and the nuclear spins is significant, resulting in the alignment of the $M_S = 1/2$ $M_I = 9/2 \rightarrow M_S = -1/2$ $M_I = -9/2$ transition with a frequency accessible by conventional EPR. Such a field-independent transition is a clock transition, not sensitive to magnetic fluctuations at least of first order ($df/dB = 0$) hence suppressing one of the most important sources of decoherence and leading to large T_2 for the system.

A threefold increase in the coherence time was observed for the clock transition, leading to $T_2(\text{nuclear}) = 2.7$ s at 4.3 K for a concentration of 3.6×10^{14} spins/cm³. The transition is particularly significant because only one decoherence mechanism remains, the flip-flop one. This purely dipolar mechanism can be quantified by increasing the distance between the spins. However, accessing its value is challenging in practice, as it requires extremely low concentrations ($< 10^{16}$

spins/cm³) and the ability to separate it from other mechanisms such as spectral diffusion. This example represents one of the few examples where all mechanisms have been precisely discriminated.

Silica offers the advantage of being compatible with instrument implementation because the technology is already used in semi-conductor industry. However, in the case of doping with shallow donors, it is not possible to form quantum logic gates and thus perform calculations. Thus, from these two samples, the following conclusions can be drawn:

- (i) The mechanisms related to decoherence have been extracted.
- (ii) Silica constitutes a good matrix for diluting qubits.
- (iii) The clock transition significantly improves the coherence time of the qubit.
- (iv) Spin qubits can compete with other qubit systems.

I.5. MOLECULAR-BASED QUBIT

This demonstration on an assembly of single spins has motivated researchers to continue investigating spin qubits and to shift their focus from studying individual spins to studying a multitude of spins interacting within the same material, such as in molecules.[25] Molecules can be divided into two families: organic radicals,[26] and inorganic molecules. The spin can either be electronic or nuclear. Nuclear spins are typically better isolated from their environment, resulting in longer relaxation times. However, this isolation also makes nuclear spins more challenging to manipulate than electronic spins. The goal is to combine these two types of spins to use electronic spins as information carriers for nuclear spins using (super)hyperfine interaction.

Molecules offer several advantages compared to the previously presented systems. Firstly, it is possible to easily modulate the energy levels corresponding to the qubit, particularly in the case of inorganic molecules. The energy levels of these molecules are entirely defined by their Hamiltonian, and it is known that the energy associated with these levels depends on the coordination sphere, geometry, and symmetry of the molecule. These are parameters that chemists can manipulate, but to a certain extent. Secondly, it is possible to functionalize the

molecules with non-innocent groups in order to initialize the qubit with external stimuli such as light or an electric field. Ultimately molecules are easy to manipulated since they can be studied as powder, oriented single crystals or deposited on surfaces.

I.5.a Qubit embedded in a CT

A significant portion of research on molecules has focused on finding systems that exhibit one or more clock transitions accessible through classical spectroscopic techniques. This approach aims to leverage the protection offered by these transitions to achieve coherence times that can compete with those of superconducting qubits developed by Google or IBM (1 ms). Subsequently, the most relevant examples are described.

I.5.a.i Clock transition induced by hyperfine coupling

Among the molecules studied as qubits, most efforts have been made to obtain clock transition systems based on hyperfine coupling. A Holmium(III)-containing mononuclear complex ($\text{Na}_9[\text{Ho}_x\text{Y}_{(1-x)}(\text{W}_5\text{O}_{18})_2] \cdot n\text{H}_2\text{O}$) stands out as one of the most interesting examples.[27], [28], [29] From a structural point of view, the complex has a slightly distorted square-antiprismatic environment that results in a splitting of the $M_J = \pm 4$ ground sub-levels by 0.3 cm^{-1} leading to two low-lying levels that play the role of a qubit (in zero applied magnetic field), hence a clock transition (see Chapter II for a detailed description of clock transition systems). Here, the unusually large gap corresponds to the X-band EPR frequency (0.33 cm^{-1}). The hyperfine coupling allows the observation of four clock transitions that correspond to resonances with different electron-nuclear spin states $|m_J, m_I\rangle$ with $m_J = \pm 4$ and $m_I = -1/2, -3/2, -5/2, \text{ or } -7/2$ (from low to high fields)

Introduction and state-of-the-art

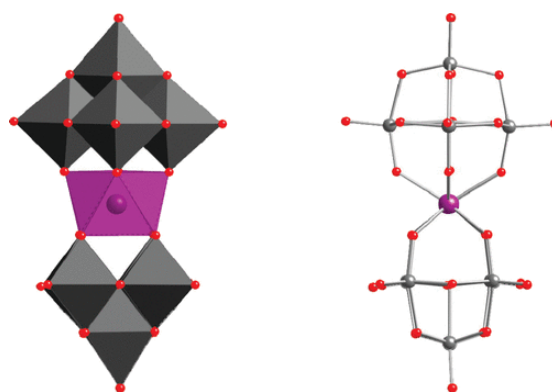


Figure 0-8. Crystallographic structure of $\text{Na}_9[\text{Ho}_x\text{Y}_{(1-x)}(\text{W}_5\text{O}_{18})_2]$. Reproduced from reference [29].

The complex was investigated in the form of oriented single crystals, despite its relatively low crystalline stability (due to a significant number of solvent molecules within the lattice).

Pulsed EPR studies revealed that the coherence time was enhanced by a factor of 80 ($T_2(\text{CT}) = 8 \mu\text{s}$ vs. $T_2(\text{nCT}) = 0.1 \mu\text{s}$) within the clock transitions, which confirms that such transitions are decoupled from the magnetic field fluctuations induced by the nuclear spins bath (solvent H atoms mainly, in this case) and the still close electronic spins from other molecules.

Two phenomena may explain why the coherence time is not so long despite the presence of a clock transition. Firstly, the dilution remains relatively low (0.1 %), indicating that purely dipolar flip-flop mechanisms ($1/r^3$) remain a significant source of decoherence as the clock transition does not protect against this mechanism. Secondly, the T_1 relaxation time remains relatively short ($T_1(5\text{K}) = 20 \mu\text{s}$), and T_2 is limited by T_1 .

Those results are consistent with other examples in the literature as in the case of $\text{Cp}'_3\text{Pr}^-$, [30] or in the case of a Lu(II) complex where the giant hyperfine interaction ($A = 3467 \text{ MHz}$) also leads to a clock transition. It was shown that at the CT the coherence time is 10 times longer than outside the CT ($T_2(\text{CT}) = 12 \mu\text{s}$ vs $T_2(\text{nCT}) = 1 \mu\text{s}$). [31]

Another interesting property of the Ho(III) system is its slight structural distortion, associated with an electric dipole moment. [32] Thus, it is possible to apply an electric field to the molecule to tune the transition frequency value and to discriminate molecules that may be magnetically identical in the crystal but connected by a symmetry element. It was demonstrated that within

the clock transition, the introduction of an electric field, a source of noise, had little influence on the coherence time. It is highly advantageous to obtain systems compatible with the application of an electric field, as it allows for extremely precise modulation of the transition frequency compared to a magnetic field. Moreover, the coupling with an electric field is compatible with device realization.

1.5.a.ii Clock transition induced by ZFS

There exist a unique example of a clock transition directly attributable to zero-field splitting (ZFS) wherein hyperfine coupling does not intervene, namely Cr_7Mn . [33] The metals within these clusters are stabilized through a combination of bidentate carboxylate ligands and monoatomic bridges, typically fluoride or alkoxide groups. The ZFS, lifts the degeneracy of the $S = 1$ state in zero field leading to two low-lying levels with an energy separation of 3.8 GHz. Using a resonator that possesses a frequency (4.4 GHz) close to the energy separation between the two levels allows performing pulsed EPR study on the compound with an applied field of 2 mT.

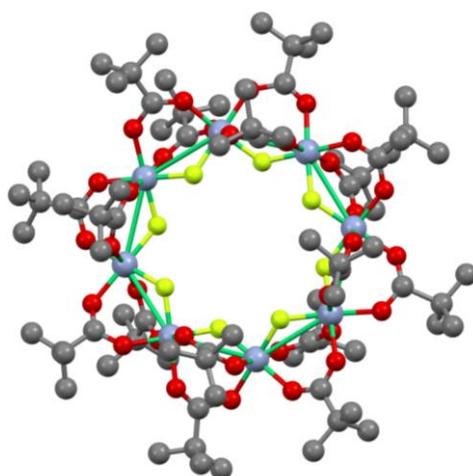


Figure 0-9. Crystallographic structure of Cr_7Mn . Reproduced from reference [33]

The coherence times have been found to be $T_2(\text{CT}) = 0.4 \mu\text{s}$ inside the CT, and $T_2(\text{nCT}) = 0.2 \mu\text{s}$ outside the CT for dilutions ranging from 10 % to 0.5 % in an isomorphous diamagnetic matrix of the complex. Unlike the previous case, the increase in T_2 at the clock transition is minimal. The dilution is still high indicating that at these concentrations, flip-flop processes likely dominate decoherence. However due to the weak signal observed further dilutions were not

possible. Additionally, the report mentions an issue of homogeneity in the dilution process which is coherent with the low signal observed (some molecules aggregate rendering them impossible to be recorded while others are very well isolated and have long coherence time).

I.5.b Qubit non-embedded in a CT

Achieving a clock transition accessible using commercial EPR apparatus is challenging (see Chapter II), that is why less instrumentally restrictive systems are investigated. Now the transition studied will be sensitive to magnetic fluctuations. It is possible to mitigate the effect of those fluctuations by working with spin $S = 1/2$. In fact, in most systems the lift of degeneracy is due to Zeeman effect, in this case the slope of the energy curve is proportional to M_S . Thus, a magnetic fluctuation for a transition involving $M_S = \pm 3/2$ will lead to larger change in the qubit energy than for a transition involving $M_S = \pm 1/2$. Based on this consideration, radicals, Cu(II) or V(IV) have been extensively studied. Some examples are presented in the following section.

I.5.b.i Spin nuclear free molecules

Coordination complexes with organic ligands made from atoms with no nuclear spin (C, O, S) have been proposed. For example, a chemically engineered copper molecule with the organic ligand mnt (maleonitriledithiolate) has shown coherence time of 1 μs at room temperature.[34] For this system (Figure 0-10), $T_2 = 68 \mu\text{s}$ was measured at 7 K and for a copper concentration in diamagnetic matrix of 0.001%. This coherence time rivals those of molecules featuring clock transitions.

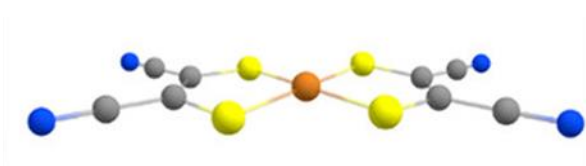


Figure 0-10. Crystallographic structure of $[\text{Cu}(\text{mnt})_2]^{2+}$. Reproduced from reference [35]

Furthermore, it is anticipated that this time could even be increased further in the absence of a counter-anion containing protons. These protons have facilitated the observation that magnetic fluctuation is proportional to the magnetic moment of the atom in question. Notably,

the coherence time T_2 is observed to be 10 times longer when the counter-anion is deuterated.[35]

This concept was further developed by D. Freedman, who synthesized a vanadium complex, $(\text{Bu}_4\text{N})_2[\text{V}(\text{C}_8\text{S}_8)_3]$ (Figure 0-11), [36] free of nuclear spins and diluted in a solvent, CS_2 , also lacking nuclear spins. At a relatively high concentration of $3 \cdot 10^{17}$ spins/ cm^3 and at 10 K, a T_2 value of 675 μs was obtained, which is to date the longest coherence time recorded for a molecule. In this series of compounds, nuclear spins were progressively distanced from the molecule, highlighting the existence of a radial zone for which nuclear spins had no significant impact on T_2 . From a synthetic point of view this strategy is limited because one needs to do nuclear free chemistry, which means that H/N/X (where X = F, Cl, Br, I) atoms cannot be used. Numerous other studies on vanadium-based molecules have been conducted by R. Sessoli's group, focusing particularly on the influence of geometry on relaxation times [37].

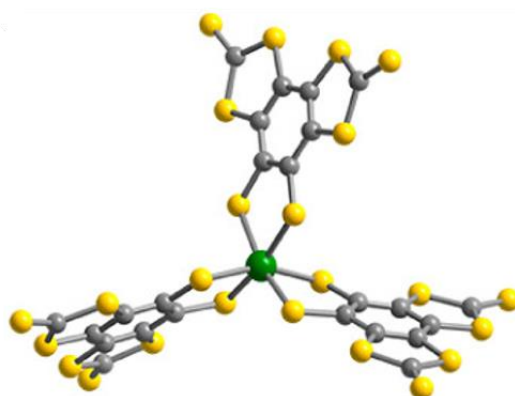


Figure 0-11. Crystallographic structure of $[\text{V}(\text{C}_8\text{S}_8)_3]^{2+}$. Reproduced from reference [36]

1.5.b.ii Radical-based systems

Radical-based systems especially the ones using enzymes, have been highly investigated, mainly by biologists.[38]. Radicals have the advantages of being extremely well-defined because their Lande factor (g) value does not change regarding the chemical environment. This is why they exhibit naturally long coherence times and also lead to very sharp transitions in EPR (hence a very intense signal), thus allowing to perform experiments in very diluted systems. Recently, J. Van Slageren and coworkers have investigated a biradical system called bPTM (Figure 0-12) that possesses a long coherence time $T_2 = 148 \mu\text{s}$ for temperatures below 100K.

Introduction and state-of-the-art

The two radicals have been separated using an alkyne-based spacer. The addressability of each qubit was also evidenced, thus demonstrating that it can play the role of a two-qubit gate.[39]

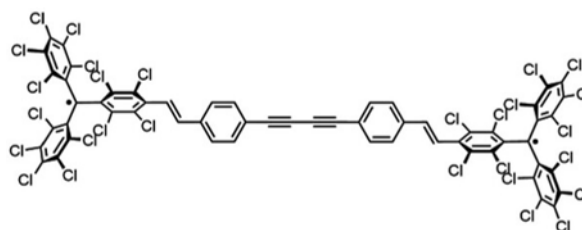


Figure 0-12. Chemical structure of bPTM.

A Japanese team led by T. Takui has also presented a system based on a biradical molecule.[40] Each radical corresponds to a TEMPO moiety that has been deuterated. The radicals have been separated by a long bridging ligand inducing a very small antiferromagnetic coupling, which is one of the requirements to act as a genuine two-qubit gate.

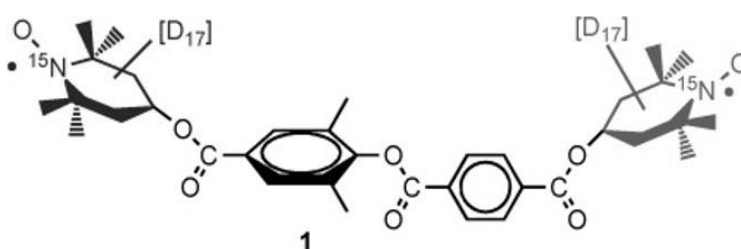


Figure 0-13. Chemical structure of 2,2,6,6-tetramethylpiperidin-*N*-oxyl-4-yl 3,5-dimethylbenzoate-4-yl terephthalate. Reproduced from ref [40].

1.5.c From mononuclear to polynuclear complexes

All the molecules presented so far have demonstrated the potential of using molecules as qubits and have shown that they can compete with the superconductor-based systems in terms of coherence time. The next step is to implement quantum algorithm on the molecule, to do so is it necessary to couple at least two qubits (the case of radicals is presented in the previous section). G. Aromí and co-workers theoretically demonstrated the feasibility of realizing quantum logic gates with inorganic molecules and proposed systems possessing all the necessary characteristics to do so,[41], [42]. The ligand used H₃L (6-[3-oxo-3-(2-hydroxyphenyl)-propionyl]pyridine-2-carboxylic acid) exhibits seven different donor atoms and three distinct chelating pockets, enabling the possibility of asymmetrical coordination

sphere. The resulting trinuclear system obtained with lanthanides (Ln^{3+}) in an ABA series exhibits three different coordination spheres and weak coupling rendering possible a precise addressability of each qubit. Thus, the system could act as quantum logic gate,[43] and be directly compatible with error correction algorithms. [44]

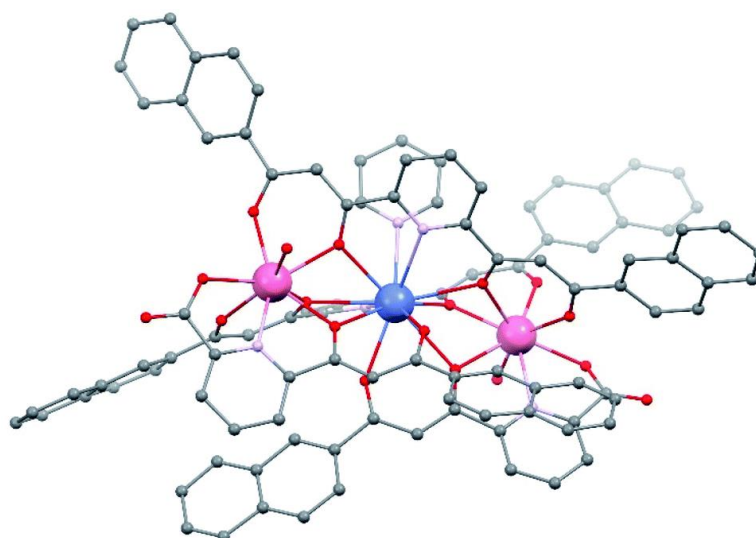


Figure 0-14. Representation of the molecular structure of $[\text{Er}_2\text{Pr}(\text{LA})_2(\text{LB})_2(\text{py})(\text{H}_2\text{O})_2](\text{NO}_3)$. Colors: pink, Er; blue, Pr; red, O; grey, C; purple, N. Reproduced from reference [43].

Recently R. Sessoli *et al.* have proposed a heteronuclear compound based on V(IV)-Cu(II) bisporphyrin (Figure 0-15).[45] The choice of the metallic ions has been motivated by two factors. On the one hand, $S = 1/2$ species possesses long coherence times, as previously mentioned for V(IV) and Cu(II). The assumption was that the property of the monomeric unit will remain the same inside the dimer. On the other hand, the difference in g value allows one to address specifically one or the other metallic centre with pulsed EPR. However, they did not perform any DEER sequence in order to precisely determine the coupling between the two centres in order to experimentally prove the possibility to form a quantum logical gate. The only coupling given is $J = 8 \cdot 10^{-3} \text{ cm}^{-1}$ which was obtained with X band cw-EPR.

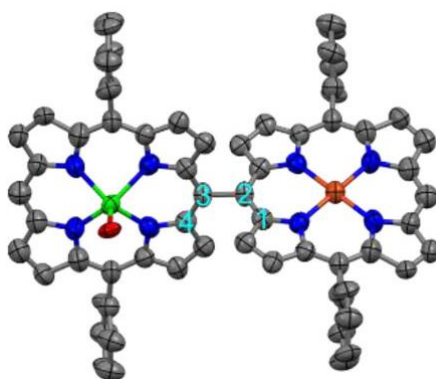


Figure 0-15. Structure of heterometallic meso-meso (m-m) singly-linked $V^{VO}-Cu^{II}$ porphyrin dimer. Reproduced from reference [45].

The next step is to prove that it is possible to realize quantum logic gates using these molecules. Up to now, the only experimental evidence of the implementation of a quantum algorithm on a molecule was made by W. Wernsdorfer who implemented the Grover algorithm on a single molecule that has four levels (qudit) stemming from the coupling between the electronic and the nuclear spins of a Tb(III) atom of (TbPc₂) [46].

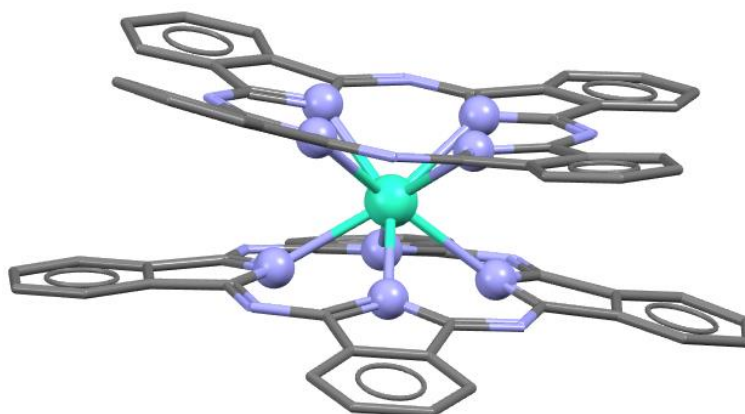


Figure 0-16. Crystallographic structure of [TbPc₂].

I.6 CONCLUSION

The major difficulty faced by chemists is of instrumental nature. Indeed, a variety of molecules has been synthesized, and many of them possess all the characteristics for the realization of quantum logic gates. However, no experimental measurements are available. The first reason concerns the measurement method, namely Electron Paramagnetic Resonance. This technique suffers from the fact that there are very few accessible tunable cavities and the accessible frequency ranges are very restricted. Consequently, properties such as the clock transition, which enables long coherence times and is inherently present in many systems, cannot be exploited.

In addition to the problems of accessible frequencies, there is the issue of echo detection. To increase the coherence time of a molecule, it is necessary to dilute it in order to isolate it. This strategy is interesting in the case of molecules since it is not necessary to couple them together because, unlike doping in silicon, they possess all the necessary resources to perform an operation. However, the detection limits of devices make it very difficult to observe an echo for spin concentrations below 10^{15} . Few instruments are capable of studying single-molecule systems, and the principle of combining Scanning Tunnelling Microscopy (STM) and EPR was only demonstrated in 2023.[47] Also, in 2023, P. Bertet *et al.* have developed an ultra sensitive detector in the microwave region relevant to electronic spins capable of measuring one molecule.[48] The increased sensitivity combined with the development of new cavities will allow one to study ultra diluted systems or to fully exploit the CT.

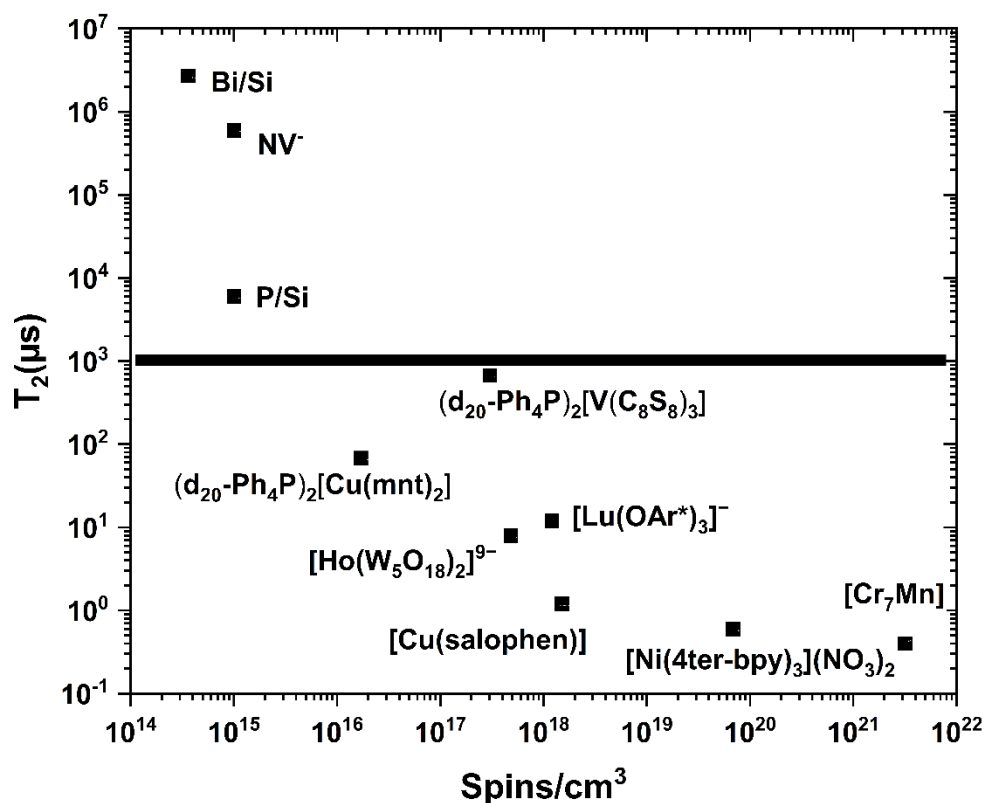


Figure 0-17. Coherence time of spins-based qubit. Below the black line, systems that have coherence times too short, above the black line, system that actually possess coherence times long enough to be used.

In conclusion, this brief state-of-the-art review has highlighted that molecules can be promising candidates as qubits (Figure 0-17) or quantum logic gates. However, there are only few families of referenced compounds. In this manuscript, we propose several systems that could bring useful insight on the qubit gate realization.

I.7 REFERENCES

- [1] R. P. Feynman, *Int J Theor Phys* **1982**, *21*, 467–488.
- [2] P. W. Shor *SIAM Journal on Computing*, **1997**, *26*, 5
- [3] L. K. Grover, *arXiv* **1996**, DOI [10.48550/arXiv.quant-ph/9605043](https://doi.org/10.48550/arXiv.quant-ph/9605043).
- [4] P. C. E. Stamp, A. Gaita-Ariño, *J. Mater. Chem.* **2009**, *19*, 1718–1730.
- [5] G. J. Milburn, *Phys. Scr.* **2009**, *T137*, 014003.
- [6] I. Bloch, *Nature* **2008**, *453*, 1016–1022.
- [7] D. P. DiVincenzo, *Fortschritte der Physik* **2000**, *48*, 771–783.
- [8] M. Steffen, D. P. DiVincenzo, J. M. Chow, T. N. Theis, M. B. Ketchen, *IBM J. Res. & Dev.* **2011**, *55*, 13:1-13:11.
- [9] U. Skosana, M. Tame, *Sci Rep* **2021**, *11*, 16599.
- [10] J. L. Chuang, L. M. K. Vandersypen, X. Zhou, D. W. Leung, S. Lloyd, *Nature* **1998**, *393*, 143–146.
- [11] F. Arute, K. Arya, R. Babbush, D. Bacon, J. C. Bardin, R. Barends, R. Biswas, S. Boixo, F. G. S. L. Brandao, D. A. Buell, B. Burkett, Y. Chen, Z. Chen, B. Chiaro, R. Collins, W. Courtney, A. Dunsworth, E. Farhi, B. Foxen, A. Fowler, C. Gidney, M. Giustina, R. Graff, K. Guerin, S. Habegger, M. P. Harrigan, M. J. Hartmann, A. Ho, M. Hoffmann, T. Huang, T. S. Humble, S. V. Isakov, E. Jeffrey, Z. Jiang, D. Kafri, K. Kechedzhi, J. Kelly, P. V. Klimov, S. Knysh, A. Korotkov, F. Kostritsa, D. Landhuis, M. Lindmark, E. Lucero, D. Lyakh, S. Mandrà, J. R. McClean, M. McEwen, A. Megrant, X. Mi, K. Michielsen, M. Mohseni, J. Mutus, O. Naaman, M. Neeley, C. Neill, M. Y. Niu, E. Ostby, A. Petukhov, J. C. Platt, C. Quintana, E. G. Rieffel, P. Roushan, N. C. Rubin, D. Sank, K. J. Satzinger, V. Smelyanskiy, K. J. Sung, M. D. Trevithick, A. Vainsencher, B. Villalonga, T. White, Z. J. Yao, P. Yeh, A. Zalcman, H. Neven, J. M. Martinis, *Nature* **2019**, *574*, 505–510.
- [12] F. Jelezko, T. Gaebel, I. Popa, M. Domhan, A. Gruber, J. Wrachtrup, *Phys. Rev. Lett.* **2004**, *93*, 130501.
- [13] I. Bloch, *Nature* **2008**, *453*, 1016–1022.
- [14] A. Schweiger, G. Jeschke, A. Schweiger, G. Jeschke, *Principles of Pulse Electron Paramagnetic Resonance*, Oxford University Press, Oxford, New York, **2001**.
- [15] J. M. Frost, K. L. M. Harriman, M. Murugesu, *Chem. Sci.* **2016**, *7*, 2470–2491.
- [16] H. Morishita, S. Kobayashi, M. Fujiwara, H. Kato, T. Makino, S. Yamasaki, N. Mizuochi, *Sci Rep* **2020**, *10*, 792.

- [17] H. J. Mamin, M. Kim, M. H. Sherwood, C. T. Rettner, K. Ohno, D. D. Awschalom, D. Rugar, *Science* **2013**, 339, 557–560.
- [18] B. e. Kane, *Fortschritte der Physik* **2000**, 48, 1023–1041.
- [19] H. Büch, S. Mahapatra, R. Rahman, A. Morello, M. Y. Simmons, *Nat Commun* **2013**, 4, 2017.
- [20] A. M. Tyryshkin, S. Tojo, J. J. L. Morton, H. Riemann, N. V. Abrosimov, P. Becker, H.-J. Pohl, T. Schenkel, M. L. W. Thewalt, K. M. Itoh, S. A. Lyon, *Nature Mater* **2012**, 11, 143–147.
- [21] G. Feher, E. A. Gere, *Phys. Rev.* **1959**, 114, 1245–1256.
- [22] W. M. Witzel, M. S. Carroll, A. Morello, Ł. Cywiński, S. Das Sarma, *Phys. Rev. Lett.* **2010**, 105, 187602.
- [23] J. J. L. Morton, A. M. Tyryshkin, R. M. Brown, S. Shankar, B. W. Lovett, A. Ardavan, T. Schenkel, E. E. Haller, J. W. Ager, S. A. Lyon, *Nature* **2008**, 455, 1085–1088.
- [24] G. Wolfowicz, A. M. Tyryshkin, R. E. George, H. Riemann, N. V. Abrosimov, P. Becker, H.-J. Pohl, M. L. W. Thewalt, S. A. Lyon, J. J. L. Morton, *Nature Nanotech* **2013**, 8, 561–564.
- [25] Daniel Loss and David P. DiVincenzo, *Phys. Rev. A* **1998**, 57, 120
- [26] D. Schäfter, J. Wischnat, L. Tesi, J. A. De Sousa, E. Little, J. McGuire, M. Mas-Torrent, C. Rovira, J. Veciana, F. Tuna, N. Crivillers, J. van Slageren, *Advanced Materials* **2023**, 35, 2302114.
- [27] K. Kundu, J. R. K. White, S. A. Moehring, J. M. Yu, J. W. Ziller, F. Furche, W. J. Evans, S. Hill, *Nat. Chem.* **2022**, 14, 392–397.
- [28] S. Giménez-Santamarina, S. Cardona-Serra, J. M. Clemente-Juan, A. Gaita-Ariño, E. Coronado, *Chem. Sci.* **2020**, 11, 10718–10728.
- [29] M. Shiddiq, D. Komijani, Y. Duan, A. Gaita-Ariño, E. Coronado, S. Hill, *Nature* **2016**, 531, 348–351.
- [30] P. W. Smith, J. Hrubý, W. J. Evans, S. Hill, S. G. Minasian, *J. Am. Chem. Soc.* **2024**, 146, 5781–5785.
- [31] K. Kundu, J. R. K. White, S. A. Moehring, J. M. Yu, J. W. Ziller, F. Furche, W. J. Evans, S. Hill, *Nat. Chem.* **2022**, 14, 392–397.
- [32] J. Liu, J. Mrozek, A. Ullah, Y. Duan, J. J. Baldoví, E. Coronado, A. Gaita-Ariño, A. Ardavan, *Nat. Phys.* **2021**, 17, 1205–1209.
- [33] C. A. Collett, K.-I. Ellers, N. Russo, K. R. Kittilstved, G. A. Timco, R. E. P. Winpenny, J. R. Friedman, *Magnetochemistry* **2019**, 5, 4.

- [34] K. Bader, D. Dengler, S. Lenz, B. Endeward, S.-D. Jiang, P. Neugebauer, J. van Slageren, *Nat Commun* **2014**, *5*, 5304.
- [35] K. Bader, M. Winkler, J. van Slageren, *Chem. Commun.* **2016**, *52*, 3623–3626.
- [36] C.-J. Yu, M. J. Graham, J. M. Zadrozny, J. Niklas, M. D. Krzyaniak, M. R. Wasielewski, O. G. Poluektov, D. E. Freedman, *J. Am. Chem. Soc.* **2016**, *138*, 14678–14685.
- [37] M. Atzori, E. Morra, L. Tesi, A. Albino, M. Chiesa, L. Sorace, R. Sessoli, *J. Am. Chem. Soc.* **2016**, *138*, 11234–11244.
- [38] F. Soualmia, M. V. Cherrier, T. Chauviré, M. Mauger, P. Tatham, A. Guillot, X. Guinchard, L. Martin, P. Amara, J.-M. Mouesca, M. Daghmoum, A. Benjdia, S. Gambarelli, O. Berteau, Y. Nicolet, *J. Am. Chem. Soc.* **2024**, *146*, 6493–6505.
- [39] D. Schäfter, J. Wischnat, L. Tesi, J. A. De Sousa, E. Little, J. McGuire, M. Mas-Torrent, C. Rovira, J. Veciana, F. Tuna, N. Crivillers, J. van Slageren, *Advanced Materials* **2023**, *35*, 2302114.
- [40] S. Nakazawa, S. Nishida, T. Ise, T. Yoshino, N. Mori, R. D. Rahimi, K. Sato, Y. Morita, K. Toyota, D. Shiomi, M. Kitagawa, H. Hara, P. Carl, P. Höfer, T. Takui, *Angewandte Chemie International Edition* **2012**, *51*, 9860–9864.
- [41] G. Aromí, D. Aguilà, P. Gamez, F. Luis, O. Roubeau, *Chem. Soc. Rev.* **2012**, *41*, 537–546.
- [42] F. Luis, A. Repollés, M. J. Martínez-Pérez, D. Aguilà, O. Roubeau, D. Zueco, P. J. Alonso, M. Evangelisti, A. Camón, J. Sesé, L. A. Barrios, G. Aromí, *Phys. Rev. Lett.* **2011**, *107*, 117203.
- [43] D. Maniaki, D. Garay-Ruiz, L. A. Barrios, D. O. T. A. Martins, D. Aguilà, F. Tuna, D. Reta, O. Roubeau, C. Bo, G. Aromí, *Chem. Sci.* **2022**, *13*, 5574–5581
- [44] E. Macaluso, M. Rubín, D. Aguilà, A. Chiesa, L. A. Barrios, J. I. Martínez, P. J. Alonso, O. Roubeau, F. Luis, G. Aromí, S. Carretta, *Chem. Sci.* **2020**, *11*, 10337–10343.
- [45] D. Ranieri, A. Privitera, F. Santanni, K. Urbanska, G. J. Strachan, B. Twamley, E. Salvadori, Y.-K. Liao, M. Chiesa, M. O. Senge, F. Totti, L. Sorace, R. Sessoli, *Angewandte Chemie International Edition* **2023**, *62*, e202312936.
- [46] C. Godfrin, A. Ferhat, R. Ballou, S. Klyatskaya, M. Ruben, W. Wernsdorfer, F. Balestro *Phys. Rev. Lett.* **2017**, *119*, 187702
- [47] Y. Wang, M. Haze, H. T. Bui, W. Soe, H. Aubin, A. Ardavan, A. J. Heinrich, S. Phark, *npj Quantum Inf* **2023**, *9*, 1–6.
- [48] A. Bienfait, J. J. Pla, Y. Kubo, M. Stern, X. Zhou, C. C. Lo, C. D. Weis, T. Schenkel, M. L. W. Thewalt, D. Vion, D. Esteve, B. Julsgaard, K. Mølmer, J. J. L. Morton, P. Bertet, *Nature Nanotech* **2016**, *11*, 253–257.

**CHAPTER I: ELECTRONIC STRUCTURE OF
MONONUCLEAR Ni(II) COMPLEXES AS $S = 1$
SPIN QUBITS**

The objective of this chapter is to rationalize the ZFS parameters (anisotropy) of Ni(II) complexes and see how one can control them to find interesting compounds with an accessible clock transition. We will, therefore, first briefly introduce the concept of electronic clock transition for integer spin systems to justify our interest in investigating the spin structure of the mononuclear Ni(II) complexes.

I.1 CONCEPT OF CLOCK TRANSITION ($S = 1$)

For a (spin) qubit, one of the basic operations is the achievement of a superposition between the two states of the two-level system that lasts long enough for one to implement a gate operation for example. In other words, the system must have a relatively long coherence time (T_2). One of the main sources of decoherence is the fluctuation of the magnetic field from the surroundings (spin bath, nuclear and electronic) that alters the energy difference between the two levels put in superposition. One possible solution to increase the coherence time is to operate within a transition that is as insensitive as possible to the magnetic field fluctuations. A (spin) clock transition is a class of transitions in which a fluctuation of the magnetic field does not change the energy of the transition to the first order. [1], [2] The variation of the spin sublevels energy with the magnetic field follows the scheme depicted in Figure I-1. At zero field and for fields very close to zero (region 1), the derivative of the energy to the field is equal to zero, so that magnetic fluctuations do not affect the energy difference, this is called a clock transition. In region 2, a fluctuation in the magnetic field only slightly alters the transition energy ($\Delta E = \alpha g\beta\Delta B$ with $\alpha < 1$). Similarly, as long as $\alpha < 1/2$, the variation remains less significant than in the case of a half-integer spin. In region 3, outside the CT region, the magnetic field fluctuation causes a variation that is proportional to the transition energy ($\Delta E = g\beta\Delta B$).

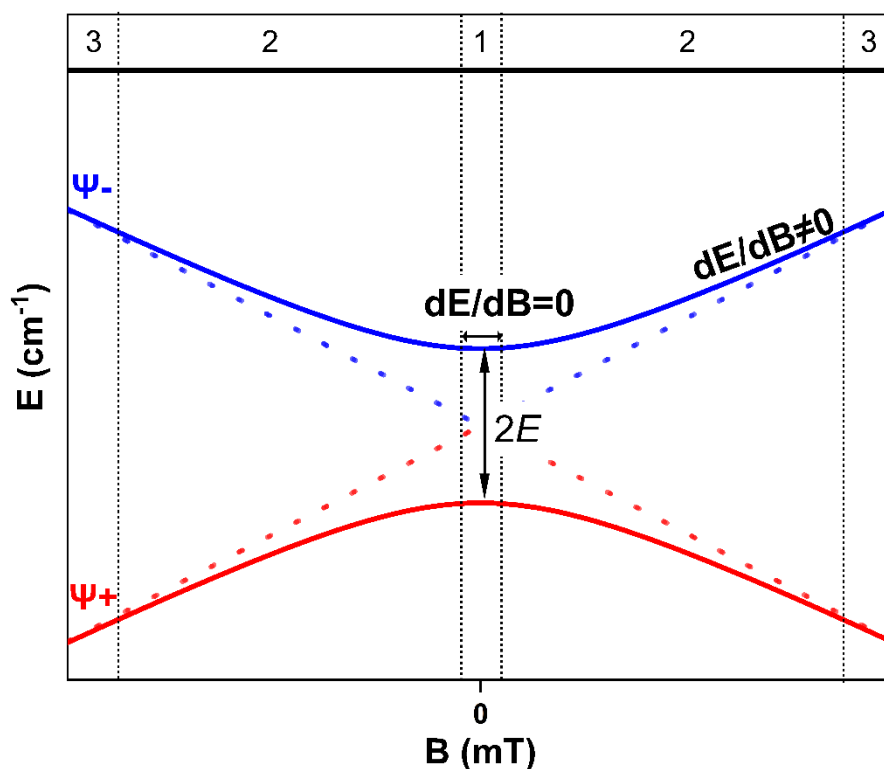


Figure I-1. Zeman level for $S=1$

To obtain a clock transition, three conditions must be fulfilled: i) the complex must have an integer spin, ii) an uniaxial anisotropy, and iii) a weak rhombicity (see next sections).

I.2 INTRODUCTION

We use the spin levels of a spin state as a qubit, and if we aim at producing a clock transition, the spin levels must be an integer, neglecting the hyperfine coupling between local electronic and nuclear spins. The simplest system that can be considered is a $S = 1$ (with $M_s = 0, \pm 1$) complex and Ni(II) complexes are the best choice because Ni does not possess a nuclear spin. We will, therefore, focus on understanding the spin structure (ZFS) of such complexes. We want to obtain a lift of the three-fold degeneracy of the $S = 1$ spin state to obtain two low-lying levels with a magnetic field energy dependence similar to the one of Figure I-1, for which EPR can be used to induce a superposition of the states. Furthermore, one must be able to adjust the energy of the transition to the EPR cavity in order to exploit it, due to the fact that today's commercial devices only operate at fixed frequencies (9.64 GHz and 34 GHz).

Chapter I: Electronic structure of mononuclear Ni(II) complexes as $S = 1$ spin qubits

The question that arises is: how can we engineer the ligand field in the coordination sphere of Ni(II) to obtain such lift of degeneracy? The following chapter aims to demonstrate that the ZFS of the M_S sub-levels can be, to a certain extent addressed chemically.

The understanding of the origin of ZFS and its relation to the geometrical structure of Ni(II) complexes has been (and still is) extensively investigated in our laboratory over the past 20 years. We have established general qualitative rules that allow from the crystallographic structure of Ni(II) complexes, [3], [4] and thanks to wavefunction type quantum chemical calculations, to predict ZFS to a certain extent. The accuracy of the calculation is sufficient to be used to design targeted molecules for our purpose.

In this chapter, we start by elucidating the physical origins of ZFS (Part II.2.a) and how it can be harnessed to realize a clock transition (Part II.2.b). Subsequently, we will examine the applicability of these principles to a selection of Ni(II) compounds exhibiting varying symmetries (Part II.3.a/b/c). Finally, we will address the feasibility, to some extent, of controlling ZFS by introducing minor structural variations in the molecule and/or in the crystal lattice (Part II.3.d).

I.2 INTRODUCTION ON ZERO-FIELD SPLITTING

For an isolated paramagnetic ion, the absence of a ligand field leads to a magnetically isotropic system i.e. the ground state spin levels are degenerate. In the presence of a ligand field (i.e. for a complex), a lift of the degeneracy of the m_s levels can be observed if the symmetry is lower than cubic. This is known as zero-field splitting (ZFS), and is characterised by the two parameters D and E obtained from the following spin Hamiltonian:

$$H = \mathbf{S} \cdot \mathbf{D} \cdot \mathbf{S} \quad (\text{II-1})$$

Where \mathbf{S} is the spin operator and \mathbf{D} a tensor. The Hamiltonian can be reduced to the following form:

$$H = DS_z^2 + E(S_x^2 - S_y^2) \quad (\text{II-2})$$

where D and E are the axial and rhombic ZFS parameters, respectively. They are related to the three diagonal matrix elements of the \mathbf{D} tensor. D corresponds to the energy difference between the $M_s = 0$ sublevel and the centre of gravity of the two $M_s = \pm 1$ levels, and $2E$ to the energy difference between the $M_s = \pm 1$ sublevels. There are two cases (Figure I-2): $D > 0$ and $D < 0$ depending on the effect of the ligand field. For $D < 0$ (and $E \neq 0$), the two $M_s = \pm 1$ levels have the lowest energy, which leads to two low-lying levels and corresponds, therefore, to the definition of a qubit. This system is easy to initialise by reducing the temperature. [5] For positive D values, it is possible to consider the $M_s = 0$ level and one of the $M_s = \pm 1$ as a two-level system, but the relaxation time of a superposed state is expected to be shorter than that between the two $M_s = \pm 1$ sub-levels, because the transition is allowed ($\Delta M_s = \pm 1$, for the microwave perpendicular mode of the cavity). We will now rationalise the origin and nature of ZFS.

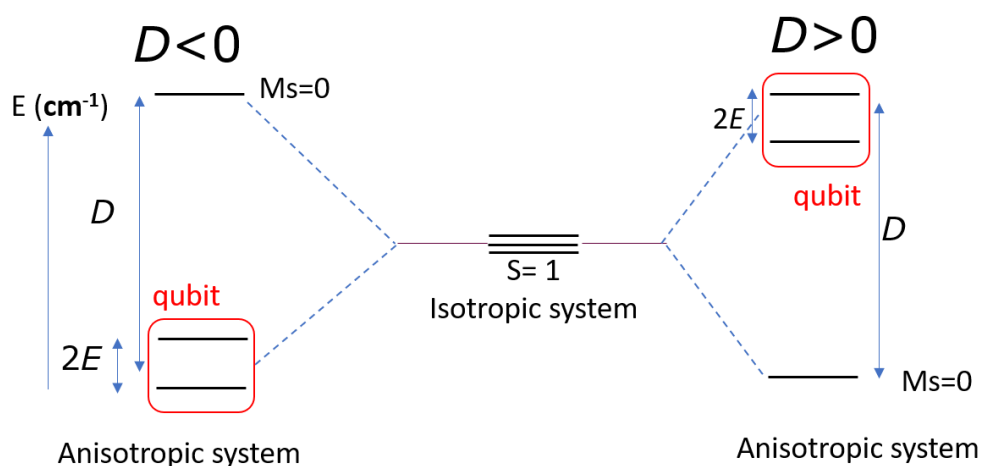


Figure I-2. Zero field splitting for spin $S=1$

I.2.a Origin of ZFS

ZFS is the result, for a complex, of the conjugated effects of spin-orbit coupling (SOC) and a low ligand field symmetry. Understanding the physical phenomena involved is fundamental to modulate and control the energy of the spin levels and hence the properties of the qubits. The various parameters will be described in detail below.

Hexacoordinated NiL_6 complexes generally adopt an octahedral geometry. For strict O_h symmetry, the ground electronic state is ${}^3A_{2g}$, with no orbital angular momentum, the three M_s sublevels are therefore degenerate and no axial magnetic anisotropy is expected. The admixture of the ground state with the excited states having the same spin multiplicity (${}^3T_{1g}$, ${}^3T_{2g}$ and ${}^3T_{1g}$) via the spin-orbit operator brings some orbital momentum to the ground state. However, this admixture does not lift the degeneracy of the ground spin states in O_h symmetry because the three components of the orbital angular momentum (L_x , L_y and L_z) are base of the triply degenerate irreducible representation T_{1g} of O_h . Because the three-fold degeneracy of the ground state is not lifted by the second order spin-orbit coupling, ZFS does not occur and consequently the magnetic anisotropy remains equal to zero. In order to obtain a ZFS for the ground state, the spin-orbit coupling must be different in the three directions of space (rhombic anisotropy) or at least in two directions of space (axial anisotropy) [6]. This can be achieved if the symmetry of the hexacoordinate complex is lower than O_h , in other terms, if the complex is distorted. If the distortion is axial (D_{4h} , C_{4v} , etc. symmetry), the rhombic term (E) will be equal to zero and the axial term (D) will be different from zero. If the distortion is lower

than axial, the E term becomes different from zero as depicted in Figure I-2. The sign of D depends on the nature of the distortion. For hexacoordinate complexes, an axial *tetragonal compression* leads to a negative D value, while an axial *tetragonal elongation* to a positive D value (Figure I-2). The situation is, generally, reversed for a *trigonal* distortion.

With these simple ideas in mind, one can try to engineer the coordination sphere of Ni(II) complexes to prepare molecules with the desired magnetic structure. It is clear that for low symmetry complexes, it is not possible to do any prediction. One example of such a case is given and analysed below. In order for a molecule to behave as a qubit (low-lying two-levels), one must prepare complexes with a negative D value and try as much as possible to tune the rhombic parameter in order to match the EPR electromagnetic radiation energy (X-, Q-band or W-band). However, it is important to bear in mind that the notion of distortion is electronic and not only structural. It can be structural if the ligands in the coordination sphere of Ni(II) have very close electronic effects as we will see in the examples detailed below.

For the case discussed above where ZFS stems from second order SCO (coupling between the ground and excited states), the magnitude of D is inversely proportional to the energy difference between the ground and the excited states and is proportional to the strength of the SOC. We will not discuss the case where first order SOC occurs because this cannot be the case for hexacoordinate complexes. It is worth stressing that we are interested in hexacoordinate complexes with distorted octahedral geometry in order to obtain weak ZFS, because as we mentioned above, we use EPR transitions that are in the microwave energy range ($0 - 1 \text{ cm}^{-1}$) to manipulate the qubits, so that ZFS must be in this energy range. If we had access to pulsed EPR apparatus with larger incident quantum energy, we would have prepared complexes with larger ZFS values. For the D parameter, a large value means a better separation between the $M_S = \pm 1$ sublevels and the $M_S = 0$ allowing one to operate at higher temperatures. For the E parameter, in the case of a clock transition, a larger value means a better-quality factor of the CT. i.e. a larger protection range.[7] This is due to the fact that for a large E value, a larger magnetic field is required to change the slope of the Energy = $f(B)$ curves, so that the difference remains close to zero for larger values of the magnetic field and hence the protection from magnetic fluctuations. This is possible for pentacoordinate complexes with weaker ligand fields, where the difference in energy between the ground and the excited states are weaker

than for hexacoordinate complexes, leading to larger D values, and eventually larger E values [3].

1.2.b Rationalisation of the sign of D

In order to rationalize the magnitude and the sign of the axial parameter D , we use the results of wavefunction based quantum chemical calculations including SOC. The calculations provide the contributions of the different excited states (D_i) to the overall D value of the complex. Details on the calculations of some Ni(II) complexes can be found in references [3] and [4].

The overall D value for the complex is taken as the sum of the D_i values of the excited state. D_i is proportional to the SOC matrix element between the ground and the excited state considered, that determine its sign, and is inversely proportional to the energy difference between the ground and the corresponding excited state.

The spin-orbit Hamiltonian is given by the following expression:

$$H = \sum \zeta [l_z s_z + \frac{1}{2}(l_- s_+ + l_+ s_-)] \quad (II-3)$$

where ζ is the spin orbit constant, l_i and s_i refer to the local orbital and spin angular moments operators, respectively.

This Hamiltonian is composed of two parts: one along the z and one along the x, y directions. It is then possible to analyze the magnitude of each component considering a coupling between a ground and an excited state. Here, we restrain our analysis to the coupling between the ground state and the excited states with same spin multiplicity, so triplets in the case of Ni(II) complexes. An excited state is obtained thanks to an excitation between d orbitals. Let us remind that the d orbitals have the following orbital momentum values $m_l = \pm 2$ ($d_{xy}, d_{x^2-y^2}$), $m_l = \pm 1$ (d_{yz}, d_{xz}), and $m_l = 0$ (d_{z^2}). The excitations may, thus, occur between orbitals with the same m_l values or with different m_l values. If Δm_l is equal to two, the SOC does not operate since it does not have a term that couples orbital momenta that differ by 2. It can couple only m_l values that are equal ($\Delta m_l = 0$), along the z direction so that the $l_z s_z$ component shall be considered, or that differ by one ($\Delta m_l = \pm 1$) along the x and y directions, the $l_- s_+ + l_+ s_-$ part the SO Hamiltonian is considered in such a case. For example, an excitation involving the d_{xy}

Chapter I: Electronic structure of mononuclear Ni(II) complexes as $S = 1$ spin qubits

and $d_{x^2-y^2}$ orbitals allows a coupling between the two corresponding states by $l_z s_z$, therefore aligning the spin angular momentum along the orbital one along the z direction (Figure I-3). While if the excitation involves d_{xz} and $d_{x^2y^2}$ with $\Delta m_l = \pm 1$, the two states are coupled by the $(l_- s_+ + l_+ s_-)$ part of the SO Hamiltonian. The orbital angular momentum blocks the spin angular momentum in the plane perpendicular to the z axis.

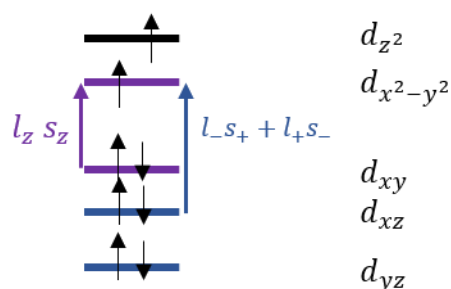


Figure I-3 Energy diagram of d orbitals in a Nickel (II) complex for an octahedral geometry. Blue energy levels correspond to $\Delta m_l = \pm 1$, purple energy levels correspond to $m_l = \pm 2$ and black energy levels correspond to $\Delta m_l = 0$.

We will show now that when Δm_l between the ground and excited states is equal to 0, the $M_S = \pm 1$ sublevels are stabilized ($D_i < 0$, see Figure I-2) and when $\Delta m_l = \pm 1$, the $M_S = 0$ sublevel is stabilized ($D_i > 0$, see Figure I-2). When the $l_z s_z$ part of the SO Hamiltonian couples the ground and the excited states, the $M_S = +1$ of these two states interact leading to a stabilization of the ground M_S and destabilization of the excited M_S levels (see Figure I-4-left). The same situation occurs for the two $M_S = -1$ sublevels. While for the two $M_S = 0$ sublevels, the calculation of the interaction matrix element gives zero and no stabilization occurs. The net result is a stabilization of the M_S sublevels ± 1 belonging to the ground state (Figure I-4-left). The same reasoning holds when the $(l_- s_+ + l_+ s_-)$ acts. As depicted in Figure I-4-right, the $M_S = 0$ sublevel of the ground state interacts with the $M_S = +1$ and the $M_S = -1$ sublevels of the excited state (red arrows in Figure I-4-right), while the $M_S = \pm 1$ sublevels of the ground state interact each with the $M_S = 0$ sublevel of the excited states, leading to a larger stabilization of the $M_S = 0$ sublevel of the ground state over the $M_S = \pm 1$ sublevels, which corresponds to a positive D_i value (Figure I-4-right).

Chapter I: Electronic structure of mononuclear Ni(II) complexes as $S = 1$ spin qubits

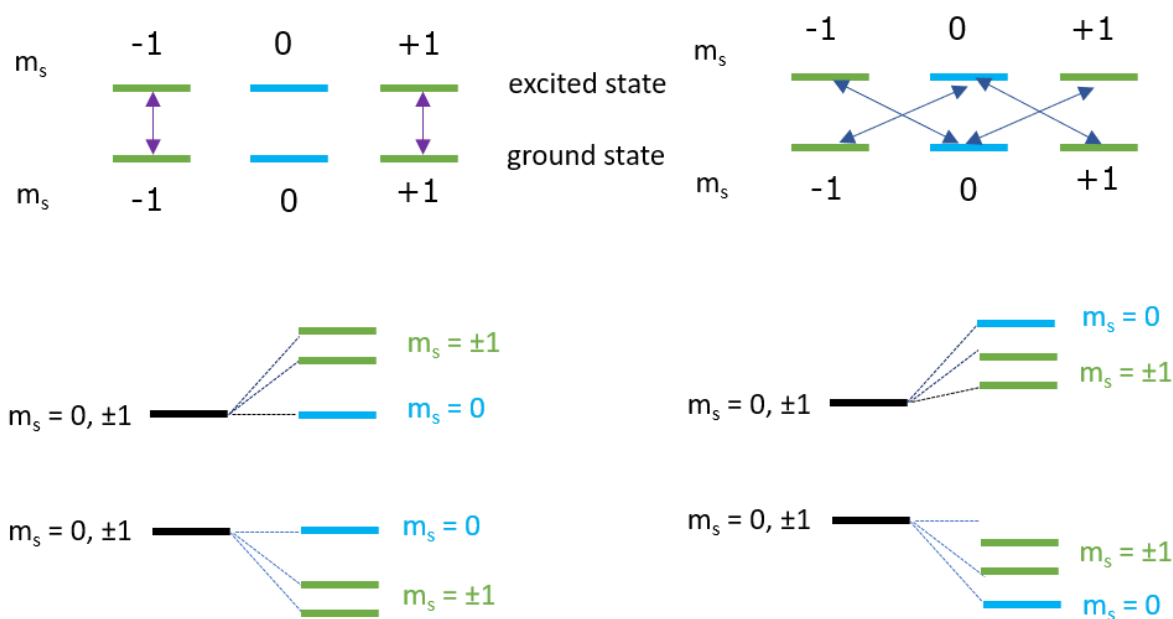


Figure I-4. Schematic representation of the stabilization or destabilization of M_s levels depending of the transition observed.

For a given complex, there are several contributions (D_i) corresponding to the different excited states coupled to the ground state, some may be negative and some positive. In order to have an overall negative value, the negative contributions must be larger in absolute value. Therefore, the relative energy of the d orbitals plays a major role in determining the sign of D . At a very simple level, coordination chemistry allows to a certain extent predicting (ligand field theory) the relative energy of the d orbitals and therefore gives a qualitative idea on the sign of D . It should be noted that for some complexes there is a competition between negative and positive D_i values. As the total D is a sum of all the D_i , its sign cannot be predicted but, in this scenario, D will necessarily be small (positive or negative).

Concretely, in order to determine the sign and magnitude of D , we proceed in two steps. First, we design a complex whose d relative energy orbitals can be predicted qualitatively and then we perform wavefunction based theoretical calculations that give, generally, the right sign for D and a very good estimation of its magnitude. The theoretical results are compared to experimental values of ZFS extracted from the EPR spectrum of the complex. Because rhombicity (E term) is the result of a structural anisotropy in the plane (x is not equivalent to y), it is almost impossible to estimate correctly its magnitude. It is necessary to determine experimentally this parameter by EPR.

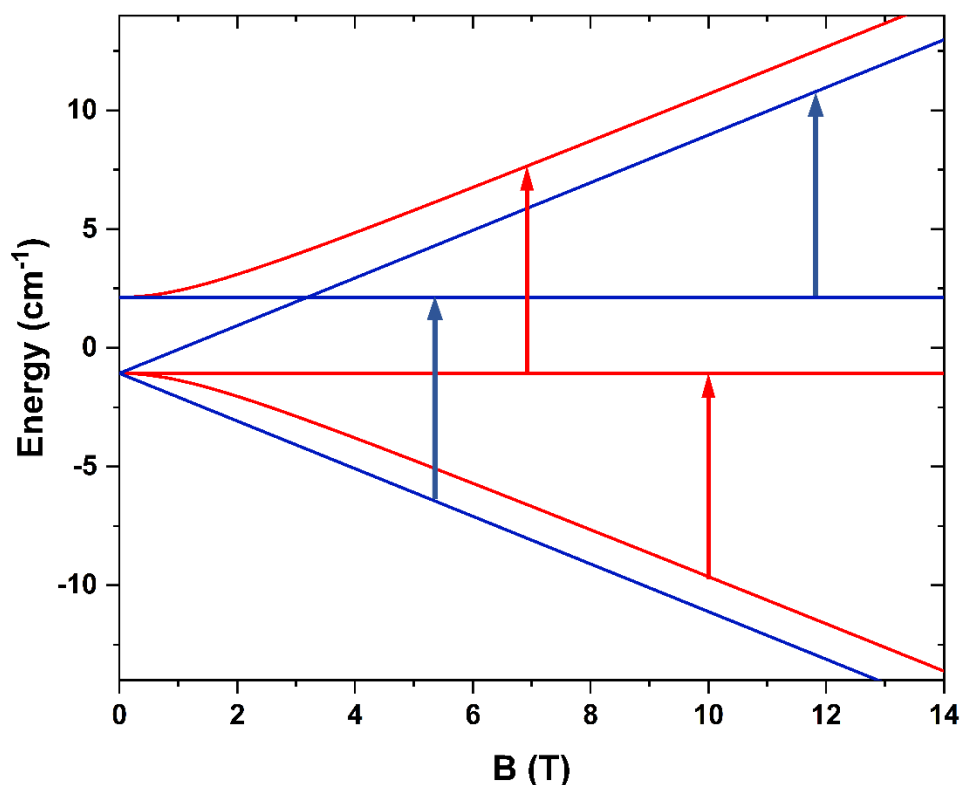
I.2.c Introduction of High Field High Frequency EPR (HF-HFEPR)

In the following chapter, most of the ZFS parameters will be obtained or confirmed using High Field-High Frequency EPR (HF-HFEPR) spectroscopy. In this subsection, we will propose a brief introduction of the technique.

HF-HFEPR offers significant advantages over classical EPR. One of the principal advantages of HF-HFEPR is the substantial reduction in the complexity of spectra. In HF-HFEPR, the ZFS can be treated as a perturbation to the Zeeman effect, resulting in better-separated transitions. This separation facilitates the attribution of the transitions, thereby enabling a more accurate determination of the ZFS parameters even when these parameters are large. This capability enhances the accuracy and ease with which the magnetic properties of various systems can be characterized. The system is described by the following Hamiltonian:

$$H = \mu_B (g_x B_x S_x + g_y B_y S_y + g_z B_z S_z) + D [S_z^2 - S(S+1)/3] + E [S_x^2 - S_y^2] \quad (\text{II-4})$$

We will consider a case where $E = 0 \text{ cm}^{-1}$, $D = -3.6 \text{ cm}^{-1}$ and $g_x = g_y = g_z = 2.15$.



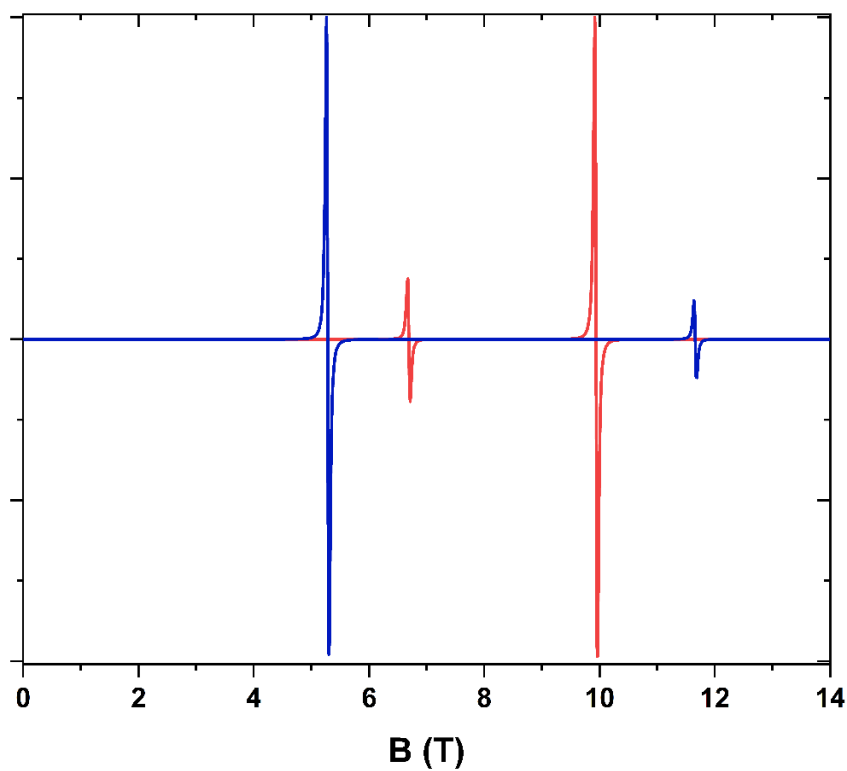


Figure I-5. (Top) Energy Level Diagram of a spin system with $S = 1$, $D = -3.2 \text{ cm}^{-1}$, $E/|D| = 0$ and g_x (red) = g_y (red) = g_z (blue) = 2.15. Transition positions for incident radiation of 255 GHz Frequency. (Bottom) Simulated EPR spectrum ($T = 5 \text{ K}$).

In this situation, the extreme parallel transitions along the z-axis are centred around the g_z position and are separated by $2|D|/(g_z\mu_B)$.

We will now consider a case where $E = 0.6 \text{ cm}^{-1}$, $D = -3.6 \text{ cm}^{-1}$ and $g_x = g_y = g_z = 2.15$ (Figure I-6)

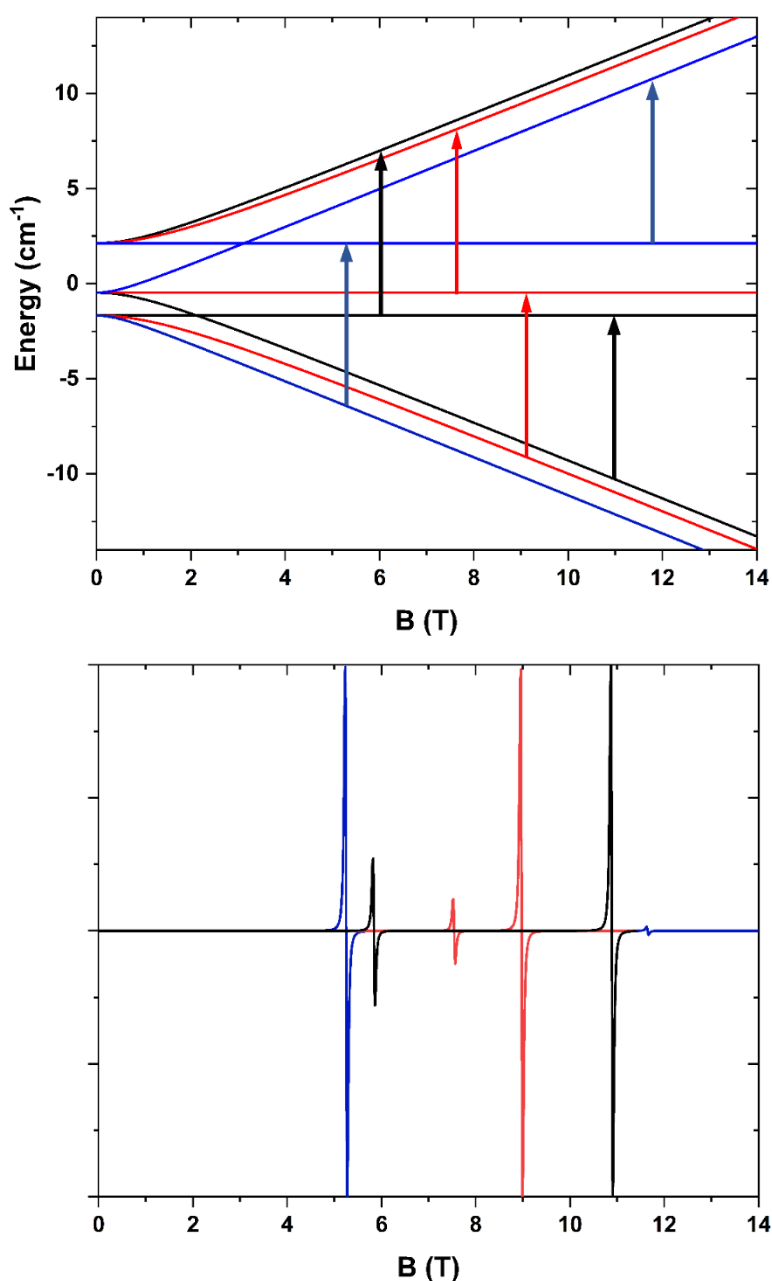


Figure I-6. (Top) Energy level diagram of a spin system with $S = 1$, $D = -3.2 \text{ cm}^{-1}$, $E/|D| = 0.187$ and g_x (red) = g_y (black) = g_z (blue) = 2.15. Transition positions for incident radiation of 255 GHz Frequency. (Bottom) Simulated EPR spectrum ($T = 15 \text{ K}$).

In this situation we see that the transitions associated with g_x and g_y are splitted. The transitions along the x (red) and y (black) axes are centered around g_x and g_y , respectively. The x and y transitions are approximately separated by $2|E|/(g\mu_B)$.

The sign of D can be determined using HF-HFEPR. If D is negative it means that the ground

state corresponds to the $M_s = \pm 1$ levels and if D is positive the ground state corresponds to the $M_s = 0$ state. We can see from Figure I-7 that the first transition occurs between the ground state and excited state if $D < 0$ while if $D > 0$ it involves a transition between two excited states. This means that the intensity of the first transition is directly dependent on the temperature, because if one is able to populate only the ground state, the first transition will not be observed in the case of $D > 0$. However, for an octahedral Ni(II) complex, $|D| < 10 \text{ cm}^{-1} \approx 14 \text{ K}$, this means that even at low temperature all energy level states are populated. This is why we used HF-HFEPR spectroscopy, because it allows a better separation between the energy levels. In fact, the Zeeman effect will separate the M_s levels to create a significant difference in population between the ground and excited states. Since the M_s levels are well separated, one needs a large frequency to observe the transitions, which is why we also need high frequency EPR.

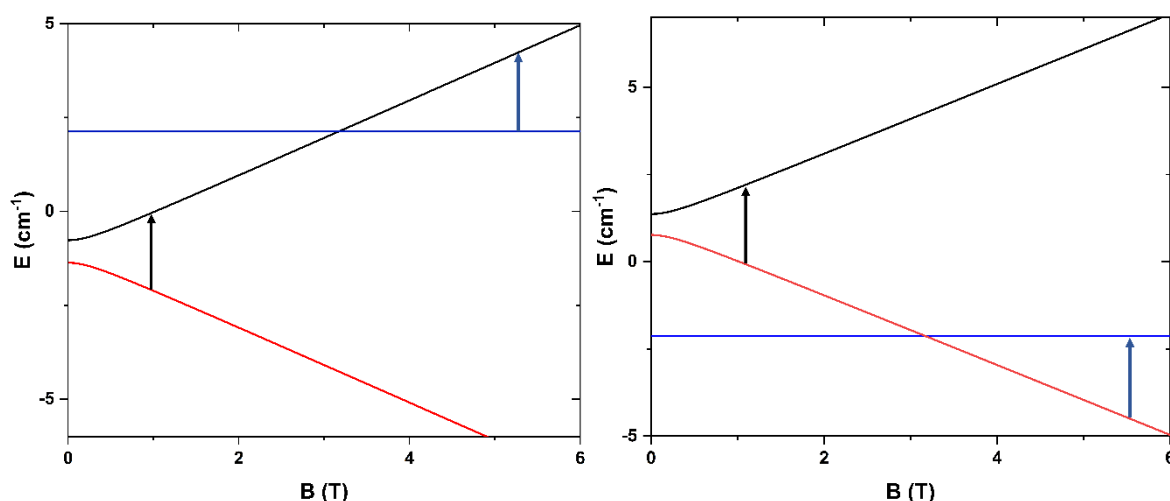


Figure I-7. (Left) Energy Level Diagram of a Spin System with $S = 1$, $D = -3.2 \text{ cm}^{-1}$, $E/|D| = 0.1$ and $g_x = g_y = g_z = 2.15$. (Right) Energy Level Diagram of a Spin System with $S = 1$, $D = 3.2 \text{ cm}^{-1}$, $E/|D| = 0.1$ and $g_x = g_y = g_z = 2.15$.

I.3 STUDY OF MONONUCLEAR Ni(II) COMPOUND

The aim of this section is to establish a connection between the ZFS of Ni(II) complexes and their structure, based on the elements of theory presented in the previous section. The structures were obtained by X-ray crystallography, and the anisotropy parameters were determined using EPR and HF-HFEPR spectroscopy. Theoretical calculations will be employed to help in rationalizing the magneto-structural relationship.

For this study, various mononuclear octahedral Ni(II) complexes were selected and compared in order to find a rational pathway to obtain a clock transition. As mentioned above, octahedral complexes lead to weak ZFS and hence to $2E$ values smaller than 1 cm^{-1} . The main challenge is

to obtain a negative D value, so that the two-levels are the ground levels. In this chapter all computations were performed in collaboration with Dr. Nicolas Suaud (LCPQ, UnIII. Toulouse) using ORCA,[8] HF-EPR measurements were performed by Dr. Anne-Laure Barra (LNCMI, UnIII. Grenoble) and X and Q-band EPR were done by Dr. Christian Herrero (ICMMO). Most of the structures have been collected and refined by Dr. Régis Guillot (ICMMO).

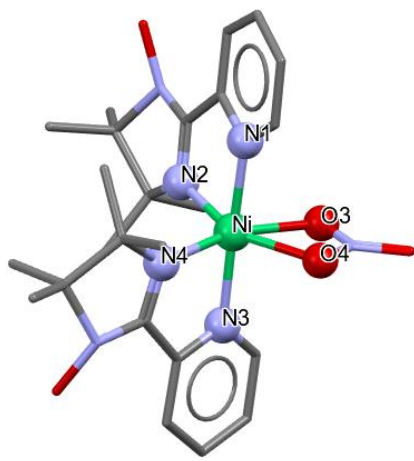
I.3.a Distorted octahedra

I.3.a.i Case of a slightly distorted octahedra: [Ni(imidazoline)(NO₃)](NO₃)

In order to find compounds that can have the adapted ZFS parameters, we first check the literature and particularly we check the complexes previously studied in our team. The first compound, the [Ni(imidazoline)(NO₃)](NO₃) was synthesized and studied twenty years ago in our group by Dr. Guillaume Rogez. A description of the study conducted on the compound is available here.[9] The ZFS values of this compound ($D = -10.1\text{cm}^{-1}$ and $E = 0.14\text{-}0.16\text{cm}^{-1}$) show that it is an ideal complex to play the role of a qubit with a zero-field clock transition. We, therefore, decided to take this complex as a study example and explain how the structure leads to a negative D value with a rhombic E parameter small enough to be in the right range required to be addressed by X-band EPR.

Crystallographic data

The compound crystallizes in space group $P2_12_12_1$ (Table I-2) and takes the form of green parallelepipedic crystals). The geometry around the Ni(II) center is a distorted octahedron, where the imidazoline ligands has each one pyridine (referred to as N1 and N3 in Table I-2) and one imidazole (referred to as N2 and N4 in Table I-2), and two oxygen atoms belonging to the nitrate group (O3 and O4).



Formula	$C_{24} H_{34} N_8 Ni O_8$
Space Group	$P 2_1 2_1 2_1$
Cell Lengths	a 10.9890(10) b 13.2620(10) c 20.2230(10)
Cell Angles	α 90.00 β 90.00 γ 90.00
Cell Volume	2947.22
Z, Z'	Z: 4 Z': 1
R-factor (%)	3.78

Table I-2. Crystallographic data of $[Ni(imidazoline)(NO_3)](NO_3)$

For the complex, we assume that electronic effects of the ligands are close enough so that a reasoning on the Ni-ligand bond lengths is sufficient to draw a preliminary conclusion on the relative energy of the d orbitals. We first compute the mean Ni-ligand bond lengths for the three following planes (N1N2N3O4, N1N4N3O3 and N2N4O4O3) and we compare the values obtained for the average axial Ni-ligand bond lengths (N4O3, N2O4 and N1N3). We find that the difference between the average in a plane and the corresponding axial distances is the largest for the N2N4O4O3 plane (2.099 Å) and its axial positions N1N3 (2.070 Å). The average axial distance is shorter than the average distance in the plane, which corresponds to a compressed octahedron along the N1-Ni-N3 axis bearing the pyridine groups of the two imidazoline ligands.

Bond	Distance (Å)
N1-Ni	2.062
N2-Ni	2.035
N3-Ni	2.078
N4-Ni	2.054
O3-Ni	2.135
O4-Ni	2.172

Table I-3. Selected distances in $[\text{Ni}(\text{imidazoline})(\text{NO}_3)](\text{NO}_3)$

This leads to the conclusion that the z axis (along which the compression occurs) is along the Ni-N(pyridine groups) direction. Therefore, the $d_{x^2-y^2}$ and d_{z^2} orbitals that are degenerate for the O_h symmetry are not anymore and $d_{x^2-y^2}$ has an energy lower than d_{z^2} .

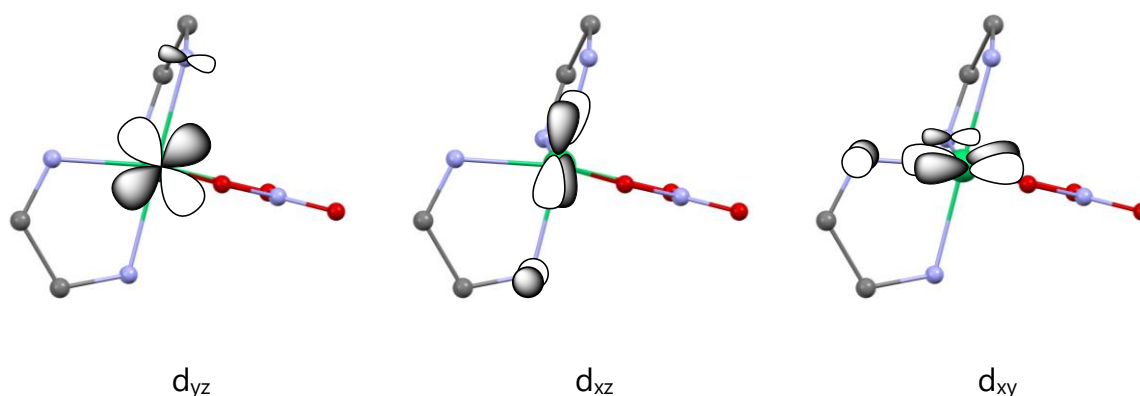


Figure I-8. Schematic representation of three low-lying molecular orbitals (OMs) within the frame where the x axis is perpendicular to the plane and the z axis vertical. The z axis is therefore along the compression axis, the $N_{py}NiN_{py}$ direction. The orbitals of the O atoms of NO_3 are assumed to only slightly alter the relative energy of the OMs because of the much larger Ni-O bond distances.

The d_{yz} and the d_{xz} orbitals interact each only with one π orbital of only one pyridine N atom because the other pyridine and the imidazole are both perpendicular to the planes of the two orbitals (Figure I-8). The larger (π) interaction of the d_{xy} orbital leads to a lift of the degeneracy of the triply degenerate orbitals (in O_h symmetry), with d_{xy} lying higher in energy than the two others that remain almost degenerate. The reasoning neglects the effect of the π orbitals of the nitrate oxygen atoms, which is reasonable because they are at longer distances than the nitrogen atoms. In summary, it is possible to conclude that the relative energy levels of this

complex are as depicted in Figure I-9. This is what is found from theoretical calculations (see below).

The key point here is that the highest fully occupied orbital is d_{xy} , and the lowest semi-occupied one is $d_{x^2-y^2}$. Therefore, the lowest energy excitation occurs between orbitals having the same m_l values (± 2), which lead to a large negative contribution to D because D is inversely proportional to the energy difference between the ground and the excited state. There is another reason that makes this negative contribution very large (in absolute value), it involves orbitals with the largest orbital momentum ($m_l = \pm 2$). Since D_i is proportional to the spin-orbit matrix element (see above), it is proportional to the orbital momentum value that is the largest for this excitation. We, therefore, expect an overall D value that is negative for this complex, because the other excited states that have positive D_i contributions should not counterbalance the large negative value. Furthermore, the rhombic term should be small because the difference in energy between the d_{xz} and the d_{yz} orbitals is expected to be very small.

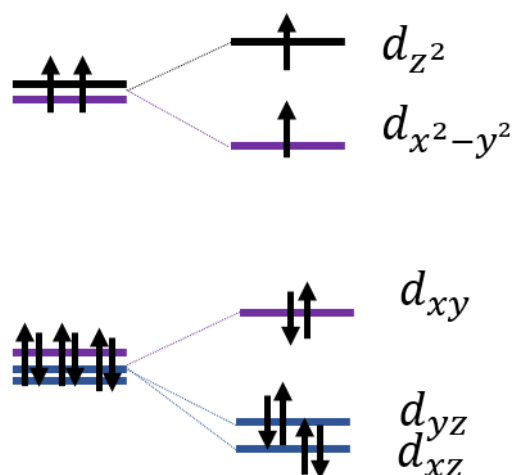


Figure I-9. Energy levels of d orbitals. Blue energy levels correspond to $m_l = \pm 1$, purple energy levels correspond to $m_l = \pm 2$ and black energy levels correspond to $m_l = 0$.

Computation study

Here we rationalize the value of the ZFS parameters with the computational study based on the structure of $[\text{Ni}(\text{imidazoline})(\text{NO}_3)](\text{NO}_3)$. The calculations give the d energy levels diagram depicted in Figure I-10-left, that is qualitatively the same as the one predicted from the analysis of the structure of the complex. The z axis of the \mathbf{D} tensor is almost aligned along the $\text{N}_{\text{py}}\text{NiN}_{\text{py}}$ direction with a deviation of about 3 degrees as shown in Figure I-10-right.

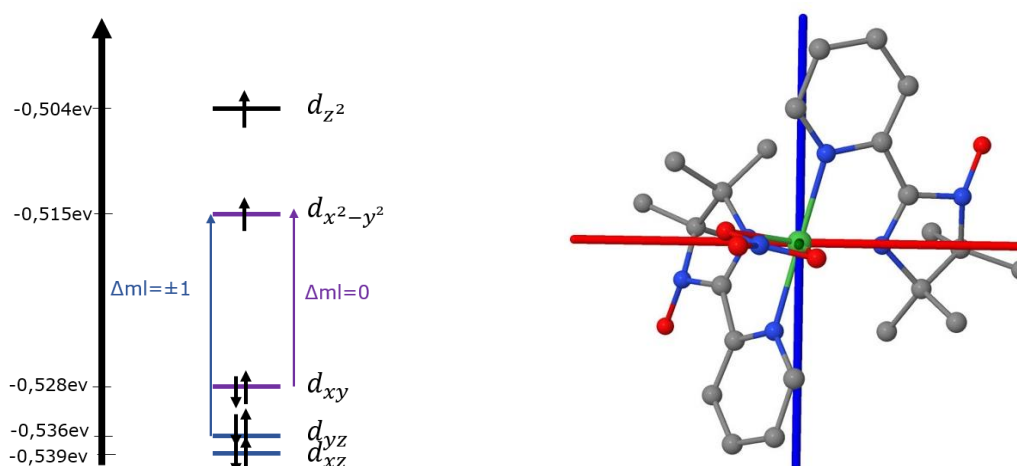


Figure I-10. Energy level of d molecular orbitals of $[\text{Ni}(\text{imidazoline})(\text{NO}_3)]^{2+}$ (left) and orientation of the \mathbf{D} tensor axes with respect to the molecule (z , blue; y , green and x , red) (right).

The representation of the MOs obtained from calculations (Figure I-11) correspond to what was predicted (Figure I-9).

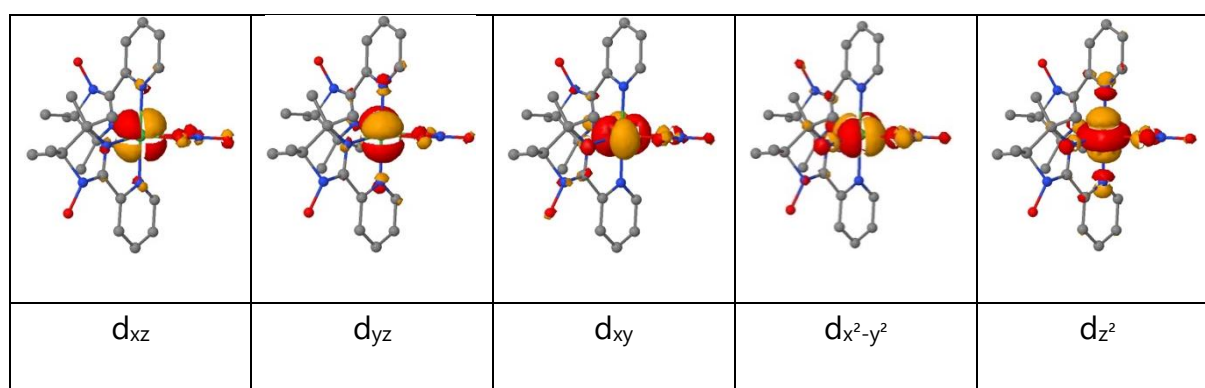


Figure I-11. MOs of $[\text{Ni}(\text{imidazoline})(\text{NO}_3)](\text{NO}_3)$ obtained from calculations.

The D_i values of the triplet states that contribute to D are given in Table I-4. There is one large negative contribution and two weaker positive ones. Here we will not discuss the contributions of the singlet states because their sum is very small ($< 0.1\text{cm}^{-1}$) compared to those of the triplet states.

Individual contributions to D		
ESi	$E(\text{ESi}) - E(\text{GS})$ (cm^{-1})	D_i (cm^{-1})
ES1	6264	-48.45
ES2	8301	17.72
ES3	8581	17.07

Table I-4. Individual contributions to D (in cm^{-1}) for $[\text{Ni}(\text{imidazoline})(\text{NO}_3)]^+$.

The calculations give the following ZFS parameters:

$$D = -11.551 \text{ cm}^{-1}, E = 0.66 \text{ cm}^{-1}$$

Chapter I: Electronic structure of mononuclear Ni(II) complexes as $S = 1$ spin qubits

We will consider now each excitation and analyse the sign of the corresponding D_i . The ORCA output file gives the determinants of the ground and all excited states so that one can consider all orbital excitations. In Table I-5, the Slater determinants correspond to the following sequence of orbitals $|d_z^2 d_{xz} d_{yz} d_{xy} d_{x^2-y^2}|$, so $|12221|$ indicates an unpaired electron in the d_z^2 and $d_{x^2-y^2}$ orbitals and electron doublets in each of the other three orbitals. The ground state (GS) and the first excited state (ES1) are both made by two main determinants (Table I-5). There are two excitations involving the d_{xy} and $d_{x^2-y^2}$ orbitals so that the $L_z s_z$ operator acts leading to a large negative D_1 value (-48.45 cm^{-1}).

GS determinants	ES1 determinants (6264 cm^{-1})	Orbital excitation GS \rightarrow ES1	Acting SO Operator	$D_1 \text{ (cm}^{-1}\text{)}$
0.60 $ 12221 $	0.59 $ 12212 $	$d_{xy} \rightarrow d_{x^2-y^2}$	$l_z s_z$	-48.45
0.24 $ 12212 $	0.24 $ 12221 $	$d_{x^2-y^2} \rightarrow d_{xy}$		
GS determinants	ES2 determinants (8301 cm^{-1})	Orbital excitation GS \rightarrow ES2	Acting SO Operator	$D_2 \text{ (cm}^{-1}\text{)}$
0.60 $ 12221 $	0.41 $ 22121 $	$d_{xy} \rightarrow d_{z^2}$	$l_+ s_- + l_- s_+$	17.72
0.24 $ 12212 $	0.15 $ 12122 $	$d_{yz} \rightarrow d_{xy}$		
0.24 $ 12212 $	0.15 $ 11222 $	$d_{xz} \rightarrow d_{xy}$		
GS determinants	ES3 determinants (8581 cm^{-1})	Orbital excitation GS \rightarrow ES3	Acting SO Operator	$D_3 \text{ (cm}^{-1}\text{)}$
0.60 $ 12221 $	0.33 $ 21221 $	$d_{xy} \rightarrow d_{z^2}$	$l_+ s_- + l_- s_+$	17.07
0.24 $ 12212 $	0.16 $ 11222 $	$d_{xz} \rightarrow d_{xy}$		
0.24 $ 12212 $	0.15 $ 21212 $	$d_{xz} \rightarrow d_{z^2}$		

Table I-5. Composition of the wavefunctions corresponding to the ground and the excited states; the numbers corresponds to the weight of the Slater determinant.

The same reasoning can be made for the second and third excited states, where the excitations

involved orbital with different m_l number so that the $(l_-s_+ + l_+s_-)$ part of the SOC operator acts leading to positive D_2 and D_3 values (Table I-4).

From computation it appears that the value of E (0.66 cm^{-1}) is not suitable for pulsed X-band EPR where a value close 0.16 cm^{-1} is needed.

EPR study

The HF-HFEPR spectra of this complex were recorded,[9] and analysed to give the following ZFS parameters ($D = -10.1 \text{ cm}^{-1}$ and $E = 0.14\text{-}0.16 \text{ cm}^{-1}$) which are in excellent agreement with the theoretical ones. It is worth noting that even an excellent agreement between theory and experiment is not sufficient to rely on theory to determine the E value because E must match almost perfectly the X-band (or Q-band) energy. (we will see below that actually is not strictly right and E needs to be in the right range) But for D , calculations are valuable because they can predict its sign and magnitude with an accuracy sufficient to our purpose. The ZFS parameters extracted from the HF-HFEPR studies, and particularly the value of E indicate that this complex is a candidate to be a qubit with a clock transition at zero magnetic field.

We recorded the X-band EPR spectra of the compound at 10 K in parallel mode (Figure I-12), in order to ensure the presence of a transition close to zero field between the $M_S = \pm 1$ sub-levels that form the qubit. The selection rule for the parallel mode is $\Delta M_S = \pm 2$, so only transitions between $M_S = \pm 1$ levels can be observed. The experimental spectrum (black dots) shows the presence of a band close to zero field, a transition around 450 mT and a low intensity band at 600 mT. When simulating the data with the PHI software,[10] using as a starting point the parameters determined for the HF-HFEPR experiments, only the first band could be simulated leading to the parameters:

$$D = -10.2 \text{ cm}^{-1}, E = 0.156 \text{ cm}^{-1}, g = 2.01$$

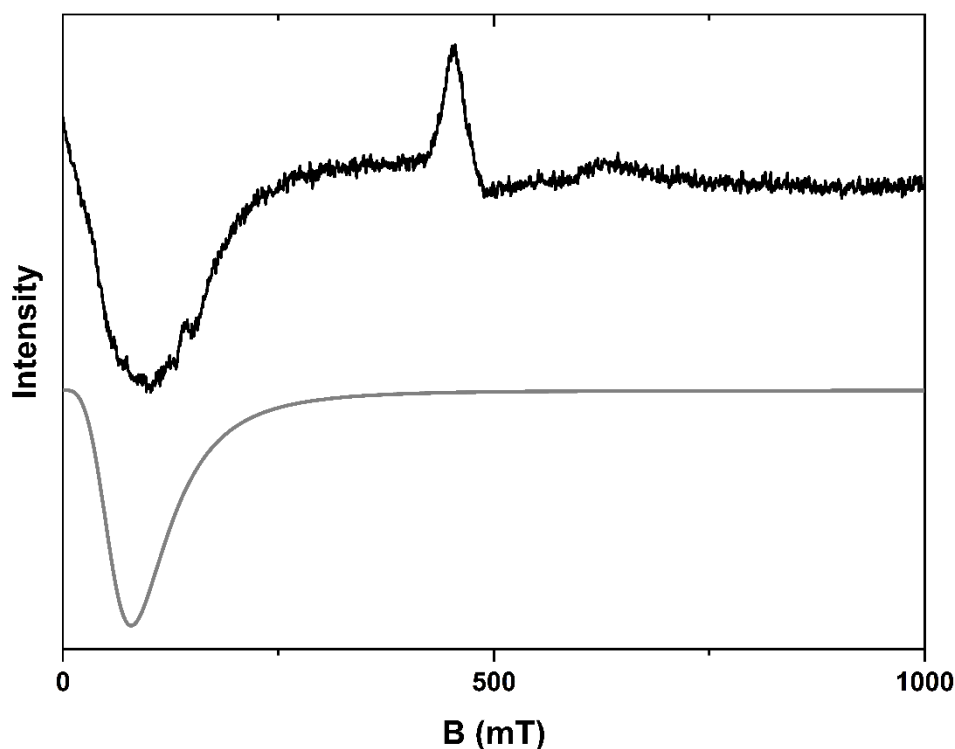


Figure I-12. CW-EPR spectra of $[\text{Ni}(\text{imidazoline})(\text{NO}_3)](\text{NO}_3)$ at $T = 10 \text{ K}$ and 9.45 GHz . In black experimental spectra and in grey simulated spectra.

Additional EPR studies with the perpendicular mode of the cavity reveal the presence of spin $S = 1/2$ impurity in almost all the samples with a concentration that can vary from 1 to 5%. Indeed, we noticed an evolution of the colour of the material if it is kept without protection from light. We did not investigate in details this aspect. We think that the additional bands in the parallel mode spectrum are due to these impurities that interact with Ni(II).

This complex has all the characteristics to be studied by pulsed EPR with the perspective of observing an EPR transition near zero field.

1.2.a.ii Evidencing electronic distortion

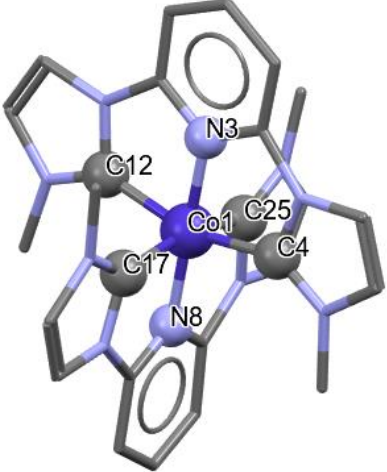
Most (even all) complexes undergo a strain due to a distribution in the coordination sphere of the metal ions due to structural inhomogeneity in the material. This results in a distribution of molecular geometries within the material with ZFS parameters distributed around central values of D and E , this is called D -strain and E -strain. Important values of strain will lead to broad bands in EPR spectra which are deleterious to coherence (cf Chapter I.4.b.ii). We do the assumption that a rigid complex would reduce the deformations that the complex may

undergo and consequently decrease strain. Saying that, it is worth stressing that the presence of some strain turns out to be valuable for Ni(II) complexes as we will see Chapter II.

In our search for octahedral Ni(II) complexes with a tetragonal compression, we found a Co(II) complex possessing these characteristics in the Cambridge data bank.[11] We assumed that the analogous Ni(II) complex would have the same local structure. The synthesis of the complex was challenging, we therefore decided to first perform the theoretical calculations on the Co(II) structure, but replacing Co(II) by Ni(II). This is reasonable because for most octahedral complexes, Co(II) and Ni(II) have very close coordination sphere, everything else being equal. The ligand that imposes the *structural* tetragonal compression is composed by one central pyridine group linked to two N-heterocyclic carbene units (called NHC).

Crystallographic investigation of $[\text{Co}(\text{NHC})_2](\text{PF}_6)_2$

The compound is described to crystalize in the space group $C2/c$ (Table I-6) and takes the form of a dark orange long plate. The geometry around Co is a distorted octahedron, with two NHC moieties: one pyridine and two carbene groups.



Formula	$C_{26} H_{26} Co N_{10}^{3+}, 3(F_6 P^-), 3(C_2 H_3 N)$
Space Group	C 2/c
Cell Lengths	a 19.2943 b 14.2346 c 31.6092
Cell Angles	α 90 β 95.934 γ 90
Cell Volume	8634.84
Z,Z'	Z : 8 Z' : 1
R-factor (%)	5.65

Table I-6. Crystallographic data of $[Co(NHC)_2](PF_6)_2$

The bond distances (Table I-7) correspond to an octahedron compressed along the $N_{py}CoN_{py}$ direction, with a slight distortion in the plane of the four carbon atoms similar from the geometry point of view to the $[Ni(\text{imidazole})(NO_3)](NO_3)$.

Bond	Distance (Å)
N3-Co	1.880
N8-Co	1.880
C12-Co	1.945
C4-Co	1.951
C17-Co	1.942
C25-Co	1.936

Table I-7. Selected distances in $[\text{Co}(\text{NHC})_2](\text{PF}_6)_2$.

Computation study

Theoretical calculations give the following ZFS parameters:

$$D = 1.28 \text{ cm}^{-1}, E = 0.056 \text{ cm}^{-1}$$

With a positive and relatively small D value, which is very different from the previous Ni(II) complex whose geometry distortion is similar (structural tetragonal compression).

The relative energy of the d molecular orbitals (Figure I-13-left) show that the d_{z^2} has lower energy than $d_{x^2-y^2}$, which corresponds to an *elongation* along the z axis. The axes of the \mathbf{D} tensor are perfectly aligned along the Ni-ligand bonds with the z axis along the $\text{N}_{\text{py}}\text{NiN}_{\text{py}}$ direction.

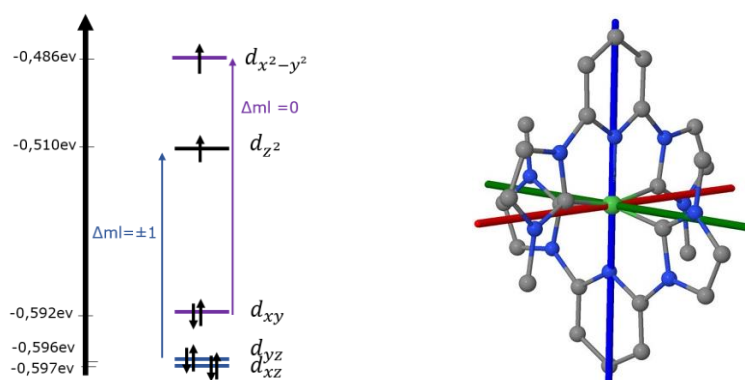


Figure I-13. Energy level of d molecular orbitals of $[\text{Ni}(\text{NHC})_2]^{2+}$ (left) and orientation of the \mathbf{D} tensor axes with respect to the molecule (z , blue; y , green and x , red).

This result leads to the conclusion that the pyridine ligands interact less with the d_{z^2} than does

$d_{x^2-y^2}$ leading to an *electronic* elongation. This is responsible of the positive D value. Even though, we suspected this will be the case, this is an interesting example on the relation between electronic effects and magnetic anisotropy. Finally, the d_{xy} has a larger interaction with the π orbitals of the four carbon atoms of the carbene groups than the d_{xz} and the d_{yz} orbitals that interact each with only the π orbital of only one pyridine groups, the π orbitals of the carbene groups being in the nodal planes of these two d orbitals.

The contributions to D of the different excited states are given in Table I-8. As for the previous complex, there are three contributions as the complexes have both an octahedral geometry. However, there are important differences:

- (i) The values are much smaller than for $[\text{Ni}(\text{imidazoline})(\text{NO}_3)](\text{NO}_3)$
- (ii) The negative contribution is due to the highest energy state, while it was for the lowest one for the previous complex,
- (iii) All the excited states are at much higher energy than the imidazoline containing complex
- (iv) The negative contribution does not compensate the two positive ones so that the overall D value is positive. The difference between the absolute value of D_3 and $D_1 + D_2$ is not very large so that D could have been negative but small at any rate.

Individual contributions to D		
ESi	E(ESi)-E(GS) (cm^{-1})	D_i (cm^{-1})
ES1	18226.6	7.60
ES2	18479.5	7.55
ES3	20714.5	-12.55

Table I-8. Individual contribution of each transition to D for $[\text{Ni}(\text{NHC})_2]^{2+}$.

We will consider now each excitation and analyse the sign of the corresponding D_i . The ground state is made by one determinant (Table I-9). The first two excitations involve orbitals with different m_l number so that the $(l_-s_+ + l_+s_-)$ part of the SOC operator acts leading to positive D_1 and D_2 values (Table I-3). Only the third excitation involves orbitals with the same m_l , thus the l_zs_z operator, leading to a negative D_3 value.

GS determinants	ES1 determinants (18226.6 cm^{-1})	Orbital excitation GS \rightarrow ES1	Acting SO Operator	D_1 (cm^{-1})
0.99 12212	0.78 21212	$d_{xz} \rightarrow d_{z^2}$	$l_{+s_-} + l_{-s_+}$	7.60
0.99 12212	0.17 11222	$d_{xz} \rightarrow d_{xy}$		
GS determinants	ES2 determinants (18479.5 cm^{-1})	Orbital excitation GS \rightarrow ES2	Acting SO Operator	D_2 (cm^{-1})
0.99 12212	0.79 22112	$d_{yz} \rightarrow d_{z^2}$	$l_{+s_-} + l_{-s_+}$	7.55
0.99 12212	0.16 12122	$d_{yz} \rightarrow d_{xy}$		
GS determinants	ES3 determinants (20714.5 cm^{-1})	Orbital excitation GS \rightarrow ES3	Acting SO Operator	D_3 (cm^{-1})
0.99 12212	0.99 12221	$d_{x^2-y^2} \rightarrow d_{xy}$	$l_z s_z$	-12.55

Table I-9. Composition of the wavefunctions corresponding to the ground and the excited states; the numbers correspond to the weight of the Slater determinant.

In summary, the large σ donating effect of the carbon atoms of the carbene lifts the degeneracy of the MOs orbitals much more than the two imidazoline and the nitrate ligands, so that the excitations are at higher energy and the D_i contributions are smaller in the carbene containing complex. This is because the contributions are inversely proportional the energy difference between the ground and the excited states. More importantly, the negative contribution is due to the highest excited state because of the change of the relative energies of the d_{z^2} and the $d_{x^2-y^2}$ based MOs, it is smaller than it should have been and do not compensate the positive contributions leading to an overall positive D value for the complex. The E value is small as expected because the local symmetry is very close to tetragonal.

In order to take advantage of the large donating effect of carbene, the carbon atoms must be in axial position. We may anticipate a lift of the degeneracy of the d orbitals resulting in a negative D value, because $d_{x^2-y^2}$ would have a lower energy than d_{z^2} . The excitation with the lowest energy will involve the d_{xy} and $d_{x^2-y^2}$ responsible of the large negative contribution as for the imidazoline containing complex. A ligand with one carbene and two pyridines (Figure I-14)

should lead to a large negative D value, a small distortion in the plane will ensure an E value not so far from the X-band microwave energy.

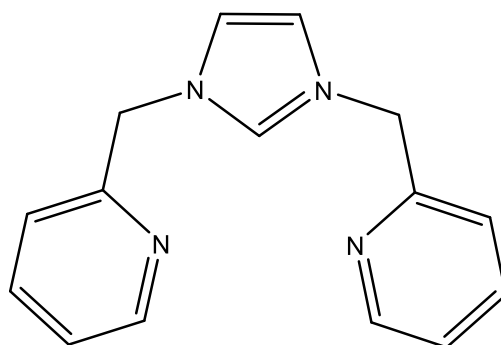


Figure I-14. New ligand proposal

I.3.b C_3 symmetry

The previous octahedral complexes studied exhibit distortions close to tetragonal. It appeared that it was very difficult to prepare a tetragonally compressed octahedron in order to ensure a negative D parameter. Actually, apart from few cases, hexacoordinate Ni(II) complexes seem to be more stable in an elongated tetragonal geometry. The trigonal distortion is the other interesting one for octahedral complexes. We wanted to explore such systems with the hope of finding a molecular systems that can present negative D values.

The trigonal distortion of an octahedron is along one of its four threefold symmetry axes. A simple crystal field reasoning gives the following energy diagram for the d orbitals (Figure I-15).

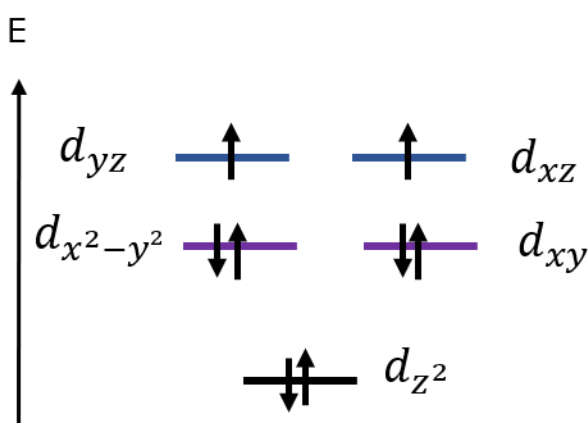


Figure I-15. Lift of degeneracy of d orbitals in the case of a trigonal distortion of an octahedron. Blue energy levels correspond to $m_l = \pm 1$, purple energy levels correspond to $m_l = \pm 2$ and black energy levels correspond to $m_l = 0$.

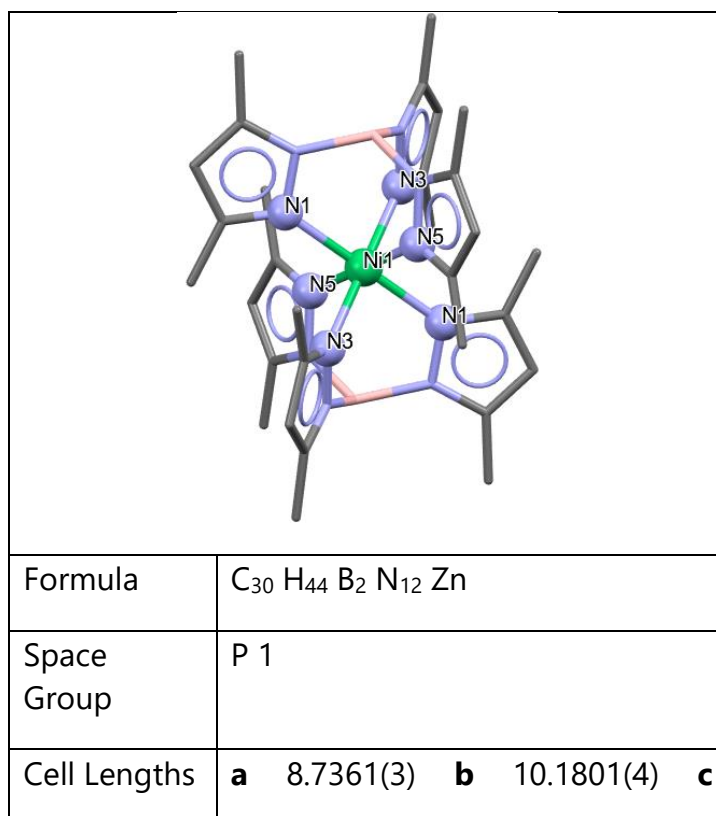
The d_{z^2} is expected to be the less destabilized by the crystal field because the six ligands are

Chapter I: Electronic structure of mononuclear Ni(II) complexes as $S = 1$ spin qubits

located very close to its nodal cone. The d_{xz} and d_{yz} orbitals point towards the ligands, they are the most destabilized. Of course, if the symmetry of the complex is not strictly trigonal, the orbitals will not be degenerate. One can see that if the GS is made by a single determinant ($|21122\rangle$), all excitations will correspond to a change of the orbital momentum leading to positive D_i contributions. But if, the GS is multi-determinantal including determinants of the type $|21212\rangle$, negative contributions may be present. The presence of several determinants is due to the fact, for example, that it costs less energy to have one electron in a xy and two in a yz orbitals than two electrons in the xy and one in the yz orbital, because of electronic repulsion. Without computation, it is difficult to predict the interaction between the ligands and the metallic ion thus the lift of degeneracy. Here we selected a well-known Ni(II) complex with the ligands derived from the tris-pyrazolylborate (noted MPZ in the following) that imposes a symmetry close to trigonal.[12]

I.3.b.i $[\text{Ni}(\text{MPZ})_2]$

The compound was synthesized according to the literature procedure.[13] The compound crystallizes in space group P 1. The geometry around Ni is a distorted octahedron, where the B atoms are along the pseudo C_3 symmetry axis (Table I-10).



	10.7486(4)
Cell Angles	α 63.242(2) β 84.897(2) γ 79.905(2)
Cell Volume	840.287
Z,Z'	Z : 1 Z' : 0.5
R-factor (%)	4.13

Table I-10. Crystallographic data of $[\text{Ni}(\text{MPZ})_2]$.

The angles between the pseudo C_3 axis (taken along the BNiB direction) and the NiN direction are given in Table I-11. For a perfect octahedron these angles are equal to the magic angle (54.74°). It is therefore not possible to state whether we have a trigonal elongation or compression. One angle is different from the two others, which means that we have some rhombicity i.e. $E \neq 0$. From such structure, we can already predict that the one-electron energy diagram of the d orbitals will be similar to that of Figure I-12, but with a lift of degeneracy of the degenerate orbitals because of the distortion in the plane. Only theoretical calculations can give us information about the sign of the D parameter.

Bond	Angles ($^\circ$)
BNiN1	55.5
BNiN3	53.0
BNiN5	55.6

Table I-11. Angles between the BNiB direction and the NiN one for $[\text{Ni}(\text{MPZ})_2]$.

I.3.b.ii Computational study

The calculations give the d energy level diagram depicted in Figure I-16, correspond to the case of a distorted trigonal octahedron. This can be explained with the **D** tensor which is only slightly shifted from the C_3 axes of the molecule.

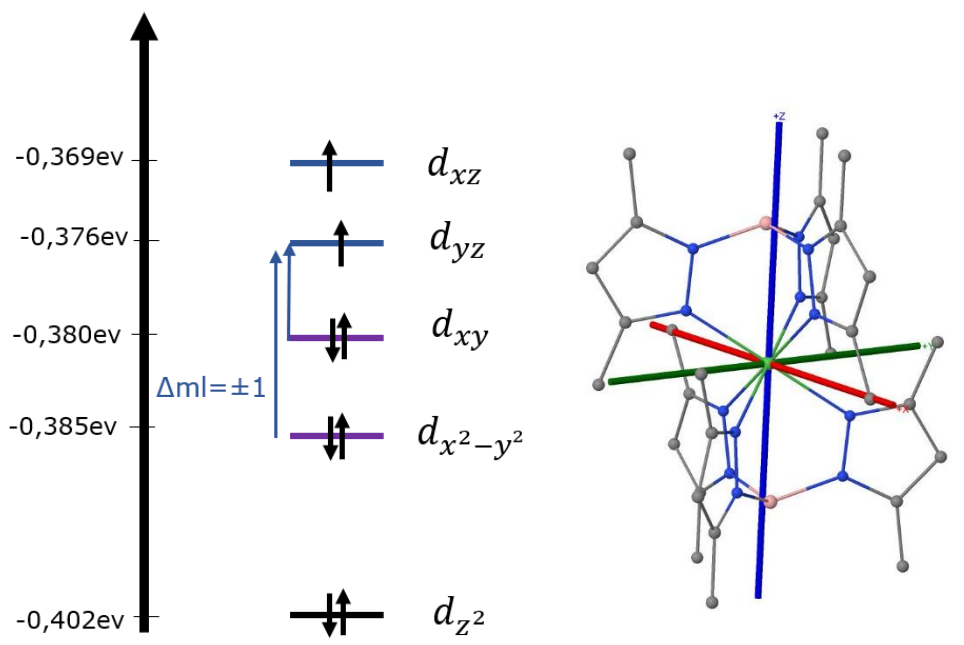


Figure I-16. Energy level of d molecular orbitals of $[\text{Ni}(\text{MPZ})_2]$ (left) and orientation of the \mathbf{D} tensor axes with respect to the molecule (z , blue; y , green and x , red) (right).

The excitations correspond all to a change in the m_l value and thus should yield an overall positive D value. Nevertheless, calculations give a negative D value, but relatively large rhombicity. The ZFS parameters are:

$$D = -4.94 \text{ cm}^{-1}$$

$$E/D = 0.249$$

We will consider now each excitation and analyse the sign of the corresponding D_i in order to understand the origin of the negative sign of D .

Individual contributions to D		
ES $_i$	$E(\text{ES}_i) - E(\text{GS}) \text{ (cm}^{-1}\text{)}$	$D_i \text{ (cm}^{-1}\text{)}$
ES1	7725.7	-38.01
ES2	8455.9	15.27
ES3	8581	16.87

Table I-12. Individual contribution of each transition to D for $[\text{Ni}(\text{MPZ})_2]$.

The D_i values of the triplet states that mainly contribute to D are given in Table I-12. There is one large negative contribution and two weaker positive ones. The overall negative D value is due to the presence of several determinants for the GS and ES allowing excitations between determinants with the same m_l value between the GS and the first ES giving a large negative D_i contribution.

GS determinants	ES1 determinants (7726 cm^{-1})	Orbital excitation GS \rightarrow ES1	Acting SO Operator	D_1 (cm^{-1})
0.40 21122	0.73 21212	$d_{xy} \rightarrow d_{yz}$	$l_+s_- + l_-s_+$	-38.01 cm^{-1}
0.40 21122	0.15 22112	$d_{xy} \rightarrow d_{xz}$		
0.31 21221	0.10 22211	$d_{xy} \rightarrow d_{xz}$		
0.31 21221	0.23 22121	$d_{yz} \rightarrow d_{xz}$	l_zs_z	
GS determinants	ES2 determinants (8456 cm^{-1})	Orbital excitation GS \rightarrow ES2	Acting SO Operator	D_2 (cm^{-1})
0.40 21122	0.30 11222	$d_{z^2} \rightarrow d_{xy}$	$l_+s_- + l_-s_+$	15.27
0.31 21221	0.53 22121	$d_{yz} \rightarrow d_{xz}$	l_zs_z	
GS determinants	ES3 determinants (8581 cm^{-1})	Orbital excitation GS \rightarrow ES3	Acting SO Operator	D_3 (cm^{-1})
0.40 21122	0.26 22112	$d_{xy} \rightarrow d_{xz}$	$l_+s_- + l_-s_+$	16.87
0.40 21122	0.24 12122	$d_{z^2} \rightarrow d_{xz}$		
0.31 21221	0.23 12221	$d_{z^2} \rightarrow d_{xz}$		
0.40 21122	0.21 21221	$d_{x^2-y^2} \rightarrow d_{yz}$		

Table I-13. Composition of the wavefunctions corresponding to the ground and the excited states; the numbers corresponds to the weight of each Slater determinant.

I.3.b.iii EPR spectra

The HF-HFEPR spectra of this complex were recorded and analysed (Figure I-17) to give the following ZFS parameters, with $g_x = 2.15$, $g_y = g_z = 2.17$:

$$D = -1.25 \text{cm}^{-1}$$

$$E/D = 0.28$$

Chapter I: Electronic structure of mononuclear Ni(II) complexes as $S = 1$ spin qubits

The parameters found are in agreement with the sign of D obtained from calculations but not its magnitude, and the presence of rhombicity. The value of the $2E$ (0.7 cm^{-1}) for this compound is not suitable neither for X-band nor for Q-band pulsed EPR study. However, we will see below that a signal in X-band was observed.

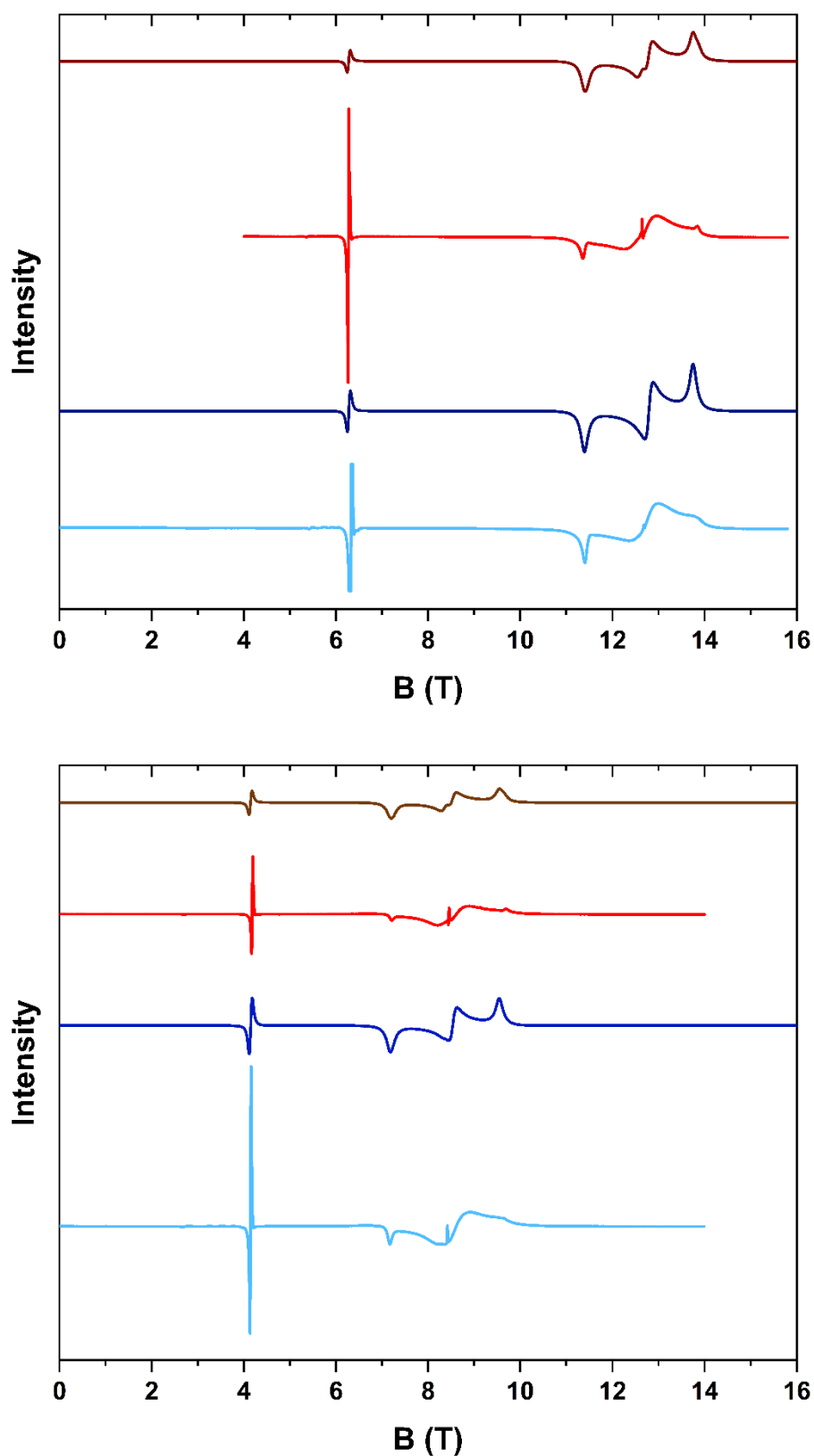
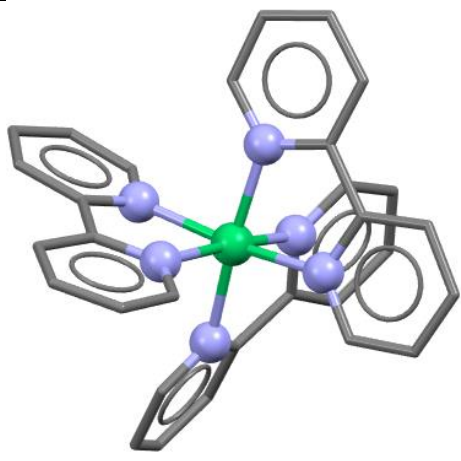


Figure I-17. HF-HFPR spectra of $[\text{Ni}(\text{MPZ})_2]$ at $T = 5$ K (blue) and $T = 25$ K (red) and their respective simulation dark blue and brown lines. (Bottom) Spectra recorded at 255.36 GHz. (Top) Spectra recorded at 383 GHz.

I.3.c Tuning of ZFS in trigonal Ni complexes

In our group, few years ago the compound $[\text{Ni}(\text{bpy})_3](\text{BPh}_4)_2$ (bpy is 2,2' bipyridine) was studied by HF-HFEPR and a negative D value was found, $D = -1.18 \text{ cm}^{-1}$ and $E = 0.2 \text{ cm}^{-1}$.^[14] The E value is close to the ideal one (0.16 cm^{-1}) suitable an EPR transition near zero field. We therefore, decided to investigate a series of complexes based on Ni-trisbipyridine with bipyridine ligands bearing different groups in order to tune the E value as close as possible to the microwave energy of the X or Q-band EPR. Before preparing and studying different complexes we searched the Cambridge data bank and found that the compound $[\text{Ni}(\text{bpy})_3](\text{PF}_6)_2$ crystallizes in the trigonal space group $P\bar{3}c1$, with the threefold symmetry axes of the molecules all aligned along the c axis of the unit cell.^[15] While the same complex with the BPh_4^- anion crystallizes in the monoclinic space group $P21/n$ (Table I-14). Consequently, for the former, the local symmetry is axial (the rhombic parameter E should be exactly equal to zero), while the latter is not axial and $E \neq 0$, as we observed. It is therefore possible to tune the E value in this family of complexes if one is able to introduce very slight structural changes so that the axuality is only very slightly altered. The system is not an ideal one because the D value, even though negative, is small so that structural changes may well switch D to positive.



	PF_6^-	BPh_4^-
Formula	$\text{C}_{30} \text{H}_{24} \text{N}_6 \text{Ni}_2(\text{F}_6 \text{P})$	$\text{C}_{30} \text{H}_{24} \text{N}_6 \text{Ni}_2(\text{C}_{24} \text{H}_{20} \text{B})$
Space Group	$P 3_1$	$P 2_1/n$
Cell Lengths	a 10.3534(4) b 10.3534(4) c 26.1231(14)	a 12.467(1) b 14.215(1) c 34.433(3)
Cell Angles	α 90 β 90 γ 120	α 90 β 97.970(2) γ 90
Cell Volume	2425.05	6043.22
Z,Z'	Z : 3 Z' : 1	Z : 4 Z' : 1
R-factor (%)	2.78	4.65

Table I-14. Crystallographic data of $[\text{Ni}(2,2'\text{bpy})_3](\text{X})_2$. From left to right $\text{X} = \text{PF}_6, \text{BPh}_4$.

The examination of the local structure of the previous compounds indicates that small modifications in the crystal packing, due to the counter anion, induces very small changes in the coordination sphere of Ni(II) that breaks the trigonal symmetry and lift the degeneracy of the $M_S = \pm 1$ sub-levels. Similar observations were previously made during the thesis of Guillaume Rogez, where a comparison was made between $[\text{Ni}(\text{pydipa})(\text{NO}_3)](\text{NO}_3)$, $[\text{Ni}(\text{pydipa})(\text{NO}_3)](\text{PF}_6)$, and $[\text{Ni}(\text{pydipa})(\text{NCS})](\text{PF}_6)$ (pydipa is N-methyl N,N-bis{3-[(2-pyridylmethyl)-amino]-propyl}-amine).[16] It was evidenced that the disparity observed in the rhombic anisotropy was not attributable to electronic effects but was primarily structural in nature.

Therefore, investigations were carried out by exploring different counter anions for $[\text{Ni}(\text{bpy})_3](\text{X})_2$ and different functionalized bpy. Ideal values of ZFS are $D < 0$ and $E = 0.153 \text{ cm}^{-1}$ or $E = 0.5 \text{ cm}^{-1}$.

Before discussing the EPR results on this series of complexes, we present the results of the theoretical study of $[\text{Ni}(\text{bpy})_3](\text{PF}_6)_2$ in order to understand the origin of the negative D value. It is worth noting for the trigonal symmetry of the complex, the z axis of the \mathbf{D} tensor is aligned along the threefold symmetry axis and lead to the lift of the degeneracy of the d orbitals as depicted in Figure I-12. Therefore, only positive D_i contributions should be present as we hypothesized for $\text{Ni}(\text{MPZ})_2$.

The calculations give the following ZFS parameters: $D = -2.46 \text{ cm}^{-1}$ and $E = 0$. The relative energy for the MOs is as expected with the z axis of the \mathbf{D} tensor along the threefold symmetry axis of the complex. The results are shown in Table I-15. Again here, the origin of the negative contribution to D of the first ES is the multi-determinantal nature of the states.

	ES1 determinants (9779 cm^{-1})	Orbital excitation GS \rightarrow ES1	Acting SO Operator	D_1 (cm^{-1})
0.41 21122	0.5 22112	$d_{x^2-y^2} \rightarrow d_{xz}$	$l_{+s_-} + l_{-s_+}$	-33.50
0.41 21122	0.5 21221	$d_{xy} \rightarrow d_{yz}$		
0.24 21212	0.5 22112	$d_{yz} \rightarrow d_{xz}$	$l_z s_z$	
0.24 21212	0.5 21221	$d_{xy} \rightarrow d_{x^2-y^2}$		
0.24 22121	0.5 22112	$d_{x^2-y^2} \rightarrow d_{xy}$		
0.24 22121	0.5 21221	$d_{xz} \rightarrow d_{yz}$		
GS determinants	ES2/ES3 determinants (9928 cm^{-1})	Orbital excitation GS \rightarrow ES2	Acting SO Operator	D_2 and D_3 (cm^{-1})
0.41 21122	0.31 11222	$d_{z^2} \rightarrow d_{yz}$	$l_{+s_-} + l_{-s_+}$	2x14.94
0.41 21122	0.24 22121	$d_{xy} \rightarrow d_{yz}$		
0.41 21122	0.24 21212	$d_{x^2-y^2} \rightarrow d_{yz}$		
0.24 22121	0.20 12221	$d_{z^2} \rightarrow d_{yz}$		
0.24 22121	0.20 12221	$d_{z^2} \rightarrow d_{yz}$		

Table I-15. Composition of the wavefunctions corresponding to the ground and the excited states; the numbers corresponds to the weight of the Slater determinant.

The GS wave function has four determinants (only three appear in the Table I-15). The one that has the largest coefficient (0.41) corresponds to what is expected from simple mono-electronic theory. However, because the mono-electronic energy difference between the first set (d_{xy} and $d_{x^2-y^2}$) and the second set (d_{xz} , d_{yz}) of degenerate orbitals is not very large, determinants with an unpaired electron in each degenerate orbital contribute to the wavefunction of the ground state. There are two determinants related by symmetry with coefficients 0.24 (Table I-15). The wave function of the first excited state is made by two determinants similar to the extra ones of the ground state. Therefore, there are four excitations between these determinants $\Delta m_l = 0$ giving large negative contributions to D .

In this part, all the complexes have been synthesized according to the literature procedure. 14]

1.3.c.i Variation of the counter anion

First, we will compare the structural difference in a series of $[\text{Ni}(\text{bpy})_3](\text{X})_2$ complexes.

Bond	Distance (PF ₆)	Distance (BPh ₄)	Distance (SO ₄) [17]	Distance (ClO ₄) [18]	Distance (NO ₃)
N1-Ni	2.093	2.069	2.096	2.071	2.077
N2-Ni	2.093	2.079	2.083	2.086	2.083
N3-Ni	2.093	2.089	2.083	2.090	2.086
N4-Ni	2.093	2.105	2.103	2.086	2.082
N5-Ni	2.093	2.066	2.089	2.071	2.088
N6-Ni	2.093	2.069	2.080	2.090	2.098

Table I-16. Selected distances in $[\text{Ni}(\text{bpy})_3]\text{X}_2$

This series demonstrates that the Ni-N distances in all the complexes are different, which indicates that the counter anion influences the molecular packing. In this series PF₆⁻ represents the reference distance. When the average distances in the various complexes are compared, it appears that BPh₄ exhibits the greatest distortion. It can be anticipated that the smallest distortion observed in the other complexes will result in a smaller rhombicity value, with one of them potentially aligning with the cavity frequency.

A comparison of the ZFS of the different complexes was attempted using cw-EPR. The signal obtained in the case of NO₃⁻ was relatively weak (Figure I-18), exhibiting a profile close to the zero-field signal desired, yet also exhibiting a profile close to a parasitic signal from the cavity. Unfortunately, the instrument malfunctioned before the scheduled low-temperature campaign

measurement, preventing the verification of the aforementioned measurements.

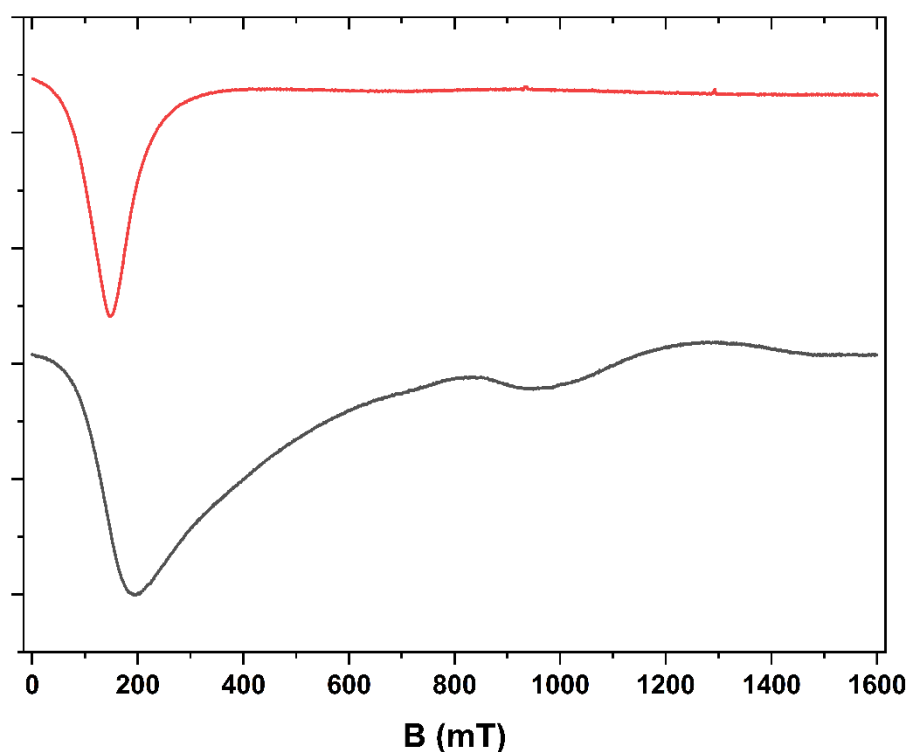


Figure I-18. cw-EPR spectra of $[\text{Ni}(\text{bpy})_3](\text{NO}_3)_2$ at 9.69 GHz (black) and 9.40 GHz (red) at $T = 90$ K.

Nonetheless, the same powder was able to be measured using HF-HFEPR. Surprisingly, the measurement of this spectrum in HF-HFEPR yielded $D = -1.25 \text{ cm}^{-1}$ and $E = 0 \text{ cm}^{-1}$, contradicting the structure and confirming that the band observed in X-band is probably due to an impurity. Therefore, drawing conclusions regarding the implemented strategy, particularly the role of the counter-anion modification, was impossible regarding the available data. Probably here, the result of the HF-HFEPR data is due to the fact that the rhombic parameter is very small.

1.3.c.i Functionalization of the 2,2'-bpy ligand

Following the modification of the counter-anion, it was decided that the functional groups on the bpy ligand should be changed in order to investigate in addition to the structural effect, a potential electronic effect. In order to address solubility issues and facilitate recrystallization, nitrate was selected as the counter anion. Among the various possibilities, only two systems appear to possess the desired properties. Their studies are presented in the second part of this report. The following section presents a brief overview of two systems that did not meet the desired criteria.

Introducing small substituents

The first attempt of modification of the trigonal structure was made by investigating the properties of $[\text{Ni}(4,4'\text{Me-}2,2'\text{bpy})_3](\text{NO}_3)_2$ and $[\text{Ni}(5,5'\text{Me-}2,2'\text{bpy})_3](\text{NO}_3)_2$. Both structures have a slightly distorted octahedral geometry (Table I-17).

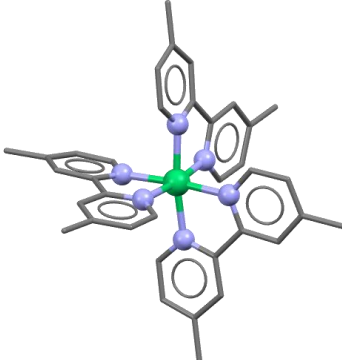
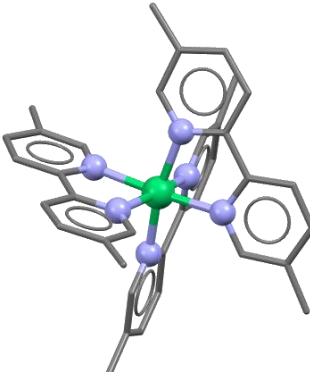
		
Formula	$\text{C}_{36}\text{H}_{36}\text{N}_6\text{Ni}_2(\text{NO}_3)_3 \cdot 3(\text{C}_2\text{H}_6\text{O})$	$\text{C}_{36}\text{H}_{36}\text{N}_6\text{Ni}_2(\text{NO}_3)_2 \cdot \text{C}_2\text{H}_3\text{N} \cdot \text{H}_2\text{O}$
Space Group	$P 2_1/c$	$P 1$
Cell Lengths	a 11.2276(14) b 28.656(4) c 13.7137(15)	a 10.2850(3) b 12.7463(3) c 14.4262(4)
Cell Angles	α 90 β 99.963(4) γ 90	α 87.3610(1) β 80.353(1) γ 87.636(1)
Cell Volume	4345.68	1861.41
Z, Z'	Z : 4 Z' : 1	Z : 2 Z' : 1
R-factor (%)	9.76	3.63

Table I-17. Crystallographic structure of $[\text{Ni}(4,4'\text{Me-}2,2'\text{bpy})_3](\text{NO}_3)_2$ (left) and $[\text{Ni}(5,5'\text{Me-}2,2'\text{bpy})_3](\text{NO}_3)_2$ (right).

HF-HFEPR spectra were measured on a microcrystalline powder obtained by grinding large crystals. In the case of $[\text{Ni}(4,4'\text{Me-}2,2'\text{bpy})_3](\text{NO}_3)_2$, the spectrum exhibited significant rhombicity (Figure I-19). All spectra were simulated, resulting in the following parameters:

$$D = +1.73(3) \text{ cm}^{-1}, E = 0.398(17) \text{ cm}^{-1}$$

$$g_x = 2.145(7), g_y = 2.150(7), g_z = 2.138(7)$$

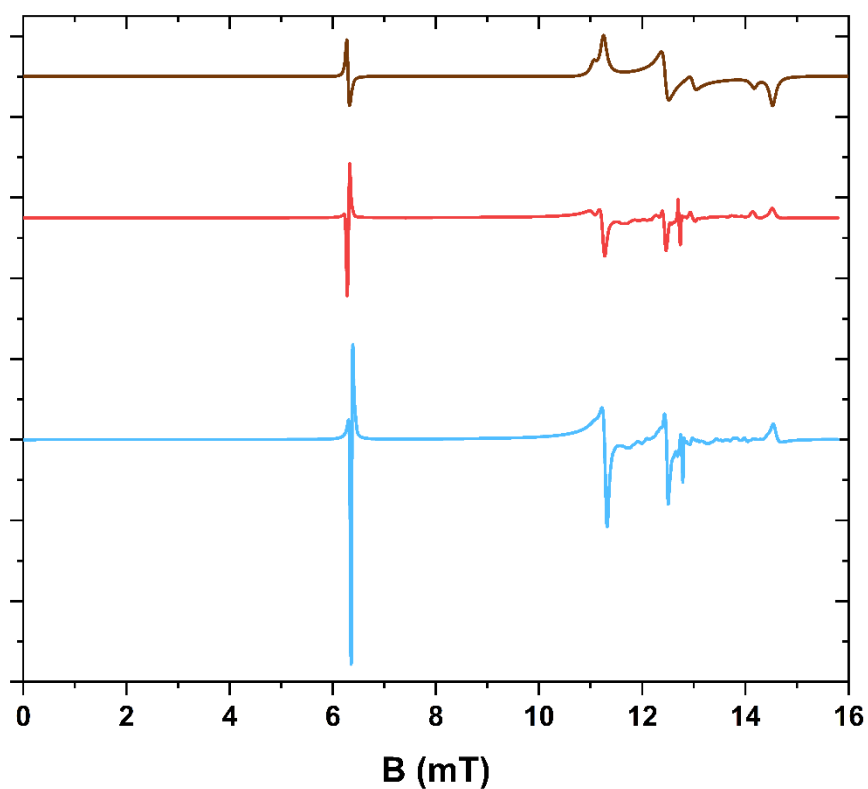
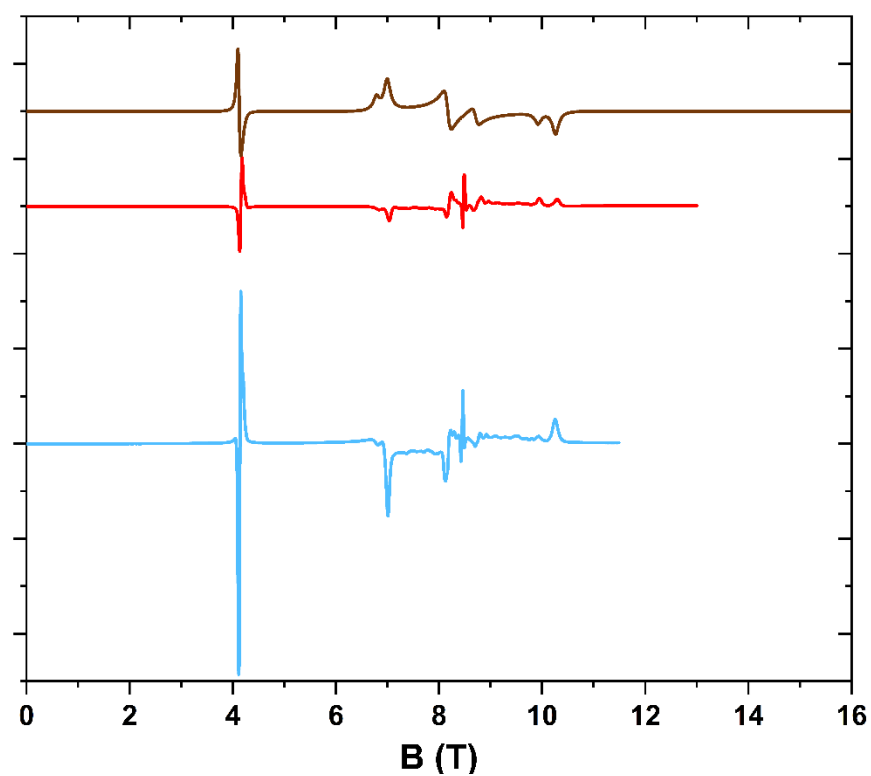


Figure I-19. a) HF-EPR spectra of $[\text{Ni}(\text{4,4'-Me-2,2'-bpy})_3](\text{NO}_3)_2$ at 255.2 GHz and $T = 5$ K (blue) and $T = 15$ K (red). b) HF-EPR spectra of $[\text{Ni}(\text{4,4'-Me-2,2'-bpy})_3](\text{NO}_3)_2$ at 383.2 GHz and $T = 5$ K (blue) and $T = 15$ K (red). Simulated spectra at $T = 15$ K (brown).

In the case of $[\text{Ni}(5,5'\text{-Me-}2,2'\text{bpy})_3](\text{NO}_3)_2$, the spectrum displayed a significant distribution of signals, as illustrated in Figure I-20. Despite the fact that the crystallographic structure is of excellent quality (R-factor = 3.86%), simulating the data proved to be extremely challenging. This was primarily due to the presence of at least three different orientations, which necessitated the adjustment of nine different parameters. The three different orientations can be due to the loss of the water molecule or the ACN one. In the structure the ACN molecule is linked to the counter-anion through hydrogen bonding. That is why a loss of solvent molecules can lead to a different phases hence anisotropy parameters. If this is the case, crystals with solvent molecules are clearly not adapted to our purpose. The best attempt at simulating the data is presented in Figure I-20 and parameters reported in Table I-18.

	Orientation A	Orientation B	Orientation C
D (cm^{-1})	-1.44	-0.86	-0.52
E (cm^{-1})	0.1	0.1	0.1
$g_x = g_y$	2.13	2.13	2.13
g_z	2.15	2.18	2.2

Table I-18. Value of anisotropy parameters for each orientation of $[\text{Ni}(5,5'\text{-Me-}2,2'\text{bpy})_3](\text{NO}_3)_2$

The presence of a factor three between orientation A and C had no explanation.

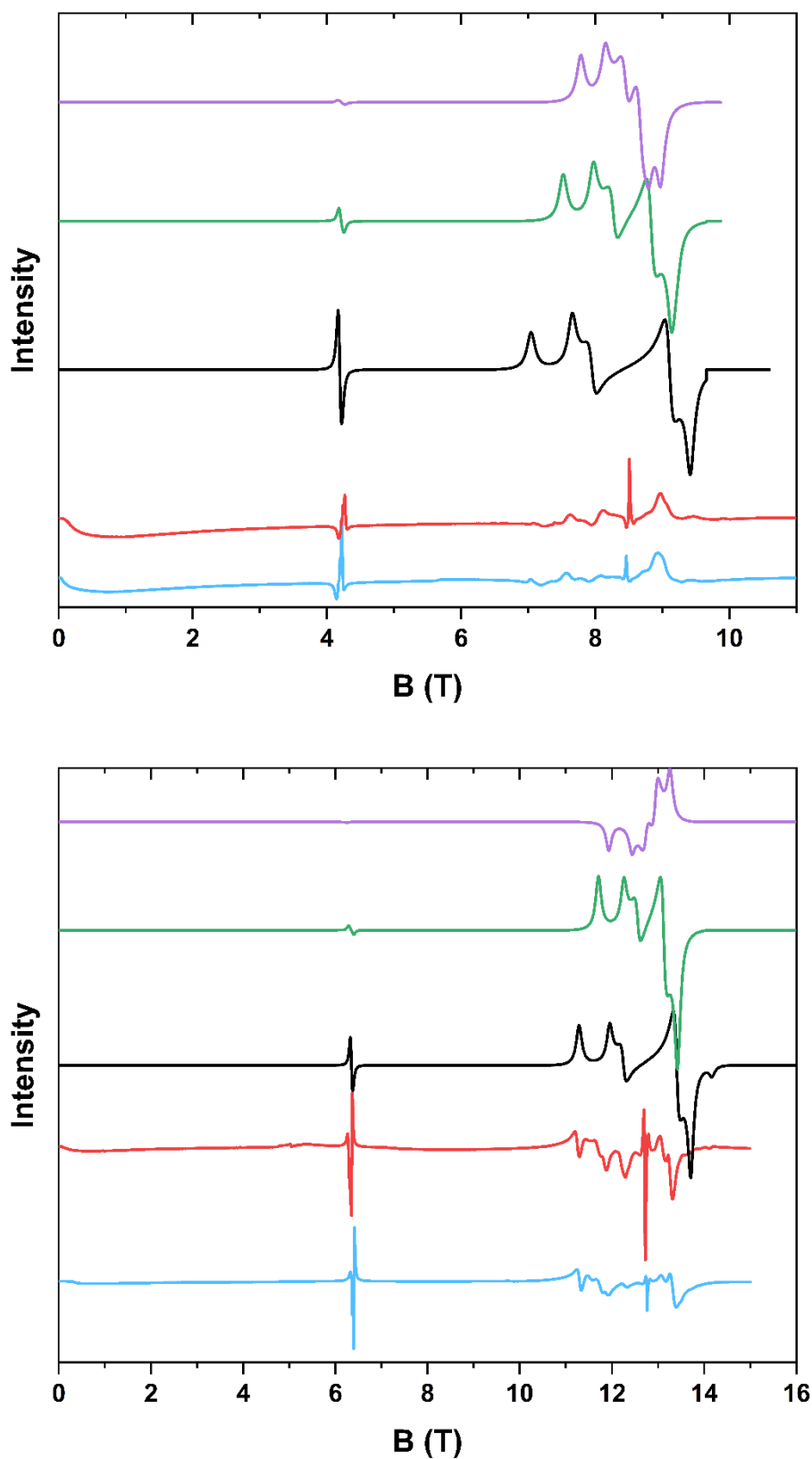


Figure I-20. a) HF-HFEPR spectra of $[\text{Ni}(5,5'\text{-Me-}2,2'\text{bpy})_3](\text{NO}_3)_2$ at 255.2GHz and $T = 5$ K (blue) and $T = 15$ K (red). b) HF-HFEPR spectra of $[\text{Ni}(5,5'\text{-Me-}2,2'\text{bpy})_3](\text{NO}_3)_2$ at 383.2GHz and $T = 5$ K (blue) and $T = 15$ K (red). Simulated spectra at $T = 15$ K for orientation 1 (black), orientation 2 (green) and orientation 3 (purple).

With both systems, we observe that even with very small modifications of the molecule, far from the coordination sphere, we are able to radically change the ZFS parameters, confirming our hypothesis. Therefore, three other compounds have been investigated.

Both compounds are not suitable for pulsed EPR experiments one ($[\text{Ni}(4,4'\text{-Me-}2,2'\text{bpy})_3](\text{NO}_3)_2$) because it has $D > 0$ and the other one ($[\text{Ni}(5,5'\text{-Me-}2,2'\text{bpy})_3](\text{NO}_3)_2$) because of the important distribution of E value. In the case in all the orientations have the same weights, this could lead to a very low signal. Furthermore, the very low value of D determined means that even at 5 K, the population of the M_s levels will be quite the same.

Introducing bulkier substituents

We attempted to induce a stronger electronic effect with introduction of a NO_2 group in the para position of the pyridine groups, but the compound could not be crystallized, preventing the rationalization of its properties. Three other compounds were attempted by functionalizing the 4 position of the bpy. In one case, we aimed to add a tert-butyl group, which corresponds to a strong inductive donor effect, another with Br, corresponding to a lower inductive effect, and one with an OMe group. For the latter no HF-HFEPR has been performed so despite the obtention of a crystallographic structure the compound will not be discussed here.

From the crystallographic data (Table I-19), the R factor of the $[\text{Ni}(4,4'\text{-Di-tert-butyl-}2,2'\text{bpy})_3](\text{NO}_3)_2$ compound is high ($> 8\%$). This result can be easily explained: the tert-butyl group can rotate easily, leading to significant disorder. With each molecule containing six tert-butyl groups, this disorder is further exacerbated. Additionally, the presence of an independent molecule in the unit cell contributes to the observed disorder.

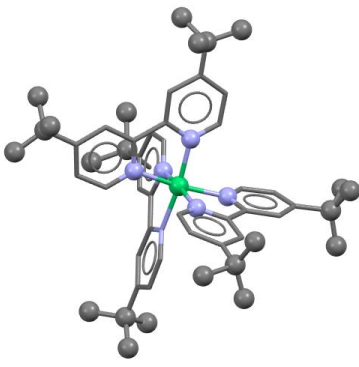
	
Formula	$C_{54} H_{72} N_6 Ni, 2(N O_3), 3(O)$
Space Group	$C 2$
Cell Lengths	a 20.4647(15) b 14.9768(10) c 21.408(2)
Cell Angles	α 90 β 116.158(3) γ 90
Cell Volume	5889.45
Z, Z'	Z : 4 Z' : 1
R-factor (%)	8.41

Table I-19. Crystallographic information of $[Ni(4,4'\text{-Di-tert-butyl-2,2'bpv})_3](NO_3)_2$.

The microcrystalline powders were subjected to HF-HFEPR spectroscopy for analysis. The spectra show the presence of a molecular distribution within the sample (Figure I-21), the ZFS parameters were determined, and it was found that $D < 0$.

$$D = -1.65 \text{ cm}^{-1},$$

$$E = 0.1 \text{ cm}^{-1},$$

$$g_x = g_y = g_z = 2.15.$$

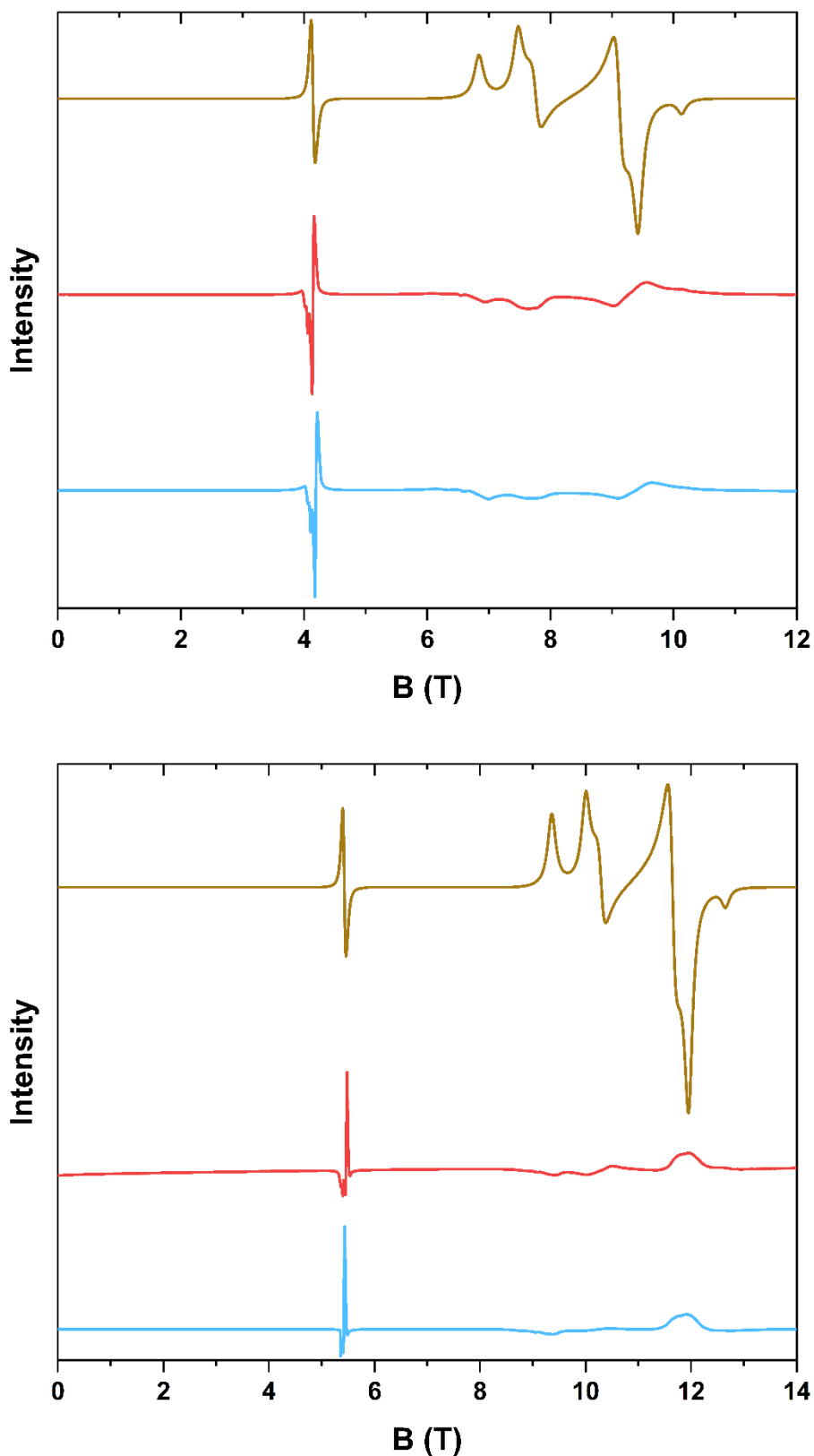


Figure I-21. Top HF-HFEPR spectra of $[\text{Ni}(4,4'\text{-Di-tert-butyl-2,2'bpy})_3](\text{NO}_3)_2$ at 255.3GHz and $T = 5 \text{ K}$ (blue) and $T = 15 \text{ K}$ (red). simulated data at $T = 15 \text{ K}$ (brown). b) Bottom. HF-HFEPR spectra of $[\text{Ni}(4,4'\text{-Di-tert-butyl-2,2'bpy})_3](\text{NO}_3)_2$ at 255.3GHz and 5K (blue) and $T = 15 \text{ K}$ (red). simulated data at $T = 15 \text{ K}$ (brown).

Subsequently, cw-EPR measurements at the X-band were conducted. In the perpendicular

mode, three distinct bands were observed (Figure I-22), with a band at zero field. Unfortunately, it was not possible to simulate this data using neither the PHI software nor Easyspin.

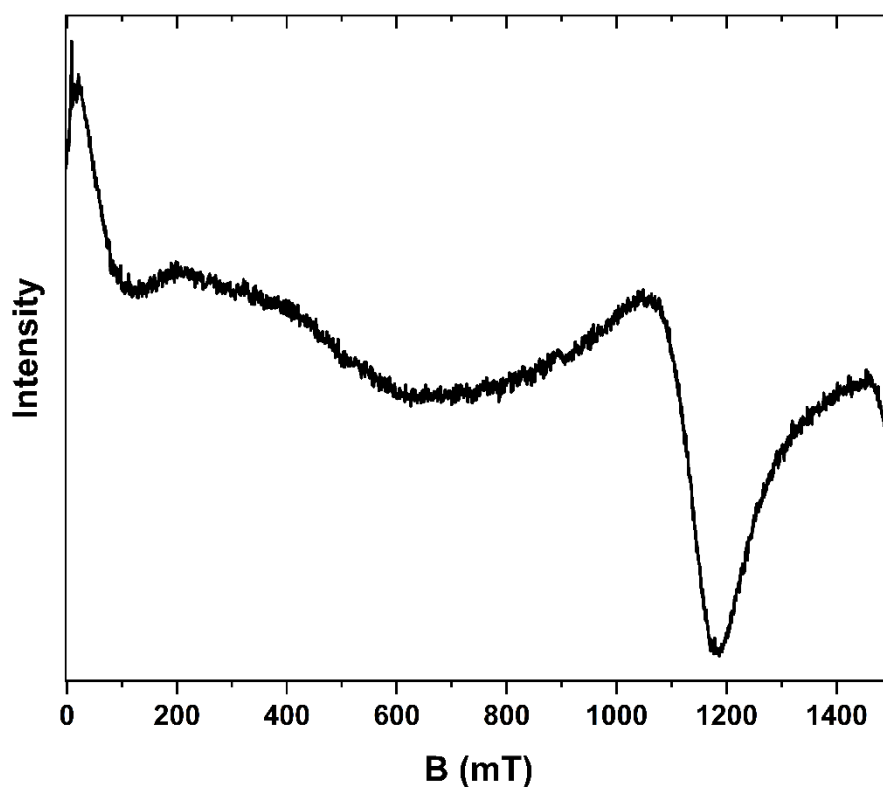


Figure I-22. CW EPR spectra of $[\text{Ni}(4,4'\text{-Di-tert-butyl-2,2'bpy})_3](\text{NO}_3)_2$ at $T = 90 \text{ K}$ and 9.69 GHz .

Then we investigated another compound $[\text{Ni}(4,4'\text{-Br-2,2'bpy})_3](\text{NO}_3)_2$. From the crystallographic data (Table I-20), we also see that the R factor of the compound is high ($>7\%$) but disorder is mostly due to solvent molecules, meaning that the coordination sphere of nickel is well described.

Formula	$C_{31} H_{18} Br_6 N_{7.5} Ni O_8$
Space Group	$C 2/c$
Cell Lengths	a 27.8080(13) b 19.9318(10) c 20.5480(16)
Cell Angles	α 90 β 132.246(2) γ 90
Cell Volume	8430.88
Z, Z'	Z : 8 Z' : 1
R-factor (%)	7.01

Table I-20. Crystallographic information of $[Ni(4,4'-Br-2,2'bpy)_3](NO_3)_2$.

The microcrystalline powders were subjected to HF-HFEPR spectroscopy for analysis. The broad transitions observed are due to the presence of a molecular distribution within the sample (Figure I-23), the anisotropy parameters were determined:

$$D = -1.83 \text{ cm}^{-1}$$

$$E = 0.146 \text{ cm}^{-1}$$

$$g_x = 2.130, g_y = 2.121, g_z = 2.163$$

It was found that $D < 0$, this indicates that the qubit state corresponds to the ground state of the system. Interestingly the value of E was found to be nearly ideal.

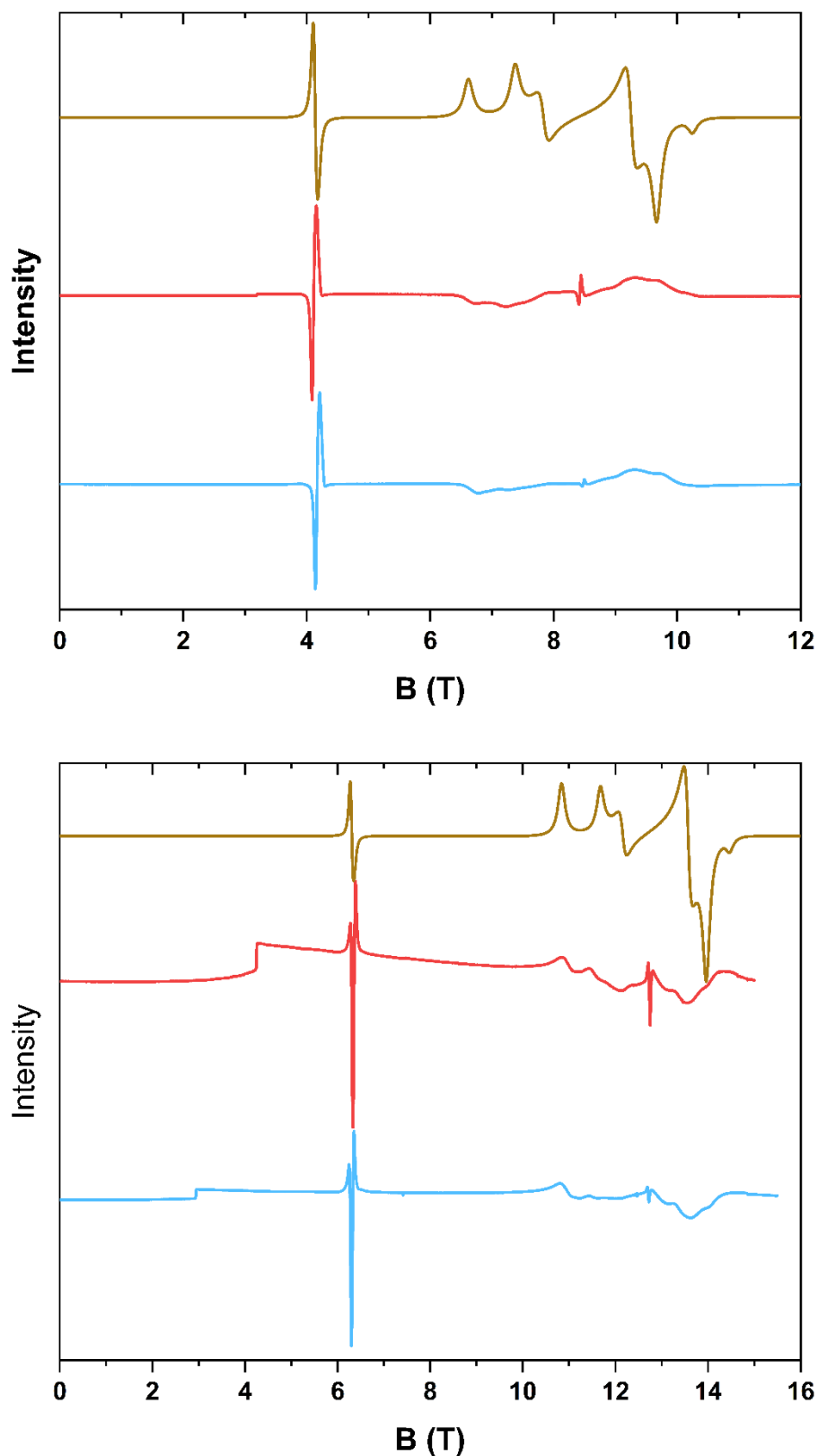


Figure I-23. (Top) HF-EPR spectra of $[\text{Ni}(4,4'\text{-Br-}2,2'\text{bpy})_3](\text{NO}_3)_2$ at 255.3GHz and $T = 5\text{ K}$ (blue) and $T = 15\text{ K}$ (red) and simulated data at $T = 15\text{ K}$ (brown). (Bottom) HF-EPR spectra of $[\text{Ni}(4,4'\text{-Br-}2,2'\text{bpy})_3](\text{NO}_3)_2$ at 383.3GHz and $T = 5\text{ K}$ (blue) and $T = 15\text{ K}$ (red) and simulated data at $T = 15\text{ K}$ (brown).

The compound could not be studied in X-band because the instrument was broken.

Here we have evidenced that our method can help identifying a clock transition. The initial approach involved changing the counter-anion and manipulating the molecules' packing. Structurally, we observed deformations, indicating the success of this strategy. Unfortunately, no HF-HFEPR experiments were conducted to confirm this methodology. However, by functionalizing the 2,2'bpy ligand, we have demonstrated that it is also possible to manipulate the packing, thereby adjusting the value of E relative to the cavity frequency.

I.3.d A tricky case: [Ni(imdipa)(NCS)](NCS)

The [Ni(imdipa)(NCS)](NCS) compound, has previously been investigated in magnetometry and HF-HFEPR within our team. A description of the study conducted on the compound is available here.^[2] The complex was studied by magnetometry on a single crystal and results gave values of $D = -2.96 \text{ cm}^{-1}$ and $E = 0.06 \text{ cm}^{-1}$. Specific heat measurements at low temperature showed the presence of a low-lying energy gap of 0.21 cm^{-1} , corresponding to a rhombic parameter E value of 0.105 cm^{-1} . Finally, recent HF-HFEPR studies give the following parameters: $D = -2.79(3) \text{ cm}^{-1}$, $E = 0.109(18) \text{ cm}^{-1}$, $g_x = 2.152(7)$, $g_y = 2.155(7)$ et $g_z = 2.183(8)$, compatible with the specific heat data for the rhombic parameter. For this complex, the gap ($2E$) is close to the X-band energy and we thought it was worth being investigated. In addition, well-shaped and relatively large single crystals could be grown so that a single crystal EPR study (X-band) could be envisaged. We, therefore, carried out theoretical studies to understand the origin of the negative D value, because its distorted structure does not allow any prediction based on simple symmetry considerations. We also studied its X-band EPR spectrum to check the presence of a transition near zero field.

I.3.d.i Structural study

The compound crystallizes in space group $P2_1/n$ and takes the shape of purple hexagons. There are two crystallographically independent molecules in the unit cell which differ by around 1° in their relative orientation. Both exhibit quasi identical coordination spheres (distances and angles). The geometry around the Ni center is a distorted octahedron where the pentadentate ligand has three amines (called N2, N3 and N4 in Table I-21) and two nitrogen atoms belonging to imidazoline groups, one in the plane (N1) and the other in the axial position (N5). The other apical position is occupied by a nitrogen atom belonging to NCS.

Formula	$2(\text{C}_{16}\text{H}_{27}\text{N}_8\text{NiS}), 2(\text{NCS}), \text{CH}_4\text{O}$
Space Group	$P 2_1/n$
Cell Lengths	a 14.8018(4) b 16.4349(4) c 19.1348(5)
Cell Angles	α 90 β 102.4940(10) γ 90
Cell Volume	4544.62
Z, Z'	Z: 4 Z': 1
R-factor (%)	3.68

Table I-21. Crystallographic information on $[\text{Ni}(\text{imdipa})(\text{NCS})](\text{NCS})$.

For the complex, if we assume that the electronic effects of the ligands are close enough, a reasoning on the Ni-ligand bond distances is sufficient to draw a preliminary conclusion on the relative energy of the d orbitals. We find that the difference between the average plane and the corresponding axial distances is the largest for the N1N2N3N4 plane (2.137 Å) and its axial positions N1N3 (2.060 Å). Also, the average axial distance is shorter than the average distance in the plane, which corresponds to a compressed octahedron along the N5-Ni-N6 axis (Table I-22).

Bond	Distance (Å)
N1-Ni	2.098
N2-Ni	2.138
N3-Ni	2.185
N4-Ni	2.128
N5-Ni	2.061
N6-Ni	2.060

Table I-22. Selected distances in $[\text{Ni}(\text{imdipa})(\text{NCS})](\text{NCS})$.

This leads to the conclusion that the $d_{x^2-y^2}$ and d_{z^2} orbitals are not degenerate anymore as it is for the Oh symmetry are and that $d_{x^2-y^2}$ has an energy lower than d_{z^2} . The different distances reported in the plane associated with the different nature of the ligand (amine vs imidazole) are consistent with a small lift of degeneracy of the t_{2g} orbitals thus with $E \neq 0$.

In summary, it is possible to conclude that the relative energy levels of this complex are as depicted in Figure I-24.

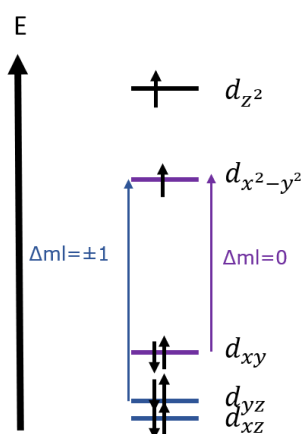


Figure I-24. Energy levels of d orbitals. Blue energy levels correspond to $m_l = \pm 1$, purple energy levels correspond to $m_l = \pm 2$ and black energy levels correspond to $m_l = 0$.

Based on the energy diagram of the d orbitals and on the theoretical analysis above, one can conclude that the excited state that lies lower in energy involves the excitation from the d_{xy} to the $d_{x^2-y^2}$, which leads to a negative contribution to D . We therefore expect an overall D value that is negative for this complex, because the other excited states that have positive D_i

contributions should not counterbalance the large negative value. Furthermore, the rhombic term should be small because the difference in energy between the d_{xz} and the d_{yz} orbitals is very small.

I.3.d.ii Theoretical computation

The calculations give the d energy level diagram depicted in Figure I-25. The energy diagram obtained is surprising because the lift of degeneracy does not correspond to the case of a tetragonally distorted Oh symmetry but is similar to the one of C_3 symmetry. This is confirmed by the orientation of the **D** tensor which is near a pseudo C_3 axis of the molecule.

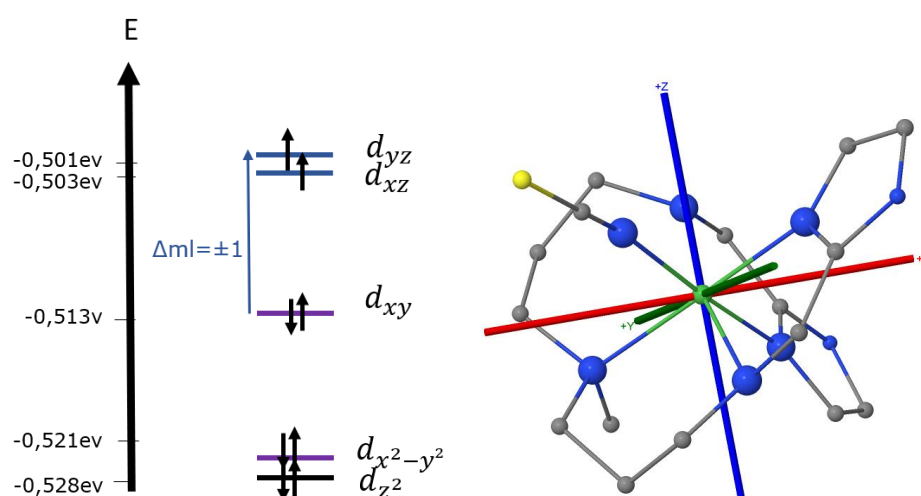


Figure I-25. Energy level of d molecular orbitals of $[\text{Ni}(\text{Imdipa})(\text{NCS})]^+$ (left) and orientation of the **D** tensor axes with respect to the molecule (z , blue; y , green and x , red) (right).

In our case we have supposed that every coordinating part of the ligands (imidazole, secondary, tertiary amine and NCS) are electronically equivalents which is clearly wrong according to the calculation. Thus, we have an electronic distortion. In this situation only, computation can provide us information about the lift of degeneracy and about the orientation of **D** tensor.

In Figure I-25, we can see that the **D** tensor does not lie within the molecular axes. The z axis for example, lies in the middle of three bonds. This means that the interactions among the d_{z^2} and the ligands are very weak. The same reasoning also works for the $d_{x^2-y^2}$ orbitals. We can see that the x and y axis go into the middle of the bonds. This means that the t_{2g} -like orbitals and especially the d_{xz} and d_{yz} will have a good overlap with the ligands orbitals (Figure I-25). This explains the energy diagram obtained above.

The individual contributions to D are given below.

Individual contributions to D -tensor:		
ES1	D_1	16.11
ES2	D_2	-0.66
ES3	D_3	-14.48

Table I-23. Individual contributions to D -tensor (in cm^{-1})

The calculations give the following ZFS parameters:

$$D = -2.55\text{cm}^{-1}$$

$$E/D = 0.014$$

It is not possible considering only the three first excited states to explain the sign of D in this case. Here, it is necessary to consider each excited state to find the value of ZFS. The details will not be presented here.

I.3.d.iii EPR study

The EPR spectra were recorded at 90 K in perpendicular mode at 9.69 GHz. The experimental spectrum (black dots) shows the presence of a band close to zero field, a transition around 450 mT and a band of lower intensity at 600 mT. The spectrum was simulated, with PHI software, starting from the parameters obtained from HF-HFEPR studies.[16] The best simulation (Figure I-26) was obtained with the following parameters:

$$D = -2.6\text{cm}^{-1}, E = 0.119\text{cm}^{-1}$$

$$g_x = 2.08, g_y = 2.22 \text{ and } g_z = 2.19$$

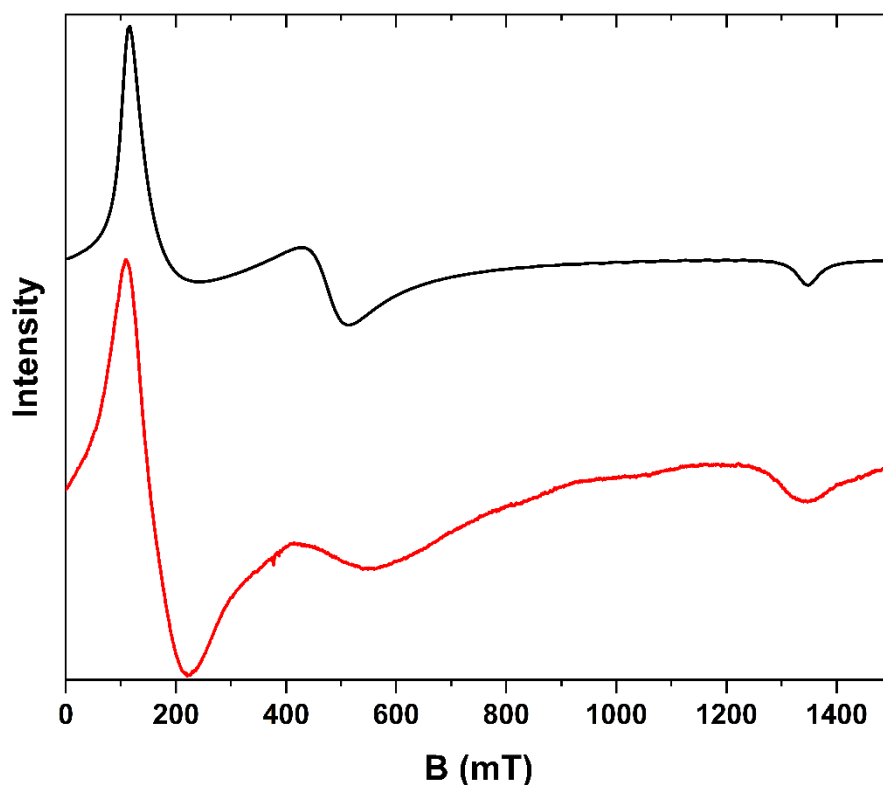


Figure I-26. CW-EPR spectra of $[\text{Ni}(\text{imdipa})(\text{NCS})](\text{NCS})$ in X band (9.69GHz) at $T = 90$ K. In red the experimental data, black curve corresponds to the fitting curve.

The experimentally determined gap ($2E$) is suitable for this complex to be studied by pulsed EPR with the perspective of observing an EPR transition near zero field.

I.3.d.iii Crystal orientation

Since crystals are relatively large (2 mm) and resistant to air, humidity and temperature change, we wanted to confirm the orientation of the anisotropy tensor found from computation. We tried to confirm the orientation of the anisotropy tensor using X-band studies on a single crystal in order to experimentally determine the orientation of the \mathbf{D} tensor axes and compare it to the calculations results. During this work, we faced two important problems. First, the goniometer was manual rendering the experiment very time-consuming and not precise. Secondly, in the crystal there are two molecules linked by a symmetry plan that is orthogonal to the b crystallographic axis. This means that for some angles, two transitions were observed. The absence of a goniometer imposed that we had to manually change the orientation of the crystal, which introduced a lot of errors. After three months of failure, we decided to ask for

the help of a colleague who has the adequate set-up and who is a specialist of these kind of experiments. Dr. Sylvain Bertaina from IN2MP (Marseille, France) helped us by recording the cw-EPR spectra with three different positions (Shonland's method [19]) of the crystal and then using the matlab software to simultaneously fit all positions. The results are under analysis.

Simultaneously, in collaboration with Dr. Iurii Kibalin from ILL (Grenoble, France) and Dr. Arsen Goukassov from CEA (Saclay, France), polarized neutron powder diffraction measurements were conducted at the HB-2A diffractometer at ORNL, utilizing a neutron wavelength of $\lambda = 2.41 \text{ \AA}$. These measurements were performed at 2 K under an external field of 3 T after zero-field cooling. To prevent any rotation of the crystallites in the applied field, the powder sample was pressed. The sum and the difference of the spin-up and spin-down polarized patterns were refined simultaneously using the local susceptibility approach incorporated in the new software package CrysPy, specially developed for the flipping ratio method on polycrystalline samples. However, the outcome of this experiment was somewhat mitigated due to a very noisy signal. Therefore, a new project has been proposed at ILL for a more powerful spectrometer to obtain better resolution. The last results are very promising because very good quality signals were obtained at different temperatures and magnetic fields. The analysis of these data that are underway will allow the determination of the susceptibility tensor that could be confronted with the EPR results on single crystal.

I.4 CONCLUSION

In this chapter, we have explained the origin of anisotropy in mononuclear nickel(II) complexes and see in what extent the ZFS could be tuned to obtain a clock transition accessible using EPR. We then explored various nickel compounds with different geometry, attempting to predict the nature of the axial anisotropy based on their structure. Computations allowed us to rationalize the sign of D . Subsequently, when possible, we measured the EPR spectra of these compounds to access and confirm the ZFS parameters. In most of the cases, the D value was accurately determined while E was poorly estimated.

We have seen that we need weak ligand field in order to maximise the anisotropy value of D and E by comparing weak and strong ligand field in Oh symmetry. In the cases of lower symmetry such as $[\text{Ni}(\text{MPZ})_2]$ or $[\text{Ni}(\text{imdipa})(\text{NCS})](\text{NCS})$, it is necessary to resort to calculations to determine the sign of D .

We have gone further by attempting to control the value of E . We started with $[\text{Ni}(\text{bpy})_3](\text{X})_2$ and by varying the counter anion, we observed different bond lengths, evidencing the importance of the packing on the ZFS parameters. Then we functionalized the bpy and showed using HF-HFEPR that even small modifications on the ligands due to electronic and steric effects changes the value of the ZFS. Thus, we have obtained a nickel compound with a value of $E = 0.146 \text{ cm}^{-1}$, namely $[\text{Ni}(4,4'\text{-Br-}2,2'\text{bpy})_3](\text{NO}_3)_2$, validating the strategy implemented. However, this compound cannot be diluted in its diamagnetic isomorphous matrix and will be not studied later.

Compounds exhibiting $D < 0$ and a value of $E > 0.1 \text{ cm}^{-1}$ will be further studied using pulsed EPR in the next chapter.

I.5 REFERENCES

- [1] G. Wolfowicz, A. M. Tyryshkin, R. E. George, H. Riemann, N. V. Abrosimov, P. Becker, H.-J. Pohl, M. L. W. Thewalt, S. A. Lyon, J. J. L. Morton, *Nature Nanotech* **2013**, *8*, 561–564.
- [2] M. Rubín-Osanz, F. Lambert, F. Shao, E. Rivière, R. Guillot, N. Suaud, N. Guihéry, D. Zueco, A.-L. Barra, T. Mallah, F. Luis, *Chemical Science* **2021**, *12*, 5123–5133.
- [3] R. Ruamps, L. J. Batchelor, R. Maurice, N. Gogoi, P. Jiménez-Lozano, N. Guihéry, C. de Graaf, A.-L. Barra, J.-P. Sutter, T. Mallah, *Chemistry – A European Journal* **2013**, *19*, 950–956.
- [4] B. Cahier, M. Perfetti, G. Zakhia, D. Naoufal, F. El-Khatib, R. Guillot, E. Rivière, R. Sessoli, A.-L. Barra, N. Guihéry, T. Mallah, *Chemistry – A European Journal* **2017**, *23*, 3648–3657.
- [5] S. Giménez-Santamarina, S. Cardona-Serra, J. M. Clemente-Juan, A. Gaita-Ariño, E. Coronado, *Chem. Sci.* **2020**, *11*, 10718–10728.
- [6] O. Kahn, *Molecular Magnetism*, Courier Dover Publications, **2021**.
- [7] M. M. Boyd, T. Zelevinsky, A. D. Ludlow, S. M. Foreman, S. Blatt, T. Ido, J. Ye, *Science* **2006**, *314*, 1430–1433.
- [8] F. Neese, F. Wennmohs, U. Becker, C. Riplinger, *The Journal of Chemical Physics* **2020**, *152*, 224108.
- [9] G. Rogez, J.-N. Rebilly, A.-L. Barra, L. Sorace, G. Blondin, N. Kirchner, M. Duran, J. van Slageren, S. Parsons, L. Ricard, A. Marvilliers, T. Mallah, *Angewandte Chemie* **2005**, *117*, 1910–1913.
- [10] N. F. Chilton, R. P. Anderson, L. D. Turner, A. Soncini and K. S. Murray *J. Comput. Chem.* **2013**, *34*, 1164–1175
- [11] Jonathan T. Yarranton, James K. McCusker, *Journal of the American Chemical Society*, **2022**, *144*, 12488,
- [12] C. D. Polyzou, O. Malina, J. Tuček, R. Zbořil, N. Panagiotou, A. J. Tasiopoulos, N. Boukos, J. Parthenios, A. N. Kalarakis, V. Tangoulis, *Inorg. Chem.* **2019**, *58*, 13733–13736.
- [13] M. D. Santana, L. López-Banet, G. García, L. García, J. Pérez, M. Liu, *Eur J Inorg Chem* **2008**, *2008*, 4012–4018.

- [14] G. Charron, E. Malkin, G. Rogez, L. J. Batchelor, S. Mazerat, R. Guillot, N. Guihéry, A.-L. Barra, T. Mallah, H. Bolvin, *Chem. Eur. J.* **2016**, *22*, 16850–16862.
- [15] J. Breu, H. Domel, A. Stoll, *European Journal of Inorganic Chemistry*, 2000, 2401
- [16] G. Rogez, *Modulation Des Propriétés Électroniques et de l'anisotropie Magnétique de Complexes Mono et Polynucléaires: Influence Des Ligands Pontants et Périphériques*, **2002**.
- [17] Y. Zhou, X. Li, Y. Xu, R. Cao, M. Hong, *Acta Crystallographica Section E* **2003**, *59*, m300–m302.
- [18] A. Wada, N. Sakabe, J. Tanaka, *Acta Crystallographica Section B* **1976**, *32*, 1121–1127.
- [19] D. S. Schonland, *Proc. Phys. Soc.* **1959**, *73*, 788–79

CHAPTER II: PULSED EPR STUDY OF MONONUCLEAR Ni(II) COMPLEXES

In this chapter, we study the relaxation time of mononuclear Ni(II) compounds at the clock transition using pulsed EPR.

In this chapter all experiments have been performed under the supervision of Dr. Serge Gambarelli (SYMMES, Grenoble).

II. INTRODUCTION

When it comes to qubits, the primary concern revolves around their relaxation times. On one hand, there is the spin-lattice relaxation, T_1 , which corresponds to the available computation time. On the other hand, there is the coherence time, T_2 , which corresponds to the time available to perform an operation. The spin-lattice relaxation time is temperature dependent,[1] and can therefore be drastically increased by reaching sub-kelvin temperatures. The coherence time, on the other hand, is sensitive to the fluctuations of the magnetic field bath.[2] As mentioned in the literature reviews, one way to protect the qubit against these fluctuations is to operate within a clock transition. In Chapter I.1.c., the difficulties associated with achieving such a transition in the case of molecules were discussed. In Chapter I.2, numerous Ni(II) mononuclear complexes exhibiting negative D values were investigated. Among them, some complexes displayed rhombicity ($2E$) values close to the frequency of the X-band cavity (close to 0.32 cm^{-1}). It is, however, almost impossible that the energy difference between the two $M_S = \pm 1$ sublevels, equal to $2E$, matches exactly the energy of the electromagnetic microwave radiation of the X-band EPR apparatus in order for the transition to be exactly at $B = 0$. Therefore, for a given complex with an E parameter, determined from EPR studies, close to X-band incident energy, $h\nu$ there may be some molecules with their E value that matches exactly $h\nu$ (X-or Q-band) at exactly $B = 0$ due to strain.[3]

The most effective technique for accessing the relaxation times of a compound is pulsed EPR. Pulsed EPR is an extremely sensitive technique, theoretically capable of distinguishing between the different parameters responsible for decoherence. In practice, the sensitivity of the instrument depends on the type of sample (a radical has a much narrower linewidth than Ni(II)), the relaxation time of the species studied, only $T_2 > 80 \text{ ns}$ are observable because of the dead time) and the number or power of the amplifiers.

In this chapter, a brief introduction on pulsed EPR is presented (Part III.1) then we study how

Chapter II: Pulsed EPR study of mononuclear Ni(II) complexes

in a clock transition, T_1 and T_2 evolve by changing different parameters. Those parameters will be the nature of the matrix in which the complex is embedded (part II), the coordination sphere of Ni(II) (part III) and the presence/absence of paramagnetic species in the material (part III.).

II.1 INTRODUCTION OF PULSED EPR SPECTROSCOPY

Some of the basic pulsed EPR measurements will be briefly described below, more detailed explanations are available elsewhere.[4]

II.1.a Nutation experiment

When a species with an electronic (or nuclear) spin is placed in a static magnetic field, its magnetic moment precesses around the field axis at a frequency called the Larmor frequency, which indirectly depends on its spin value and its gyromagnetic ratio. When an oscillating magnetic field is applied (blue rectangle in Figure II-1) in addition to the static field, the magnetic moment deviates from its axis and begins to oscillate between different states (for example, the levels $M_s = \pm 1/2$ for a spin 1/2) resulting in what is known as the Rabi oscillations. Since these oscillations are linked to the Larmor frequency, they provide insight into the value of the spin being studied.

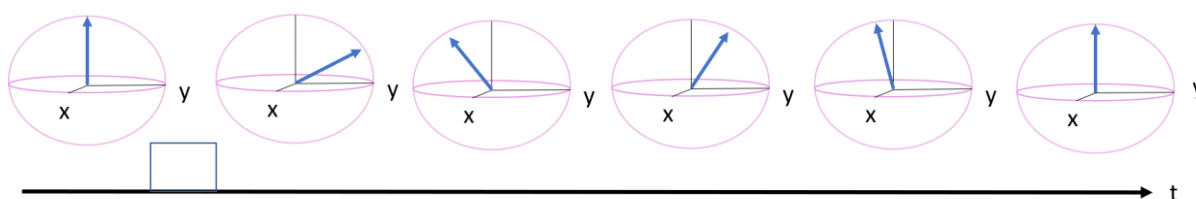


Figure II-1. Rabi oscillations after magnetic field oscillation is applied (blue rectangle).

In a nutation experiment, the length of the pulse is increased and the intensity of the echo as a function of time is recorded. Since the intensity corresponds to the value of the magnetization in the plane, a $\pi/2$ pulse will lead to a greater intensity than a $\pi/8$ one. Such experiment allows manipulating the vector within the Bloch sphere (create a superposition of the states) and gives information on the coherence time by measuring the intensity of the observed echo.

II.1.b Echo Detected Field Sweep

The preliminary step for every pulsed EPR measurement is to record an Echo-Detected Field Sweep (EDFS) curve. It consists of performing a Hahn echo sequence while sweeping the magnetic field, and recording the echo for each value of the magnetic field. If the intensity of the echo is zero, this means that either there is no transition at this field or the coherence time associated with the transition is too short-lived to be detected. This is why some transitions observed in a cw-EPR experiment are not detected in a pulsed EPR experiment, or conversely,

very low-intensity transitions in cw-EPR can yield to intense signals in the EDFS experiment if the associated relaxation time is long enough.

II.2 STUDY OF THE RELAXATION TIMES OF MONONUCLEAR Ni(II) COMPOUNDS WITH $D < 0$

III.2.a Influence of the matrix

The objective of this study is demonstrating that the spin-lattice relaxation time (T_1) may be tuned with the nature of the matrix in which the complex is embedded. To illustrate this phenomenon, we performed pulsed EPR studies and measured T_1 for [Ni(imdipa)(NCS)](NCS) in different matrices, i.e. silica, acetonitrile/methanol and deuterated acetonitrile/methanol. The study was carried out as followed:

- (i) Proving the presence of a CTs
- (ii) Measuring spin-lattice-relaxation time at different temperatures in each matrix
- (iii) Evaluating the matrices' influence on the coherence time

The spin relaxation time T_1 depends among, other things, on the extent of deformation of the complex within a given time interval. Such deformations are related to the vibration modes of the complex and to those of the lattice and their interaction. Therefore, a "rigid" lattice with a low density of phonons at the temperature at which the experiment is carried out may lead to a longer T_1 than a rather soft lattice (high density of phonons at low temperature). The density of phonons can be appreciated from the Debye temperature, θ_D , of the matrix that is around 275 K for silica,[5] and in the 60-90 K range for organic materials (the lattice of coordination complexes can be considered as an organic lattice).

We prepared three samples where the complex was diluted in 1) silica, 2) a mixture of acetonitrile/methanol (1/1) and 3) a mixture of deuterated acetonitrile/methanol (1/1), with a concentration of $6 \cdot 10^{19}$ spins/cm³ (which correspond to a dilution of 0.1 mol/L) for the three compounds. Unfortunately, we were not able to prepare the isomorphous diamagnetic Zn(II) complex in order to perform measurements of the Ni(II) in its own diamagnetic matrix because we could not prepare the Zn(II) derivative of this complex.

The silica materials were prepared by diluting the complex (37.5 mg) in 1 mL of MeOH. Then 1 mL of HClO₄ (10^{-2} mol/L) was added. Then 0.5 mL of this solution was added to 0.5 mL of TMOS

(tetramethyl orthosilicate). The mixture was stirred and allowed to dry resulting to a concentration around 6.10^{19} spins/cm³.

Experimental conditions

The experiment on [Ni(imdipa)(NCS)](NCS) in silica at 10, 1% and 0.1% have been performed with an attenuation of 14 dB while the experiment on [Ni(imdipa)(NCS)](NCS) in silica at 50% and in solutions have been performed with an attenuation of 13 dB.

Echo-detected EPR. The echo-detected field-swept (EDFS) spectra were recorded with a two-pulse primary Hahn-echo sequence ($\pi/2-t-\pi-t$ -echo), with microwave pulse lengths of 16 and 32 ns respectively, a fixed delay time $t = 120$ ns for [Ni(imdipa)(NCS)](NCS) in silica at 10, 1% and 0.1%, $t = 140$ ns for [Ni(imdipa)(NCS)](NCS) in silica at 50% and $t = 150$ ns for [Ni(imdipa)(NCS)](NCS) in solution and with the variation of the static B_0 magnetic field.

Hahn echo sequence. The spin-spin relaxation (T_2) spectra were recorded with a two-pulse primary Hahn-echo sequence ($\pi/2-t-\pi-t$ -echo), with microwave pulse lengths of 16 and 32 ns respectively, a fixed delay time $t = 120$ ns for [Ni(imdipa)(NCS)](NCS) in silica at 10, 1% and 0.1%, $t = 140$ ns for [Ni(imdipa)(NCS)](NCS) in silica at 50% and $t = 150$ ns for [Ni(imdipa)(NCS)](NCS) in solution.

Inversion recovery curves were collected by application of a three-pulse sequence ($\pi-T-\pi/2-\tau-\pi-t$ -echo), with microwave pulse lengths of -32, 16 and 32 ns respectively, pulse lengths and a fixed delay time $t = 120$ ns for [Ni(imdipa)(NCS)](NCS) in silica at 10, 1% and 0.1%, $t = 140$ ns for [Ni(imdipa)(NCS)](NCS) in silica at 50% and $t = 150$ ns for [Ni(imdipa)(NCS)](NCS) in solution.

II.2.a.i Proving the presence of CT

The first step is to ensure that the properties of the compound were conserved in the silica matrix. In Figure II-2, the cw-EPR spectra in X-band of the compound in powder form and at two different dilutions in silica were recorded. The spectra recorded at 90 K in silica (red and blue) are particularly noisy, and the baseline, due to instrumental issues, was highly distorted. However, both spectra showed the presence of a transition near zero field, as in the powder (black trace). Thus, we can conclude that the complex has not decomposed when embedded in silica. However, the transition near zero field seems to be slightly shifted towards low magnetic

fields compared to the powder sample (Figure II-2). This variation indicates that the ZFS parameters are slightly different. The cw spectrum of a methanol/DMSO solution of the complex is noisy, but shows a signal close to 150 mT, attesting the stability of the molecules in these solvents (Figure II-3).

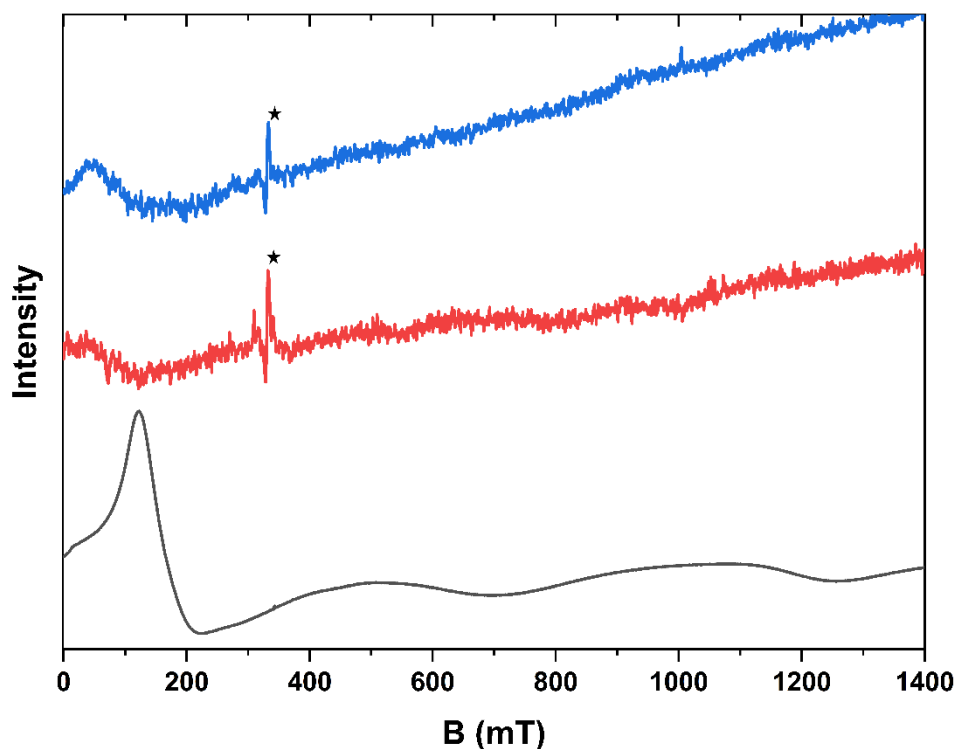


Figure II-2. CW EPR spectrum of $[\text{Ni}(\text{imdipa})(\text{NCS})(\text{NCS})]$ in powder (black) diluted in silica at 50% (red) and 25% (blue) at $T = 90 \text{ K}$ and at 9.69 GHz. Black stars correspond to the cavity resonance.

The Echo Detected Field Sweep (EDFS) spectra (Figure II-4) show the presence of an echo closed to zero field and at 150 mT for the three samples (the transition observed around 340 mT corresponds to the cavity). The transition at 150 mT corresponds to the main one observed in the cw spectrum, as indicated by the derivative of the EDFS curves (Figure II-5). First, we observe a signal at zero field that is not detected in the cw spectrum, indicating that there are species with a relaxation time long enough to be detected in the EDFS spectrum but with very low concentration so that they are absent in the cw spectra of the powder and of the solution (Figure II-5). Second, for the silica sample, the transition at 150 mT has relatively larger intensity than for the other two samples when compared to the transitions at zero-field.

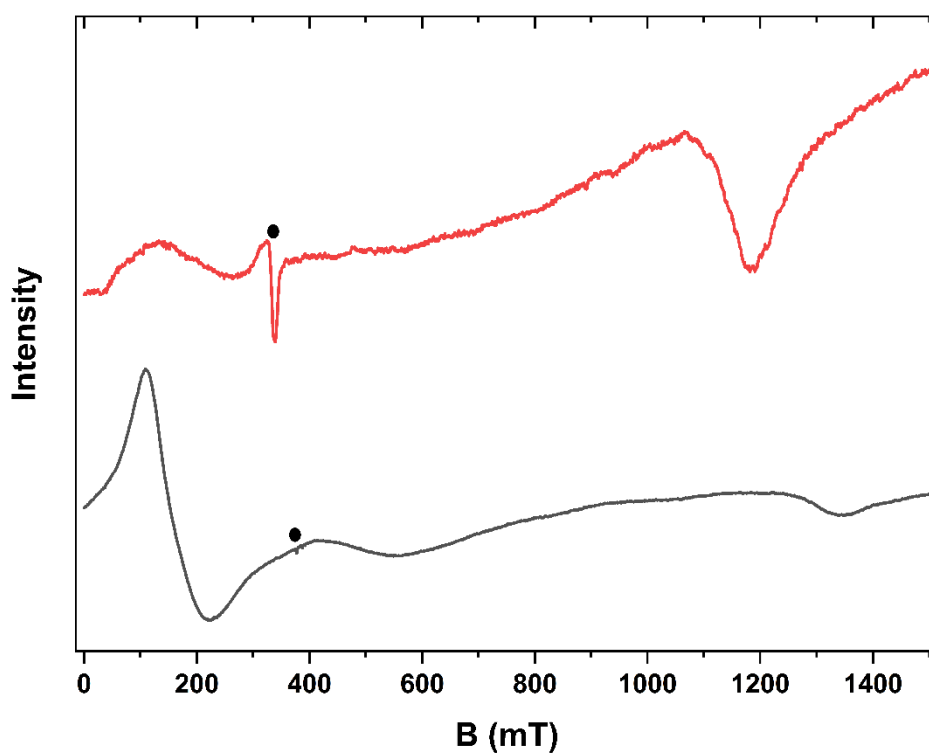


Figure II-3. cw-EPR spectra of $[\text{Ni}(\text{imdipa})(\text{NCS})](\text{NCS})$ in MeOH/ACN solution (red) and powder (black) at $T = 10 \text{ K}$ and at 9.69 GHz.

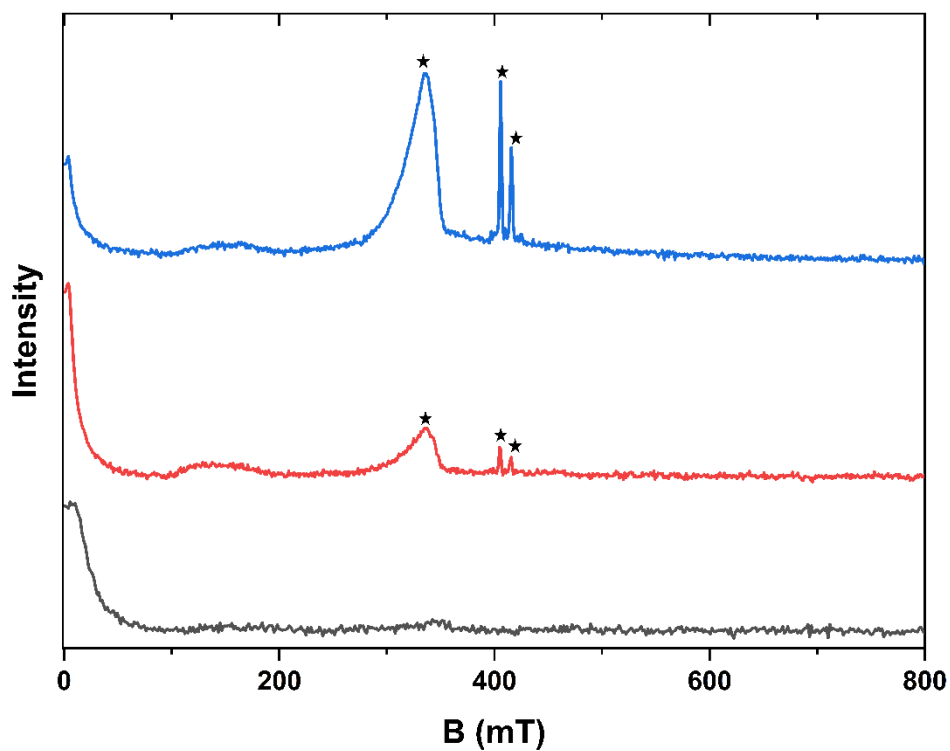


Figure II-4. EDFS spectra of $[\text{Ni}(\text{imdipa})(\text{NCS})](\text{NCS})$ diluted in silica (black), in ACN(D)/MeOD (red) and in ACN/MeOH (blue) and at $T = 5 \text{ K}$, 9.69 GHz.

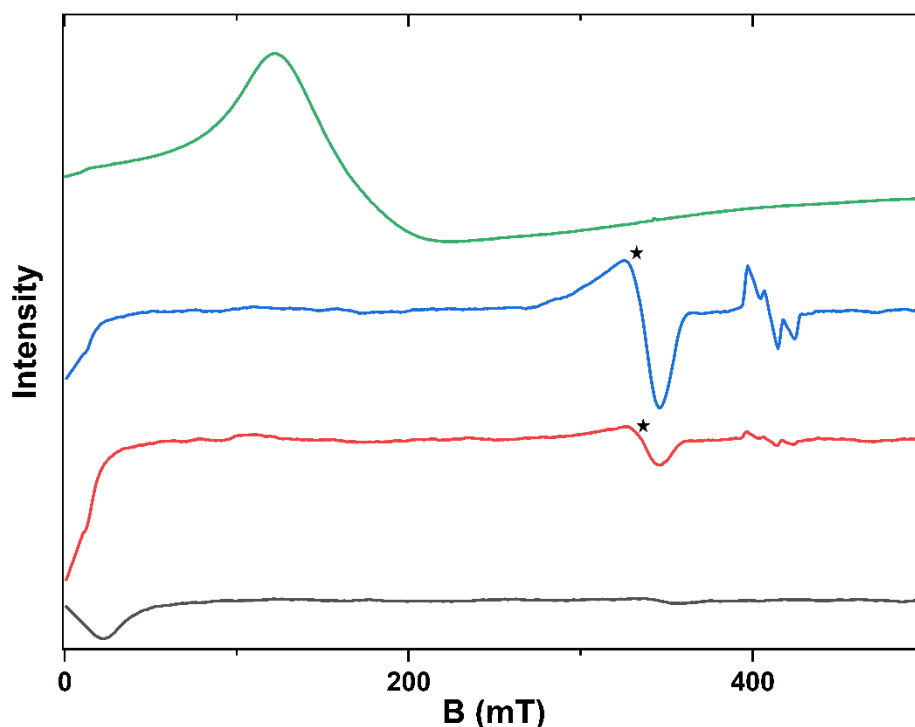


Figure II-5. Derivative of the EDFS spectra of $[\text{Ni}(\text{imdipa})(\text{NCS})](\text{NCS})$ diluted in silica (black), in $\text{ACN}(\text{D})/\text{MeOD}$ (red) and in ACN/MeOH (blue) at $T = 5 \text{ K}$ and 9.69 GHz , and cw-EPR spectrum of $[\text{Ni}(\text{imdipa})(\text{NCS})](\text{NCS})$ in powder form (green) at $T = 90 \text{ K}$ and 9.69 GHz .

The only possible explanation to the presence of an EDFS signal at zero field (Figure II-5), therefore with a transition equal to 9.69 GHz (0.32 cm^{-1}) is the presence within the samples of molecules with an E value equal to 0.16 cm^{-1} ($h\nu/2$) different from that measured for the complex in the powder form (0.119 cm^{-1} , see Chapter I), and also different from that of the molecules in solution, because in solution only the signal around 150 mT is detected in the cw spectrum (Figure II-2). It is interesting to note that for the silica sample a multiple signal with non-negligible intensity is observed in the $100 - 250 \text{ mT}$ region in the EDFS spectrum, while in solution the transition in this region is extremely weak (Figure II-4). The presence of two signals for the silica sample is consistent with ensembles of molecules having different E (and D) values. A simple simulation shows that in this region an increase of 50 mT for the transition corresponds to a decrease of around 0.03 cm^{-1} for the E value, which corresponds to a very slight change in the coordination sphere of the molecules, probably due to the constraint imposed by the silica matrix. The striking feature, however, is that these ensembles of molecules have a relaxation time long enough to be detected even at $B \neq 0$. For the samples in solution, no signal is observed in this region in the EDFS spectra indicating that the

acetonitrile/methanol matrix does not promote molecules with “long” relaxation at $B \neq 0$. Finally, the fact that the intensity of the EDFS signal at zero field is larger for the silica sample than for the other two indicates that either the concentration of molecules is larger for the silica sample or/and that the relaxation time of the molecules at zero-field is longer. The previous analysis is made under the assumption that the dilution process led to a random distribution of well isolated molecules for the three samples. This is not probably the case particularly for the silica sample where crystallites (nanometric size) may form. For these crystallites, the relaxation time is expected to be very short, so that the concentration of the molecules detected within the sample would be much smaller than the nominal concentration of the sample.

In summary, even though the large majority of the molecules have an E value close to the electromagnetic radiation $h\nu$ of the X-band used for the experiment, strain within the sample allows to select molecules that have an E value that matches $h\nu$, therefore allowing the detection of the clock transition. The silica sample seems to contain molecules with longer relaxation times, but also induce larger distribution of the ZFS parameters of the embedded molecules.

The last step to confirm the presence of a CT at zero field was to verify that the spin measured correspond to a $S = 1$ system. For this purpose, the nutation frequency of the compound (black line) and that of the organic radical TEMPO reference ($S = 1/2$) were compared at an attenuation value of 12 db. From Figure II-6, we can see that the oscillation for TEMPO (2,2,6,6-tetramethyl-1-piperidinyloxy) are twice slower (frequency two times larger) than for $[\text{Ni}(\text{imdipa})(\text{NCS})](\text{NCS})$ proving that the spin studied is a $S = 1$ spin. In the next sections, we present the measurements of T_1 and T_2 for the three samples.

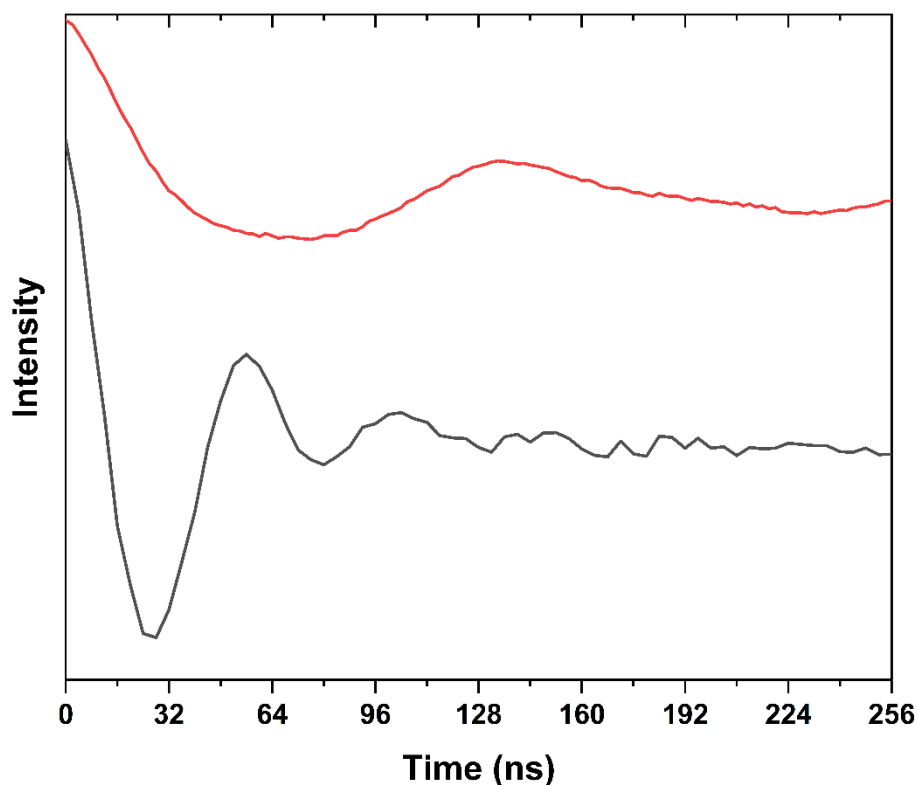


Figure II-6. Nutation experiment at 12 db of TEMPO (red) at $B = 324$ mT and $[\text{Ni}(\text{imdipa})(\text{NCS})](\text{NCS})$ diluted in silica (black) at $B = 1$ mT, at $T = 5$ K and at 9.69GHz.

II.2.a.ii Spin-lattice relaxation study

Our assumption was that a material with a higher Debye temperature would result in a longer T_1 . To test this assumption, an inversion recovery sequence was performed on the three samples at varying temperatures. We started with the silica sample by recording T_1 vs. time after an inversion recovery sequence (Figure II-7) at $T = 5$ K and fitted to the model using a stretched exponential (Equation III-1).

$$y(t) = Ae^{(-\frac{t}{T_1})^\alpha} \quad (\text{III-1})$$

A: pre-exponential factor which correspond to a decay rate; T_1 : Spin-lattice relaxation time; t: time; α : stretched factor which describes the distribution of T_1 values.

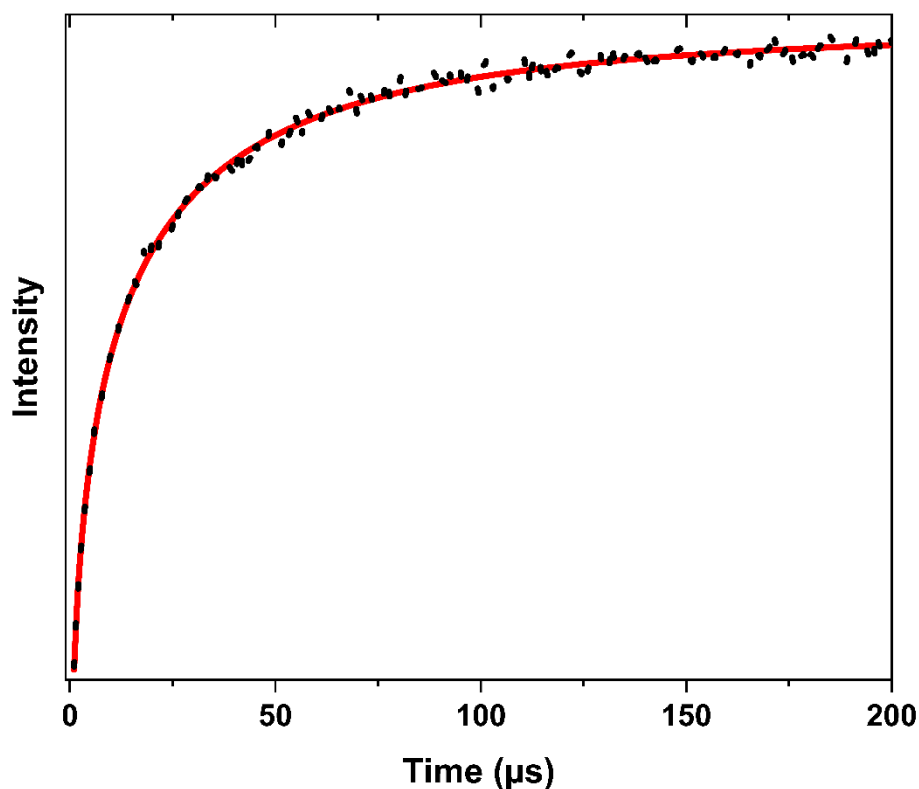


Figure II-7. Spin-lattice relaxation time curve of $[\text{Ni}(\text{imdipa})(\text{NCS})](\text{NCS})$ diluted in silica (black dot) measured at $T = 5 \text{ K}$, at $B = 1 \text{ mT}$ and at 9.69 GHz . The data were fitted using a stretched exponential model (black line).

One can see that the model employed fit well the data. The relaxation time T_1 is found equal to $10.75 \mu\text{s}$ at $T = 5 \text{ K}$. In Equation III-2, we see that the alpha value (0.62) is smaller than 1 which means that spin diffusion does not control the relaxation time.[6] The alpha value is compatible with a distribution of exponentials, which can be due to a distribution of molecules inside the sample, may be coming from the presence of ensembles of molecules, which naturally will have different relaxation time.

$$y(t) = -1.03e^{\left(-\frac{t}{10.75}\right)^{0.62}} \quad (\text{III-2})$$

The study of T_1 at $T = 5 \text{ K}$ shows a very small dependence on the magnetic field (Figure II-8). This mean that probably tunnelling and direct process mechanisms are not involved in the relaxation pathways (cf Chapter I.2). To confirm this hypothesis, the same experiment must be repeated at different temperatures.

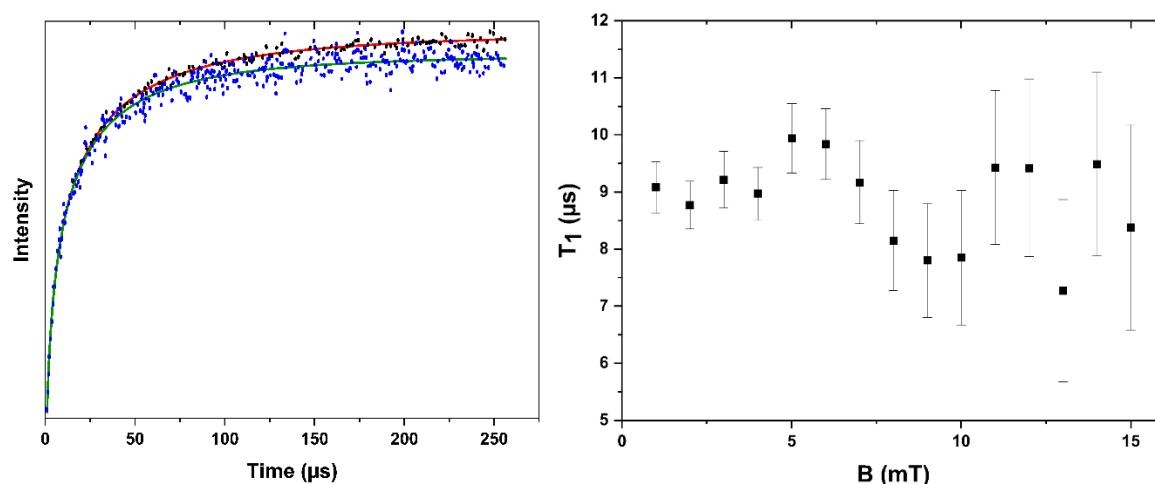


Figure II-8. (Left) Spin-lattice relaxation time curve of $[\text{Ni}(\text{imdipa})(\text{NCS})](\text{NCS})$ diluted in silica (black dot) measured at $T = 5 \text{ K}$, at $B = 1 \text{ mT}$ (black dot) and $B = 9 \text{ mT}$ (blue dot) and at 9.69 GHz . The data were fitted using a stretched exponential model (red line for $B = 1 \text{ mT}$ and green line for $B = 9 \text{ mT}$). (Right) Variation of T_1 GHz along the magnetic field for $[\text{Ni}(\text{imdipa})(\text{NCS})](\text{NCS})$ diluted in silica (6%) at $T = 5 \text{ K}$ and at 9.69 GHz .

We measured the variation of T_1 vs. temperature (Figure II-9), that follows a mono-exponential decay (Equation III-3) indicating that the Orbach mechanism controls the relaxation.

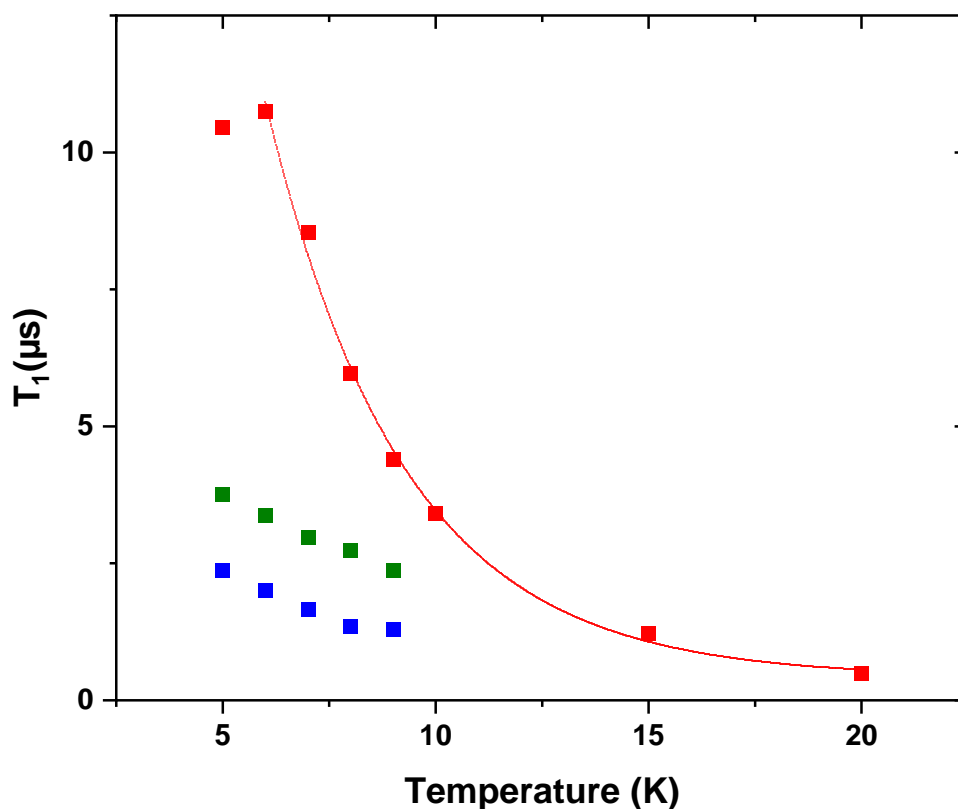


Figure II-9. Temperature dependence of the spin-lattice relaxation time for $[\text{Ni}(\text{imdipa})(\text{NCS})](\text{NCS})$ diluted in silica (red), ACN(D)/MeOD (blue) and ACN/MeOH (green) at $B = 1 \text{ mT}$ and at 9.69 GHz .

$$T_1(T) = 67.34 \times e^{\left(\frac{-T}{3.23}\right)} \quad (\text{III-3})$$

To validate this hypothesis or to determine more precisely the contribution of each mechanism, one needs to perform experiments for a larger range of temperature. This was not possible because no echo could be detected for temperatures larger than 25 K in silica.

The same experiments as for silica were performed for the two other samples (in solution). Both samples exhibited very close spin-lattice relaxation time ($T_{1-ACN/MeOH}$ (5K) = 3.76 μ s and $T_{1-ACN(D)/MeOD}$ (5K) = 2.37 μ s), which is consistent since the only difference between the two lattices is the substitution of protons by deuterium atoms. The comparison of the results obtained for the molecules embedded in the solvents and those in silica showed that the latter possesses a T_1 two times longer than the formers. Furthermore, for the silica material it was possible to record T_1 at higher temperatures due to the longer spin-lattice relaxation time that gives a more intense signal. This is consistent with the rigidity of the lattice that leads to longer T_1 . It is worth mentioning that the alpha value remains smaller to 1 for all samples, indicating a distribution of species with different relaxation times.

II.2.a.iii Coherence time study

We will focus now on the study of the coherence time of the three samples. The magnetic moment of deuterium is six times lower than that of the proton. Therefore, for qubits sensitive to magnetic fluctuations, the coherence time is expected to be longer for the deuterated sample than for the non-deuterated one. But for qubits protected by the clock transition, the coherence time should be the same for the two samples. In most of the cases we studied, the recorded coherence times are longer in the deuterated solution than in the protonated one.[11]

As shown in Figure II-10 (top), the use of a mono-exponential does not allow the data to be fitted correctly, particularly at the level of the inflection of the exponential, when all the molecules are considered. On the other hand, as shown in Figure II-10 (bottom), the use of a stretched exponential perfectly fits the experimental data. This means that there is a distribution of exponentials and therefore of relaxation mechanisms or populations. In our CT case, only the flip-flop is supposed to be present, which means that the distribution comes from a population distribution.

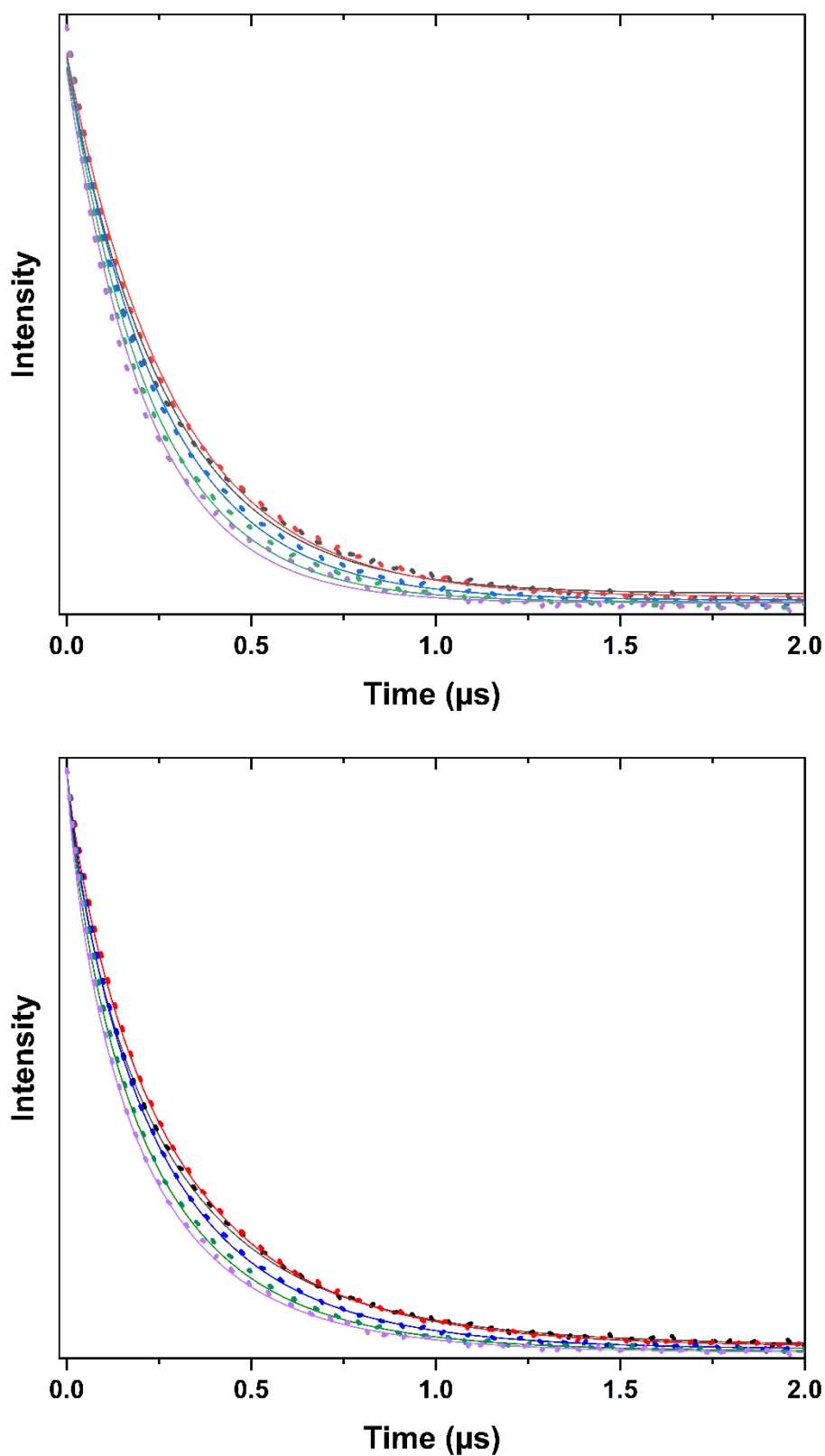


Figure II-10. Spin-Spin relaxation after an Hahn echo sequence for the ACN(D)/MeOD 10^{13} mol/L (top) at $B = 1$ mT (black), $B = 2$ mT (red), $B = 3$ mT (blue), $B = 4$ mT (green) and $B = 5$ mT (purple) at $T = 5$ K and 9.69 GHz. Dots correspond to the experimental point and line to the fitted data. (Top) Data fitted using mono-exponential model. (Bottom) Data fitted using stretched-exponential model.

Figure II-11 shows the dependence of the coherence times with the magnetic field. At zero

field the coherence time of the deuterated sample ($T_2 = 0.28 \mu\text{s}$) is three times longer than that of the protonated one ($T_2 = 0.1 \mu\text{s}$).

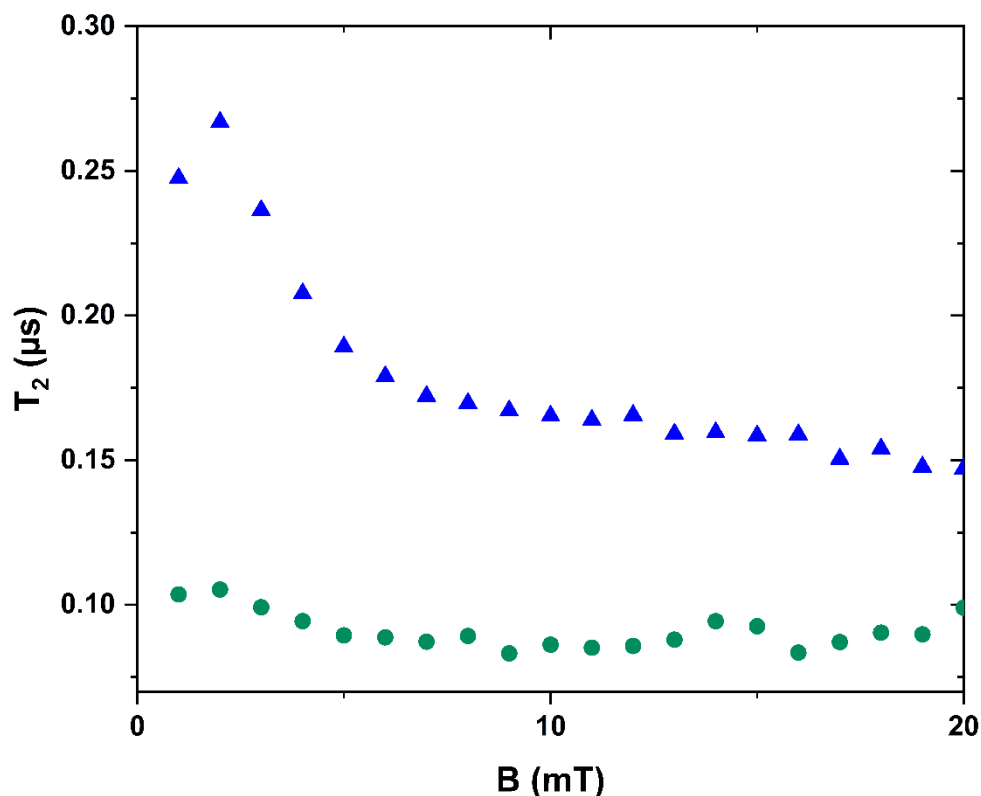


Figure II-11. Variation of the coherence time with magnetic field at $T = 5 \text{ K}$ and at 9.69 GHz band. Blue triangles correspond to $[\text{Ni}(\text{imdipa})(\text{NCS})](\text{NCS})$ diluted in the deuterated solution, and green circles correspond to $[\text{Ni}(\text{imdipa})(\text{NCS})](\text{NCS})$ diluted in the protonated solution. All data were fitted using a stretched exponential model.

One possible explanation of this result is the following: the clock transition area is proportional to E , and because E is very small, the magnetic field region where the protection is efficient is very narrow (cf Chapter 1 part 1b), so that the second order term becomes significant. The field dependent variation of T_2 shows a decrease of around 25% for the non-deuterated sample, while a decrease of 40% is observed for the deuterated one. Maybe this difference is not significant due to experimental error. However, assuming the samples are protected from magnetic field fluctuations, one should observe a much larger decrease of T_2 for the non-deuterated sample than for the deuterated one, which is not the case. The previous analysis is made assuming the two samples are identical i.e. the distribution of the diluted molecules is the same which should be the case. If it is not and if for the non-deuterated sample "clusters" of molecules are formed with a mean average distance between the molecules smaller than for

the deuterated sample, one can propose that the main mechanism that governs the coherence time in the two samples is the dipolar interaction that leads to a relaxation with no energy exchange (flip-flop). Such relaxation mechanism highly depends on the concentration of the magnetic species within a given sample.[7]

The quality of the dilution could be appreciated by the parameter α . If we compare the parameter α we find that $\alpha_D = 0.87$ at 1 mT to 1 at 150 mT for the deuterated solution while α_P vary from 0.7 at 1mT to 0.6 at 150 mT. It is difficult to attribute a mechanism or physical effect from $\alpha < 1$ value. As mentioned previously, we measured an ensemble of molecules and the resulting curve is an average. Here $\alpha < 1$ means that we have a distribution of T_2 values, so we measure the coherence time of different molecules or different ensembles some of them have long T_2 while others have short T_2 . The molecules are different because their local environment is not the same for reasons explained in Chapter I.2.

It is possible to discriminate between the two populations in order to extract the longer values T_2 value. We will remove the contribution of molecules that possess short coherence times. We make the assumption that these molecules are those belonging to clusters as previously described and their coherence time is mainly governed by the flip-flop process, thus they do not give any information on the role of the CT.

In the case of the non-deuterated solution, only the five first data points will be considered due to the very noisy signal at higher fields. This is coherent with our assumption, outside the CT ($B > 3$ mT) the system is sensitive to spin diffusion and this phenomenon is stronger in the non-deuterated solution than in the deuterated one due to the difference in the magnetic moment of H and D. Now the data can be fit using a single-exponential model (Figure II-112 which is consistent with the assumption of one population of molecules with identical ZFS parameters and environment are being probed. The results are presented Figure II-13.

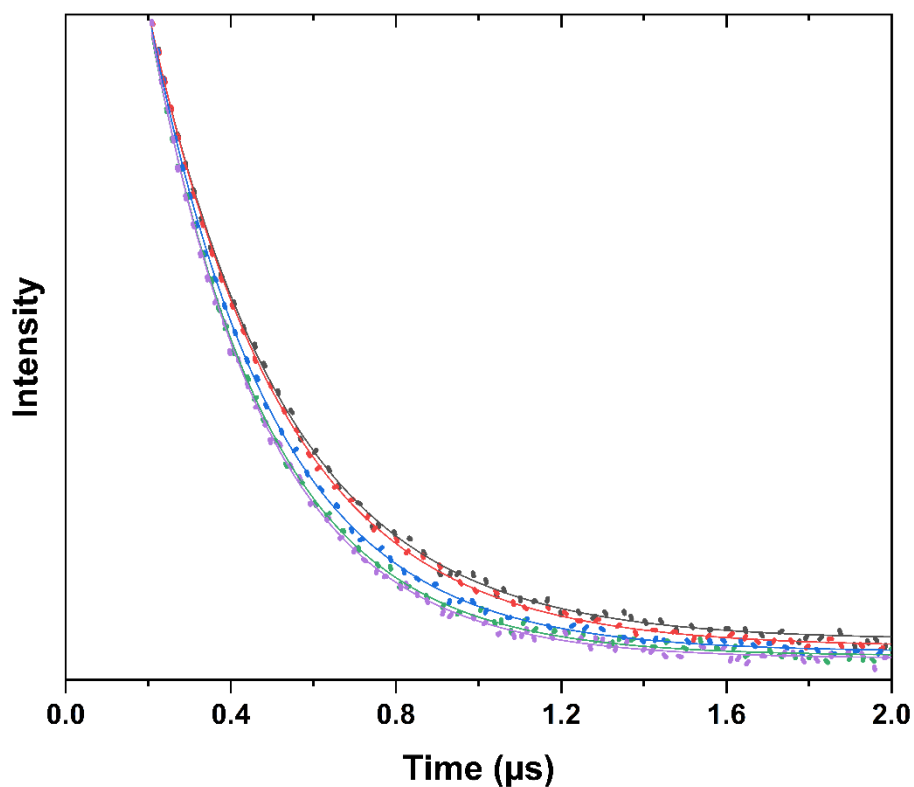


Figure II-12. Spin-Spin relaxation after an Hahn echo sequence for the ACN(D)/MeOD 10^{13} mol/L (top) at $B = 1$ mT (black), $B = 2$ mT (red), $B = 3$ mT (blue), $B = 4$ mT (green) and $B = 5$ mT (purple) at $T = 5$ K and 9.69 GHz. Dots correspond to the experimental point and line to the fitted data using mono-exponential model.

We can see that the difference between the two samples started to decrease and if we apply the same cut for both samples i.e. we remove the signal contribution for $t < 240$ μ s (which correspond approximately to 60 % of the signal), both samples exhibits roughly the same coherence time and field dependence. However due to very weak signal the quality of the fit for the non-deuterated sample is not perfect but the trend is still good.

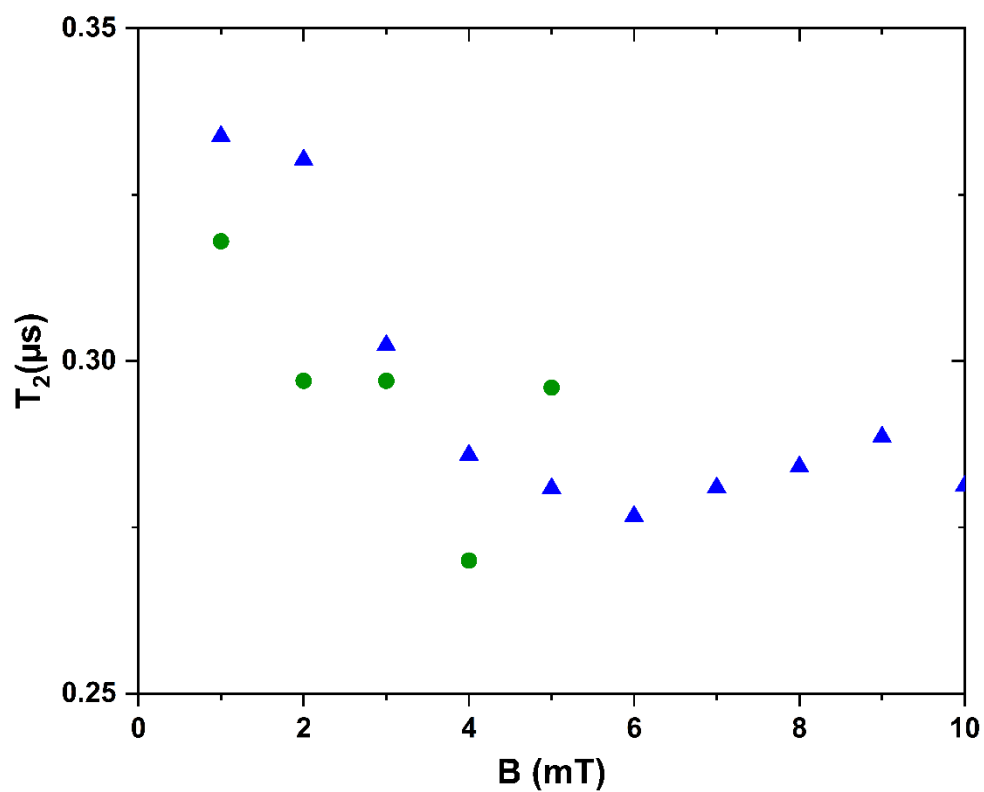


Figure II-13. Variation of the coherence time with magnetic field at $T = 5$ K and at 9.69 GHz. Blue triangles correspond to $[\text{Ni}(\text{imdipa})(\text{NCS})](\text{NCS})$ diluted in the deuterated solution, and green circles correspond to $[\text{Ni}(\text{imdipa})(\text{NCS})](\text{NCS})$ diluted in the non-deuterated solution. All data were fitted using a mono-exponential model.

The coherence time of $[\text{Ni}(\text{imdipa})(\text{NCS})](\text{NCS})$ in silica was recorded, an example of the fitted curves is given Figure II-14 with $\alpha_s = 0.82$ at $B = 1$ mT and $\alpha_s = 0.75$ at $B = 10$ mT.

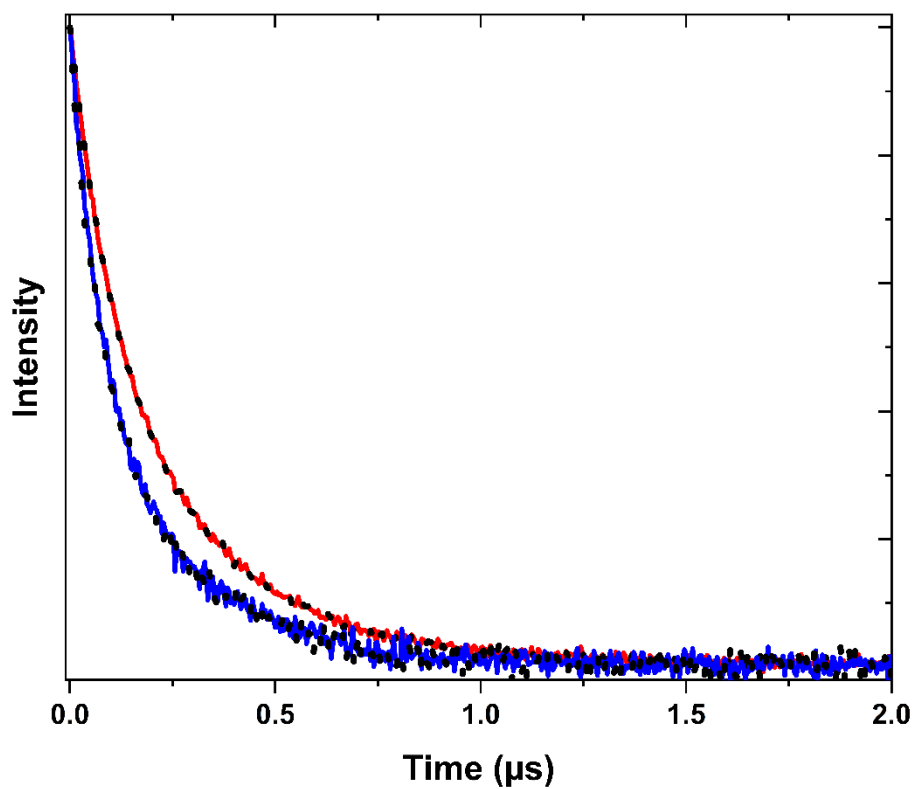


Figure II-14. T_2 Relaxation curves of $[\text{Ni}(\text{imdipa})(\text{NCS})](\text{NCS})$ diluted in silica (6%) at $T = 5 \text{ K}$ and 9.69 GHz at $B = 1 \text{ mT}$ (red) and $B = 10 \text{ mT}$ (blue). Dots correspond to experimental points, lines correspond to the fitted curve obtained. Silica and solutions were compared first without discriminating between two populations of molecules having different coherence times (Figure II-15).

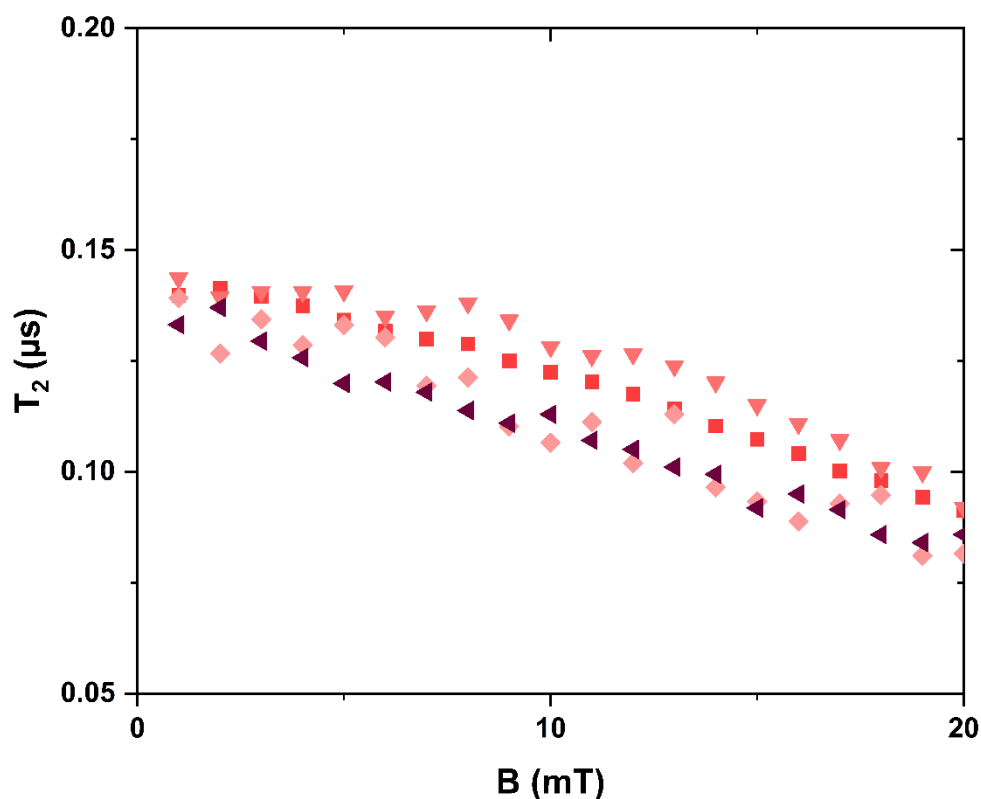


Figure II-15. Variation of the coherence time with magnetic field at $T = 5$ K at 9.69 GHz for the molecules diluted in silica 50% (pink triangles), 6% (red squares), 1% (pink squares) and 0.1%. (purple triangles). All value of T_2 have been obtained using stretched exponential on spin-spin relaxation curve.

As mentioned before, the presence of nuclear spins in the bath is responsible for spin diffusion thus decoherence. The comparison of the coherence time of the three samples is consistent with this assumption since $T_2(D) > T_2(\text{silica}) > T_2(H)$. The values found for silica and the non-deuterated solution are very close because silica still possess protons (OH that did not condensate to form SiO_2 because silica has not been calcinated). However, this does not explain the difference at the CT between silica and deuterated solution. Our hypothesis here again is that due to the presence of clusters of molecules inside the silica matrix, the flip-flop process dominates the decoherence. To verify our assumption, samples with dilutions from 0.1% to 50% of the molecules in silica were prepared and their coherence time was recorded (Figure II-14). The coherence time is found to be the same for all dilutions, indicating that diluting the sample 500 times (50% and 0.1%) has almost no effect on the coherence time, which is not reasonable if diluting the molecules was effective. The only explanation is that the dilution process was not efficient. This is probably due to a difference in kinetics between the formation

of the silica gel and the crystallization of the Ni complex.

We tried again to discriminate between two populations, but only the dilutions at 6% and 1% led to a good S/N ratio and allowed us to obtain a satisfactory fit. For the compound with a concentration of 6.10^{19} spins/cm³ (6%, red squares, Figure II-16) we do not find similar values for T_2 than for the solutions (Figure II-11) at the CT. This is not surprising when we compared the samples in silica among them, the compound diluted at 1% (pink square) corresponds to a compound 6 times more diluted than the one at 6% (red square) but the coherence time is shorter. Our conclusion here is that the dilution process in silica is not efficient, clusters of molecules form during the preparation. Therefore, we observe mainly the signal of an assembly of clusters with (probably) different sizes and not the signal of isolated molecules.

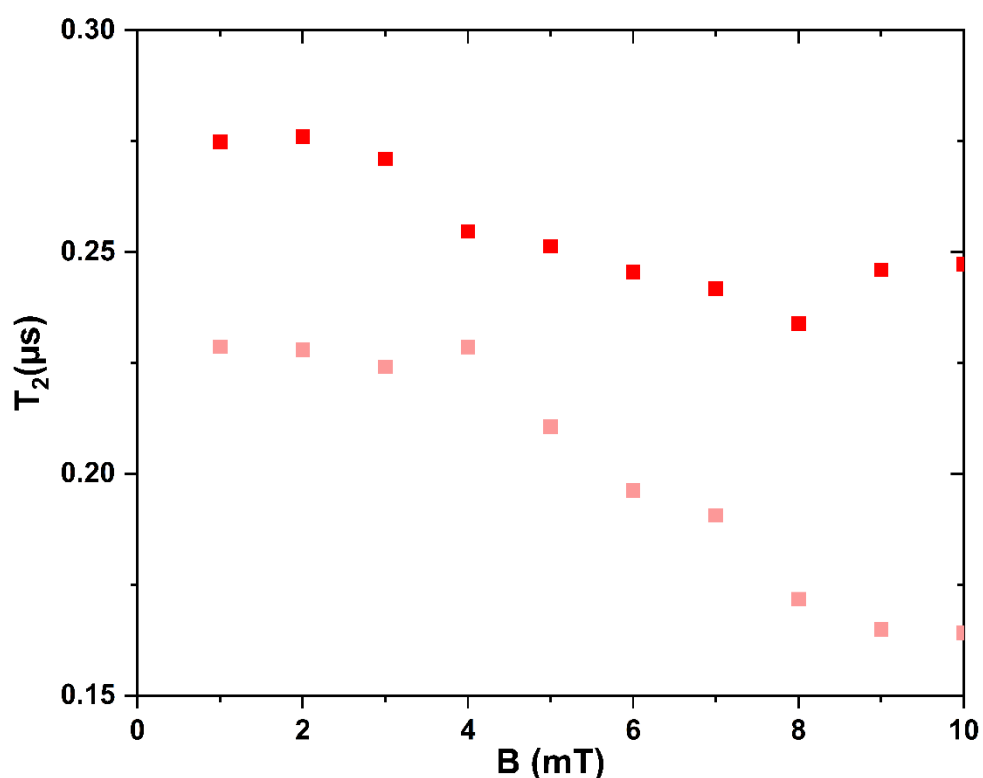


Figure II-16. Variation of the coherence time with magnetic field at $T = 5$ K and at 9.69 GHz for the molecules diluted in silica: 6% (red squares), 1% (pink squares) and 0.1% (purple triangles). All data were fitted using a mono-exponential model.

The study of [Ni(imdipa)(NCS)](NCS) in different matrices has shown:

Chapter II: Pulsed EPR study of mononuclear Ni(II) complexes

- (i) We have an accessible clock transition
- (ii) Inside the clock transition T_2 is the same in deuterated and non-deuterated solutions
- (iii) Silica has big potential for diluting the complex due to its high Debye Temperature but the process of dilution needs to be improved.

II.2.b Influence of the number of ligand

The relaxation times may be influenced by some vibration modes of the complex, if they are within an energy range that affect the crystal field parameters (ZFS). We do the assumption that for a complex, the vibration modes involving the metal-ligand bonds are not correlated. For a given vibration mode involving a stretch or a bend, there is no "correlated" another vibration that occurs in order to keep the overall energy of the complex invariant. Therefore, some vibration modes change the crystal field of the complex leading to a change of the ZFS parameters (the pertinent parameters in our case). If such process occurs within the time scale of the state of superposition, dephasing occurs and the coherence time is reduced. Also, the spin-lattice relaxation time is affected particularly if relaxation is due to the Orbach mechanism whose barrier depends on the ZFS parameters. Based on these hypotheses, reducing the number of ligands, thus using chelating ligands could be an interesting strategy for longer T_1 . In other words, using chelating ligands translates in using "rigid" ligands which reduces the entropy of the complex and brings an additional thermodynamic stabilization. In such a case, correlated vibrations with no overall energy change may be dominant decreasing the variation of the ZFS parameters with time, that is responsible of spin-lattice relaxation.

To illustrate this phenomenon, we performed pulsed EPR studies and measured the spin-lattice relaxation time T_1 of two Ni(II) complexes exhibiting C_3 symmetry as discussed in Chapter I. As described in Chapter I, one complex ($[\text{Ni}(\text{MPZ})_2]$) with two tridentate ligands while the other one ($[\text{Ni}(4,4'\text{-Di-tert-butyl-2,2'bpv})_3](\text{NO}_3)_2$) has three bidentate ligands, therefore a larger entropy contribution to its overall energy. The study was conducted as follows:

- (i) Proving the presence of a CTs
- (ii) Measuring the spin-lattice-relaxation time at different temperatures
- (iii) Evaluating influence of the coherence time

We expected longer relaxation times (T_1 and T_2) in the case of $[\text{Ni}(\text{MPZ})_2]$ than $[\text{Ni}(4,4'\text{-Di-tert-}$

butyl-2,2'bp₃](NO₃)₂ for the reason stated above.

To perform the study, the two compounds were diluted in their Zn(II) diamagnetic isomorphous matrix at 10% dilution to ensure a strong signal for the data to be easily analyzed. The crystals have been ground into micro-crystalline powders for study.

Experimental conditions

The experiment on [Ni_{0.1}Zn_{0.9}(MPZ)₂] have been performed with an attenuation of 13 dB while the experiment on [Ni_{0.1}Zn_{0.9}(4,4'-Di-tert-butyl-2,2'bp₃)](NO₃)₂ have been performed with an attenuation of 12 dB.

Echo-detected EPR. The echo-detected field-swept (EDFS) spectra were recorded with a two-pulse primary Hahn-echo sequence ($\pi/2-t-\pi-t$ -echo), with microwave pulse lengths of 16 and 32 ns respectively, a fixed delay time $t = 200$ ns for [Ni_{0.1}Zn_{0.9}(4,4'-Di-tert-butyl-2,2'bp₃)](NO₃)₂, $t = 160$ ns for [Ni_{0.1}Zn_{0.9}(MPZ)₂] and with the variation of the static B₀ magnetic field.

Hahn echo sequence. The spin-spin relaxation (T₂) spectra were recorded with a two-pulse primary Hahn-echo sequence ($\pi/2-t-\pi-t$ -echo), with microwave pulse lengths of 16 and 32 ns respectively, a fixed delay time $t = 200$ ns for [Ni_{0.1}Zn_{0.9}(4,4'-Di-tert-butyl-2,2'bp₃)](NO₃)₂, $t = 160$ ns for [Ni_{0.1}Zn_{0.9}(MPZ)₂].

Inversion recovery curves were collected by application of a three-pulse sequence ($\pi-T-\pi/2-\tau-\pi-t$ -echo), with microwave pulse lengths of 32, 16 and 32 ns respectively, pulse lengths and a 200 ns a fixed delay time $t = 160$ ns for [Ni_{0.1}Zn_{0.9}(4,4'-Di-tert-butyl-2,2'bp₃)](NO₃)₂, $t = 160$ ns for [Ni_{0.1}Zn_{0.9}(MPZ)₂].

II.2.b.i Proving the presence of a CTs

Both complexes exhibit a transition at zero field. In the case of [Ni(4,4'-Di-tert-butyl-2,2'bp₃)](NO₃)₂, the signal was strong enough to obscure the cavity resonance at 340 mT, which was not the case for [Ni(MPZ)₂]. The experiments are comparable since, the EPR detector was saturated, the same temperature, concentration, power attenuation (12 dB), and frequency

were used for both. The difference in intensity suggests that $[\text{Ni}(4,4'\text{-Di-tert-butyl-2,2'bpy})_3](\text{NO}_3)_2$ has more molecules with zero field resonance than $[\text{Ni}(\text{MPZ})_2]$, this can be explained by the E value of $[\text{Ni}(4,4'\text{-Di-tert-butyl-2,2'bpy})_3](\text{NO}_3)_2$ which is closer to the cavity frequency than for $[\text{Ni}(\text{MPZ})_2]$. The other possibility is that $[\text{Ni}(4,4'\text{-Di-tert-butyl-2,2'bpy})_3](\text{NO}_3)_2$ has a longer coherence time. The EDFS spectra are presented in Figure II-17, and nutation experiments (Figure II-18) also confirmed that the spins are $S = 1$, thus the transition studied is between $M_s = \pm 1$.

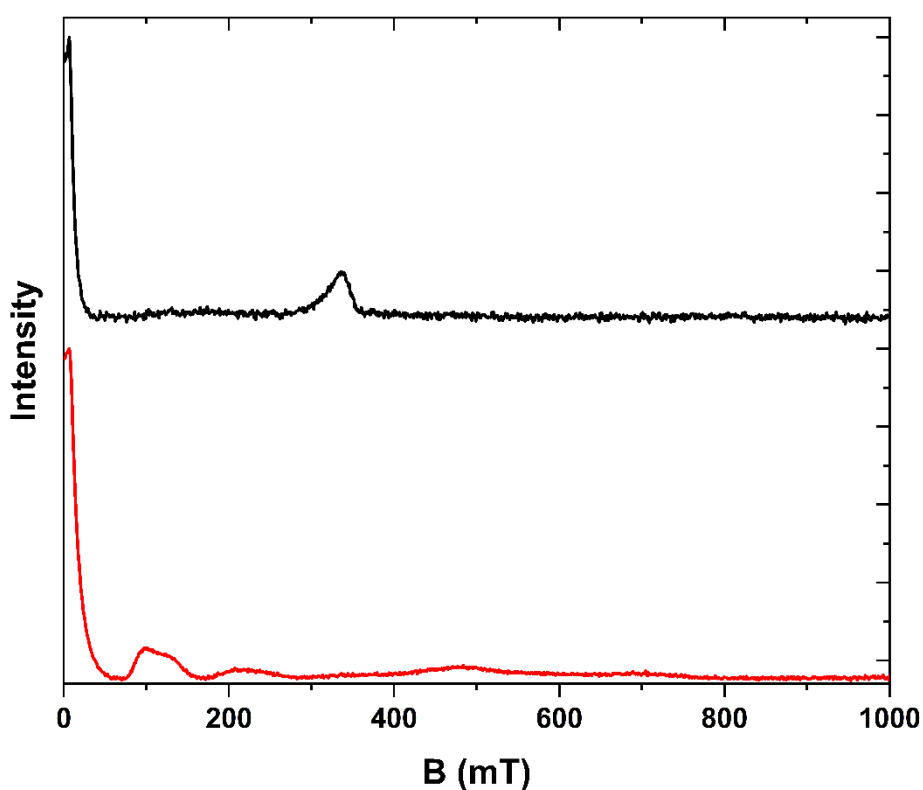


Figure II-17. EDFs of $[\text{Ni}(4,4'\text{-Di-tert-butyl-2,2'bpy})_3](\text{NO}_3)_2$ (red) and $[\text{Ni}(\text{MPZ})_2]$ (black) at $T = 5\text{ K}$ and at 9.69 GHz .

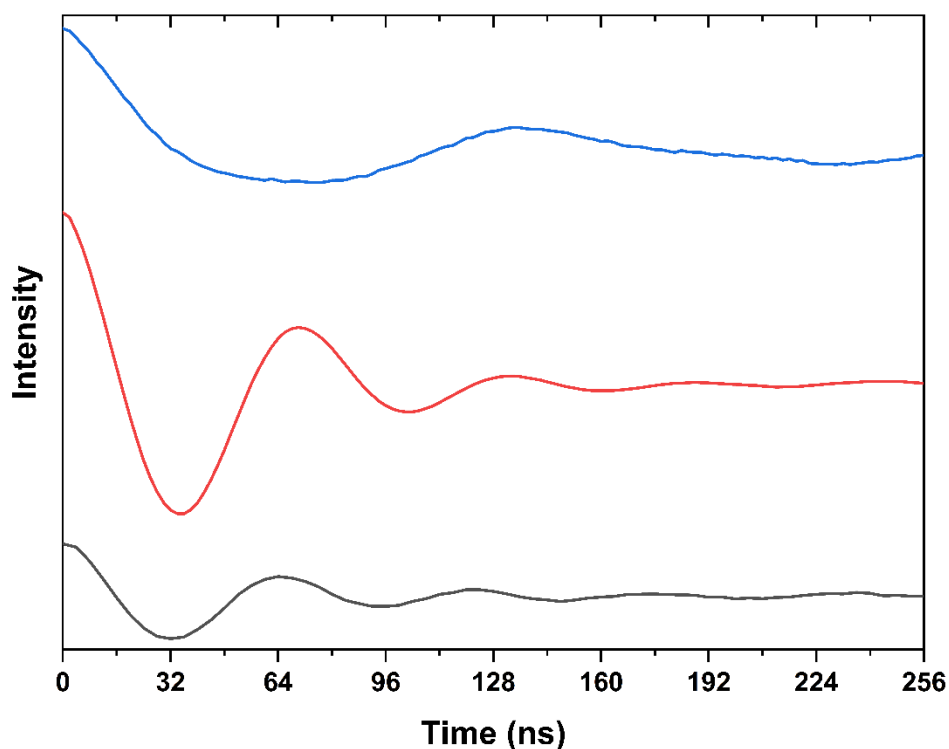


Figure II-18. Nutation experiment at 12 dB and $T = 5$ K of $[\text{Ni}(4,4'\text{-Di-tert-butyl-2,2'bpy})_3](\text{NO}_3)_2$ (red) and $[\text{Ni}(\text{MPZ})_2]$ (black) at $B = 1$ mT and TEMPO reference (blue) at $B = 324$ mT and at 9.69 GHz

II.2.b.ii Measuring spin-lattice relaxation

In a first place, we confirmed for the $[\text{Ni}(4,4'\text{-Di-tert-butyl-2,2'bpy})_3](\text{NO}_3)_2$, as for $[\text{Ni}(\text{imdipa})(\text{NCS})](\text{NCS})$, the magnetic field has no influence on T_1 (Figure II-19). The same experiment was difficult to perform for $[\text{Ni}(\text{MPZ})_2]$. due to signal issue.

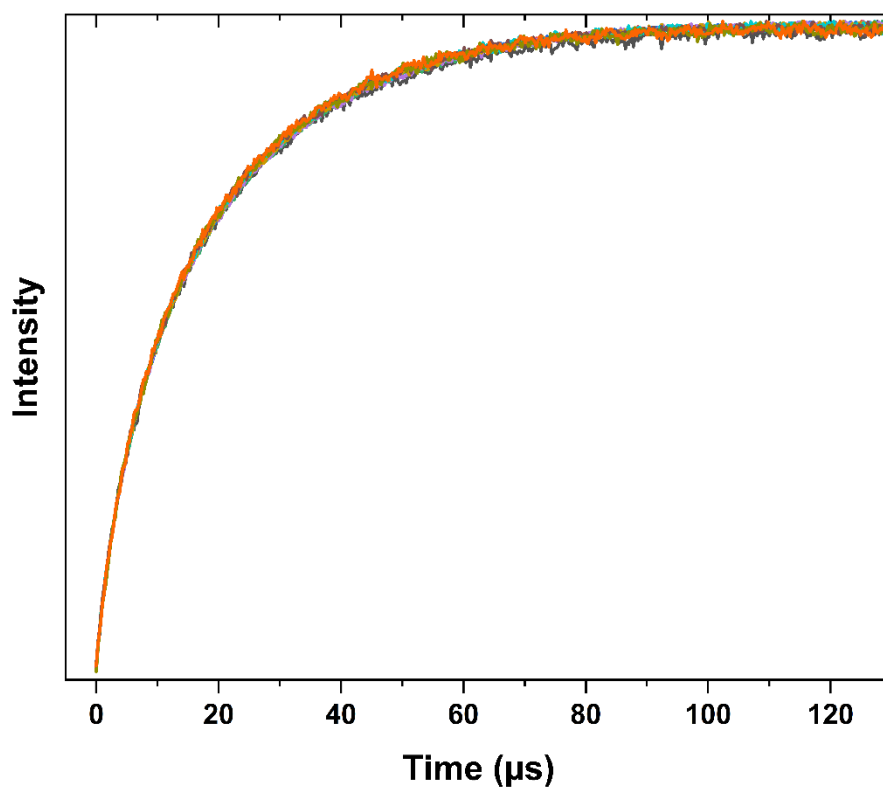


Figure II-19. T_1 curves of $[\text{Ni}(4,4'\text{-Di-tert-butyl-2,2'bpy})_3](\text{NO}_3)_2$ after an inversion recovery sequence at $T = 5\text{ K}$ and at 9.69 GHz . The magnetic field was varied from $B = 0\text{ mT}$ to $B = 10\text{ mT}$.

The spin-lattice relaxation was recorded as a function of time using an inversion recovery sequence for both compounds at different temperatures. An example is given Figure II-120 where the data were fitted using a stretched exponential model with $\alpha = 0.8$ in the case of the $[\text{Ni}(\text{MPZ})_2]$ and $\alpha = 0.83$ in the case of $[\text{Ni}(4,4'\text{-Di-tert-butyl-2,2'bpy})_3](\text{NO}_3)_2$.

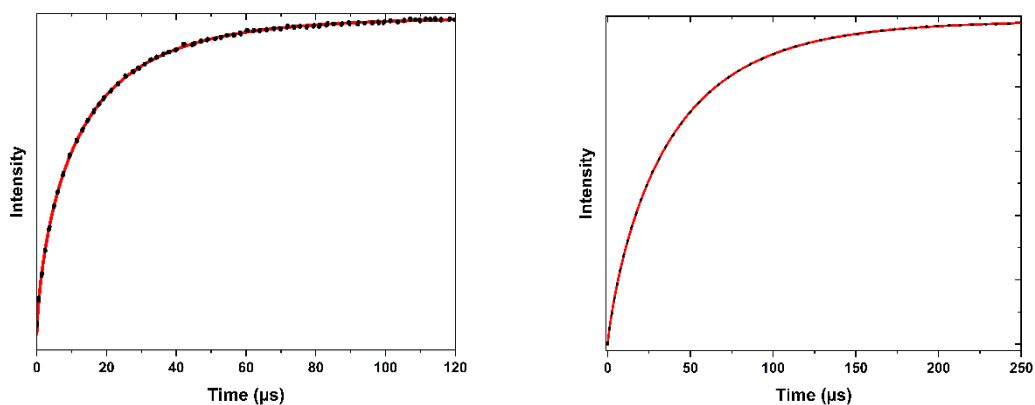


Figure II-20. (Right) T_1 curves of $[\text{Ni}(4,4'\text{-Di-tert-butyl-2,2'bpy})_3](\text{NO}_3)_2$ after an inversion recovery sequence at $T = 5$ K, at $B = 3$ mT and at 9.69 GHz (black dot) and fitted data (red line). (Left) T_1 curves of $[\text{Ni}(\text{MPZ})_2]$ after an inversion recovery sequence at $T = 5$ K, at $B = 1$ mT and at 9.69 GHz (black dot) and fitted data (red line).

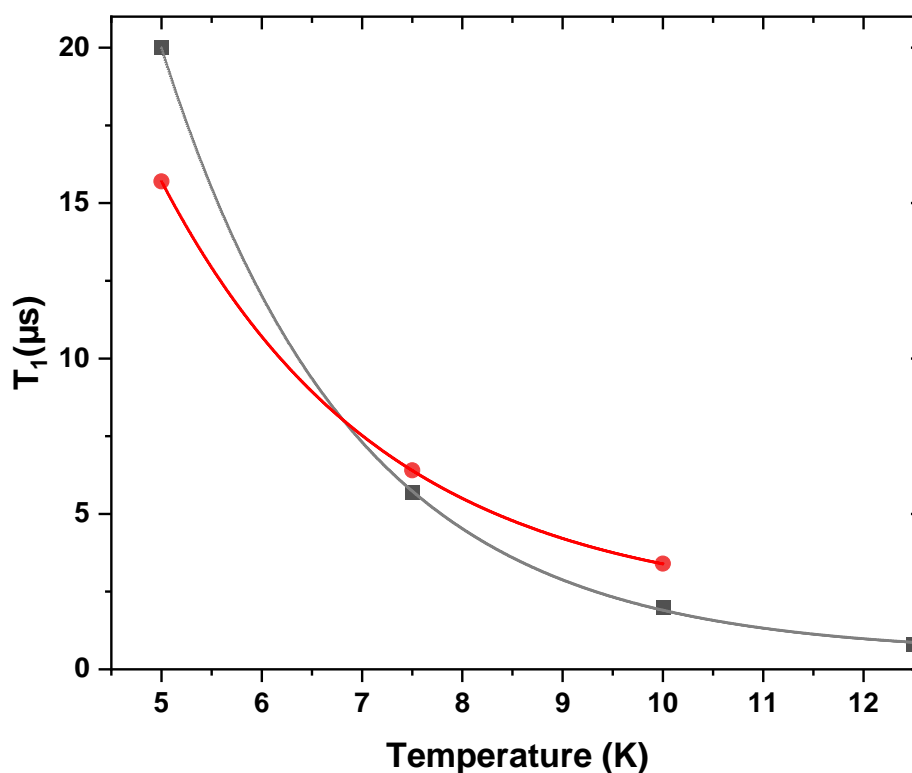


Figure II-21. Temperature dependence of the spin-lattice relaxation time for $[\text{Ni}(4,4'\text{-Di-tert-butyl-2,2'bpy})_3](\text{NO}_3)_2$ (red) and $[\text{Ni}(\text{MPZ})_2]$ (black) at $B = 1$ mT and at 9.69 GHz.

The spin-lattice relaxation time varies with temperature (Figure II-21) according to a single-exponential decay rule.

$$T_{1(\text{MPZ})}(T) = 268 \times e^{\left(\frac{-T}{1.96}\right)} \quad (\text{III-4})$$

$$T_{1(\text{bpy})}(T) = 132 \times e^{\left(\frac{-T}{2.2}\right)} \quad (\text{III-5})$$

The analysis of the decay rule shows that the difference in relaxation time is mainly given by the pre-exponential factor which can be assimilated to a relaxation rate. As expected, the spin-lattice relaxation was slightly longer for [Ni(MPZ)₂] ($T_1(5K) = 20.0 \mu s$) than for [Ni(4,4'-Di-tert-butyl-2,2'bpy)₃](NO₃)₂ ($T_1(5K) = 15.2 \mu s$). Our strategy to increase the spin-lattice relaxation time seems efficient.

In both cases, the spin-lattice relaxation times remains short. For a qubit to be implemented into a quantum system, it needs to possess a coherence time around the millisecond time scale. This mean that T_1 need to be at least 10 times longer in order to prevent any effect of the spin-lattice relaxation on T_2 . At this concentration, T_1 remains shorter than 269 μs even at 10 mK, for [Ni(MPZ)₂] and than 132 μs for [Ni(4,4'-Di-tert-butyl-2,2'bpy)₃](NO₃)₂. To improve the relaxation time, a study of the different mechanisms involved in the relaxation is needed, particularly the study of spin diffusion. The information is accessible using saturation recovery sequence. However, increasing T_1 is possible by further diluting the samples, which is possible particularly for Ni(MPZ) that possess large thermodynamic stability.

II.2.b.iii Coherence time

The coherence times were measured at different magnetic fields for the two samples (dilution of 10% in their isomorphous diamagnetic matrices). Figure II-22 reports the curves obtained at $B = 1$ mT that were fitted using stretched exponential models with $\alpha = 0.8$ for [Ni(MPZ)₂] and $\alpha = 0.83$ for Ni(4,4'-Di-tert-butyl-2,2'bpy)₃(NO₃)₂. The coherence time as a function of the magnetic field is reported in Figure II-23 for both compounds [Ni(MPZ)₂] (black square) and [Ni(4,4'-Di-tert-butyl-2,2'bpy)₃](NO₃)₂ (red dot).

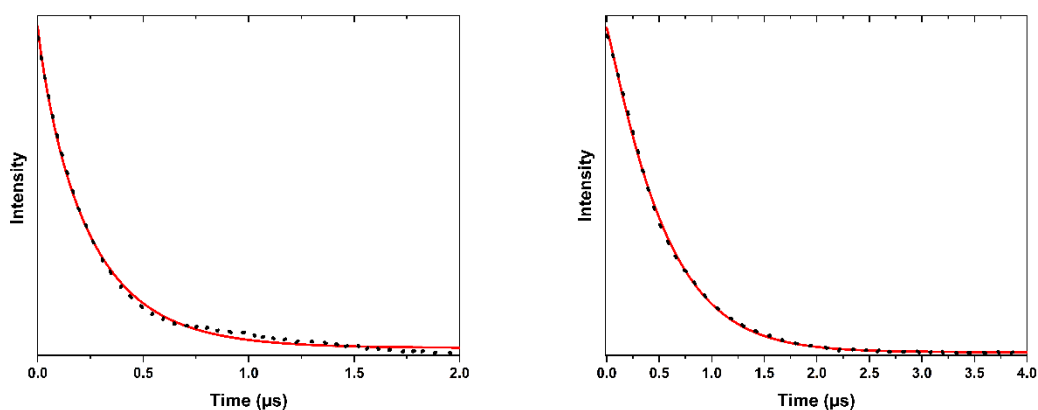


Figure II-22. (Right) T_2 curves of $[\text{Ni}(4,4'\text{-Di-tert-butyl-2,2'bpy})_3](\text{NO}_3)_2$ after an Hahn echo sequence at $T = 5 \text{ K}$, at $B = 1 \text{ mT}$ and at 9.69 GHz (black dot) and fitted data (red line). (Left) T_2 curves of $[\text{Ni}(\text{MPZ})_2]$ after an Hahn echo sequence at $T = 5 \text{ K}$, at $B = 1 \text{ mT}$ and at 9.69 GHz (black dot) and fitted data (red line).

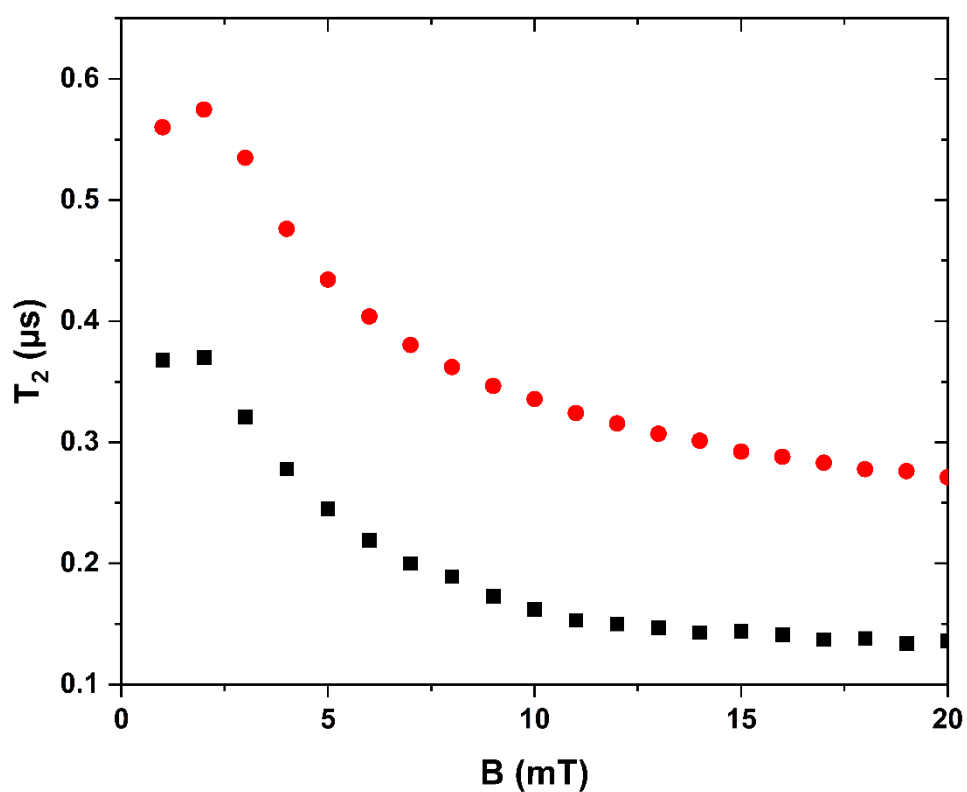


Figure II-23. Variation of the coherence time with the applied magnetic field at $T = 5 \text{ K}$ and at 9.69 GHz . In red $[\text{Ni}(4,4'\text{-Di-tert-butyl-2,2'bpy})_3](\text{NO}_3)_2$, in black $[\text{Ni}(\text{MPZ})_2]$.

The results indicate that the coherence time is constant for both compounds from 0 to 2 mT but decreases for larger magnetic field values. This suggests that the observed transition corresponds well to a CT in the 0 to 2 mT (or 3 mT) region, while the observed transitions from

3 mT to 7 mT are in the nonlinear regime (Chapter I.1.a). Beyond 7 mT, the transitions are no longer a clock transition in the case of $[\text{Ni}(\text{MPZ})_2]$, whereas they remain coherent for $B > 12$ mT in the case of $[\text{Ni}(4,4'\text{-Di-tert-butyl-2,2'bpy})_3](\text{NO}_3)_2$. The coherence time was nearly three times longer in the case of $[\text{Ni}(4,4'\text{-Di-tert-butyl-2,2'bpy})_3](\text{NO}_3)_2$ compared to $[\text{Ni}(\text{MPZ})_2]$. The difference may be due to the quality of the dilution. If the dilution was not homogeneous leading to the presence of assemblies of molecules, the flip-flop processes will be more active in these assemblies than in the molecules that are well isolated leading to populations with different relaxation times most of them relatively short.

For $[\text{Ni}(\text{MPZ})_2]$, due to solubility issues, the crystals were obtained through recrystallization from a hot solution, making it challenging to precisely control the kinetic of the crystallization process. For $[\text{Ni}(4,4'\text{-Di-tert-butyl-2,2'bpy})_3](\text{NO}_3)_2$, there was a small difference in the kinetics of recrystallization between the Ni and the Zn derivatives. In fact, while the crystallization process was followed carefully, some inhomogeneities were visible, indicating the presence of aggregates. However, we can again remove the contribution of the populations with short relaxation times (aggregated molecules). This procedure is only feasible for $[\text{Ni}(4,4'\text{-Di-tert-butyl-2,2'bpy})_3](\text{NO}_3)_2$ which exhibit a good ratio S/N. The results are presented below (Figure II-24).

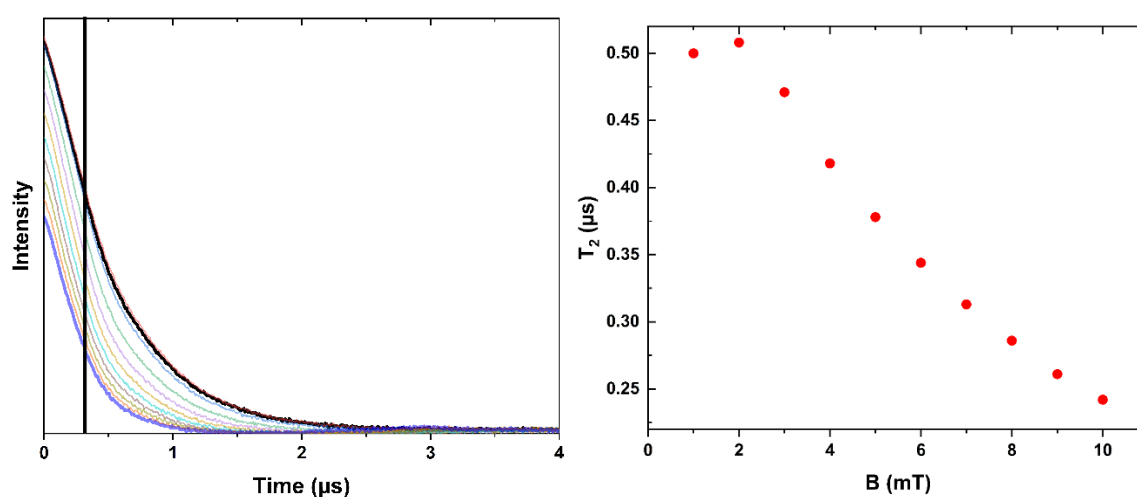


Figure II-24. (Left) T_2 curves of $[\text{Ni}(4,4'\text{-Di-tert-butyl-2,2'bpy})_3](\text{NO}_3)_2$ after an Hahn echo sequence at $T = 5$ K, from $B = 1$ mT (black) to $B = 10$ mT (purple) at 9.69 GHz. The points at the left of the black line have not been considered for the determination of the T_2 . (Right) Variation of the coherence time with the applied magnetic field at $T = 5$ K and at 9.69 GHz for $[\text{Ni}(4,4'\text{-Di-tert-butyl-2,2'bpy})_3](\text{NO}_3)_2$ after removing contribution of the short relaxation times.

In Figure II-24, the T_2 was found shorter than before removing the population with short

relaxation times because we removed the small ESEEM effect at $t = 0.02 \mu\text{s}$ that artificially increases T_2 . Here the efficiency of the CT is clearly evidenced by the drastic decrease of T_2 outside the CT region ($B > 2 \text{ mT}$) and the fact that it remains constant near zero field.

II.2.b.iv Conclusion.

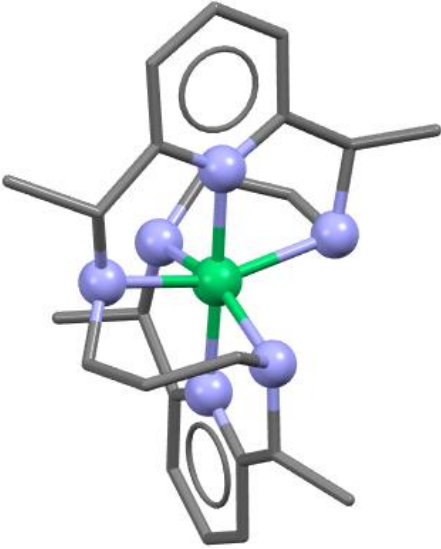
The relaxation times at the clock transition of two mononuclear Ni(II) complexes (diluted at 10%) with $D < 0$ and C_3 symmetry have been studied. For $[\text{Ni}(\text{MPZ})_2]$, $T_1(5 \text{ K}) = 20 \mu\text{s}$ and $T_2(5 \text{ K}) = 0.22 \mu\text{s}$, while for $[\text{Ni}(4,4'\text{-Di-tert-butyl-2,2'bpy})_3](\text{NO}_3)_2$, $T_1(5 \text{ K}) = 16 \mu\text{s}$ and $T_2(5 \text{ K}) = 0.55 \mu\text{s}$. It seems that chelation plays a role in spin-lattice relaxation, diminishing the number of ligands and increasing the denticity increase T_1 . To clearly demonstrate this hypothesis, two additional compounds are needed: one with six monodentate ligands and one with an hexadentate ligand.

A complex with an hexadentate ligand (L_6) was prepared [8] and crystallized (Table II-24). The crystal structure corresponds to a compressed octahedra which is compatible with $D < 0$. This is what is obtained from calculation studies.

$$D = -5.29 \text{ cm}^{-1}$$

$$E/D = 0.2 (E = 1.06 \text{ cm}^{-1})$$

The E value is close to the Q band cavity (1 cm^{-1}), unfortunately, we could not perform any EPR measurement to confirm the ZFS parameters and measure the relaxation times.



Formula	C ₂₄ H ₃₈ N ₈ Ni O ₆
Space Group	P 2 ₁ /c
Cell Lengths	a 13.865(6) b 14.339(7) c 13.165(6)
Cell Angles	α 90.00 β 90.173(8) γ 90.00
Cell Volume	2617.32
Z,Z'	Z : 4 Z' : 1
R-factor (%)	4.9

Table II-24. Crystallographic information of [Ni(L₆)](NO₃)₂

II.2.c Efficiency of the clock transition

The scope of this study is to demonstrate that clock transitions (CTs) can serve as an effective strategy to mitigate magnetic fluctuation-induced spectral diffusion. To illustrate this phenomenon, we conducted pulsed EPR studies and measured the phase memory time T_2 of the [Ni(imidazoline)(NO₃)](NO₃) complex in three different situations.

- (i) The diamagnetic isomorphous Zn(II) complex was used to dilute the complex in the first experiment, and T_2 measurements were taken while varying the external magnetic field. The objective is to evidence a difference in the coherence time inside and outside the CT.
- (ii) Different dilutions were used to estimate or at least to evidence the presence of Flip-Flop process inside the CT.
- (iii) The complex was diluted in the Zn(II) matrix with increasing amounts of the paramagnetic Co(II) complexes that possess a half integer spin value ($S = 3/2$), which are expected to cause strong magnetic fluctuations. We tried to estimate or at least to evidence that CT is insensitive to the spin-diffusion process.

It was expected that T_2 , at the CT, would remain unchanged when a small magnetic field was applied or in the presence of magnetic Co(II) molecules. For this study six samples have been prepared namely Ni_xCo_yZn_z where x,y,z represent the proportion of the element in the sample. The crystals have been ground into micro-crystalline powders for study. All the dilutions have been confirmed by Energy Dispersive X-ray (EDX) analysis (measurement done by Thibault Six (ICMMO)). In the following sections, on the figure, black star corresponds to the signal of a radical, that is always present in very small amount in the samples, and black dots to the cavity.

Experimental conditions

Echo-detected EPR. The echo-detected field-swept (EDFS) spectra were recorded with a two-pulse primary Hahn-echo sequence ($\pi/2-t - \pi - t - \text{echo}$), with microwave pulse lengths of 16 and 32 ns respectively, a fixed delay time $t = 160$ ns for [Ni_{0.07}Zn_{0.93}(HIM2-py)₂(NO₃)](NO₃), $t = 130$ ns for [Ni_{0.01}Zn_{0.99}(HIM2-py)₂(NO₃)](NO₃) and $t = 140$ ns for [Ni_{0.01}Co_{0.05}Zn_{0.94}(HIM2-py)₂(NO₃)](NO₃) and [Ni_{0.01}Co_{0.5}Zn_{0.49}(HIM2-py)₂(NO₃)](NO₃), and with the variation of the static B_0 magnetic field.

Hahn echo sequence. The spin-spin relaxation (T_2) spectra were recorded with a two-pulse primary Hahn-echo sequence ($\pi/2 - t - \pi - t - \text{echo}$), with microwave pulse lengths of 16 and 32 ns respectively, a fixed delay time $t = 160$ ns for $[\text{Ni}_{0.07}\text{Zn}_{0.93}(\text{HIM2-py})_2(\text{NO}_3)](\text{NO}_3)$, $t = 130$ ns for $[\text{Ni}_{0.01}\text{Zn}_{0.99}(\text{HIM2-py})_2(\text{NO}_3)](\text{NO}_3)$ and $t = 140$ ns for $[\text{Ni}_{0.01}\text{Co}_{0.05}\text{Zn}_{0.94}(\text{HIM2-py})_2(\text{NO}_3)](\text{NO}_3)$ and $[\text{Ni}_{0.01}\text{Co}_{0.5}\text{Zn}_{0.49}(\text{HIM2-py})_2(\text{NO}_3)](\text{NO}_3)$.

Inversion recovery curves were collected by application of a three-pulse sequence ($\pi - T - \pi/2 - \tau - \pi - t - \text{echo}$), with microwave pulse lengths of 32, 16 and 32 ns respectively, pulse lengths and a fixed delay time $t = 160$ ns for $[\text{Ni}_{0.07}\text{Zn}_{0.93}(\text{HIM2-py})_2(\text{NO}_3)](\text{NO}_3)$, $t = 130$ ns for $[\text{Ni}_{0.01}\text{Zn}_{0.99}(\text{HIM2-py})_2(\text{NO}_3)](\text{NO}_3)$ and $t = 140$ ns for $[\text{Ni}_{0.01}\text{Co}_{0.05}\text{Zn}_{0.94}(\text{HIM2-py})_2(\text{NO}_3)](\text{NO}_3)$ and $[\text{Ni}_{0.01}\text{Co}_{0.5}\text{Zn}_{0.49}(\text{HIM2-py})_2(\text{NO}_3)](\text{NO}_3)$.

Nutation experiment was performed using a X-band EPR tube containing $[\text{Ni}_{0.07}\text{Zn}_{0.93}]$ as powder and a Q-band EPR tube containing a H_2O /glycerol solution of TEMPO radical at 10^{-3} mol/L in as internal reference.

Transient nutation experiments were performed at 5 K with a three-pulse sequence ($t_p - T - \pi/2 - \tau - \pi - \tau - \text{echo}$) where t_p is a variable microwave pulsed length increasing of 2 ns for each point and fixed microwave pulse lengths of 16 and 32 ns respectively, a fixed delay time $T = 2000$ ns and $t = 200$ ns for the and a fixed delay time $T = 20\ 000$ ns and $t = 200$ ns for TEMPO reference.

II.2.c.i Study of $[\text{Co}(\text{imidazoline})(\text{NO}_3)](\text{NO}_3)$

We want to evaluate the efficiency of the clock transition in the presence of a paramagnetic impurity, additionally we will compare this robustness with the one of a non-clock transition. The paramagnetic impurity will create spin-diffusion a mechanism in which CT is supposed to be insensitive. To demonstrate this, we need to find a paramagnetic species in which Ni could be diluted and this paramagnetic species have to possess a coherence time in the same order or shorter than the Ni(II) one. Co(II) is structurally close the Ni(II) so they may form homogeneous solid solutions if the two compounds $[\text{Co}(\text{imidazoline})(\text{NO}_3)](\text{NO}_3)$ and

[Ni(imidazoline)(NO₃)](NO₃) are isomorphous. Furthermore Co(II) possesses an electronic spin $S = 3/2$ and a nuclear spin $I = 7/2$ and Cobalt(II) complexes are known to have a fast decay,[9] bringing fluctuating electronic and nuclear spins to the spin bath.

In a first step, we will determine the ZFS of the [Co(imidazoline)(NO₃)](NO₃). We recorded cw-EPR spectra of the complex (black curve Figure II-25) and as for previous samples, radical signal was observed at 338 mT. Prior to simulating the experimental spectrum, ab calculations were performed. They gave a positive D value around 50 cm^{-1} , that was used as a starting point for the simulation. The ZFS parameters were then adjusted using Easyspin to reproduce the spectrum (red curve Figure II-25) leading to the following parameters:

$$D = 52.26 \text{ cm}^{-1}, E = 4.866 \text{ cm}^{-1},$$

$$g_x = 2.48 \quad g_y = 2.31 \quad g_z = 2.11$$

$$A_x = 0.0037 \text{ cm}^{-1} \quad A_y = 0.0030 \text{ cm}^{-1} \quad A_z = 0.0110 \text{ cm}^{-1}$$

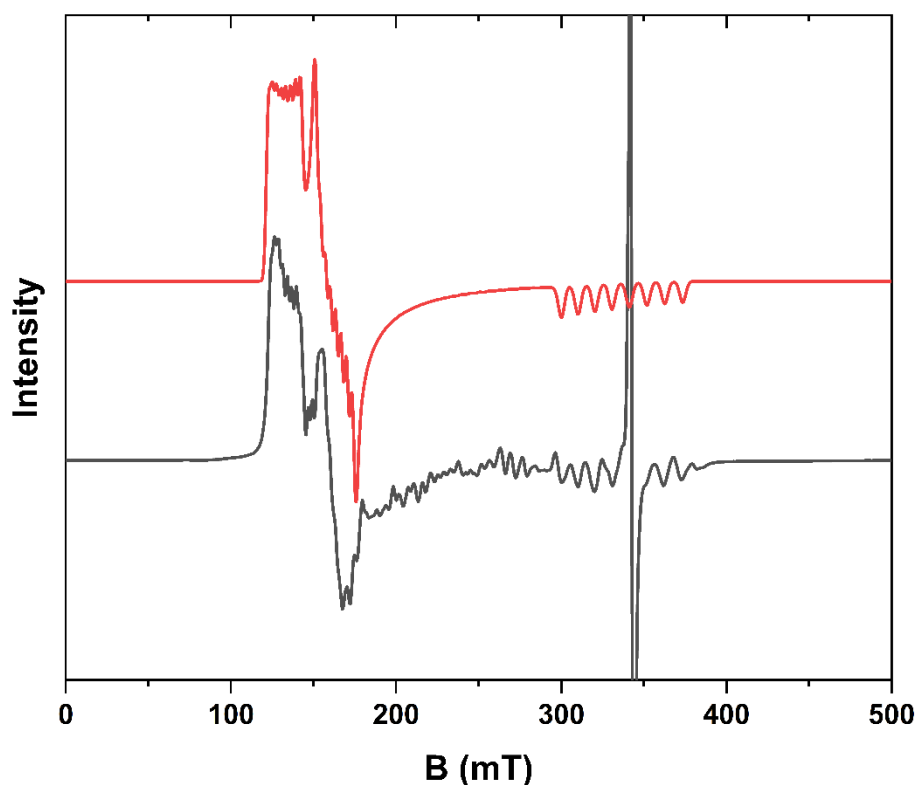


Figure II-25. CW-EPR spectra of $\text{Co}_{0.05}\text{Zn}_{0.95}$ (black) recorded at $T = 5 \text{ K}$ and 9.64 GHz . Simulated cw-EPR spectra (red).

The first transition at 145 mT corresponds to g_x , the one at 168 mT to g_y and the last one to g_z .

The positive value of D means that the ground level is $M_S = \pm 1/2$

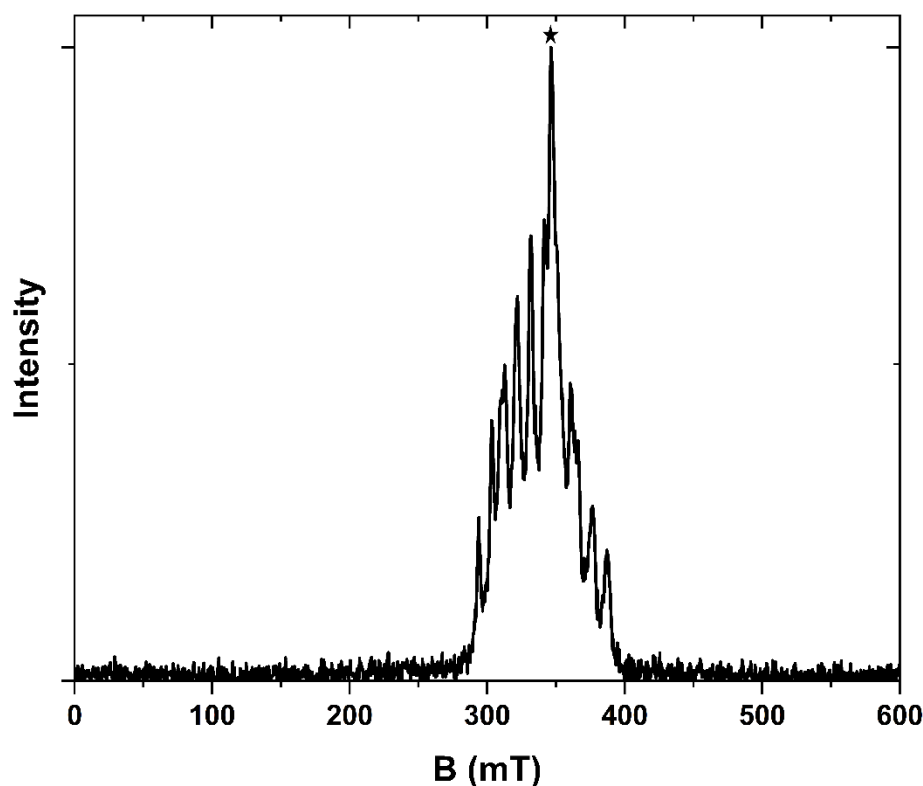


Figure II-26. EDFs spectra of $\text{Co}_{0.05}\text{Zn}_{0.95}$ at $T = 5 \text{ K}$ and 9.69 GHz

In a second step, a $\text{Co}_{0.05}\text{Zn}_{0.95}$ sample was prepared and studied as a reference for cobalt. The EDFs showed the presence of 9 bands (Figure II-26 and Figure II-27) in the 300 – 400 mT, plus one due to the presence of radicals (star transition). For Co(II) with $I = 7/2$, one expects 8 hyperfine bands. The apparent presence of 9 bands is probably due to strain in the material. The transitions around 150 mT previously observed in cw-EPR were not visible anymore. Therefore, only the transition along the g_z has enough coherence to be observed in the EDFs spectrum, while those in perpendicular direction have very short coherence time. The very short T_2 for the perpendicular transitions may be due to their large g value that results in a larger dependence on magnetic the magnetic fluctuation of the spin bath than the parallel transition (along z).

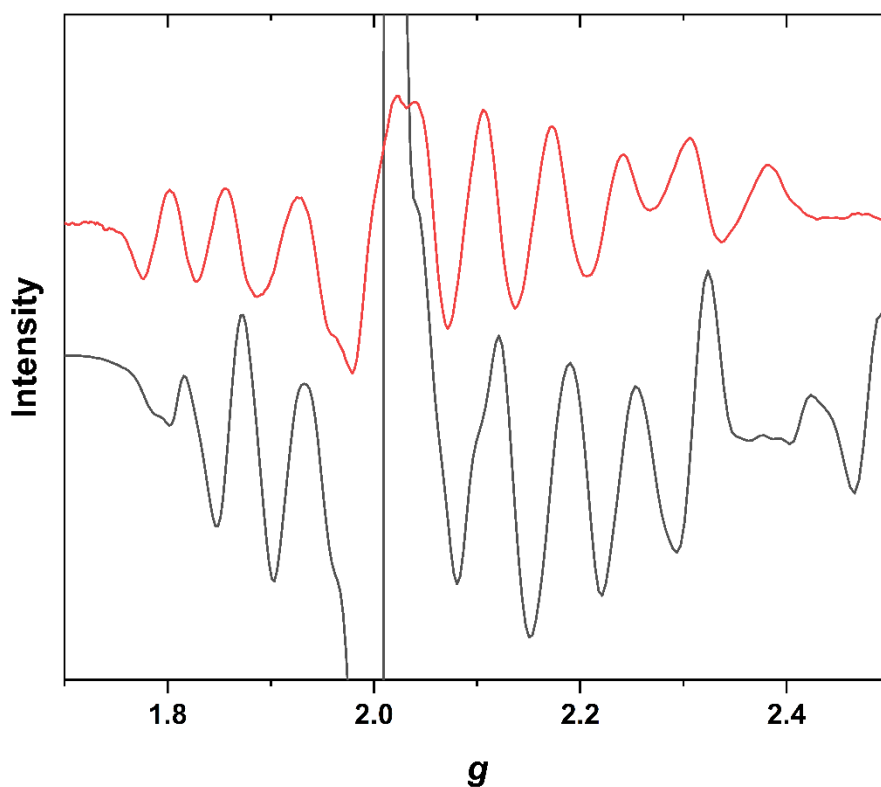


Figure II-27. Spectrum comparison between derivative of the EDFS (red) and cw-EPR (black) of $\text{Co}_{0.05}\text{Zn}_{0.95}$. The intense transition at $g = 2.023$ on the cw-epr spectra corresponds to the one of the radical impurity.

The spin-lattice relaxation of the $\text{Co}_{0.05}\text{Zn}_{0.95}$ was recorded (Figure II-28) at 5 K ($B = 342$ mT) and modelled using a stretched exponential model with $\alpha = 0.6$ and $T_1 = 8 \mu\text{s}$. Here again we have $\alpha < 1$ meaning that our sample is probably not homogenous. The T_1 value could be better estimated if we had accumulated the signal for longer time.

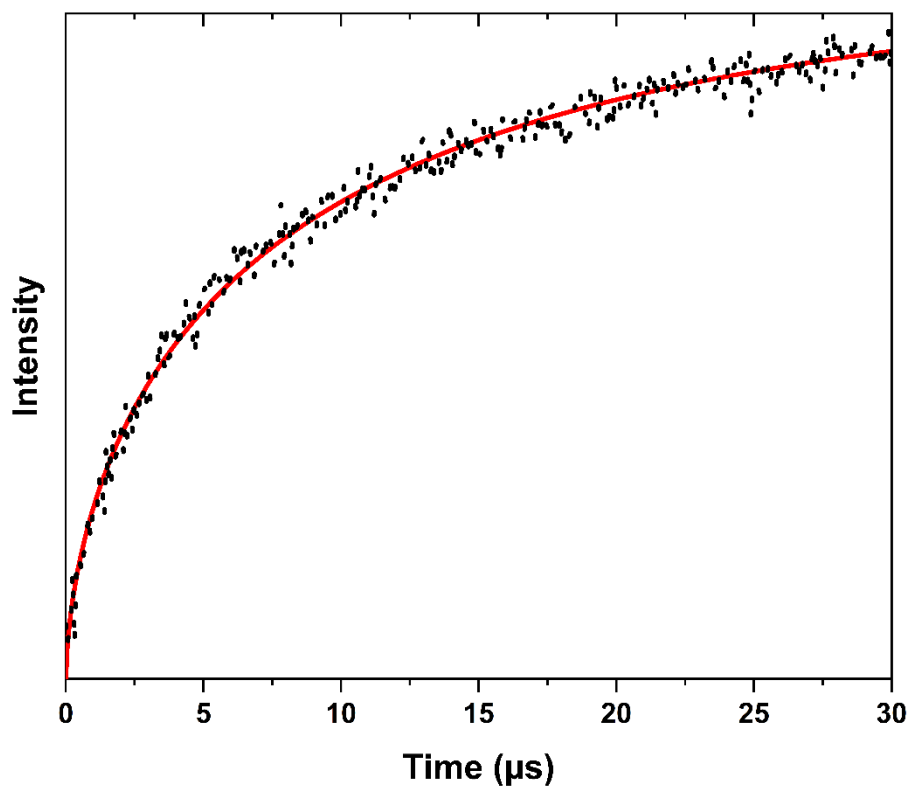


Figure II-28. Spin-lattice relaxation of $\text{Co}_{0.05}\text{Zn}_{0.95}$ at $T = 5\text{ K}$, at $B = 342\text{ mT}$ and 9.69 GHz .

Finally, we measured the coherence time of the Co(II) to have a reference before studying the compound containing Ni(II) and Co(II). We found $T_2 < 0.20\ \mu\text{s}$ for $\text{Co}_{0.05}\text{Zn}_{0.95}$ (Figure II-29). No difference of the coherence time was observed with the magnetic field. This short value was adequate to create significant fluctuations in spin bath.

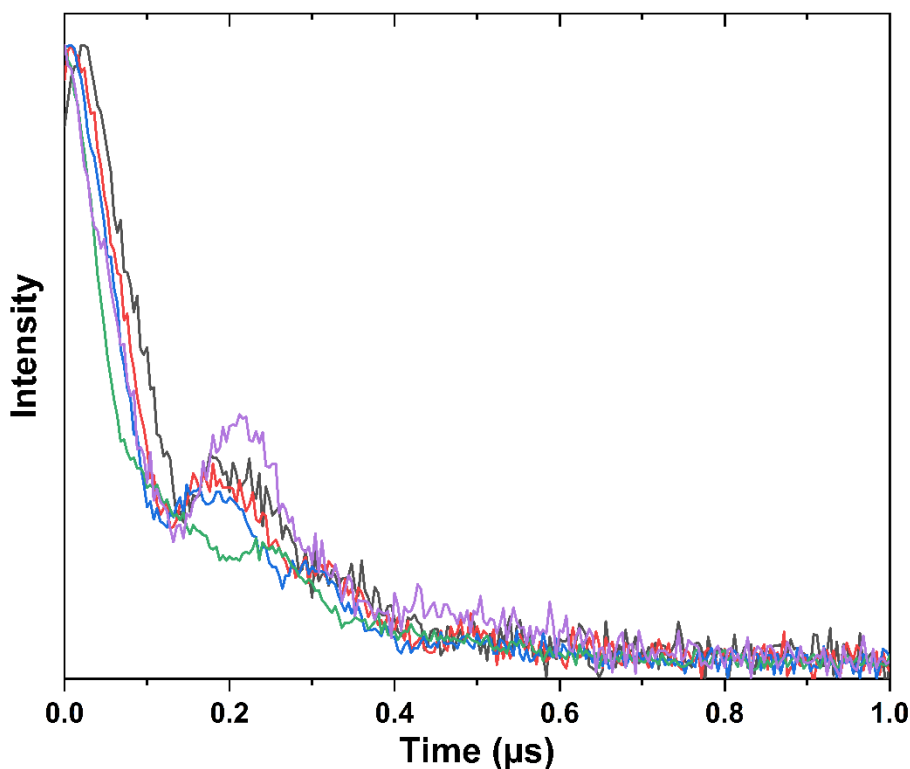


Figure II-29. Hahn echo sequence recorded spectra of $\text{Co}_{0.05}\text{Zn}_{0.95}$ at different magnetic field, $B = 294$ mT (green), $B = 313$ mT (blue), $B = 326$ mT (red), $B = 332$ mT (black) and $B = 346$ mT (purple).

II.2.c.ii Dilution in a diamagnetic matrix

First, we want to confirm that the previously found value of ZFS for $[\text{Ni}(\text{imidazoline})(\text{NO}_3)](\text{NO}_3)$ allows one to observe a CT in pulsed-EPR.

The EDFS spectrum (Figure II-30) of the sample $\text{Ni}_{0.07}\text{Zn}_{0.93}$ indicates the presence of a transition at zero magnetic field attributed to the CT. Two other transitions are visible: one large centred at 150 mT, which corresponds to the one observed in cw-EPR spectrum (Figure II-31), and another at 348 mT attributed to the presence of a radical that is difficult to avoid for the imidazoline containing complexes. This radical does not change the results because its band is at a magnetic field far from zero. On the one hand, the CT was not supposed to be affected by the spin diffusion induced by the radical. On the other hand, radicals are known to possess very long relaxation times, their fluctuations are, therefore, negligible at the time scale of the CT transition of the Ni(II) species.

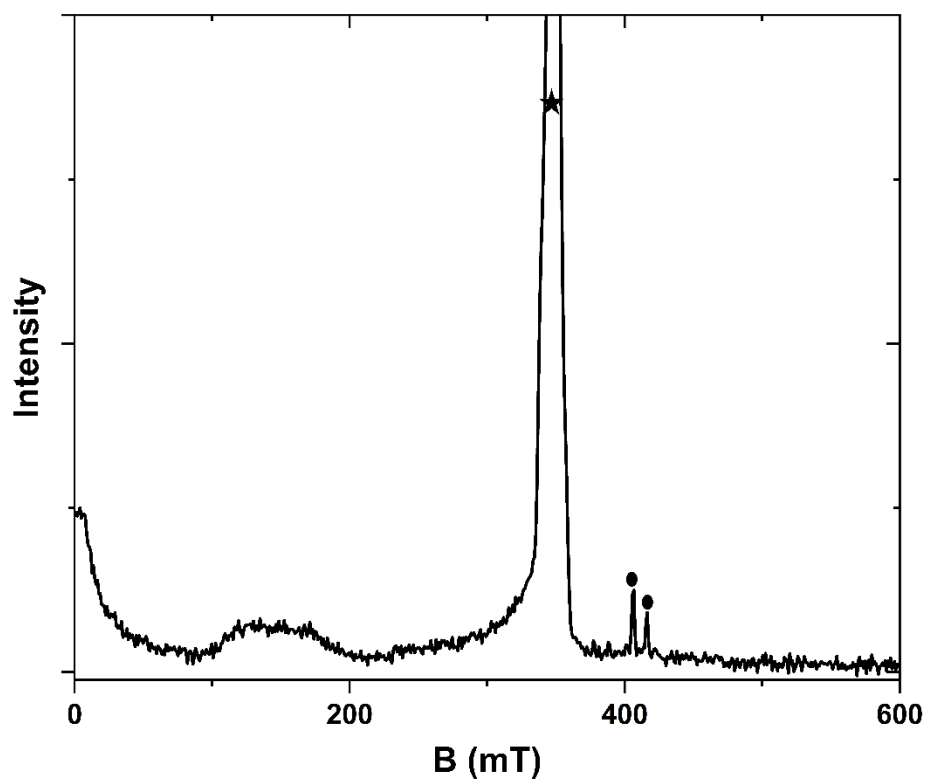


Figure II-30. EDFs of $Ni_{0.07}Zn_{0.93}$ at $T = 5$ K and 9.69 GHz. Black dots correspond to cavity artefact. Black stars correspond to the presence of a radical impurity.

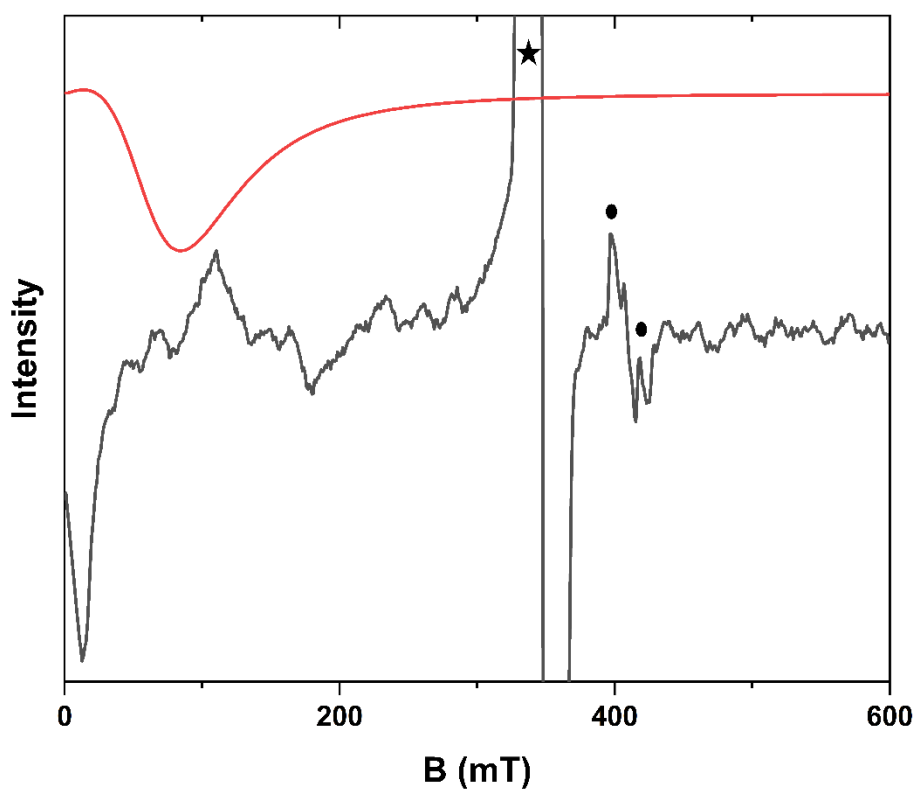


Figure II-31. Comparison of the CW-EPR spectra of $Ni_{0.07}Zn_{0.93}$ (red) at $T = 90$ K and 9.69 GHz and the derivative of the EDFS spectra of $Ni_{0.07}Zn_{0.93}$ (black) at 5K and 9.69 GHz. Black dots correspond to cavity artefact. Black star corresponds to the presence of a radical impurity.

The nutation experiment (Figure II-32) confirms that the transition observed at 0 mT is associated with $S = 1$ species.

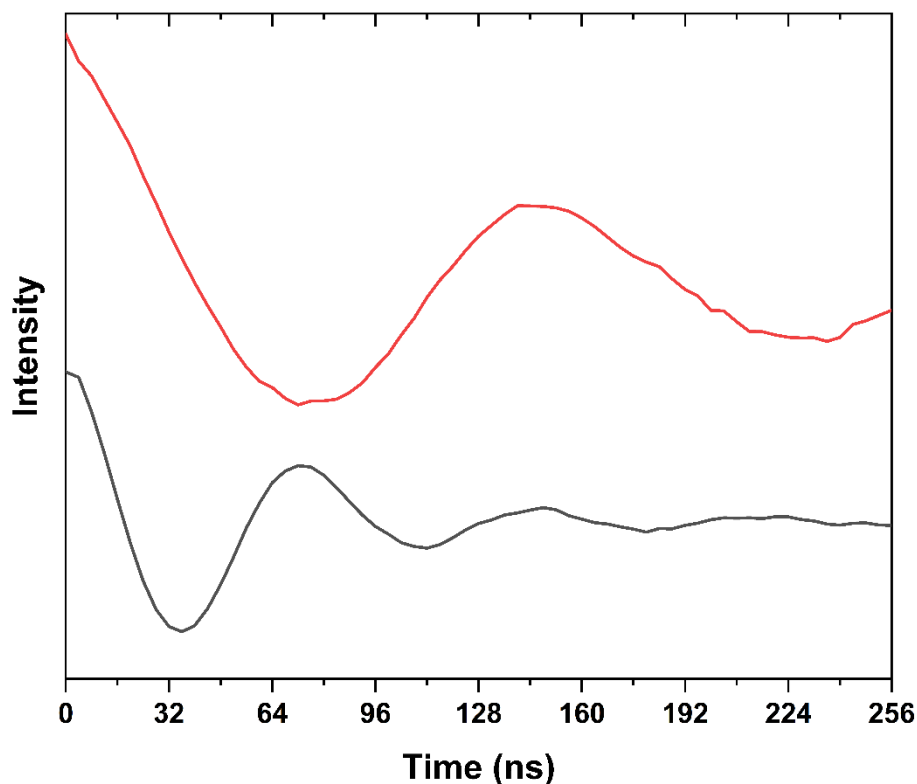


Figure II-32. Nutation experiment of $Ni_{0.07}Zn_{0.93}$ (black) at $B = 1$ mT and TEMPO at $B = 324$ mT reference (red) at 12 dB, $T = 5$ K and at 9.69 GHz.

The spin-lattice relaxation was recorded as a function of time using an inversion recovery sequence at different temperatures. An example is given Figure II-33 where the data have been fitted using stretched exponential model with $\alpha = 0.96$ and lead to $T_1 = 1.24 \mu\text{s}$. Here T_1 is relatively short in comparison to the other Ni(II) study in this chapter while in the solid state T_1 around $15 \mu\text{s}$ were found at 5 K. The explanation of the difference in the T_1 values can be explained by the difference of the rigidity of the ligands in the different complexes studied. The 2-(1H-Imidazol-2-yl)pyridine ligands have a structure (hence a rigidity) close to the bpy of the $[Ni(4,4'\text{-Di-tert-butyl-2,2'bpy})_3](NO_3)_2$ complex which possess long T_1 value ($T_1(5K) = 15.2 \mu\text{s}$). This is why we assume that 2-(1H-Imidazol-2-yl)pyridine ligands are not responsible for this fast relaxation. However, the NO_3 ligand is not rigid compared to a pyridine or an imidazoline group, we assume that this group is responsible for the fast relaxation observed. Additionally, a vibration of this ligand will change the Ni-O distance thus the ZFS parameters,

which are extremely sensitive to the environment as shown Chapter I. If the ZFS and particularly the $2E$ value is changed thus the coherence is lost hence the fast relaxation observed for T_1 .

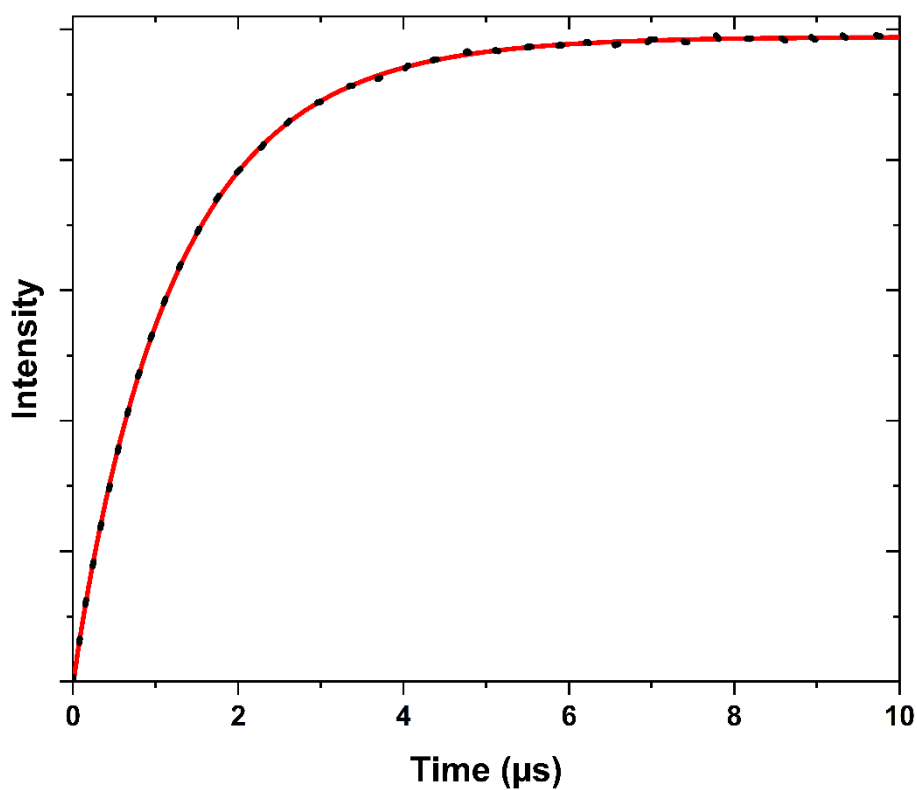


Figure II-33. Spin-lattice relaxation of $Ni_{0.07}Zn_{0.93}$ at $T = 5$ K, at $B = 1$ mT and at 9.69GHz.

We make the assumption here that the indirect T_1 -Flip process will be inoperant because it is spin-diffusion and we will demonstrate later that CT is insensitive of such process.

The coherence time variation with an applied magnetic field was studied for three different concentrations ($Ni_{0.001}Zn_{0.999}$ in black, $Ni_{0.01}Zn_{0.99}$ in red, and $Ni_{0.07}Zn_{0.93}$ in blue) as shown in Figure II-34. For the $Ni_{0.07}Zn_{0.93}$ sample, the coherence time remains stable in the CT region ($B < 3$ mT), then decreases slowly (3 mT $< B < 8$ mT) to reach a plateau for $B > 10$ mT. The two other samples have similar behaviour but less pronounced. Surprisingly, the coherence time does not increase with dilution, while the intensity of the signal drastically decreases when the concentration increases. Two hypotheses can be made. First, the dilution, which is supposed to diminish the flip-flop mechanism, is not sufficiently important, this mechanism still dominates even for the most diluted system. The second hypothesis is that the dilution was not homogeneous, making it inefficient. Here, $\alpha \approx 1$ at the CT which corresponds probably to the presence of one population of spins. The quality of dilution is very difficult to estimate in order

to discriminate between the two hypothesis.

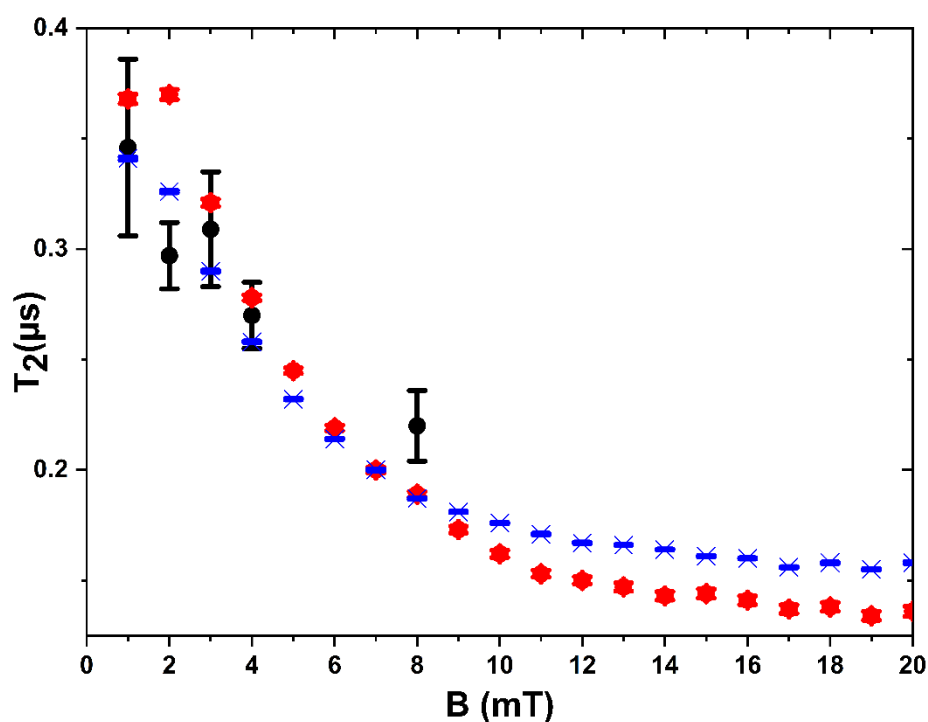


Figure II-34. Variation of the coherence time with magnetic field at $T = 5$ K at 9.69 GHz. In blue $\text{Ni}_{0.07}\text{Zn}_{0.93}$, in red $\text{Ni}_{0.01}\text{Zn}_{0.99}$ and in black $\text{Ni}_{0.001}\text{Zn}_{0.999}$.

The first hypothesis can be checked by changing the power of the pulse during the Hahn echo sequence. In fact, for weak power values of the pulse less flip-flop events occur leading to longer coherence times. The study was performed on the $\text{Ni}_{0.01}\text{Zn}_{0.99}$ sample in order to keep a signal sufficiently intense to be recorded. Figure II-35 shows a very small increase in the coherence time when going from 12 dB, the optimum attenuation power, to 18 dB. This means that at this dilution we are still saturated either in flip-flop or in spin diffusion. Ideally doing the experiment at higher attenuation and higher dilution will probably lead to another conclusion. However once again the relatively low sensitivity of the instrument did not allow us to investigate further. We can, however, conclude that probably the poor quality of the dilution is mainly responsible of the fact that T_2 remains the same for all the samples.

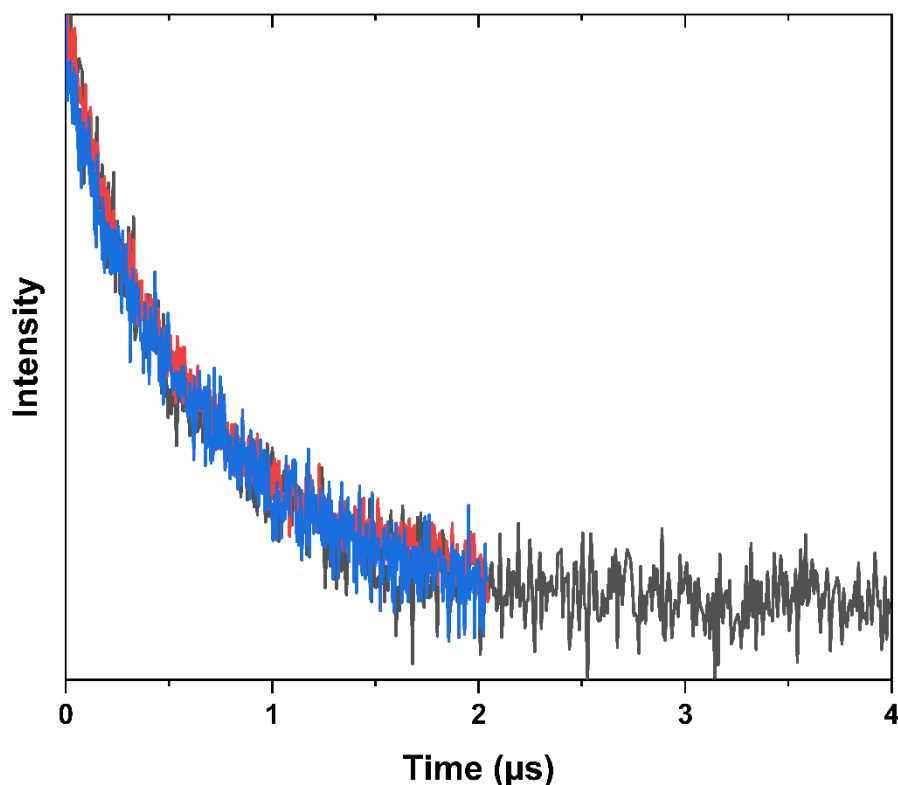


Figure II-35. T_2 curves of $[\text{Ni}(4,4'\text{-Di-tert-butyl-2,2'bpy})_3](\text{NO}_3)_2$ after an Hahn echo sequence at $T = 5 \text{ K}$, at $B = 1 \text{ mT}$ and at 9.69 GHz at 12 dB (blue), 15 dB (red) and 18 dB (black).

The coherence time of the system will be constrained by a relatively short T_1 at 5 K . In fact, for $T_2 = 0.3 \mu\text{s}$, 23% ($\exp(-T_2/T_1)$) of the molecules have their magnetization return to the z-axis (T_1 relaxation) before dephasing in the plane.

II.2.c.iii Robustness of the CT

The influence of the magnetic fluctuation due cobalt(II) on nickel(II) was investigated. We have seen previously that for both paramagnetic complexes, when they are diluted in diamagnetic matrix, it is possible to observed an echo. Now both complexes will be diluted in a diamagnetic matrix of Zn(II). Two samples have been prepared, one with a low proportion of cobalt ($\text{Ni}_{0.01}\text{Co}_{0.05}\text{Zn}_{0.94}$) which correspond to a situation with a small amount of magnetic fluctuations sources and one with an high proportion of cobalt ($\text{Ni}_{0.01}\text{Co}_{0.5}\text{Zn}_{0.49}$) which correspond to a situation with a large amount of magnetic fluctuations sources.

With first perform EDFS experiment on both samples where we worked at 12 dB which correspond to the optimize value for the Ni(II) signal. We can see Figure II-36 for a

$\text{Ni}_{0.01}\text{Co}_{0.05}\text{Zn}_{0.94}$ sample (red), we can observe the echoes of the cobalt and nickel. For the cobalt we observed 7 transitions and the last one is probably mix with the one of the radical (transition at 348 mT). For the $\text{Ni}_{0.01}\text{Co}_{0.5}\text{Zn}_{0.49}$ sample (black) the echo of the nickel remains the same. In contrast, the intensity of the echo attributed to the cobalt complex disappeared completely meaning that no superposition of state can be observed.

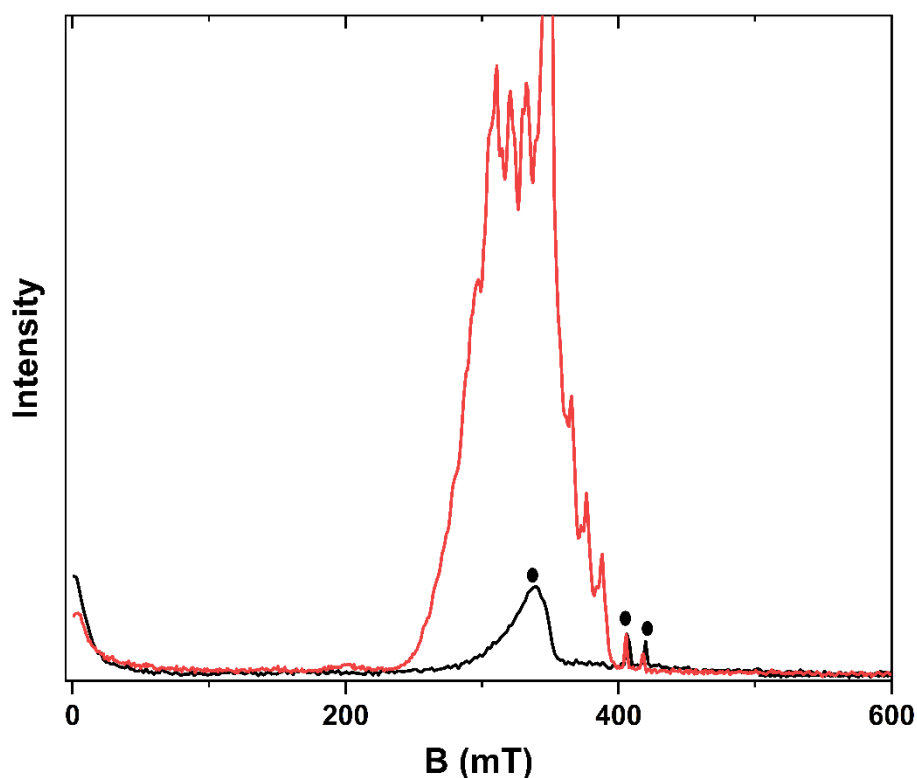


Figure II-36. EDFS of $\text{Ni}_{0.01}\text{Co}_{0.05}\text{Zn}_{0.94}$ (red) and $\text{Ni}_{0.01}\text{Co}_{0.5}\text{Zn}_{0.49}$ (black) at $T = 5$ K and at 9.69 GHz.

This indicates that the decoherence for the cobalt complex occurs at a much faster rate, making it impossible to record. This result can be explained as follows. The Ni(II) transition at 0 mT is at the CT, a fluctuation of the magnetic field (due to the Co species) will not change the difference between the levels responsible of the transition as shown in region 1 of Figure I-1, thus the state of superposition is not affected and consequently the coherence time does not become shorter. When a small magnetic field (10 mT) is applied, the Zeeman contribution is considered (area 2 of Figure I-1). At this field the slope of the energy state is small, a fluctuation of the magnetic field will very slightly change the energy gap, thus creating a weak decoherence. If a magnetic fluctuation occurs far from the clock transition regime (area 3 of

Figure I-1), the energy gap will be modified by $2\Delta B$, thus creating a significant decoherence. In the case of the Co(II) complex studied here, the slope of the curve is $\frac{1}{2}g_z\beta$ even at very low magnetic fields. In this case, a fluctuation in the magnetic field leads to a change in the energy gap of the qubit of ΔB , creating decoherence.

II.2.c.iii Influence of T_2

We thus perform Hahn echo sequence for the Ni(II) transition in order to get quantitative information about the superposition of state. We expected an important difference between the coherence times in and outside the CT particularly in the case of $\text{Ni}_{0.01}\text{Co}_{0.5}\text{Zn}_{0.49}$. The echo signal vs. time for the different samples have been fitted using a stretched exponential model with α_s [0.9; 1.1]. An example of experimental curves and their fit is given Figure II-37. The same work has been done for different magnetic fields and the resulting T_2 have been reported Figure II-38.

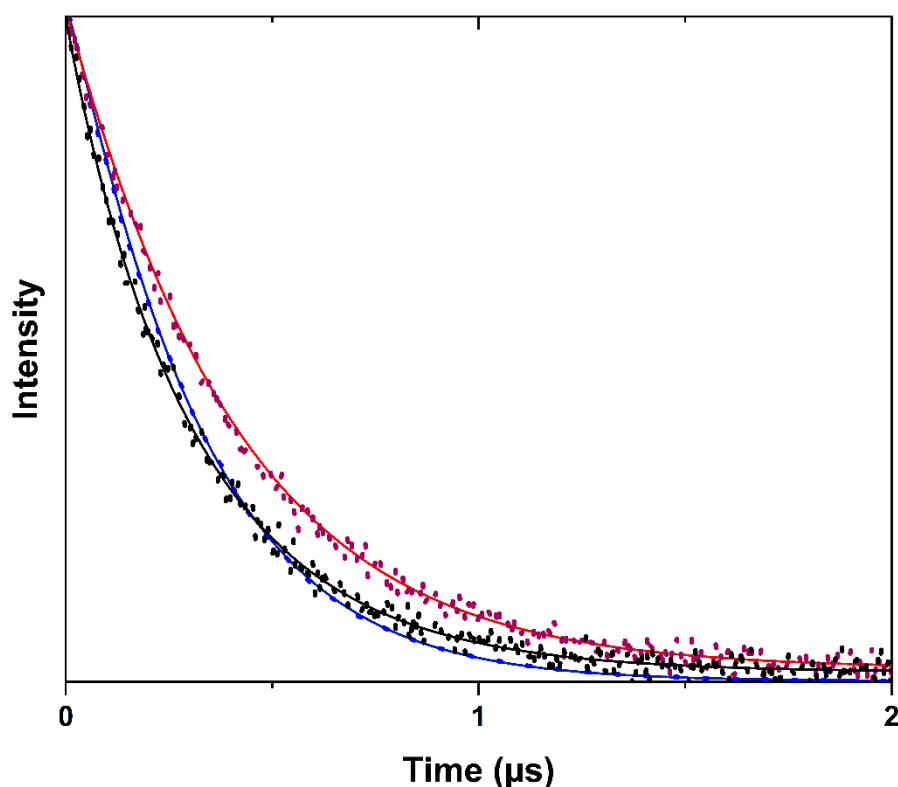


Figure II-37. Spin-spin relaxation time curves of $\text{Ni}_{0.07}\text{Zn}_{0.93}$ (blue), $\text{Ni}_{0.01}\text{Co}_{0.5}\text{Zn}_{0.49}$ (black) and $\text{Ni}_{0.01}\text{Co}_{0.05}\text{Zn}_{0.94}$ (red) at $T = 5 \text{ K}$, $B = 1 \text{ mT}$ and 9.69 GHz . The data have been fitted using stretched exponential model here with $\alpha =$

1.

From this study, we can see that the coherence time follow a similar behaviour than the one described for the $\text{Ni}_{0.07}\text{Zn}_{0.93}$. The coherence time remains stable in the CT region then decreases slowly outside the CT to reach a plateau in region 3 (Figure I-2). Surprisingly, the decay of the coherence time of the $\text{Ni}_{0.01}\text{Co}_{0.5}\text{Zn}_{0.49}$ with the applied magnetic field is not as important as for the other samples. One could expect that outside the CT the coherence time of the nickel in the $\text{Ni}_{0.01}\text{Co}_{0.5}\text{Zn}_{0.49}$ sample will be lower due to the important number of paramagnetic sources. The clock transition is insensitive to the magnetic fluctuation at first order. Probably second order terms start to play a role in the decoherence, this is why the slope of the curve is not so different among the different samples.

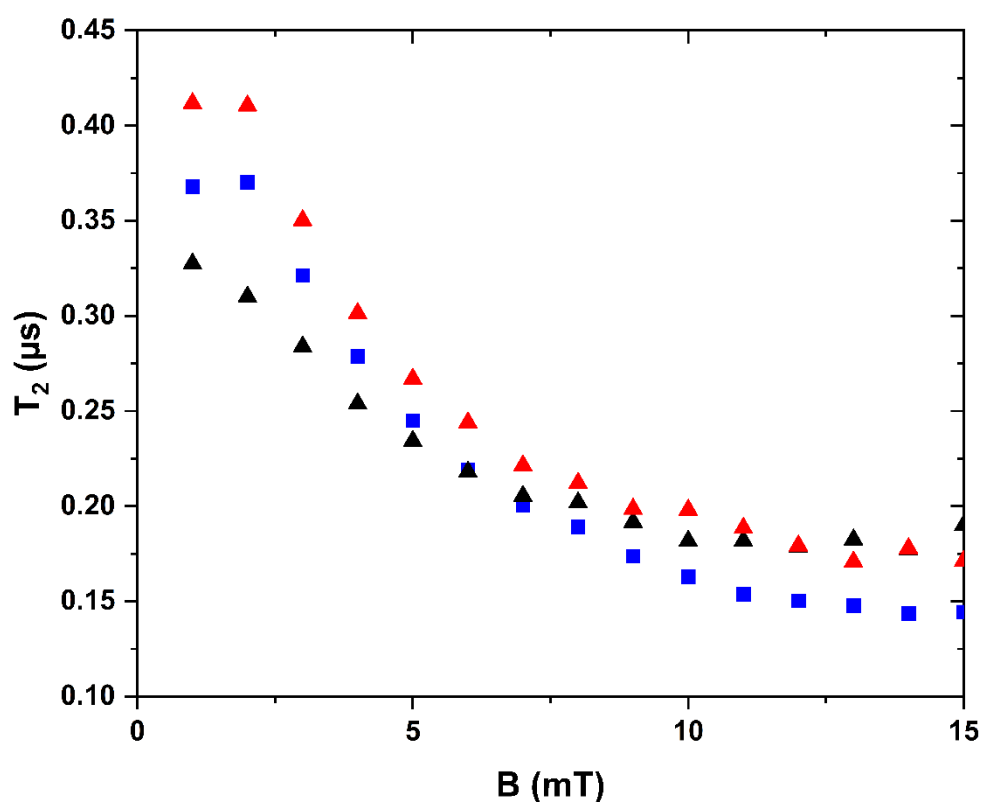


Figure II-38. Variation of the coherence time with an applied magnetic field for $\text{Ni}_{0.01}\text{Co}_{0.05}\text{Zn}_{0.94}$ (red) and $\text{Ni}_{0.01}\text{Co}_{0.5}\text{Zn}_{0.49}$ (black) and $\text{Ni}_{0.01}\text{Zn}_{0.99}$ (blue) at $T = 5$ K and 9.69 GHz.

II.2.c.iv Influence of T_1

For both compounds, $\text{Ni}_{0.01}\text{Co}_{0.05}\text{Zn}_{0.94}$ and $\text{Ni}_{0.01}\text{Co}_{0.5}\text{Zn}_{0.49}$ the T_1 values at 1 mT are 1 μs and 1.5 μs respectively (Figure II-39) for α value close to 1. The results are coherent with the one founded for $\text{Ni}_{0.07}\text{Zn}_{0.93}$. The T_1 values are only four times longer than the T_2 values, indicating

that T_2 is limited by T_1 and at 15 K, $T_2 = T_1$. As for other complexes we tried to fit the variation of T_1 with temperature even if we have only three points (Figure II-40). We found a very small pre-exponential factor comparing to the other complexes study in this chapter.

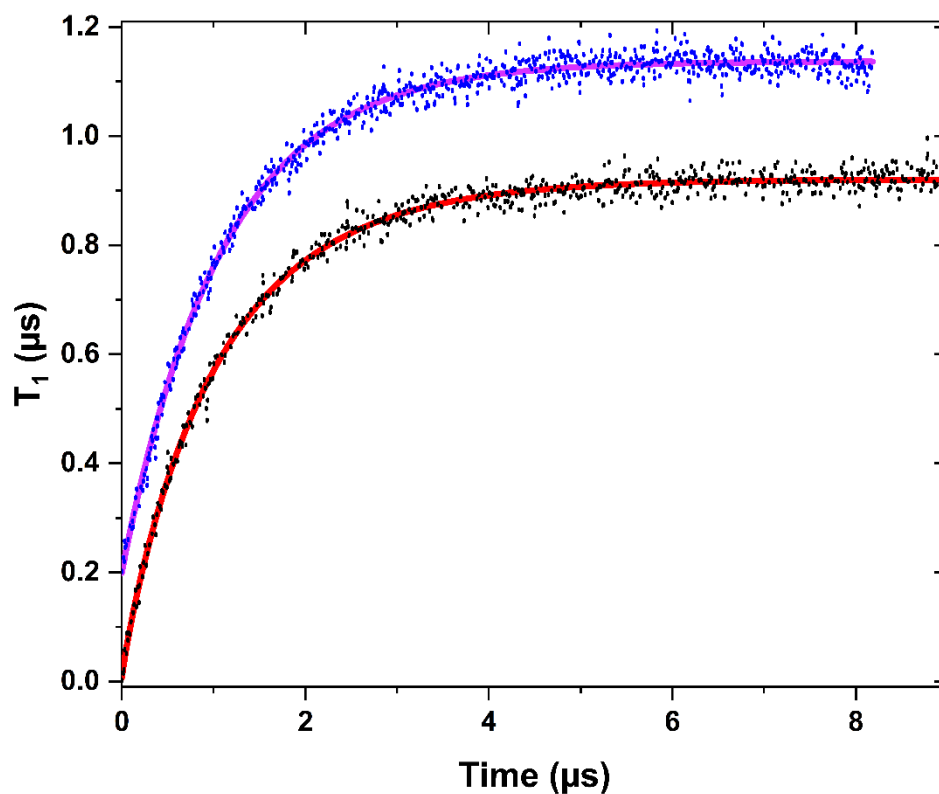


Figure II-39. Spin-lattice relaxation time of $Ni_{0.01}Co_{0.05}Zn_{0.94}$ (black dot) and $Ni_{0.01}Co_{0.5}Zn_{0.49}$ (blue dot) and their respective fit using stretched exponential model with $\alpha = 0.99$ and $\alpha = 0.92$ at $B = 1$ mT and at 9.69 GHz.

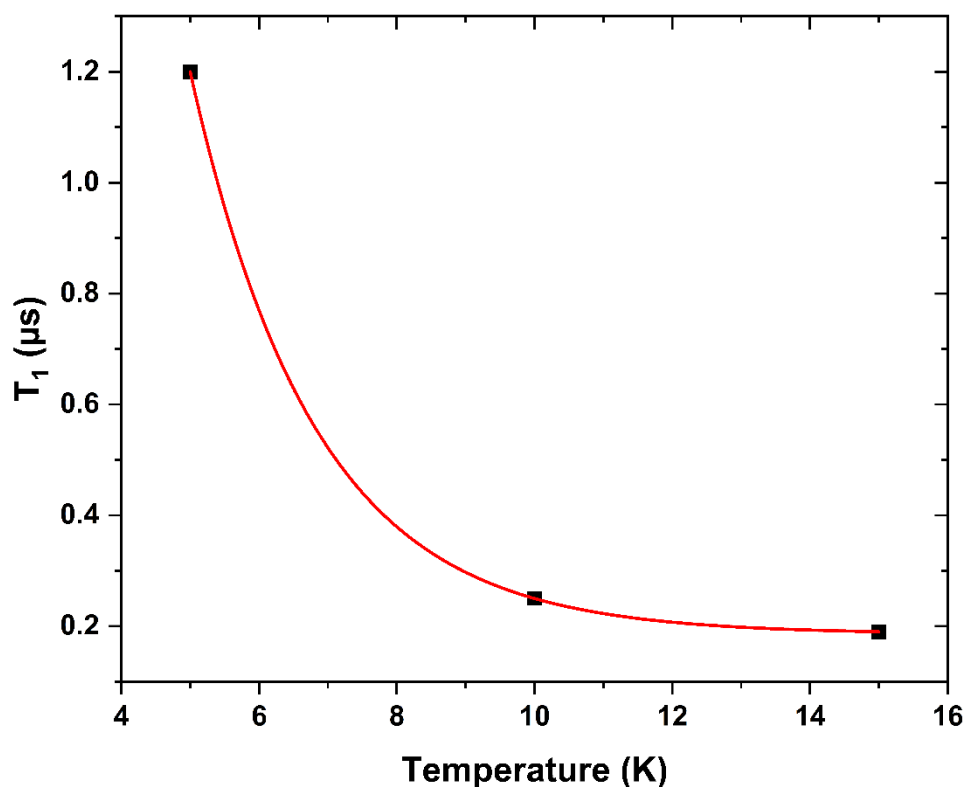


Figure II-40. Variation of the spin-lattice relaxation time of $\text{Ni}_{0.01}\text{Co}_{0.05}\text{Zn}_{0.94}$ (red) with temperature

$$T_{1(\text{imidazoline})}(T) = 16 \times e^{\left(\frac{-T}{1.81}\right)} \quad (\text{III-6})$$

Even though we found $\alpha = 1$, it is still possible that our dilution was not homogeneous. During the crystallisation process, we observed that kinetics again played a crucial role. In fact, in some samples where we tried to precipitate the powder or to get a crystal in less than two days, the ratio between the different species was not good and no cobalt signal was observed. This indicates that again the dilution was not perfect. This can also be seen in the width of the transition when examining the $\text{Co}_{0.05}\text{Zn}_{0.95}$ samples compared to the NiCoZn samples. EDX was carried out and confirmed that rapid recrystallisation resulted in inhomogeneous dilution. This confirmed our statement that an inhomogeneous sample would lead to a short T_1 . This dilution problem is certainly one of the reasons why T_2 is still short and also T_1 .

Here we have compared the evolution of the coherence time of two transitions, one normal and one CT. We have evidenced that in the presence of magnetic fluctuations cause by spin diffusion (here due to Co(II) $S = 3/2$, $I = 7/2$) the coherence time of the CT remains stable while

Chapter II: Pulsed EPR study of mononuclear Ni(II) complexes

it is not possible to observe any echo for the normal transition. This system could be ideal to perform further investigation but the short T_1 associated will always be a limiting factor.

II.3 CONCLUSION

In this chapter, mononuclear Ni(II) complexes with a $D < 0$ has been studied in pulsed EPR. We have seen that due to E -strain, it was possible to observe a clock transition behaviour for those complexes even if the average E value does not match the one of the cavity frequency.

We have introduced different ways to improve the spin-lattice relaxation (choice of matrix, reduction of the number of ligands). We have seen that the ligand has to be rigid, this ensuring that the vibration modes of the ligand will have a limited impact on the change of the energy levels of the d orbitals and therefore on the ZFS parameters within the timescale of the superposition time.

The pulsed EPR studies of the clock transition have shown that each complex has a relatively short coherence time $0.25 \mu\text{s} < T_2 < 0.60 \mu\text{s}$ for a maximum dilution of 1%. These coherence times are short but robust to magnetic fluctuations as evidenced by the [Ni(imidazoline)(NO₃)](NO₃) study.

In all cases, the experiments were difficult to carry out because only a small proportion of the molecules have the good frequency resonance. Getting a signal was always complicated. We also realised that even if the dilution seems fine and the ratio between Ni and Zn in EDX agrees with theory, at the molecular level there seems to be nano-aggregates that make the dilution irrelevant. We assume that beyond a certain dilution the probability of formation of these small aggregates decreases.

The problem with our current setup was the detection of a signal in a diluted sample (0.1% of paramagnetic specie). In fact, we only observed the molecules with the good ZFS parameters and with coherence time long enough to be detected. This correspond to a small proportion of the molecule, so if the dilution increases, this amount will diminish. In this situation one can expected that all molecules with the good ZFS parameters will have long coherence time because Flip-Flip interactions will decrease, thus all molecules could to be detected resulting in a good ratio S/N. But in our case, we have seen that most of the dilutions were not very efficient leading to a bad ratio S/N and coherence time than remain short. This limitation reduces our capacity to quantify parameters such as flip-flop/spin diffusion. This is why we have to work on two points:

Chapter II: Pulsed EPR study of mononuclear Ni(II) complexes

- (i) Find a matrix in which it is possible to dilute perfectly the sample and avoid aggregation. Porous solids such as Metal Organic Frameworks (MOFs) or mesoporous silica could be a possible solution.
- (ii) Working on oriented single crystals, for such a case all the spins are expected to have the same resonance frequency thus the signal will increase.
- (iii) Use a set up that has a better sensitivity, this is possible and the group in Grenoble is in the process of acquiring an amplifier.

However even if those points are developed, the process of adapting the compound to the frequency of the cavity is not suitable. However, there are devices (resonators) with a relatively broad band frequency that can cover few GHz and are suitable to our purpose. We are currently collaborating with research groups where a concentration of 10^{12} spins/cm³ could theoretically be studied.

II.4 EXPERIMENTAL PART

X-band EPR spectra were acquired on a Bruker Elexsys 500E spectrometer equipped with a Bruker ER 4116DM X band resonator, an Oxford Instrument continuous flow ESR 900 cryostat, and an Oxford ITC 503 temperature control system. Q-band EPR spectra were acquired on a Bruker Elexsys 500E spectrometer equipped with a Bruker ER 5106 QT-E Q band resonator, an Oxford Instrument continuous flow CF 935 cryostat and an Oxford ITC 503 temperature control system.

Pulse EPR experiments were performed on a Bruker Elexsys E580 spectrometer at liquid helium temperatures.

For nutation experiment a 1mMol intern reference (TEMPO) in H₂O/glycerol was prepared.

Nutation experiment. The nutation spectra were recorded with the following sequence $((-n\pi/16) - t_1 - (\pi/2 + n\pi/16) - t_2 - (\pi + n\pi/16) - t_2 - \text{echo})$, with microwave pulse lengths of 0, 16 and 32 ns respectively. The pulse lengths are increased gradually by 2 ns. The delay t_1 is equal to 2000 ns and the delay t_2 is equal to 150/160 ns.

II.5 REFERENCES

- [1] V. Kathirvelu, H. Sato, S. S. Eaton, G. R. Eaton, *Journal of Magnetic Resonance* **2009**, *198*, 111–120.
- [2] K. M. Salikhov, S. A. Dzuba, A. M. Raitsimring, *Journal of Magnetic Resonance (1969)* **1981**, *42*, 255–276.
- [3] J. Lawrence, E.-C. Yang, R. Edwards, M. M. Olmstead, C. Ramsey, N. S. Dalal, P. K. Gantzel, S. Hill, D. N. Hendrickson, *Inorg. Chem.* **2008**, *47*, 1965–1974.
- [4] A. Schweiger, G. Jeschke, A. Schweiger, G. Jeschke, *Principles of Pulse Electron Paramagnetic Resonance*, Oxford University Press, Oxford, New York, **2001**.
- [5] S. K. Hoffmann, W. Hilczler, J. Goslar, *Journal of Magnetic Resonance, Series A* **1996**, *122*, 37–41.
- [6] M. Rančić, M. L. Dantec, S. Lin, S. Bertaina, T. Chanelière, D. Serrano, P. Goldner, R. B. Liu, E. Flurin, D. Estève, D. Vion, P. Bertet, **2022**.
- [7] G. Wolfowicz, A. M. Tyryshkin, R. E. George, H. Riemann, N. V. Abrosimov, P. Becker, H.-J. Pohl, M. L. W. Thewalt, S. A. Lyon, J. J. L. Morton, *Nature Nanotech* **2013**, *8*, 561–564.
- [8] M. del Carmen Fernández-Fernández, R. Bastida, A. Macías, P. Pérez-Lourido, L. Valencia, *Polyhedron* **2007**, *26*, 5317–5323.
- [9] J. M. Zadrozny, A. T. Gallagher, T. D. Harris, D. E. Freedman, *J. Am. Chem. Soc.* **2017**, *139*, 7089–709

CHAPTER III: SYNTHETIC STRATEGIES OF BINUCLEAR COMPLEXES AS MOLECULAR QUANTUM GATES

The objective of this chapter is to apply the knowledge gained from mononuclear compounds to synthesize binuclear ones capable of serving as quantum logic gates.

III.1 INTRODUCTION

A two-bit classical logic gate can be described by four states noted 00, 11, 10, or 01, whereas a quantum logic gate, because of the quantum nature of qubit, can be in a superposition of the four states. The number of accessible states evolves as 2^N , where N corresponds to the number of coupled (entangled) qubits. There are several requirements for a molecule to play the role of logic gate:

- (i) Individually, each qubit must possess a long coherence time.
- (ii) The coupling between the qubits must be weak enough, allowing each qubit to be individually addressed.
- (iii) The coupling must be antiferromagnetic; otherwise, only states 00 and 11 will be accessible.

As seen in Chapter II, the relaxation time of Ni(II) is short but can be improved if the qubit corresponds to the clock transition and the molecules diluted enough to avoid as much as possible the flip-flop relaxing mechanism. For the second criterion, the coupling energy (J) must be weaker than the smallest energy gap of the qubits ($J < 2E_1 < 2E_2$, where E_1 and E_2 are the rhombic ZFS parameters of qubits 1 and 2, respectively). To satisfy the addressing criteria, it is necessary to have $E_1 \neq E_2$. Therefore, from the chemist point of view, the highly ambitious objective here is to obtain an asymmetric nickel dimer with weak coupling and E values compatible with the presence of a clock transition at zero field. This objective is very difficult to reach because of the several criteria that a molecule must meet simultaneously. We tried as much as possible to design and prepare molecules that meet these criteria. The most difficult aspect is the same as for mononuclear complexes: obtaining a negative D value for the two Ni species forming the binuclear complex. In addition, to the requirements mentioned above. There is one crucial that concerns the chemical stability of the binuclear complexes when they will be diluted either in solution or in a diamagnetic matrix. Diluting a binuclear complex in its own diamagnetic matrix (replacing Ni(II) by Zn(II)) may provide heterobinuclear complexes (NiZn) that may alter the physical properties of the assembly of molecules to be studied. We, therefore, tried to address the criteria one by one trying to consider, as much as possible, the

other criteria when designing the complexes.

Part 1 will examine the variation of the coupling energy with the evolution of the Ni-Ni distance, while part 2 focuses on an approach using building blocks.

III.2 RIGID BRIDGING LIGAND

One important criterion for binuclear complexes concerns the nature of the magnetic coupling between the two spins. For relatively short distance, the coupling is due to exchange (a through bond mechanism) that does not depend much of the local magnetic anisotropy of the local spins (if anisotropy is not very large. For large distances, the coupling is mainly dipolar and depends on the relative orientations of the local **D** tensors. In order to vary the coupling energy, we proposed a family of rigid bridging ligand with different lengths (Figure III-1).

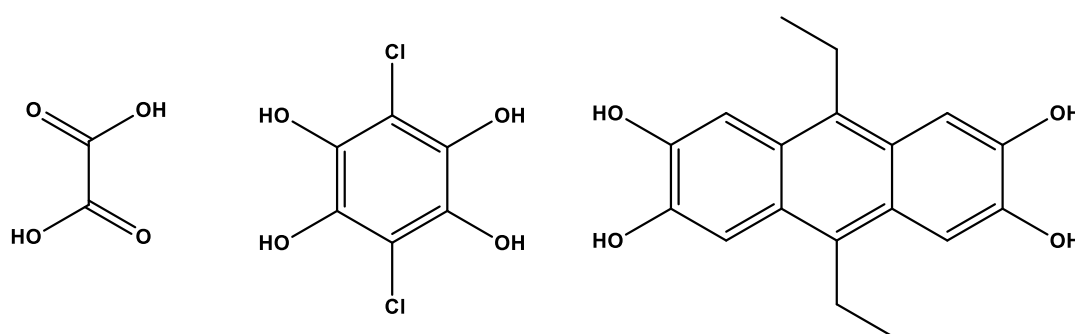


Figure III-1. Family of bridging ligand

III.2.a Synthesis

The compounds were synthesized and crystallized. In the case of the oxalate and chloranilate bridges, a structure of a binuclear complex was obtained with a chiral ligand (Figure III-2-a) as a terminal one. While for the anthracene type bridge, the crystal structure was with a non-chiral ligand (TPA, Figure III-2-b). The rationale behind using a chiral ligand was to achieve an asymmetric molecule. For a binuclear complex made of two mononuclear Ni(II) complexes connected by a bridging ligand and having a chiral ligand as a terminal one ensures the absence of a symmetry plane and an inversion centre relating the two mononuclear units, because the binuclear complex would be chiral. In such a case, the two mononuclear units forming the binuclear one cannot have the same coordination sphere and they will automatically be electronically different so will be the rhombic parameters allowing us to address individually the qubits. Only the presence of a two-fold symmetry axis is allowed in a chiral molecule. In such a case, the coordination sphere of the two mononuclear species will be identical. However, the orientation of the ZFS tensors of the two Ni(II) will not be the same, with respect to the molecular frame. This deviation will be sufficient in the case of a dipolar coupling to be able to discriminate between the two qubits.

Chapter III: Synthetic strategies of binuclear complexes as molecular quantum gates

In summary, designing a chiral binuclear complex is an interesting strategy to design complexes with different qubits using the same metal. In this situation they will be slightly different so they can be addressed within a small range of microwave energy less than 1 GHz. However, there is no guarantee that the difference in the coordination sphere would be sufficient to produce such a difference. Therefore, one of the aims here was to prepare such complexes and try to determine the ZFS parameters, at least by theoretical calculations that can serve as a guide.

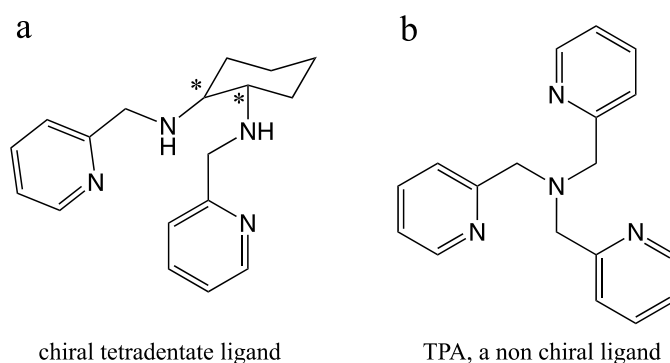


Figure III-2. Chemical structure of the capping ligand. (Left) Chiral ligand. (Right) TPA ligand

Regarding the anthracene bridge, only one single crystal was obtained with TPA as the terminal ligand. The utilization of anthracene ligand posed several challenges. Firstly, the synthesis,[2] required the use of concentrated BBr_3 , an expensive reagent that was out of stock for a significant part of the thesis. Additionally, solubility issues were encountered during the synthesis despite the intentional addition of ethyl groups to the molecule. These solubility problems arose from π -stacking and network formation,[2] despite the introduction of ethyl groups on the bridge. Ultimately, only one single crystal was obtained, and despite equivalent synthesis conditions, it was not possible to reproduce the experiment. The structures are shown below :

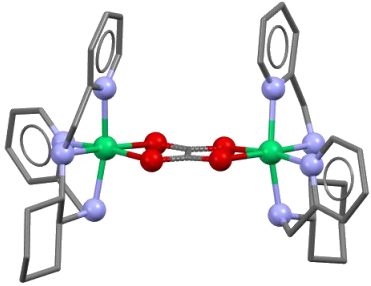
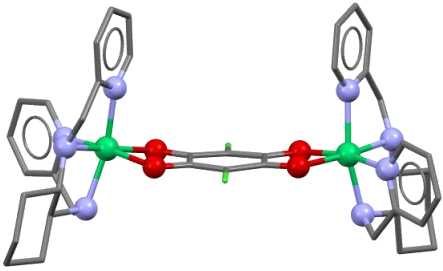
		
Formula	C ₄₆ H ₆₂ Cl ₂ N ₁₂ Ni ₂ O ₅	C ₄₂ H ₄₈ Cl ₂ N ₈ Ni ₂ O ₄ ·2(B F ₄) ₆ (C H ₄ O)
Space Group	P2 ₁	P1
Cell Lengths	a 12.5166(4) b 15.9973(5) c 13.4282(4)	a 10.8885(13) b 11.3266(13) c 12.9894(15)
Cell Angles	α 90 β 112.657(2) γ 90	α 84.603(4) β 75.542(4) γ 74.281(4)
Cell Volume	2481.25	1492.63
Z,Z'	Z : 2 Z' : 1	Z : 2 Z' : 1
R-factor (%)	4.18	Z : 1 Z' : 1
Distance Ni-Ni (Å)	5.383	3.35

Table III-1. Crystallographic information for [Ni₂(chiral)₂(μ-ox)](left) and [Ni₂(chiral)₂(μ-chloranilate)] (right).

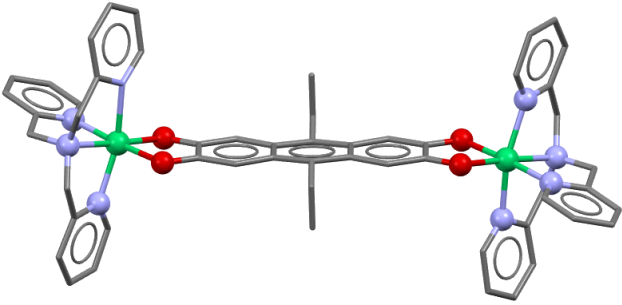
	
Formula	C ₅₄ H ₅₀ N ₈ Ni ₂ O ₁₀
Space Group	P-1
Cell Lengths	a 8.4479(6) b 12.6508(8) c 15.6940(10)
Cell Angles	α 113.468(3) β 90.888(4) γ 91.858(4)
Cell Volume	1536.97
Z,Z'	Z : 1 Z' : 0.5
R-factor (%)	9.4
Distance Ni-Ni (Å)	12.700

Table III-2. Crystallographic information [*Ni*₂(TPA)₂(μ-anthracene)]

The two binuclear complexes with the terminal chiral ligand crystallize in the chiral space groups P₂₁ and P1 for the oxalate and the chloranilate derivatives, respectively. The coordination spheres of the Ni atoms within the binuclear complexes are different in the two cases because they are not related by any symmetry operation. While for the non-chiral terminal ligand, the binuclear complex crystallizes in the centrosymmetric space group P-1, the Ni units are related by an inversion center, they have, therefore, exactly the same coordination sphere. Consequently, they will have the same ZFS parameters and cannot be electronically distinguished.

Theoretical calculations were carried out to determine the ZFS parameters in order to verify whether the difference in the coordination sphere of the Ni atoms of the chiral binuclear complexes induces a measurable difference in the ZFS parameters. We will focus on one complex, the oxalate derivative (Figure III-3).

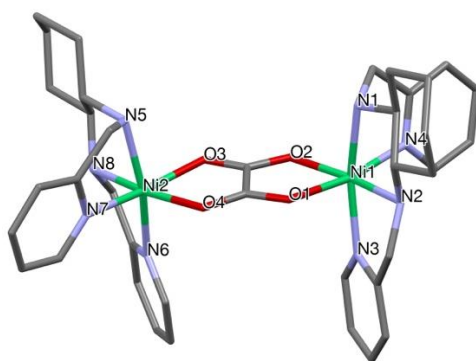


Figure III-3. Crystallographic structure of $[Ni_2(chiral)_2(\mu-ox)]$.

The calculations were made on the Ni fragments comprising the terminal ligand and oxalate for Ni1 and Ni2, the bond distances are given in Table III-3.

Bonds around Ni1	Distance (Å)	Bonds around Ni2	Distance (Å)
Ni1-O1	2.100	Ni2-O3	2.098
Ni1-O2	2.048	Ni2-O4	2.062
Ni1-N1	2.085	Ni2-N5	2.079
Ni1-N2	2.053	Ni2-N6	2.065
Ni1-N3	2.074	Ni2-N7	2.066
Ni1-N4	2.076	Ni2-N8	2.046

Table III-3. Selected distances in $[Ni_2(chiral)_2(\mu-ox)]$.

We obtain the following results for Ni1 and Ni2 respectively: $D_1 = 2.46 \text{ cm}^{-1}$, $E_1 = 0.75 \text{ cm}^{-1}$ ($E_1/D_1 = 0.3$), $D_2 = -2.54 \text{ cm}^{-1}$, $E_2 = 0.59 \text{ cm}^{-1}$ ($(E_2/|D_2|) = 0.23$). Ni1 has a positive D value but E/D is very close to the maximum rhombicity situation (0.33), so the sign has little meaning. The energy difference between the two low-lying levels that define the qubit are equal to 1.71 cm^{-1} and 0.46 cm^{-1} for Ni1 and Ni2 respectively. We therefore have two qubits with a different energy difference between their two levels, so that they can be distinguished in a coupled dimer. However, the difference between the frequencies of the qubits is too large (around 37.5 GHz), so it will be practically very difficult to address them with current devices. For the oxalate

derivative, the exchange coupling will be too large (see below), but it may be sufficient for the chloranilate derivative. In the next section we present the magnetic properties of the three complexes. The calculations give the orientation of the **D** tensors axes with respect to the molecular frame, as depicted below (Figure III-4). The axes of the tensors are not aligned as expected from the examination of the structure of the coordination sphere of the two atoms (Table III-4), where no relation can be found between the Ni-ligand bond lengths.

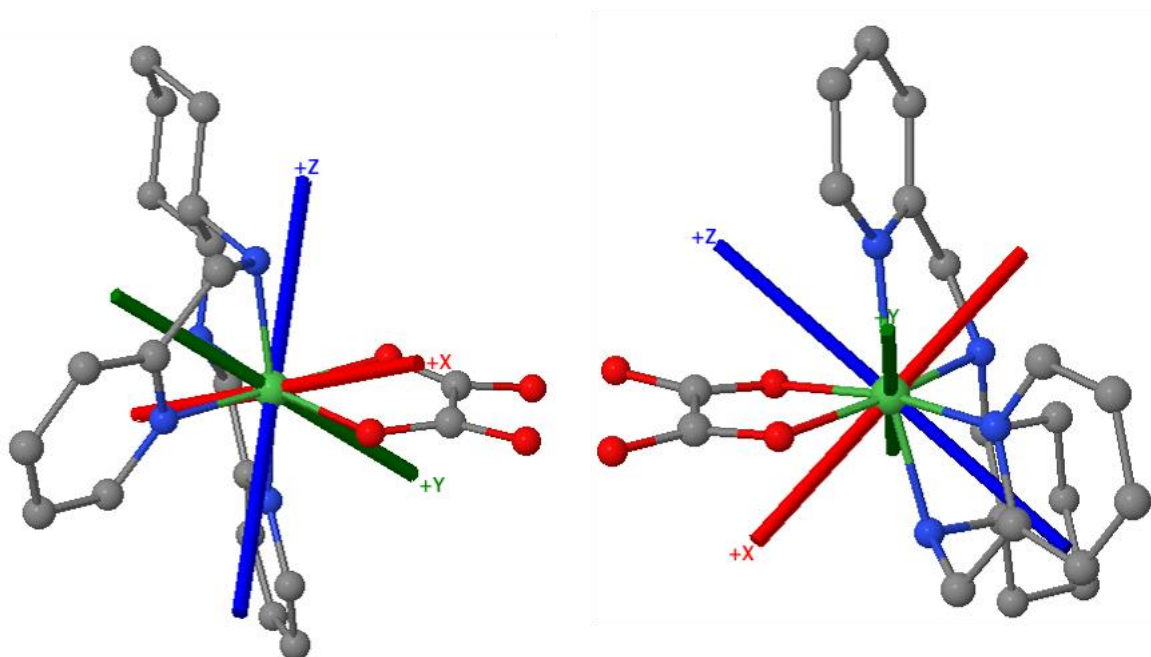


Figure III-4. Relative orientation of the **D** tensors axes for Ni1 (right) and Ni2 (left) with respect to the molecular frame.

III.2.b Magnetometry SQUID and EPR measurement

Magnetometry SQUID and EPR measurements were attempted on the three compounds, in order to measure the magnetic coupling between the Ni(II) electrons. In the case of the oxalate bridge, SQUID magnetometry allow us to determine the value the exchange coupling parameter J by fitting the $\chi T = f(T)$ data with the spin Hamiltonian:

$$H = -2J\mathbf{S}_{Ni1} \cdot \mathbf{S}_{Ni2} + D\mathbf{S}_z^2 + g\beta\mathbf{S} \cdot \vec{B} \quad (\text{III-1})$$

where **S** is the spin operator, J and D the exchange coupling and axial ZFS parameters, g the average g -factor, β the Bohr magneton and \vec{B} the applied magnetic field. The fit of the data gives the following parameters

$$2J = -34.4 \text{ cm}^{-1}, g = 2.24 \text{ and } 8\% \text{ of monomeric paramagnetic impurity of spin } 1.$$

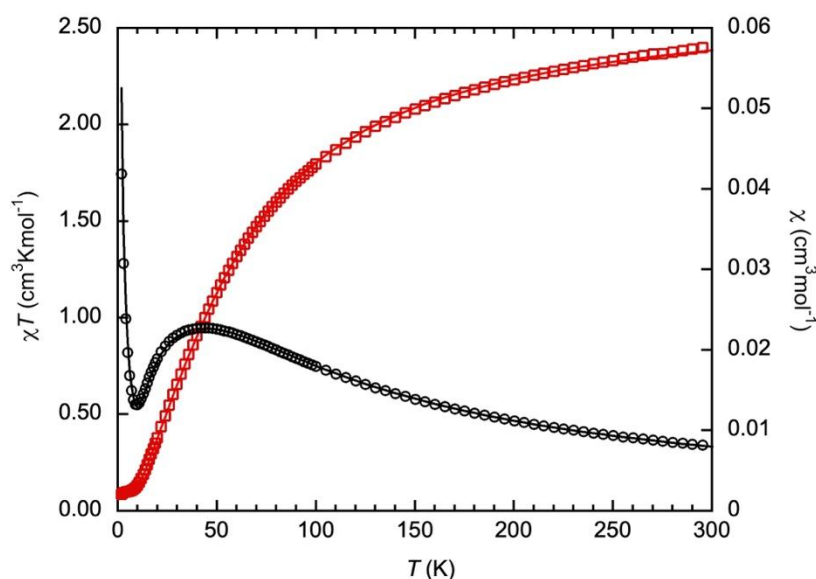


Figure III-5. χT (\square) and χ (\circ) vs. temperature plots and fit (—) for $[\text{Ni}_2(\text{chiral})_2(\mu\text{-ox})]\text{Cl}_2$

Here the ZFS parameters were not introduced in the fit because the relatively large exchange coupling parameter $2J$ that leads to a diamagnetic ground state $S = 0$ with the first excited state $S = 1$ at 34 cm^{-1} . The anisotropy will impact very slightly the shape of the $\chi T = f(T)$ curve. This is a good example of the strong coupling limit where the identity of the qubits is lost.

For $[\text{Ni}_2(\text{chiral})_2(\mu\text{-chloranilate})]$, the shape of the $\chi T = f(T)$ plot (Figure III-6) does not allow to ensure the presence of an exchange coupling between the Ni(II) electrons. The decrease at low temperature may be due only to ZFS that were estimated from theoretical calculations to be around 2.5 cm^{-1} (calculation made on the fragments of the oxalate derivatives, but those of the chloranilate complex are very similar and the ZFS parameters must be in the same range). However, the $\chi = f(T)$ plot has a maximum indicating the presence of an antiferromagnetic exchange coupling. The magnetization data measured at $T = 2, 4$ and 6 K confirm the presence of a weak exchange (Figure III-7). The magnetization (at $T = 2 \text{ K}$) has a "S" shape indicating a diamagnetic ground state and a paramagnetic excited one close in energy as expected for a weak antiferromagnetic coupling of the order of the energy provided by the magnetic field. The simultaneous fit of the data gives the following parameters:

$$2J = -3.54 \text{ cm}^{-1}, |D_1| = |D_2| = 2 \text{ cm}^{-1}, E_1 = E_2 = 0.5 \text{ cm}^{-1}, \text{TIP} = 1.5 \times 10^{-4}, g_1 = g_2 = 2.18$$

It was not necessary to introduce a paramagnetic impurity, which probably indicates that the monomeric complex with a terminal chloranilate is not present at the difference of the case of

the oxalate derivative. The data could be fitted fairly well without introducing the rhombic parameters.

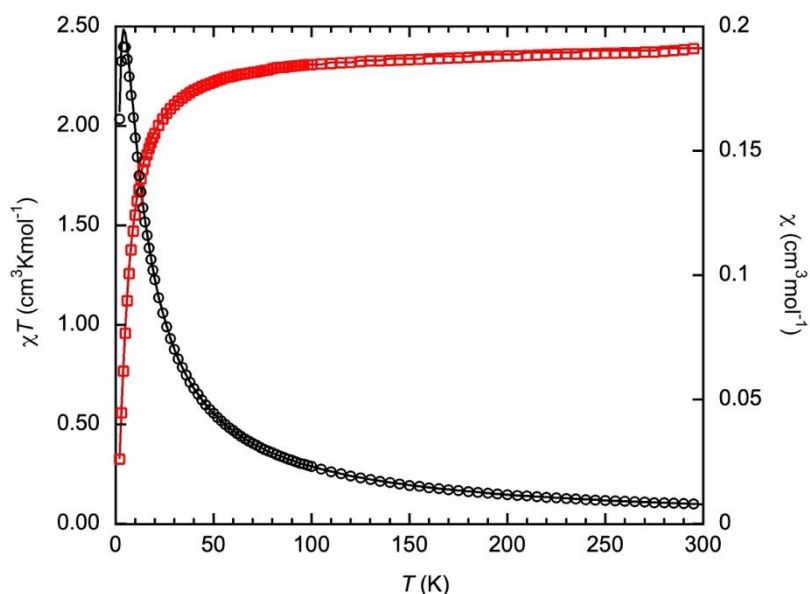


Figure III-6. χT (\square) and χ (\circ) vs. temperature plots and fit (—) for $[\text{Ni}_2(\text{chiral})_2(\mu\text{-chloranilate})](\text{BF}_4)_2$.

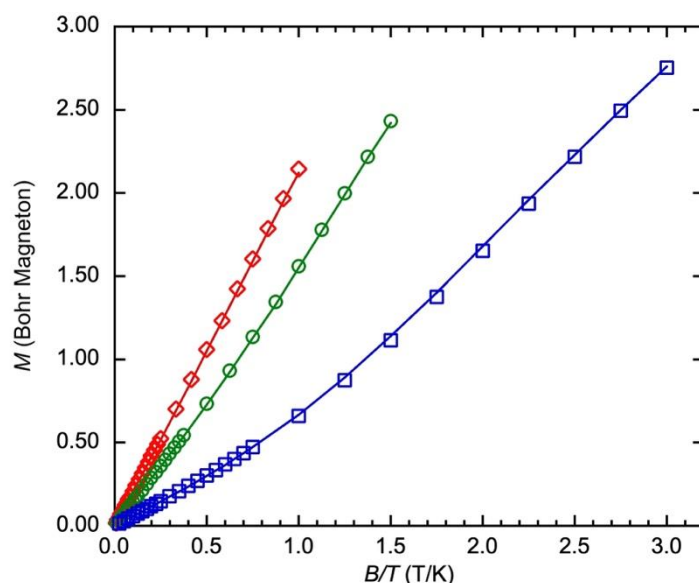


Figure III-7. $M = \cdot(B/T)$ plots at $T = 2 \text{ K}$ (\bullet), 4 K (\circ) and 6 K (\square) and fit (—) for $[\text{Ni}_2(\text{chiral})_2(\mu\text{-chloranilate})](\text{BF}_4)_2$.

The cw X-band EPR spectrum of $[\text{Ni}_2(\text{chiral})_2(\mu\text{-chloranilate})](\text{BF}_4)_2$ shows a large band at 100 mT (Figure III-8). To simulate the spectrum, it is necessary to introduce a coupling term to reproduce its shape. Different simulations have shown that only a weak antiferromagnetic can reproduce fairly well the experimental spectrum. The data were simulated by the following

parameters, similar to those extracted from the magnetic data. Unfortunately, to date the HF-HFEPR spectrum could not be recorded, it will allow to get insight into the origin the observed signal, even though this may be due to the ZFS of the first excited $S = 1$ state that is at 3.4 cm^{-1} above the ground state.

$$D = -3.45 \text{ cm}^{-1}; E = 0.145 \text{ cm}^{-1} \quad 2J = -3.4 \text{ cm}^{-1}; g = 2.1$$

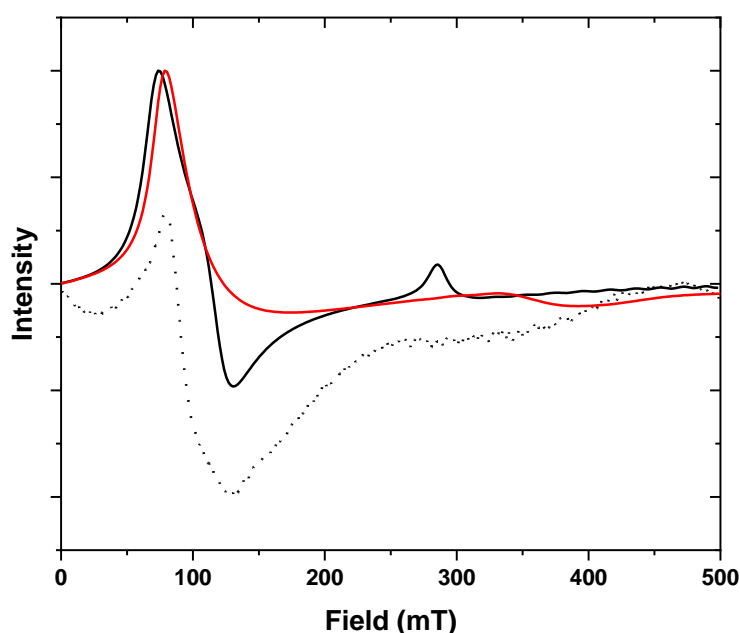


Figure III-8. cw-EPR spectra of $[\text{Ni}_2(\text{chiral})_2(\mu\text{-chloranilate})]$ (black dot) at $T = 90 \text{ K}$ and 9.69 GHz , simulated data with $J = 0 \text{ cm}^{-1}$ (red) and $J = -1.7 \text{ cm}^{-1}$ (black)

From this preliminary measurement we see that even a small increase in the Ni-Ni distance (from 5.38 to 7.86 \AA) leads to a decrease of one order of magnitude of the exchange coupling interaction. It is worth noting that the magnetic dipolar interaction is almost negligible (in comparison to exchange) for these two complexes. Following this trend, for the anthracene bridge where the Ni-Ni distance is equal to 12.70 \AA , we would expect a coupling that is two orders of magnitude weaker, so that $2J$ may become smaller than the rhombic parameter E , and the complex can be described in the weak interaction limit, which is relevant for a quantum logical gate.

It is worth reminding that for qubits, those that present a clock transition (at zero field or at $B \neq 0$) and those that do not have a clock transition, it is necessary to dilute the qubits in a matrix

in order to decrease the effects of decoherence. Molecular systems have a drawback: the presence of large concentration of H atoms that cannot be avoided (deuteration just decrease the effect but does not remove it). The advantage of clock transition molecules is their insensitivity to the spin bath. Such systems can, therefore, be diluted in their own isomorphous solid where Ni(II) is replaced by the diamagnetic metal such as Zn(II), while the same type of dilution of non-clock transition qubits does is not useful because they will still feel the spin bath of the nuclear spins of H atoms.

From the perspective of proposing molecules that play the role of quantum logic gate, it is necessary that they can be diluted avoiding the problem of forming hetero-binuclear complexes, as we explained in the beginning of this chapter. The three complexes presented above are not stable enough to avoid partial substitution of one Ni(II) in the binuclear species. We have therefore tried to develop in parallel the preparation of binuclear complexes using bis-chelating bridges. The efforts made in this direction are presented in the next section.

III.3 CHELATING BRIDGING LIGAND

We opted for a ligand architecture that can be chemically modulated and compatible with a building block approach. The ligand consists of two parts: the chelating part and the bridging part.

The chelating part can be easily modified,[1], [3] and has the advantage of being able to easily graft onto a bridging ligand via condensation. Here, we have chosen a ligand composed of two amines and two pyridines. Experience has taught us that having two pyridine groups may lead to a negative D value because if they coordinate in trans position they lead to an axially compressed octahedral geometry, in most cases. The groups in red (Figure III-9) correspond to the part that can be easily modified, for example pyridine can be replaced by imidazole or phenol.

The bridging part can also be relatively easily modified because it only needs to have an aldehyde function at each of its ends for condensation. It is possible to functionalize the aldehyde beforehand. For practical reasons, the formed imine is systematically reduced to allow one working in aqueous medium.

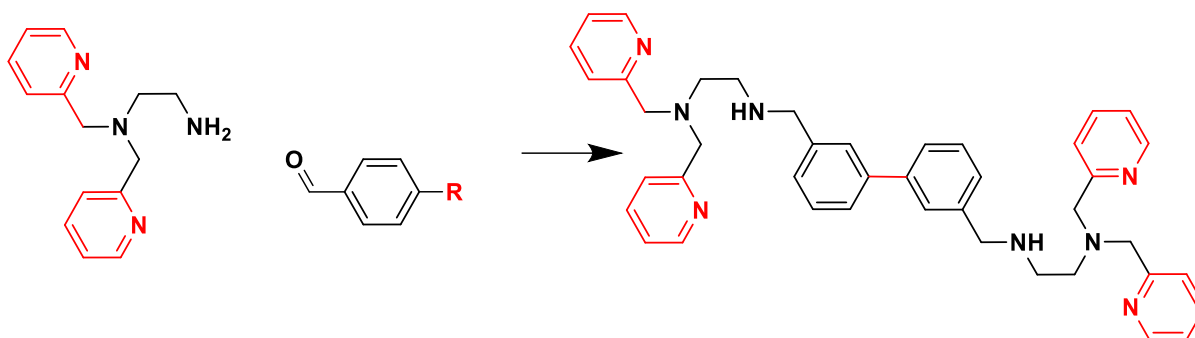


Figure III-9. Schematic representation of target ligand

The building block approach allows the study of the mononuclear complex alone, therefore we can determine its characteristics and decide whether it has the targeted electronic properties (negative D value and the right range for the rhombic parameter) before preparing the binuclear complex.

III.3.a Mononuclear study

The tetradentate ligand has been synthesised according to literature procedure.[4] Different bidentate ligands, (ethylenediamine, dimethylethylenediamine, and tetramethylethylenediamine, bipyridine) were used to complete the coordination sphere and crystals were obtained in all cases, but only one structure was measured due to instrument availability (Table III-4). The structure exhibited disorder in the secondary amine, which is expected to disappear when the compound is attached to the bridging part. Indeed, this should increase the rigidity of the ligand and thus reduce the disorder. From the structure, it is not possible to conclude whether D is positive or negative using the method employed in Chapter I.

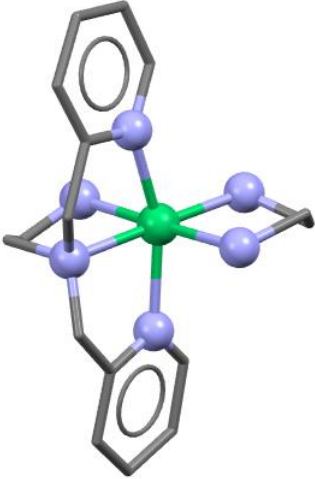
	
Formula	C ₆₆ H ₆₉ B ₂ N ₇ Ni
Space Group	P 1
Cell Lengths	a 10.7862(10) b 14.0895(13) c 18.8243(17)
Cell Angles	α 82.596(4) β 79.820(5) γ 88.777(5)
Cell Volume	2792.25
Z,Z'	Z : 2 Z' : 1
R-factor (%)	4.27

Table III-4. Crystallographic data of $[Ni(\text{tetradente})(\text{en})](NO_3)_2$

The measurement of various compounds using X-band EPR did not yield a spectrum. The compound containing ethylenediamine was also measured using HF-HFEPR, but the signal was too weak to allow for the determination of the ZFS parameters.

III.3.b From mononuclear to binuclear complexes

This work was conducted in collaboration with Dr. Kévin Magra for the synthesis of the organic ligand.

In parallel, trials on dimers were carried out with the following target molecules (Figure III-10). The size of the bridge should allow a coupling $J < E$. In the case of target molecule b the

addition of a hydroxyl group should help rigidify the molecule and thus facilitate the acquisition of crystallographic structures.

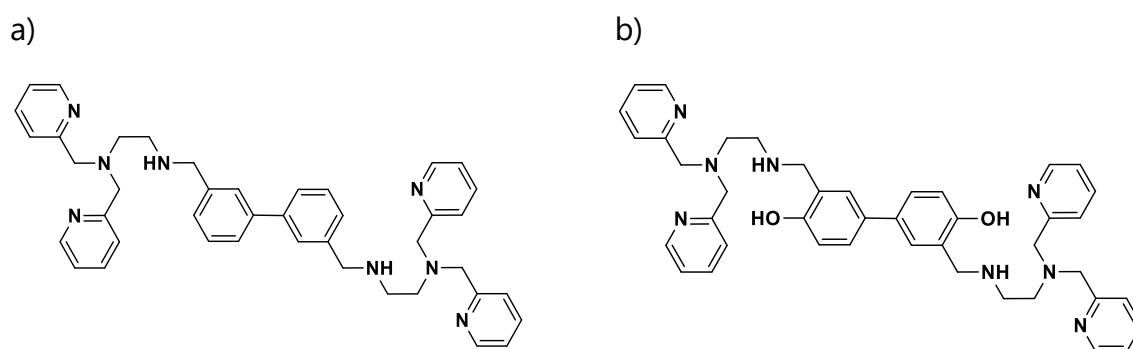


Figure III-10. Target molecules (left) Biphenyl-3,3'bis-tetradente bridge (right) Biphenyl-4,4'-diol-3,3' bis-tetradente. During the synthesis of these ligands, a number of difficulties were encountered, particularly concerning their purity. Indeed, the presence of numerous amines makes purification difficult even on alumina, and it was not possible to recrystallize the ligand. Despite challenging syntheses, three binuclear Ni(II) complexes were obtained (Figure III-11).

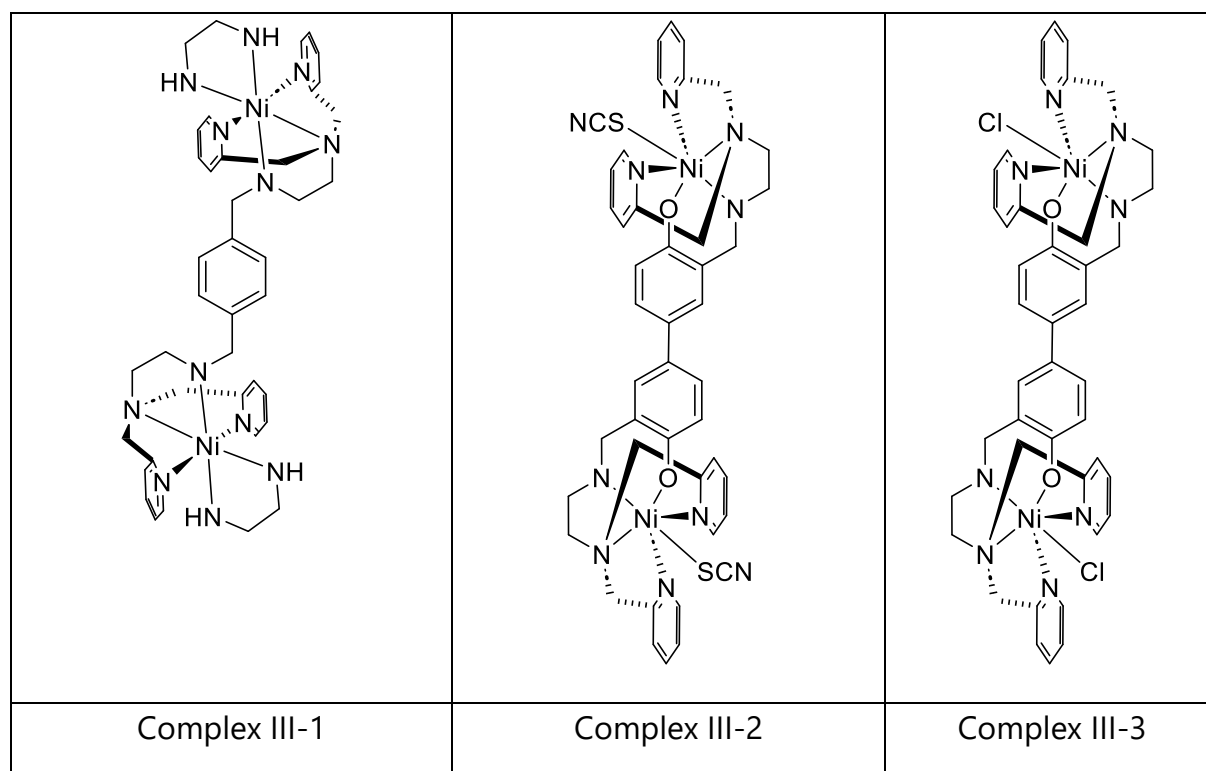
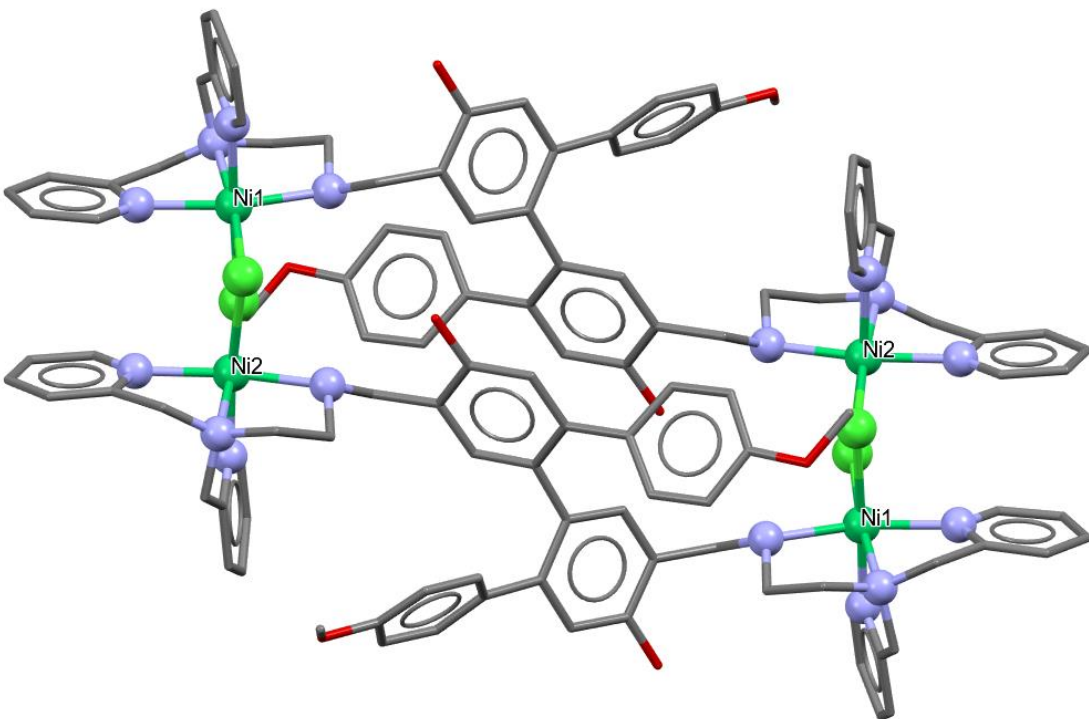


Figure III-11. Binuclear complexes synthesized

The compounds failed to crystallize, so the powders were used directly for cw-EPR measurements. In the case of complex 1, the EPR signal in the X-band was extremely noisy, corresponding to what was observed for the mononuclear model. The other two compounds

exhibited a transition at low magnetic field, but it appeared to be an artefact of the cavity. Unfortunately, as the EPR instrument was malfunctioning, the spectrum could not be verified.

As a part of related project, the bridging ligand has been functionalized with two Ph-OMe group by the Dr. Kévin Magra. Among the different recrystallization tried we finally obtained one single crystal (Table III-5) which does not correspond to the expected product. In fact, instead of a dimer we obtained a tetramer complex, this is due to the presence of Cl atoms that link the nickel between two molecules and the absence of O-Ni bond.



Formula	C ₁₁₆ H ₁₁₂ Cl ₁₂ N ₁₆ Ni ₆ O ₂₄
Space Group	P 2 ₁ /c
Cell Lengths	a 18.754(3) b 20.878(4) c 20.949(4)
Cell Angles	α 90 β 115.275(5) γ 90
Cell Volume	7417.26
Z,Z'	Z : 2 Z' : 0.5
R-factor (%)	16.71

Table III-5. Crystallographic data of the side product.

Chapter III: Synthetic strategies of binuclear complexes as molecular quantum gates

A distance about 1.41 nm between Ni1 and Ni2 have been found. In the case of a dimer we can expected a smaller distance because Ni should be linked to the O of the biphenyl leading to a "cis" like configuration. The distance between Ni centers is supposed to be in the good range to fulfil the criteria $J < E$.

III.4 CONCLUSION

The attempts to prepare mononuclear and then binuclear compounds using a building block approach, several conclusions have been drawn. This approach is potentially interesting to easily modulate the coordination sphere or to increase the solubility of the compounds. It is essential that the bridging ligand is chelating to ensure its stability in the case of dilution.

In the case of nickel specifically, as established in Chapter I, controlling the value of E is challenging due to its sensitivity to chemical environment and packing. This means that there is no guarantee that the value of E remains the same for the binuclear as for the mononuclear complex. Therefore, it would be necessary to directly modulate the value of E in the dimer. Given the difficulty in obtaining single crystals, the project becomes extremely difficult to proceed with. If it is also necessary to obtain non-symmetric molecules, the project becomes almost impossible to achieve without the access to broad band EPR spectroscopy. As seen in Chapter II, even in the presence of a clock transition, relaxation times are short. This implies that measurements using pulsed EPR will also be very challenging, without accessing an apparatus with high sensitivity and succeeding a clean dilution of the complexes.

It has been concluded that there are too many constraints and parameters to be mastered all at once. Therefore, the decision was made to shift the focus to spin $S = 1/2$ systems, which necessarily exhibit a signal in EPR and are known to have longer relaxation times. We can thus study these compounds to understand how coupling works. Once this is mastered, we can return to nickel compounds.

III.5 EXPERIMENTAL PART

All the reagents used for these syntheses were purchased commercially and were used directly without further purification unless exceptionally stated

IR spectra were recorded on a Bruker TENSOR - 27 FT - IR spectrometer equipped with an attenuated total reflectance (ATR) sample holder in the 4000 - 250 cm^{-1} range. NMR spectra were recorded on a Bruker Aspect 300 NMR spectrometer. X-ray diffraction data were collected by using a Bruker Kappa VENTURE PHOTON 100 diffractometer with graphite-monochromatic Mo $K\alpha$ radiation ($\lambda = 0.71073 \text{ \AA}$). Magnetic data were collected using a Quantum Design MPMS XL7 SQUID magnetometer.

[Ni₂(chiral)₂(μ -ox)]

(Ni(Cl₂) (129mg, 1mmol) was added to a yellow solution of (R,R)-1,2-diaminocyclohexane (296mg, 1mmol) in MeOH(20mL). Then potassium oxalate (92mg, 0.5mmol) was added. After 2h of stirring, the solution turns purple. The solvent was removed by rotary evaporation. Crystal was obtained with hot recrystallization in CAN

[Ni₂(chiral)₂(μ -chloranilate)]

Ni(Cl₂) (129mg, 1mmol) was added to a yellow solution of (R,R)-1,2-diaminocyclohexane (296mg, 1mmol) in MeOH(20mL). Then chloranilic acid (104mg, 0.5mmol) was added. After 2h of stirring, the solution turns purple. The solvent was removed by rotary evaporation. Crystal was obtained with Et₂O diffusion in MeOH.

[Ni₂(TPA)₂(μ -anthracene)]

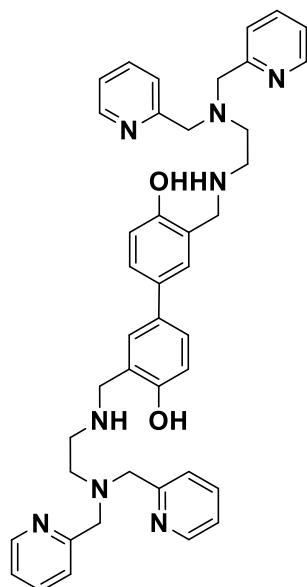
In a methanolic solution (50mL) of Ni(BF₄)₂ · 4H₂O (340mg, 1mmol) and TPA (290mg, 1mmol) was added anthracene (150mg, 0.5mmol) in 20mL of MeOH. The solution turns dark green after 2h of stirring. One crystal was obtained after one month of slow evaporation of MeOH.

[Ni(tetradente)(en)](NO₃)₂

In a round flask, N,N-(2-pyridylmethyl)ethylenediamine (1eq) and Ni(NO₃)₂ (1eq) in MeOH was stirred at RT during 1h. Then NaBPh₄ (5eq) was added to the pink solution. The solid form

was filtered washed with H₂O and MeOH. The product was dissolved in ACN and crystal was obtained with slow diffusion of Et₂O.

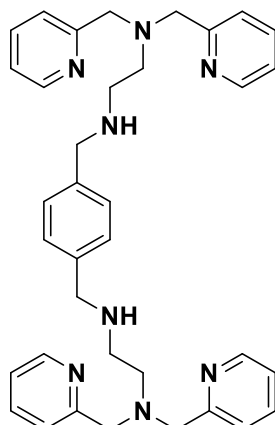
Biphenyl-4,4'-diol-3,3' bis-tetradente



In a round flask, 4,4'-Dihydroxy[1,1'-biphenyl]-3,3'-dicarboxaldehyde (1eq) and N,N-(2-pyridylmethyl)ethylenediamine (2.2 eq) were solubilized in a mixture of EtOH/DCM (3/2) and stirred 1h at 35°C. Then, NaBH₄ (6.6 eq) was added and stirred overnight at rt. Solvent was evaporated and the residue was solubilized in water and the product is extracted with DCM. Organic layer was dried with Na₂SO₄ and evaporated under reduced pressure.

NMR (CD₃Cl, 300 Hz, 1H) : 8.53 (ddd, *J* = 4.90, 1.88, 0.94 Hz, 2H), 7.66 (td, *J* = 7.92, 1.88 Hz, 2H), 7.43 (dt, *J* = 7.72, 0.94 Hz, 2H), 7.30 (dd, *J* = 8.29, 2.64 Hz, 1H), 7.18 (ddd, *J* = 7.55, 5.09, 1.32 Hz, 2H), 7.04 (dd, *J* = 2.26 Hz, 1H), 6.84 (d, *J* = 8.48 Hz, 1H), 3.86 (s, 4H), 3.83 (s, 2H), 2.79 – 2.70 (m, 4H).

Biphenyl-3,3'bis-tetradente

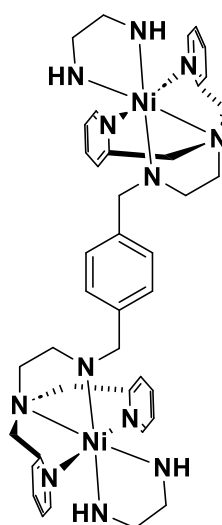


In a round flask, 1,4-Benzenedicarboxaldehyde (1eq) and N,N-(2-pyridylmethyl)ethylenediamine (2.2 eq) were solubilized in a mixture of EtOH/DCM (3/2) and stirred 1h at 35°C. Then, NaBH₄ (6.6 eq) was added and stirred overnight at rt. Solvent was evaporated and the residue was solubilized in water and the product is extracted with DCM. Organic layer was dried with Na₂SO₄ and evaporated under reduced pressure.

NMR (CD₃Cl, 300 Hz, 1H) : 8.51 (ddd, *J* = 4.91, 1.88, 0.75 Hz, 2H), 7.63 (td, *J* = 7.72, 1.88 Hz, 2H), 7.45 (d, *J* = 7.72Hz, 2H), 7.14 (ddd, *J* = 7.54, 5.09, 1.32 Hz, 2H), 3.84 (s, 4H), 3.66 (s, 2H), 2.79 – 2.75 (m, 4H).

Complex III-1

2NO₃⁻

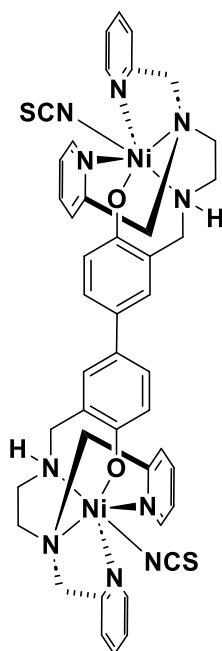


Chapter III: Synthetic strategies of binuclear complexes as molecular quantum gates

In a round flask, N1,N1'-(1,4-phenylenebis(methylene))bis(N2,N2-bis(pyridin-2-ylmethyl)ethane-1,2-diamine) (1eq) was dissolved in MeOH. Then a solution of Ni(NO₃)₂ (2.1eq) in MeOH was added and stirred at rt during 1h. Ethylenediamine (2.1 eq) was added to the purple solution. The solution was poured into Et₂O solution and the resulting powder was filtered and dried.

IR (cm⁻¹): 2940; 2884; 2399; 1607; 1784; 1487; 1434; 1383; 1049; 827; 766

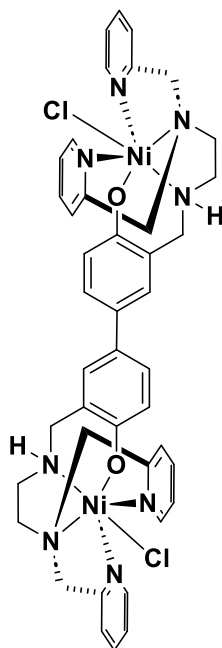
Complex III-2



In a round flask, ligand (1eq) was dissolved in MeOH. Then a solution of Ni(Cl₂) (2.2eq) in MeOH was added and stirred at rt. Then KSCN (2.2eq) was added. Et₂O was added to precipitate. Solvent was removed and Et₂O was added again 2 times. The resulting solid was filtered and dried. (m/z: 404.123)

IR (cm⁻¹): 3335; 2089; 1607; 1570; 1482; 1441; 1290; 1156; 1023; 985; 826; 766

Complex III-3



In a round flask, ligand (1eq) was dissolved in MeOH. Then a solution of Ni(Cl₂) (2.2eq) in MeOH was added and stirred at rt. Then Et₂O was added to precipitate. Solvent was removed and Et₂O was added again 2 times. The resulting solid was filtered and dried.(m/z: 404.142)

IR (cm⁻¹): 3335; 1607; 1570; 1482; 1441; 1290; 1156; 1023; 985; 826; 766

III.6 REFERENCES

- [1] N. C. Lim, C. B. Ewart, M. L. Bowen, C. L. Ferreira, C. A. Barta, M. J. Adam, C. Orvig, *Inorg. Chem.* **2008**, *47*, 1337–1345.
- [2] D. Wang, W. Hu, B. J. Reinhart, X. Zhang, J. Huang, *ACS Appl. Mater. Interfaces* **2022**, *14*, 42171–42177.
- [3] D. Utz, S. Kisslinger, F. Hampel, S. Schindler, *Journal of Inorganic Biochemistry* **2008**, *102*, 1236–1245.
- [4] A. J. Surman, C. S. Bonnet, M. P. Lowe, G. D. Kenny, J. D. Bell, É. Tóth, R. Vilar, *Chemistry – A European Journal* **2011**, *17*, 223–230.

CHAPTER IV: QUANTUM COHERENCE OF MONO- AND BINUCLEAR COMPLEXES BASED ON
THE SALOPHEN LIGAND

**CHAPTER IV: QUANTUM COHERENCE OF
MONO- AND BINUCLEAR COMPLEXES BASED ON
THE SALOPHEN LIGAND**

IV.1 INTRODUCTION

In the preceding chapter, several criteria or key points concerning the synthetic strategy required to obtain binuclear complexes suitable for serving as a quantum logic gate were exposed. The analysis of these criteria led to the conclusion that it would be interesting to explore spin $\frac{1}{2}$ systems that are known to have long relaxation times ($T_2 > 1 \mu\text{s}$ and $T_1 > 10 \mu\text{s}$ even at 20 K).[1], [2], [3] We will focus on a Cu(II) complex as the model system.

The EPR spectra of Ni(II) ($S = 1$) complexes is dominated by the ZFS parameters that are highly dependent on the chemical nature of the coordinating ligands and on small changes in geometry of the coordination sphere, as we have shown in the previous chapters. The EPR spectra of spin $\frac{1}{2}$ species is due to a transition determined by the g -factor (no ZFS for $s = \frac{1}{2}$ species) so that, for a given geometry, the transitions are not as much affected as those of $S = 1$ species by the metal chemical environment. This translates in rather longer relaxation times in comparison to Ni(II), which make such systems appealing for further studies that are much easier to perform, because of good signal/noise ratio.

Jeschke and coworkers studied the coupling between the spins of two Cu(II) and found a rather good correlation between the experimental and the theoretical distance based on magnetic dipolar interaction.[5] As stated in the previous chapter, a weak coupling is necessary to keep the individuality of each qubit and to be able to measure it by EPR. A coupling that ranges between few and a maximum of 10 MHz can be detected by a DEER experiment, which corresponds to a separation in the range of 1.5 to 2 nm between the $s = \frac{1}{2}$ species. This separation depends on the relative orientation of the component of the g -tensor with respect to the internuclear vector. (see below for details)

Subsequently, the selection of a ligand has been made. It was decided to employ a bis-chelating bridging ligand similar to those presented in the previous chapter, but without the need of terminal ligands to complete the coordination sphere of Cu(II), therefore avoiding any substitution in the metal coordination sphere with solvent molecules, for example. Additionally, the ligand should be easily cleavable to enable the study of the associated mononuclear complex, or complexes if the binuclear one is made of two different mononuclear species. Thus, a salophen-based ligand was chosen (Figure IV-1). Such ligands are known for their exceptional

CHAPTER IV: QUANTUM COHERENCE OF MONO- AND BINUCLEAR COMPLEXES BASED ON THE SALOPHEN LIGAND

stability, thereby minimizing the risk of metal loss during various synthesis/dilution steps. Furthermore, the square planar geometry ensures that the Ni(II) derivative is diamagnetic, allowing for solid-state dilution and NMR characterizations.

The ligand is modular and suitable to a building block approach with the possibility of tuning the distance between the metal ions and of adding adequate chemical functions to modulate its properties. For instance, the tert-butyl groups were introduced to enhance the compound's solubility. The selection of tert-butyl groups (in green in Figure IV-1) is also justified by the fact that, at temperatures below 70 K, their free rotation motion should not significantly impact the molecules' relaxation times.[6]

One of the objectives is to use the coupling between the spins of the metal ions to achieve quantum gate operations such as the CNOT or control phase. Practically, for some devices the microwave energy available for such operation is in the MHz energy region ($1\text{MHz} = 3.33 \times 10^{-5} \text{cm}^{-1}$). Therefore, the coupling energy must be in the same range. Generally, for such small energies the pertinent coupling is not exchange anymore but the dipolar one. Dipolar interactions can be easily estimated because they depend on the magnetic moments value, their distance r (as $1/r^3$) and their relative orientations. For example, the magnetic dipolar energy between two magnetic moment of spin $1/2$ at $r = 1 \text{ nm}$ with their z components parallel ($\theta = 0$) to each other and perpendicular to \vec{r} is equal to 13 MHz. In such a case the dipolar energy depends on $\cos(\theta)$. While if the z -components of the magnetic moments are aligned with \vec{r} , the dipolar energy is equal to 26 MHz. Therefore, the length of the bridge (Figure IV-1) we aim to achieve for a dipolar coupling (J_D) less than 10 MHz is in the range 1.5 to 2 nm, so that it can be detected by Pulsed Electron-Electron Double Resonance (PELDOR or DEER) sequence and be used to demonstrate a gate operation.

CHAPTER IV: QUANTUM COHERENCE OF MONO- AND BINUCLEAR COMPLEXES BASED ON THE SALOPHEN LIGAND

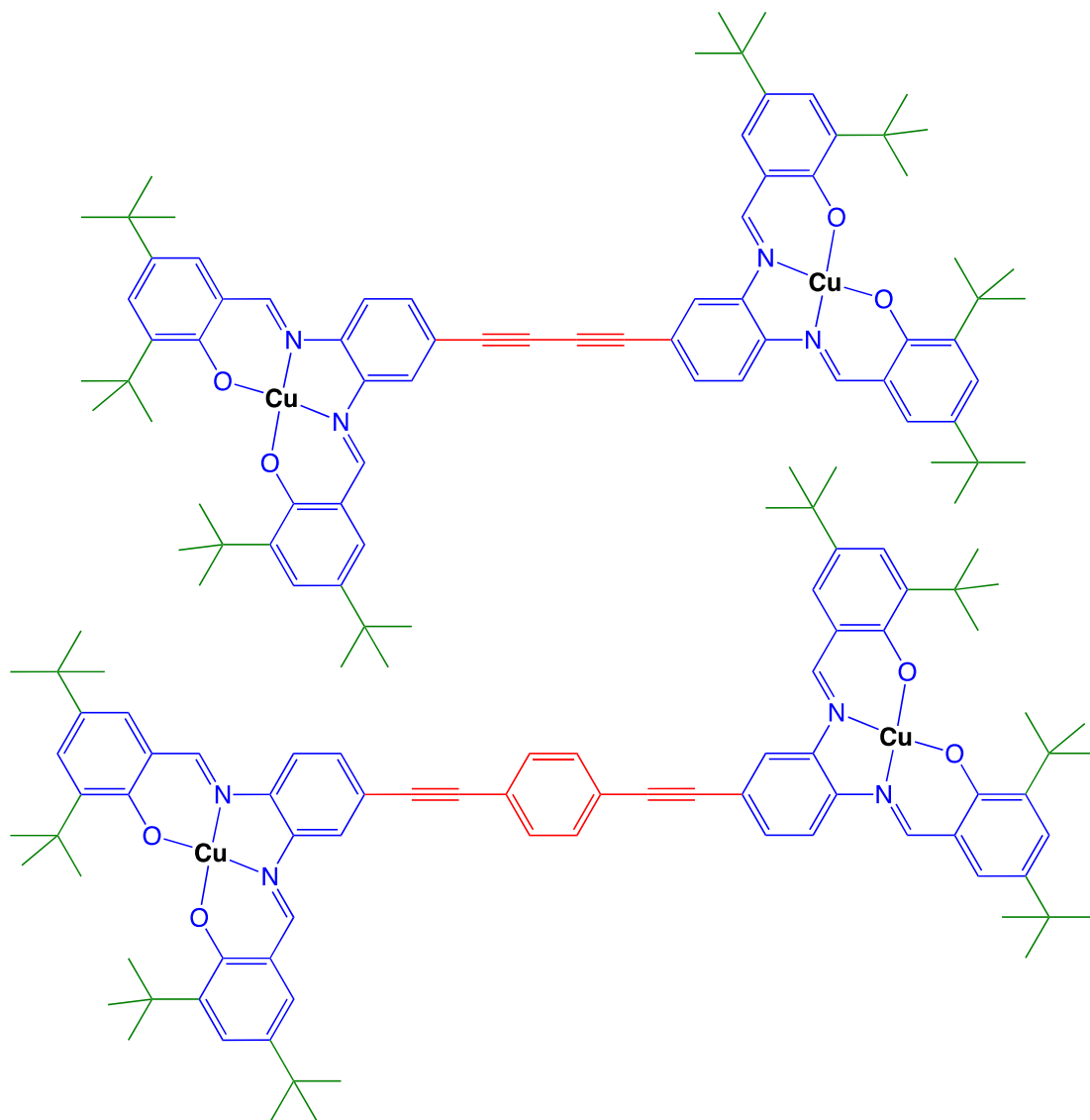


Figure IV-1. Target molecules with the different blocks that can be modulated. Red is the bridging block, blue is the chelating block, black is the metal and green is the functionalisation of the salophen to increase the solubility of the molecule. The magnetic dipolar interaction is computed to be equal to 4.3 MHz for the top molecule ($d_{\text{Cu-Cu}} = 1.63$ nm) and to 1.9 MHz for the bottom molecule ($d_{\text{Cu-Cu}} = 1.90$ nm), assuming the molecules are flat so that the z components of the g factors are perpendicular to the molecular plane.

Another important criterion is the rigidity of the backbone around the metal ions and for the whole binuclear complex in order to minimize distribution of coordination geometry and high density of soft vibration modes that may participate to the relaxation processes. The rigidity of the coordination sphere is ensured by the conjugated π system of the salophen ligand. The bridge is also expected to be rigid, even though one may worry about possible rotation about the single carbon-carbon bonds of the bridge (red part in Figure IV-1), that may give a distribution of molecules with different orientations of the planes of the two Cu(salophen) units. We think that this is not likely to occur because the overlap between the π orbitals within the red part and between the red and the blue parts of the molecule are maximum when the

CHAPTER IV: QUANTUM COHERENCE OF MONO- AND BINUCLEAR COMPLEXES BASED ON THE SALOPHEN LIGAND

molecule is flat ensuring a maximum thermodynamic stability for the flat configuration. However, one must consider this possible "problem". The criterion of addressability will be further developed later.

In this chapter, we will first study the mononuclear [Cu(salophen)] complex, which will then serve as a reference. Subsequently, we will compare its relaxation times with those of another spin $S = \frac{1}{2}$ system, the one where Cu(II) is replaced by vanadyl (V(IV)O). Ultimately, we will study a Cu(II) binuclear complex.

Before presenting the results, we will briefly present the two techniques we used ENDOR and PELDOR (or DEER). More detailed explanation can be found elsewhere.[7], [8], [9]

IV.1. ADVANCED PULSED EPR METHOD:

IV.1.a. ENDOR

In Electron Nuclear Double Resonance (ENDOR) studies employing pulsed EPR, we aim to understand the interplay between electronic and nuclear spins.

The sequence (Figure IV-2) can be understood as follows: in this absence of perturbation, we can follow the echo decay of the purple spin. This corresponds to the reference.

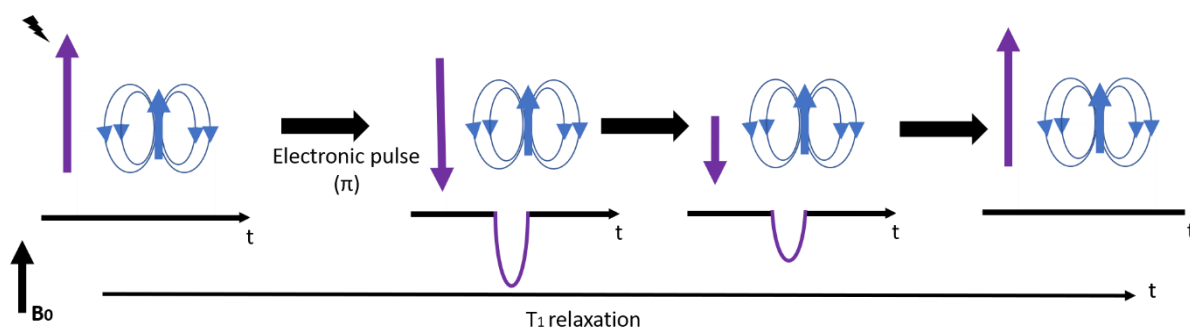


Figure IV-2. Description of the ENDOR principle in absence of RF pulse. In this case the sequence corresponds to an inversion recovery and we only observe the relaxation of the electronic spin (purple). Here the nuclear spin (blue) is assumed not to have an effect.

Now we will introduce some perturbation in the system after the first electronic pulse. Basically, we applied a radiofrequency (RF) pulse on the nuclear spin (Figure IV-3), this leads to a modification of the magnetic environment of the electronic spin thus the energy transition changes. This is why at fixed frequency; the intensity of the electronic echo decreases when we applied a RF pulse. Then we measure the time necessary for fully restoring the initial electronic echo intensity. This time is directly proportional to T_{2N} or T_{1N} depending of the type of RF pulse applied. In other words, we introduce a perturbation in our system and see how the probe responds to this perturbation.

CHAPTER IV: QUANTUM COHERENCE OF MONO- AND BINUCLEAR COMPLEXES BASED ON THE SALOPHEN LIGAND

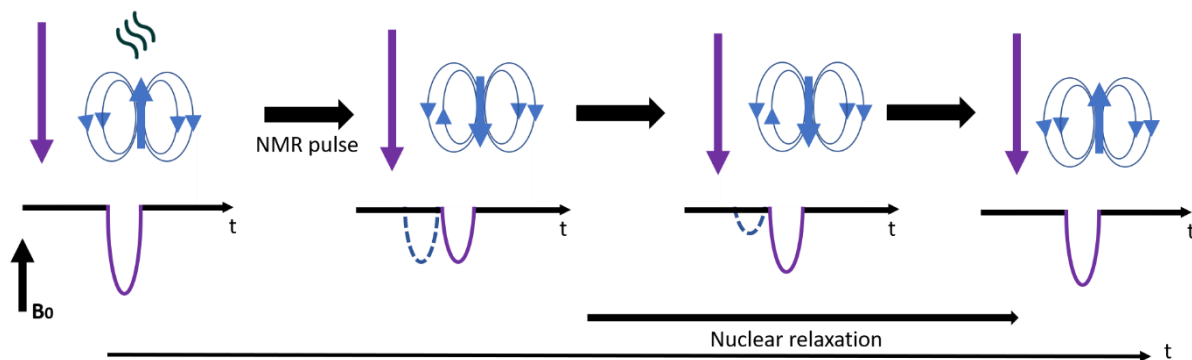


Figure IV-3. Description of the ENDOR principle in presence of RF pulse. Blue arrow corresponds to nuclear spin, and purple arrow correspond to electronic spin

Experimentally, in this technique, we first apply a π pulse on the electronic spins, representing the available experiment time, to induce a magnetic field perturbation. Subsequently, we applied RF pulses to the nuclear spins to measure their T_{1N} or T_{2N} relaxation times. Then the fluctuation of the nuclear spin will be felt by the electronic spin during the mixing state. Finally, the electronic echo provides us all the information on the lifetime of the nuclear spin (Figure IV-4).

In summary, we utilize the fluctuation of an electronic spin to address a nuclear spin, and then exploit the electronic spin to observe the behaviour of the same nuclear spin.

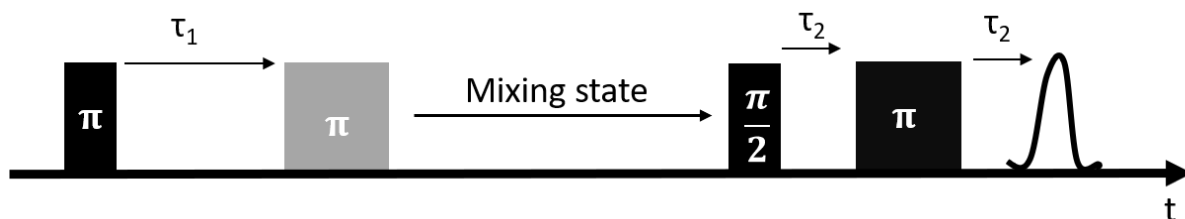


Figure IV-4. ENDOR sequence. In black electronic pulse, in grey RF pulse. In the following chapter $\tau_1 = 2 \mu\text{s}$, $\tau_2 = 0.24 \text{ ns}$.

ENDOR provides access to the superhyperfine coupling between the electronic and the nuclear spins of other atoms than those bearing the electronic spin. The energy of the different $m_S m_I$ states are given by:

$$E_i = \gamma_e B m_S - \gamma_N B m_I + m_S m_I A_i \quad (\text{V-1})$$

where B is the applied magnetic field, γ_e and γ_N the electronic and nuclear gyromagnetic ratio,

CHAPTER IV: QUANTUM COHERENCE OF MONO- AND BINUCLEAR COMPLEXES BASED ON THE SALOPHEN LIGAND

respectively and A_i is the superhyperfine coupling constant between the electronic and the nuclear spin of the considered atom.

Two types of spectra can be observed depending on the relative magnitudes of $|A_i|$ and the gyromagnetic ratio ($|\gamma_i|$) of the atom. The gyromagnetic ratio is an intrinsic property of the atom, while A_i depends on the distance and the nature of the coupling between the electronic and the nuclear spin (the sign of A_i and of γ_i cannot be distinguished from the shape of the experimental spectra).

In the case where $|\gamma_i B| \ll |A_i/2|$, we are in the strong coupling limit. The nuclear Zeeman effect can be considered as a perturbation compared to the superhyperfine interaction. The resulting lift of degeneracy is given Figure IV-5a, where ω_{34} and ω_{12} are the NMR transitions in the radiofrequency range. In this case, the spectrum is centred at $|\gamma_i B|$ and the energy difference between the two bands gives the value of $|A_i|$ (Figure IV-5b).

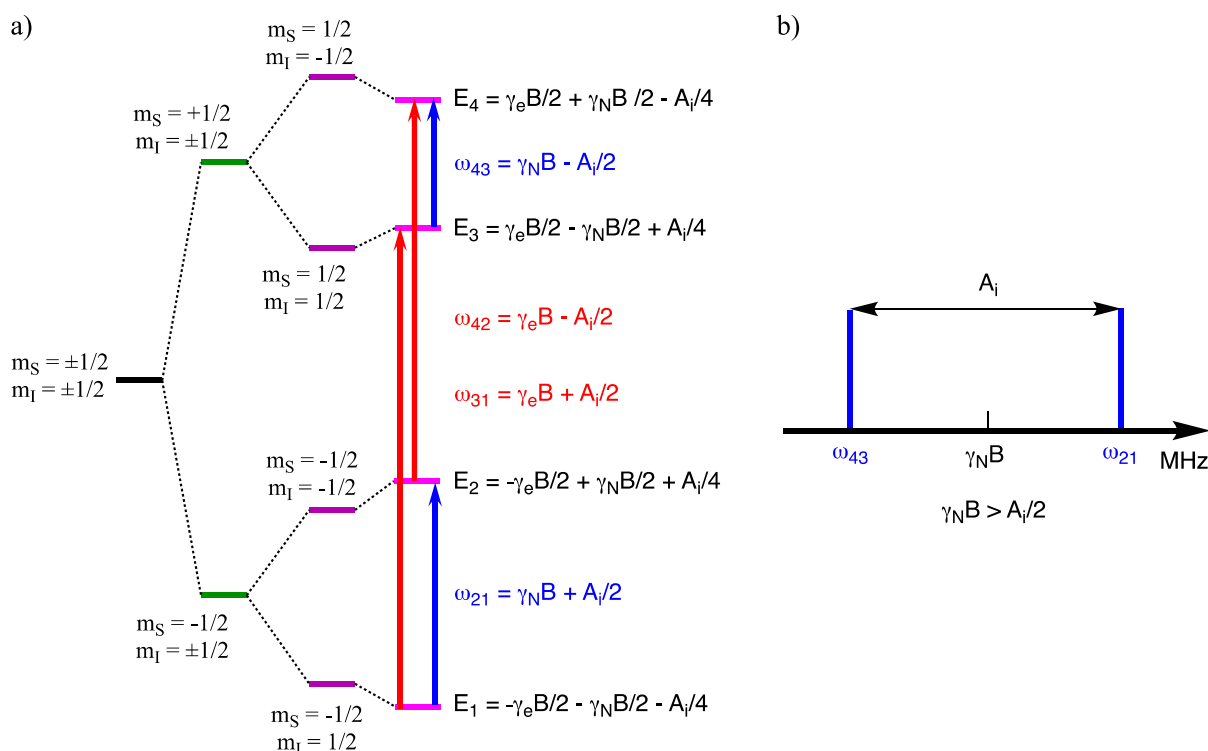


Figure IV-5.a) Lift of degeneracy of the $m_S m_I$ states in the case where, $|\gamma_i B| \gg |A_i/2|$ for $S = 1/2$ and $I = 1/2$, the EPR and the NMR transitions are given by the red and blue arrows, respectively, b) a representation of the ENDOR spectrum.

When $|\gamma_i B| \gg |A_i/2|$, we are in the weak coupling limit. The nuclear Zeeman interaction can be considered as a perturbation compared to the superhyperfine coupling. The resulting lift of degeneracy is given Figure IV-6a, where we considered the case of $S = 1/2$ and $I = 1$ (for ^{14}N , for

example)

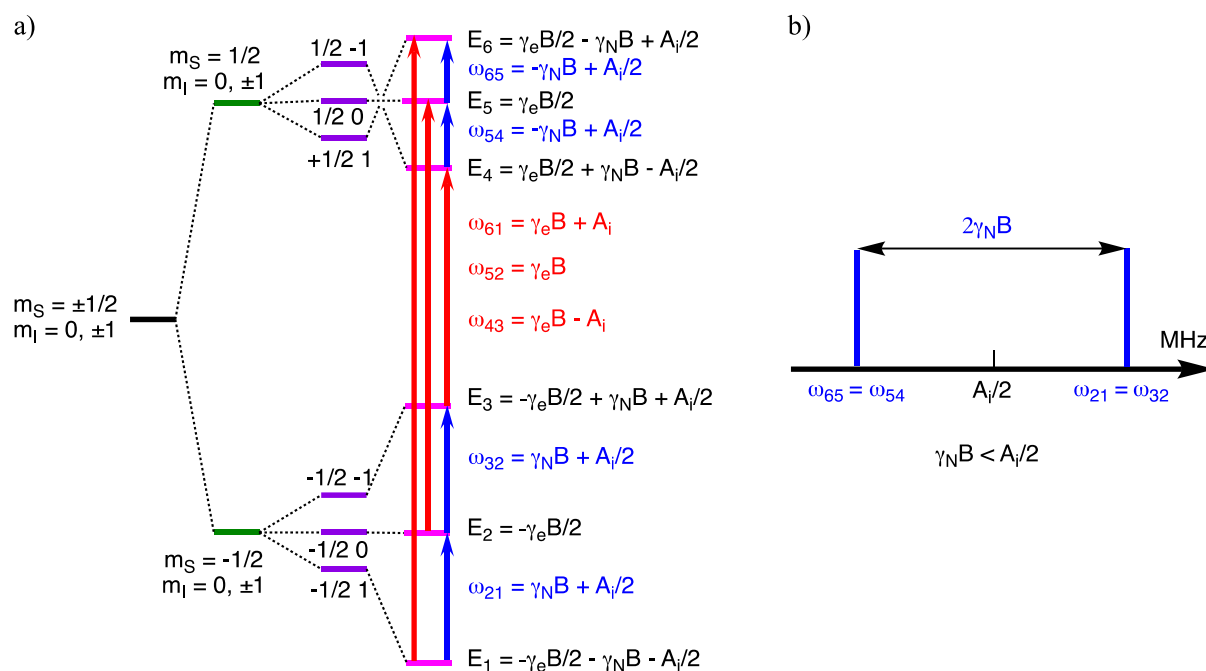


Figure IV-6. a) Lift of degeneracy of the $m_S m_I$ states in the case where, $|\gamma_e B| \ll |A_i|/2$ for $S = 1/2$ and $I = 1$, the EPR and the NMR transitions are given by the red and blue arrows, respectively, b) a representation of the ENDOR spectrum.

For this case, the ENDOR spectrum is centred at $|A_i|/2$ and the energy difference between the bands corresponds to twice the Larmor frequency of the nuclear spin of the atom considered.

IV.1.b DEER

The concept behind the Double Electronic Resonance (DEER) sequence is exactly the same as for the ENDOR experiment. Here instead of perturbing the nuclear spin, we perturb another electronic spin in the system (using a different frequency). Initially we have two electronic spins aligned with the applied magnetic field (B_0). The purple spin possesses a resonance frequency ($\nu = \gamma B_0$). The application of a pulse on the second electronic spin (green in Figure IV-7) which possesses a different resonance frequency results in a modification of the magnetic field felt by the purple spin whose resonance frequency becomes ν' ($= \gamma B_0'$). The coupling between the two electronic spins is given by $\nu' - \nu = \gamma (B_0' - B_0)$.

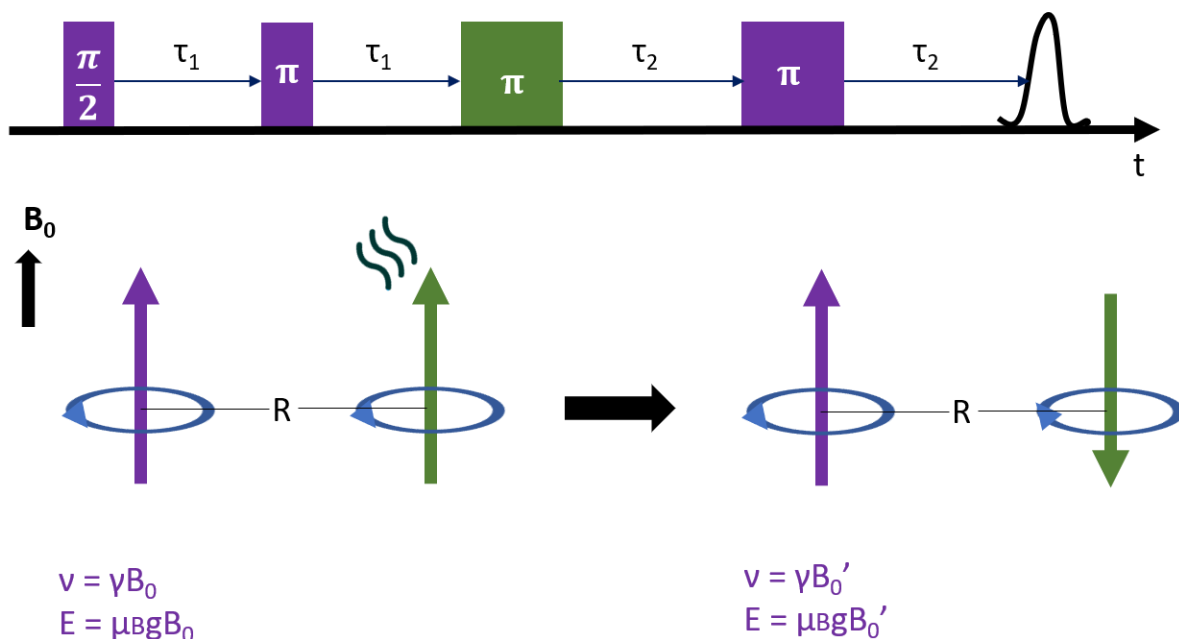


Figure IV-7. Principle of DEER sequence. Purple pulses correspond to the one at the purple spin frequency and the green pulse correspond to the one at the green spin frequency. R corresponds to a spacer.

In the following section we will assume that the two nearest electronic spins are the one belonging to the same molecule i.e. the stronger coupling observed will correspond to the one between the two electronic spins of the same molecule, while coupling between spins belonging to two different molecules is negligible. This, of course, assumes to prepare the sample with right dilution, particularly if the distance between the spins belonging to the same molecule is in the 2 nm range.

From an experimental point of view, the longest T_2 value gives the smallest coupling that it is possible to observe ($J < 1/T_2$) between the two spins which correspond to one modulation (Figure IV-8-a). In order to increase the determination accuracy of the coupling it is better to work with a stronger coupling in order to observe more modulations (Figure IV-8 b). The modulation could be observed only if the second spin have relaxed during the time of the experiment. This is why it is preferable to have one spin with short coherence time and one with a long coherence time.

In practice, a T_2 curve (after a Hahn echo sequence) is recorded for the spin possessing the longest coherence time and on this curve the modulation due to the relaxation of the spins in the vicinity are observed. The modulation occurs at a time $t = 1/J$ where J describes the strength of the coupling between the two spins. In the ideal case, we only observe one coupling thus

CHAPTER IV: QUANTUM COHERENCE OF MONO- AND BINUCLEAR COMPLEXES BASED ON THE SALOPHEN LIGAND

one or two modulations are enough to determine J (Figure IV-8 a/b).

In a non-ideal case, several couplings are observed in the same time because the observed spins could have different environments, and therefore different coupling values. The distribution could arise from a distribution of distances or a distribution of angle between the anisotropic tensors of the two spins. Each contribution results in a modulation at its own frequency, so a distribution of contributions leads to a multitude of modulations that end up overlapping. It is still possible to separate each of these contributions using advanced mathematical models, but this requires the observation of several modulations. In Figure IV-8-c we have added four additional couplings to the precedent coupling. We can see that the determination of the value of the precedent coupling is not simple, but with a longer T_2 one can observe more modulation and thus discriminate more easily the different coupling values (Figure IV-8-d).

CHAPTER IV: QUANTUM COHERENCE OF MONO- AND BINUCLEAR COMPLEXES BASED ON THE SALOPHEN LIGAND

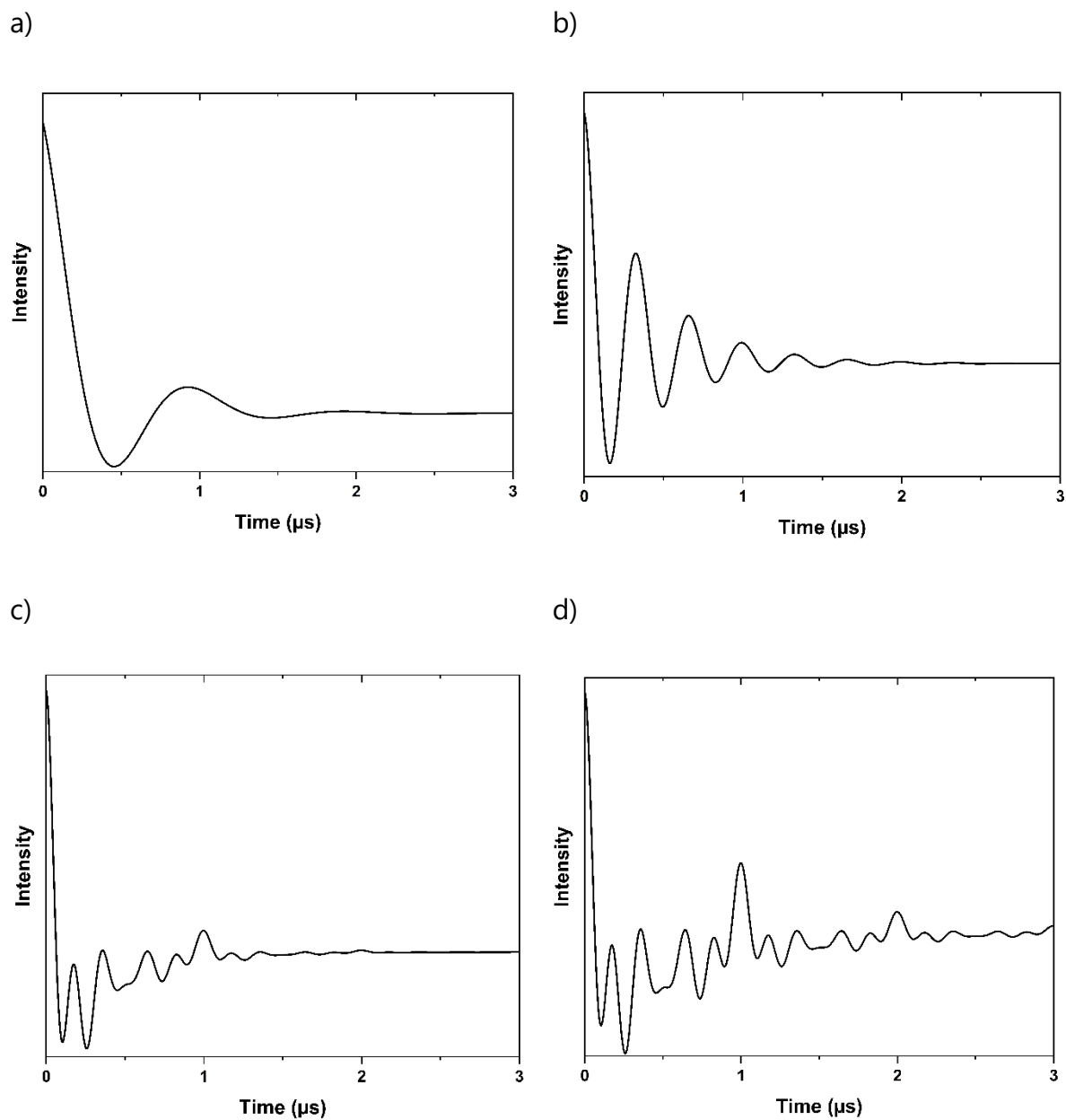


Figure IV-8. Examples of DEER curves. a) DEER curve with coherence time of $T_2 = 2.5 \mu\text{s}$ and $J = 1 \text{ MHz}$. b) DEER curve with coherence time of $T_2 = 2.5 \mu\text{s}$ and $J = 3 \text{ MHz}$. c) DEER curve with coherence time of $T_2 = 2.5 \mu\text{s}$ and $J_1 = 3 \text{ MHz}$, $J_2 = 4 \text{ MHz}$, $J_3 = 2 \text{ MHz}$, $J_4 = 6 \text{ MHz}$ and $J_5 = 5 \text{ MHz}$. d) DEER curve with the same value of J but with $T_2 = 5 \mu\text{s}$.

IV.2. [Cu(SALOPHEN)]

The key parameter to create an efficient quantum logical gate is the coupling strength between the spins, denoted as J . This coupling must be relatively weak to be detectable using the Double Electron-Electron Resonance (DEER) sequence, thereby demonstrating quantum entanglement. The coupling between the two paramagnetic centers can only be observed if $J < 1/T_2$ where T_2 represents the longer coherence time. Therefore, initially, before measuring any coupling, it is essential to determine which paramagnetic centre has the longer relaxation time. Subsequently, the addressability of each qubit must be verified, meaning that each qubit can be excited independently. In this scheme, the two magnetic centers must have resonance at different frequencies for a given applied magnetic field. If the qubits have different g values this condition is fulfilled. If the metals used are different, this condition is easy to fulfil. If the metals used are the same the discrimination is still possible if they have different coordination sphere. If the metals have also the same coordination sphere, g will be the same, thus their anisotropy tensor must have different orientation compared to the magnetic field.

As we stated above, the relaxation times and the g -values for two identical metal centers with the same environment will probably not be different enough to have different relaxation times and different qubit frequency. If one wants to rely on the orientation of the anisotropy tensor with respect to the magnetic field, a single crystal must be measured. The best strategy is to prepare a heterobinuclear complex, with two different metal ions such as Cu(II) and V(IV)O that will have different g -values and may be sufficiently different relaxation times for a given orientation of the magnetic field with respect to their g tensors. Therefore, it is necessary to have a device able to independently address each qubit at its own frequency. The modular synthetic strategy presented below allows preparing both possibilities: (i) heterobinuclear complexes and (ii) homobinuclear complexes with different electronic characteristics for the two metal ions so that they can be distinguishable.

In a first step, we will investigate the Cu(II) mononuclear complex in order to determine its relaxation times. The structure is presented below (Table IV-1). It should be noted that there are structures in which a solvent molecule occupies the apical position. We used the compound that does not possess an axial ligand and non-coordinated solvents and we diluted it in a solvent that do coordinate to the metal ion (equimolar solution of $CD_2Cl_2/CDCl_3$ at 10^{-3} mol/L

CHAPTER IV: QUANTUM COHERENCE OF MONO- AND BINUCLEAR COMPLEXES BASED ON THE SALOPHEN LIGAND

(10^{20} spins/cm³).

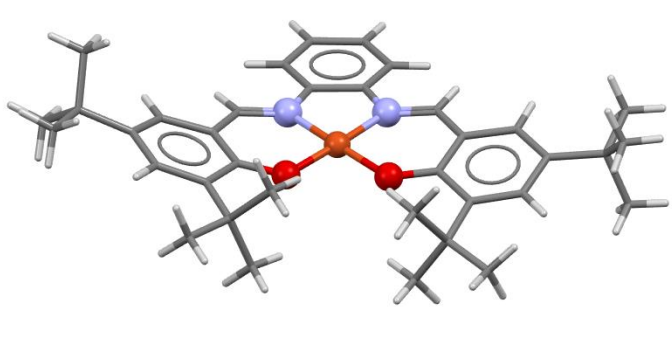
	
Formula	C ₃₆ H ₄₆ Cu N ₂ O ₂
Space Group	P 1 (2)
Cell Lengths	a 10.044(3) b 12.110(3) c 13.844(1)
Cell Angles	α 84.85(1) β 88.64(1) γ 70.95(1)
Cell Volume	1585.21
Z,Z'	Z : 2 Z' : 1
R-factor (%)	3.73

Table IV-1. Crystallographic data of [Cu(salophen)].

IV.2.a. Preliminary experiment

The first experiment conducted was to verify the spin Hamiltonian parameters of [Cu(salophen)] using cw-EPR. Figure IV-9 shows the experimental spectrum and the energy scheme corresponding to the superhyperfine interaction between the electronic spin ($S = 1/2$) and the nuclear spin ($I = 3/2$), where four EPR transitions are expected for each orientation of the g -tensor. Since, the powder (or frozen solution) spectrum of Cu(II) in a square planer geometry should presents two main orientations (at g_{\parallel} and g_{\perp}), the spectrum is expected to have two sets with four bands (hyperfine interaction between $S_{Cu} = 1/2$ and $I_{Cu} = 3/2$, as depicted in Figure IV-9), each centred at g_{\parallel} and at g_{\perp} . On the spectrum (Figure IV-9), three out of four bands (due to hyperfine coupling) associated with g_{\parallel} can be clearly identified (the bands at lower fields). The overlap between the band expected at high field associated to g_{\parallel} and the bands from g_{\perp} makes the determination of the g_{\perp} and A_{\perp} parameters challenging. The parameters determined (Table IV-2) are consistent with those reported in the literature. On the derivative curve of the

CHAPTER IV: QUANTUM COHERENCE OF MONO- AND BINUCLEAR COMPLEXES BASED ON THE SALOPHEN LIGAND

EDFS perform at 33.8 GHz (Figure IV-10) the four transitions associated to $g_{//}$ are clearly visible compared to the derivative of the EDFS perform at 9.69 GHz. The spin Hamiltonian parameters extracted at 9.69 GHz and 33.8 GHz are reported Table V -2. As described for HF-HFEP, using higher frequencies allow a better determination of the g parameters since the different transition are well resolved. However, the values found from both spectra are relatively closed.

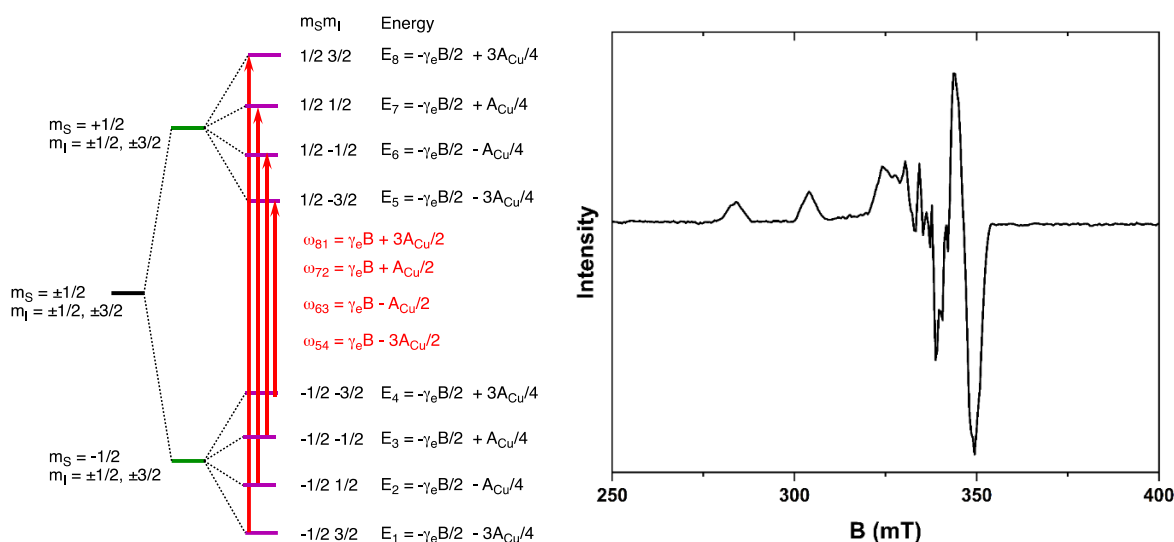


Figure IV-9. cw-EPR spectrum of $[Cu(salophen)]$ at $T = 90$ K and 9.64 GHz.

Parameters	g_{\perp}	$g_{//}$	$A_{Cu//}$ (cm^{-1})	$A_{Cu\perp}$ (cm^{-1})
Value from cw-EPR	2.043	2.194	0.019 (570) ^a	0.004 (120) ^a
Value from EDFS	2.028	2.178	0.022 (649) ^a	0.003 (99) ^a

Table IV-2. Spin Hamiltonian parameters of $[Cu(salophen)]$. ^ain MHz

CHAPTER IV: QUANTUM COHERENCE OF MONO- AND BINUCLEAR COMPLEXES BASED ON THE SALOPHEN LIGAND

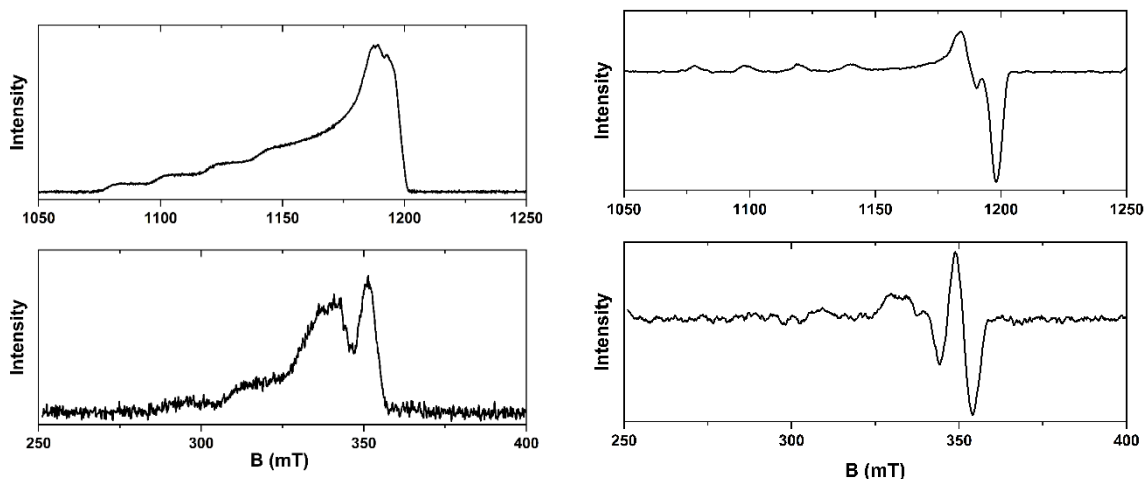


Figure IV-10. (Left) EDFS of $[\text{Cu}(\text{salophen})]$ at $T = 20 \text{ K}$ at $10^{20} \text{ spins.cm}^{-3}$. Top spectra recorded at 33.8 GHz and bottom spectra recorded at 9.69 GHz. (Right) Derivative of the EDFS at 33.8 GHz (top) and at 9.69 GHz (bottom)

As anticipated with copper, the signal remained strong, and the relaxation times were long enough (because an EDFS spectrum could be recorded at relatively high temperature i.e. $T = 20 \text{ K}$) to be readily measured. The EDFS spectrum itself demonstrates that it is possible to address distinct qubits even if they have the same coordination sphere. The discrimination could be due to the different orientation of the anisotropy tensor with respect to the magnetic field (g_{\perp} and g_{\parallel}).

Since we want to perform ENDOR on this system we will use Q band, this cavity is well adapted to this kind of experiment and the higher field allows a better separation of the resonances due to the superhyperfine coupling.

In a first time, we characterized the relaxation times T_1 and T_2 as a function of temperature at four different magnetic fields, 1100 ($m_i = +1/2$) and 1137 ($m_i = -1/2$) mT corresponding to g_{\parallel} resonances and 1186 and 1192 mT corresponding to g_{\perp} transition, in order to determine the influence of the orientation of the \mathbf{g} -tensor components with the respect to the field on the relaxation time. The spin-lattice relaxation time have been obtained by fitting the data using a stretched exponential model. The fitted curves, for $T = 10 \text{ K}$ (Figure IV-11), give $\alpha_s = 0.75$. For every magnetic field values, the stretched factor remains around 0.6 - 0.8. Such value lower than 1, indicates the presence of distributions of molecules, probably due to the high

concentration in the frozen solution.

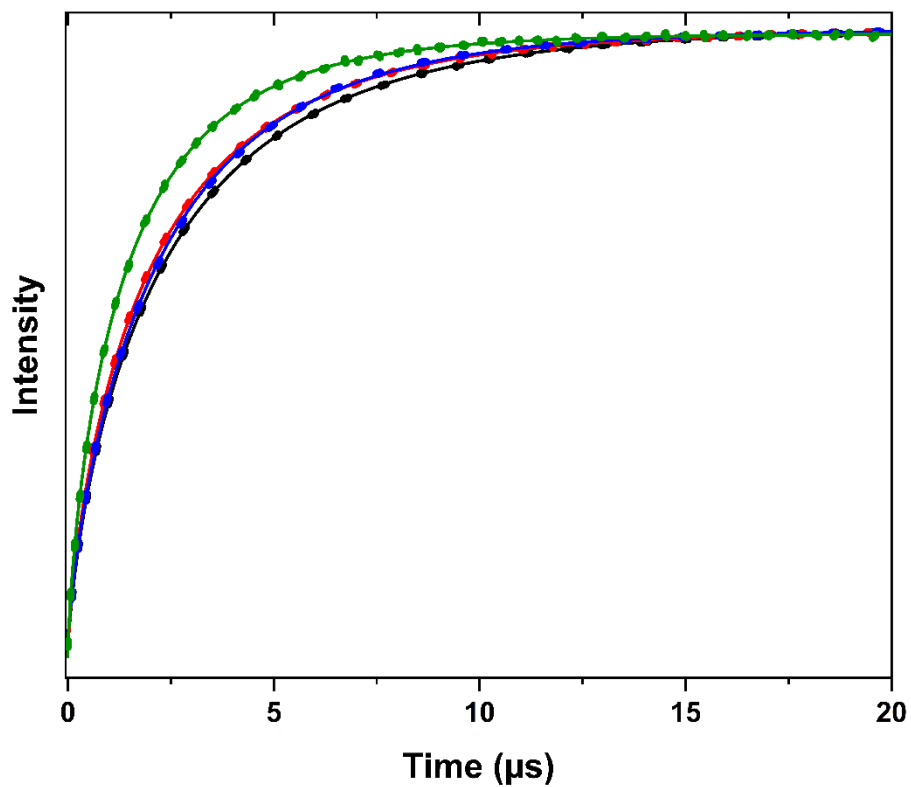


Figure IV-11. Spin-lattice relaxation time curves of $[Cu(salophen)]$ at $T = 10$ K, 33.72 GHz at $B = 1100$ mT (black), $B = 1137$ mT (red), $B = 1186$ mT (green) and $B = 1192$ mT (blue).

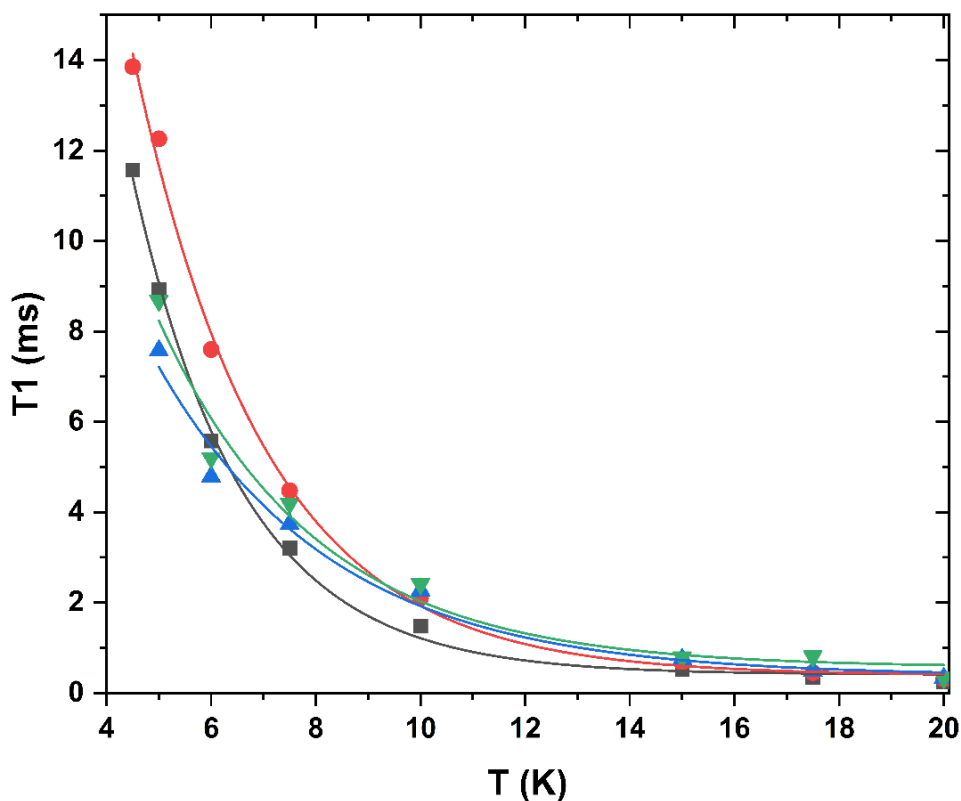


Figure IV-12. Variation of the spin-lattice relaxation time with temperature at $B = 1100$ mT (black), $B = 1137$ mT (red), $B = 1186$ mT (green) and $B = 1192$ mT (blue).

The variation of T_1 with temperature for the four values of the magnetic field is depicted in Figure IV-12. As we can see T_1 is around hundred times longer than for the Ni(II) compounds. The variation of T_1 with temperature can be described by a single-exponential model. The temperature dependences for each magnetic field are given below:

$$T_{1-1100mT}(T) = (93 \pm 10) \times e^{\left(\frac{-T}{2.1 \pm 0.1}\right)}$$

$$T_{1-1137mT}(T) = (83 \pm 10) \times e^{\left(\frac{-T}{2.5 \pm 0.1}\right)}$$

$$T_{1-1190mT}(T) = (30 \pm 8) \times e^{\left(\frac{-T}{3.36 \pm 0.6}\right)}$$

$$T_{1-1192mT}(T) = (40 \pm 14) \times e^{\left(\frac{-T}{3 \pm 0.6}\right)}$$

Those value have to be carefully considered for two reasons:

CHAPTER IV: QUANTUM COHERENCE OF MONO- AND BINUCLEAR COMPLEXES BASED ON THE SALOPHEN LIGAND

- (i) The laws are the result of a single-exponential decay regression on points obtained after using stretched exponential model on a T_1 vs. t curves.
- (ii) The absence of point at T = 4.5K for B = 1192 mT and B = 1190 mT change considerably the trend because the pre-exponential factor is poorly estimated at higher temperature.

We can see that in all cases T_1 has a temperature dependence proportional to approximately $e^{\left(\frac{-T}{2.5}\right)}$. It seems that the transitions associated to $g_{//}$ have longer T_1 than those associated to g_{\perp} . In absence of saturation recovery experiments, it is very difficult to make any assumption concerning the relaxation mechanism involved. In any case the long spin-lattice relaxation observed allows performing ENDOR experiment in good experimental conditions.

The spin-spin relaxation times (T_2) was recorded at T = 10 K. The echo signal vs. time at different magnetic fields (Figure IV-13) are fitted using a stretched exponential model with $\alpha_s = 0.70$ and T_2 around 1 μ s. T_2 is not limited by T_1 within the range of our experiment, the mechanism previously described as T_1 -flip will not affect T_2 .

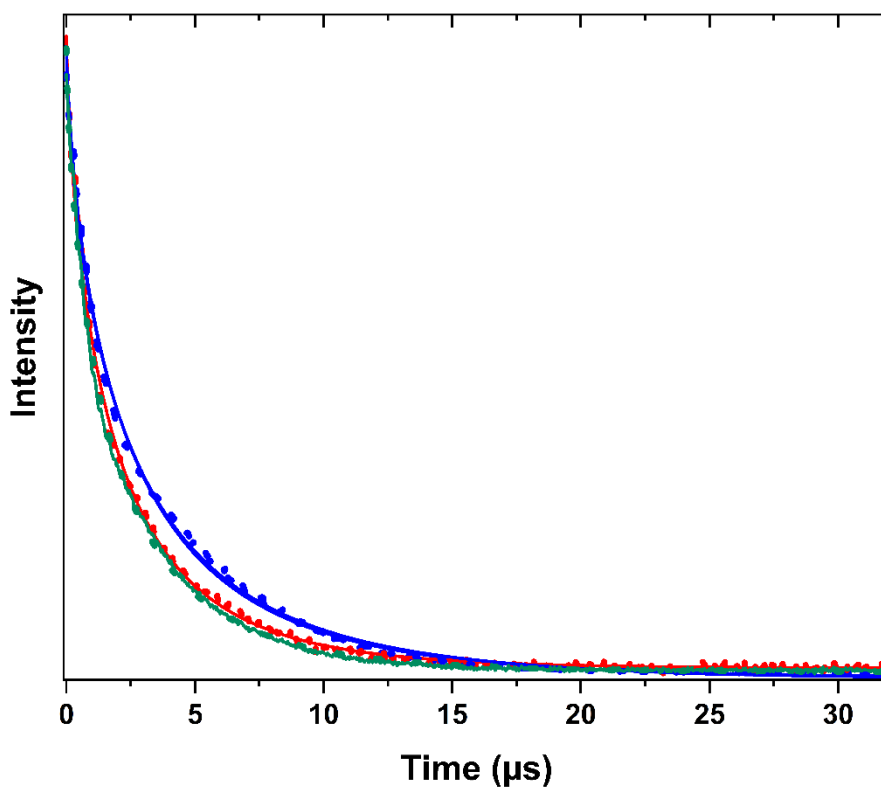


Figure IV-13. Spin-spin relaxation time curves of [Cu(salophen)] at T = 10 K, 33.72 GHz at B = 1100mT (black), B = 1137 mT (red), B = 1186 mT (green) and B = 1192 mT (blue).

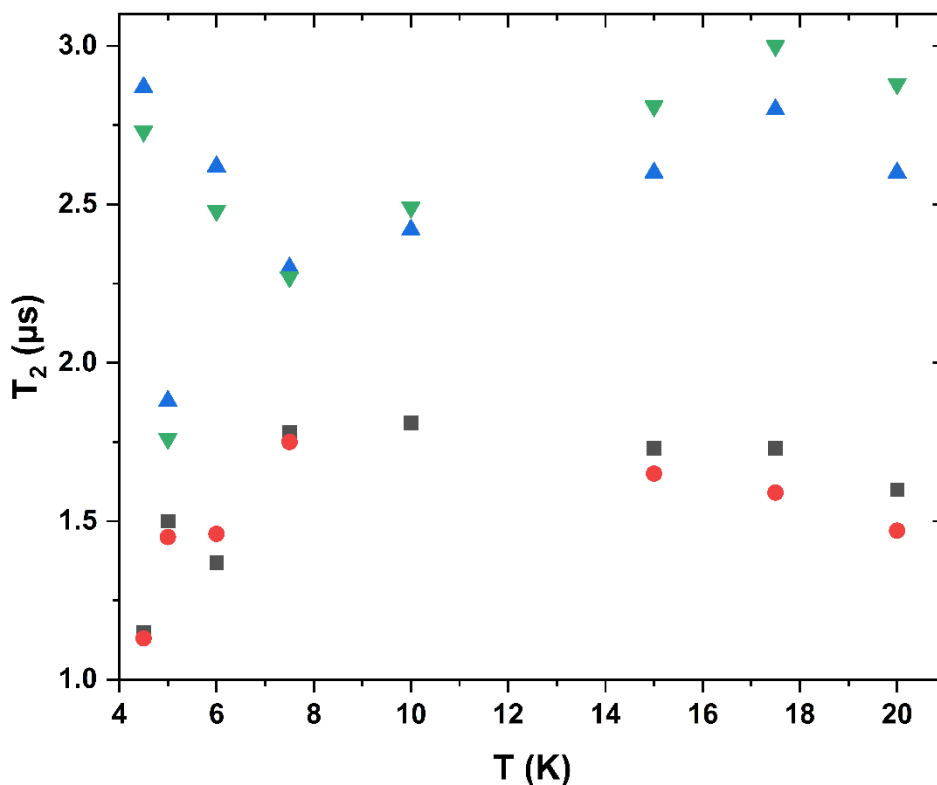


Figure IV-14. Variation of the coherence time with temperature at $B = 1100\text{mT}$ (black), $B = 1137\text{ mT}$ (red), $B = 1186\text{ mT}$ (green) and $B = 1192\text{ mT}$ (blue).

Subsequently, the spin-spin relaxation times (T_2) was recorded as a function of temperature (4.5 – 20 K) (Figure IV-14). In this range of temperature, T_2 exhibits no temperature dependence which was expected since $T_1 \gg T_2$ meaning that the vibrations of the molecule are not relevant at those temperatures. The slight variation of T_2 is probably due to different value of g because the higher g is the higher the slope of the curve is ($\Delta E \propto g$). Thus a small variation of the magnetic field will have a more important effect with larger g value. This hypothesis is supported by the fact that the stretched factors are very close ($\alpha \approx 0.7$) for all temperatures (Figure IV-15) meaning that the mechanisms involved are the same.

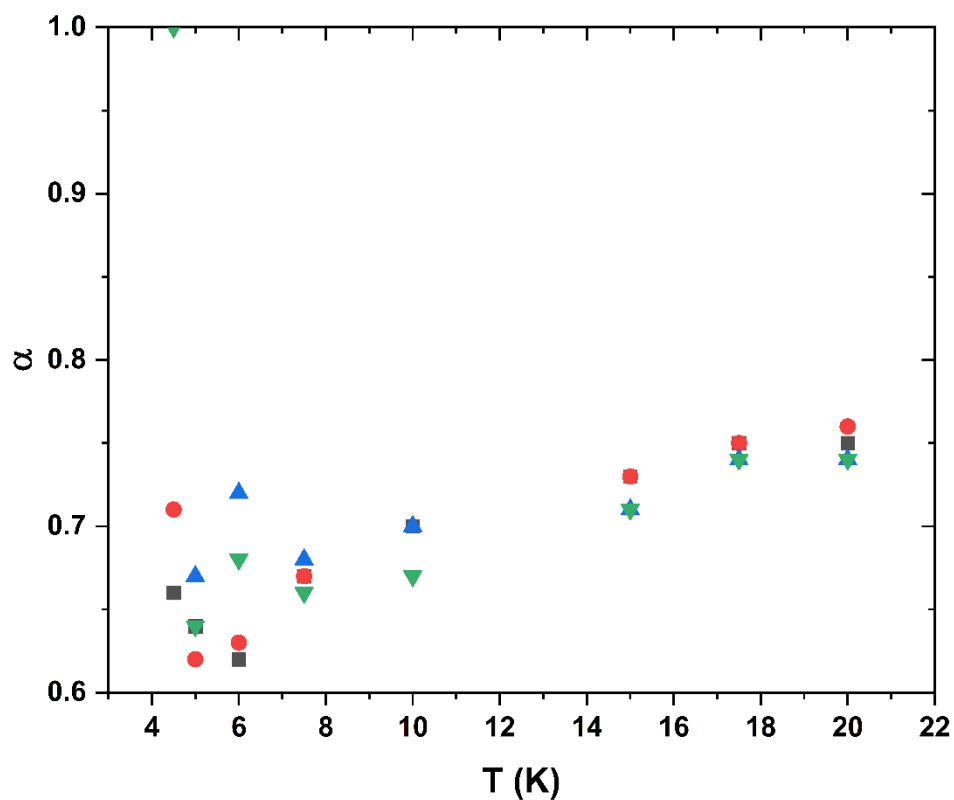


Figure IV-15. Variation of the stretched factor with temperature at 33.8 GHz, $B = 1100\text{mT}$ (black), $B = 1137\text{ mT}$ (red), $B = 1186\text{ mT}$ (green) and $B = 1192\text{ mT}$ (blue).

In order to increase the value of T_2 , we aimed at identifying factors affecting the coherence time. A coherence time was measured at 10^{-3}mol/L and at 10^{-4}mol/L in $\text{DCM(D)}/\text{CDCl}_3$ (Figure IV-16) with different power of pulse in order to see any Flip-Flop effect.

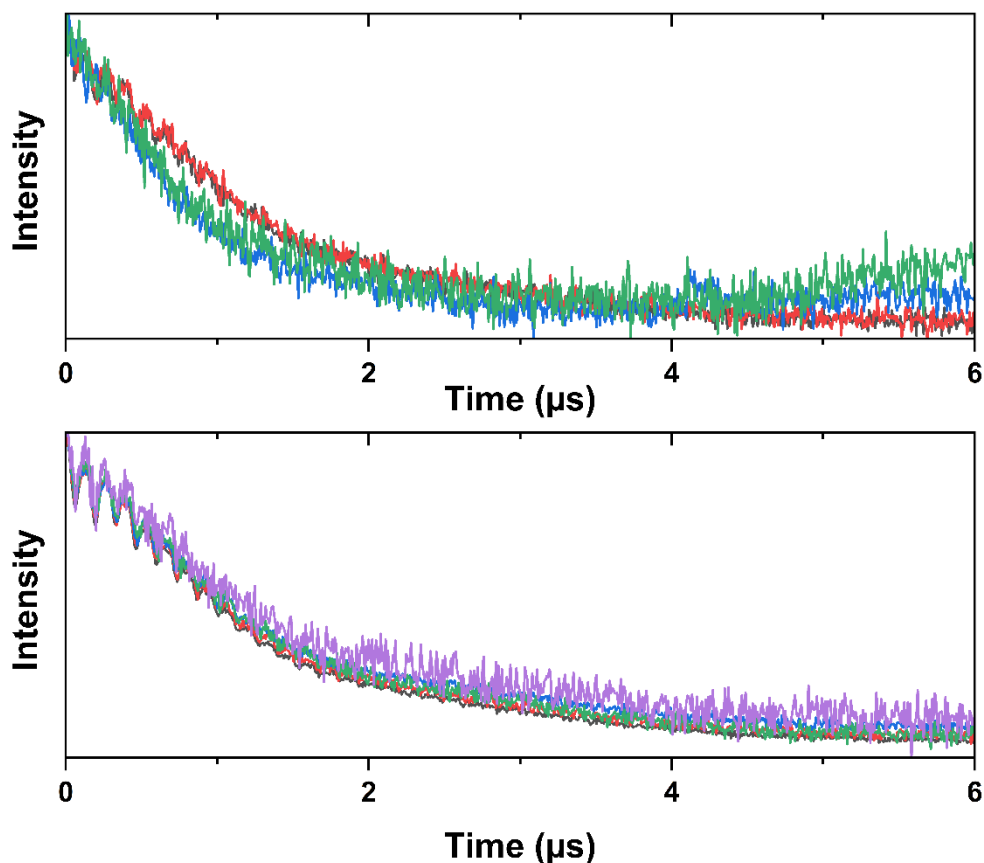


Figure IV-16. Spin-Spin relaxation after a Hahn echo sequence at 10^{-3} mol/L (top) and 10^{-4} mol/L (bottom) at $T = 20$ K, at $B = 305$ mT at 6 dB (black) 9dB (red) 12 dB (blue), 15 dB (purple) and 18 dB (yellow) at 9.69 GHz.

No significant difference was observed. This result is surprising, as one might expect a longer relaxation time upon dilution. Indeed, diluting the paramagnetic centers is expected to reduce dipolar interactions and potentially lengthen T_2 , if dipolar interactions were responsible of the short relaxation time at the pristine concentration of 10^{-1} mol/L. However, this is not observed. It can be assumed that at these concentrations, T_2 is saturated by both the nuclear spins of the molecule and Flip-Flop processes simultaneously. On one hand, a tenfold dilution is not sufficient to significantly reduce Flip-Flop interactions. On the other hand, the number of nuclear spins in the molecule remains constant regardless the dilution. Freedman's vanadium complex (possesses no nuclear spins), which was relatively undiluted, still exhibited a long coherence time.[10] This clearly demonstrates that the nuclear spins of the ligands contribute to the relaxation of the electronic spin.

V.2.b. ENDOR Experiment

We characterized the system and observed the presence of a coupling between the electronic

CHAPTER IV: QUANTUM COHERENCE OF MONO- AND BINUCLEAR COMPLEXES BASED ON THE SALOPHEN LIGAND

spin of copper(II) and the nuclear spins within the ligand, specifically protons and nitrogen. Nuclear spins are known to possess longer relaxation times than electronic spins, which are less utilized due to detection difficulties. In this study, we attempted to address the nuclear spins of protons and nitrogen via the electronic spin of copper, using ENDOR.

Using the ENDOR sequence described in the introduction, we obtained the spectra shown in Figure IV-17. These spectra reveal the presence of at least two distinct nuclei, and notably, the peaks on the right-hand side appear extremely narrow. The origin of the doubling of the peaks upon increasing the applied magnetic field is probably to two types of coupling through bond and dipolar for the same nuclear spin. The through coupling does not depend on the relative orientation of the spins, the corresponding transitions are expected to be very narrow. While dipolar coupling depends on the relative spins orientation and different orientations lead to large bands as one can observe for the right part of the black curve (Figure IV-17).

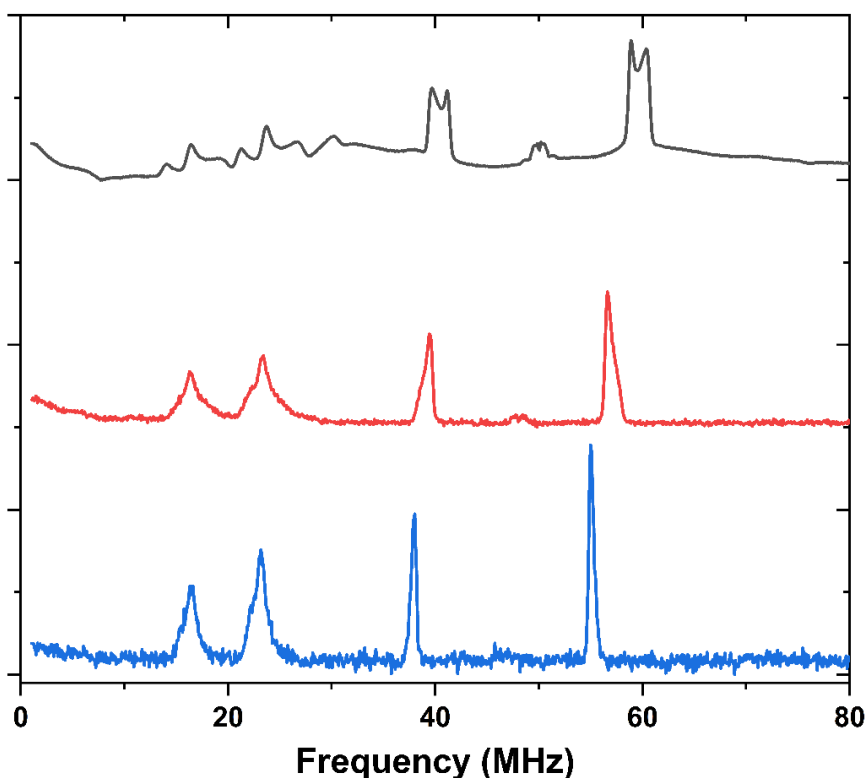


Figure IV-17. ENDOR spectra recorded at $T = 10$ K, 33.81 GHz at $B = 1100$ mT (black), $B = 1137$ mT (red), $B = 1186$ mT (green) and $B = 1192$ mT (blue).

The transitions at a lower frequency ($\nu = 16.47$ and 23.19 MHz at 1100 mT) correspond probably to the coupling with the nuclear spin of nitrogen atoms (see Figure IV-6). At $B = 1100$ mT, the Larmor frequency of the nitrogen atoms is equal to $\gamma_N B$ (3.38 MHz, with $\gamma_N = 3.077$

CHAPTER IV: QUANTUM COHERENCE OF MONO- AND BINUCLEAR COMPLEXES BASED ON THE SALOPHEN LIGAND

MHz/T) Experimentally, we find $((23.19 - 16.47)/2)$ 3.36 MHz, which ensures indeed that the low frequency resonances correspond well to the nitrogen atoms. The value of the superhyperfine coupling (A_N) is found equal to 39.66 $((23.19 + 16.47)/2)$ MHz from the analysis of the frequencies of the two resonances. The large coupling constant is due to the two nitrogen atoms directly coordinated to Cu. For H atoms (see Figure IV-5), the gyromagnetic ratio is equal to 42.58 GHz/T, we are therefore in the weak coupling limit. The resonances at the high frequency part of the spectra correspond to H atoms. The superhyperfine constant of the protons coupled to the electronic spin is found equal to $A_H = 17.03$ MHz. The protons coupled to the electronic spin are probably those depicted in black in Figure IV-18. The spectra at different magnetic fields (Figure IV-17) show that the variation of the resonances follow the Larmor frequencies expected, therefore, confirming the values of the coupling constants for both H and N. When the field is increased, the resonances due to the protons that are symmetric and very narrow at $B = 1100$ mT become less symmetric at $B = 1137$ mT and transform into doublets at $B = 1186$ mT. The origin of the doubling of the peaks is explained above. In addition, another signal of low intensity appears in the centre between the two main peaks, which can be attributed to protons having a much less superhyperfine coupling with the electronic spins, probably those depicted in green in Figure IV-18.

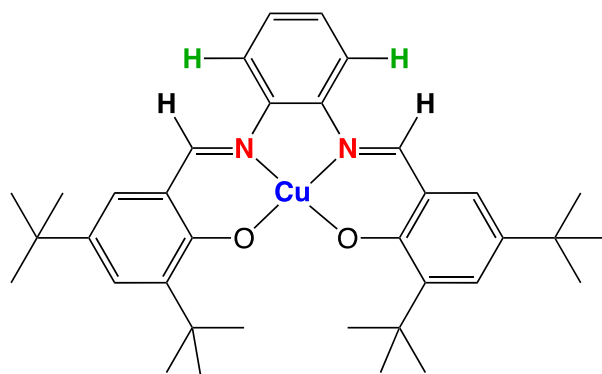


Figure IV-18. Chemical structure of $[Cu(salophen)]$, highlighting the nuclear spins that could interact with Cu.

The first step involved verifying the addressability of these nuclear spins using nutation experiments. In Figure IV-19, we assumed that the signal observed correspond to the one of the nitrogen and proton, We can see that it is possible to manipulate the nuclear spins. Unfortunately due to a lack of time it was not possible to perform the experiment at different powers in order to confirm the associated nuclear spin

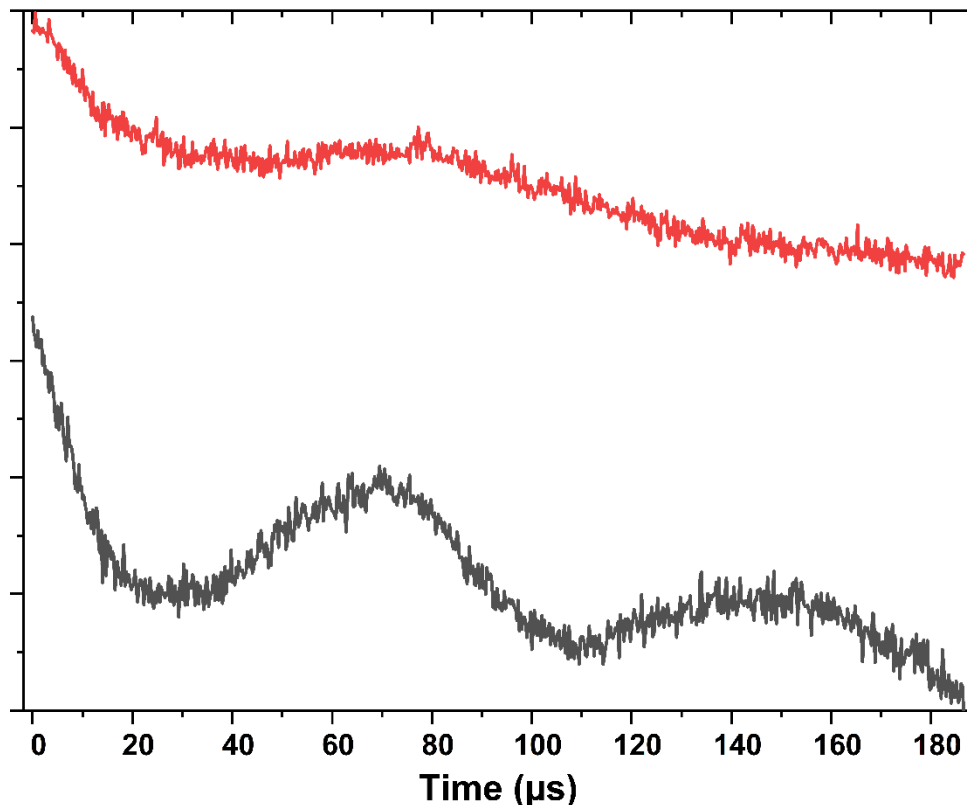


Figure IV-19. Nutation sequence of proton at 55 MHz (black) and nitrogen at 23.09 MHz (red) $B = 1100$ mT and at $T = 10$ K.

The second step was to observe the variation in echo intensity at different time intervals (τ) in order to reconstruct the characteristic exponential decay curve of T_2 . Then we tried to estimate the coherence time of the nuclear spins especially the proton which possesses the sharpest transition. For this purpose, we adapted the sequence described in the introduction in order to measure the coherence time of the H atoms that we showed are coupled to the electronic spin. The scheme of the sequence is given in Figure IV-20.

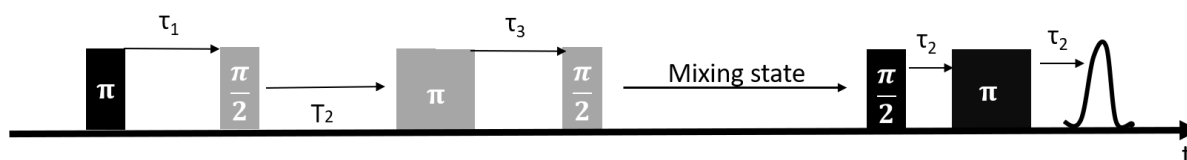


Figure IV-20. Nuclear echo detected sequence. Here $\tau_1 = 2 \mu\text{s}$, $\tau_2 = 0.24$ ns and $\tau_3 = 22 \mu\text{s}$.

In this study, we added a Hahn echo nuclear pulse (grey) to the sequence and a $\pi/2$ pulse at the time corresponding to the formation of the echo. This allows us to observe the echo with the Hahn echo electronic pulse (black). Setting up this sequence is particularly challenging due to the required numerous pulses at precise times. Another significant difficulty was calibrating

CHAPTER IV: QUANTUM COHERENCE OF MONO- AND BINUCLEAR COMPLEXES BASED ON THE SALOPHEN LIGAND

the duration of the experiment. The overall experiment needs to be shorter than T_1 . However, since T_{2N} appeared to be very long ($T_2 > 100 \mu\text{s}$), we had to extend T_1 to the millisecond range, which is why we decided to work at 5 K (long T_1). Experimentally, this temperature is very constraining because the shot repetition time (SRT) becomes very long, making the experiment particularly time-consuming. We first recorded the nuclear echo for nitrogen at 1100 mT and 10 K, despite a broad signal we succeeded to observe an echo until 0.4 ms. We could probably observe an echo at longer times but due to a weak signal and a lack of time we did not perform the experiment.

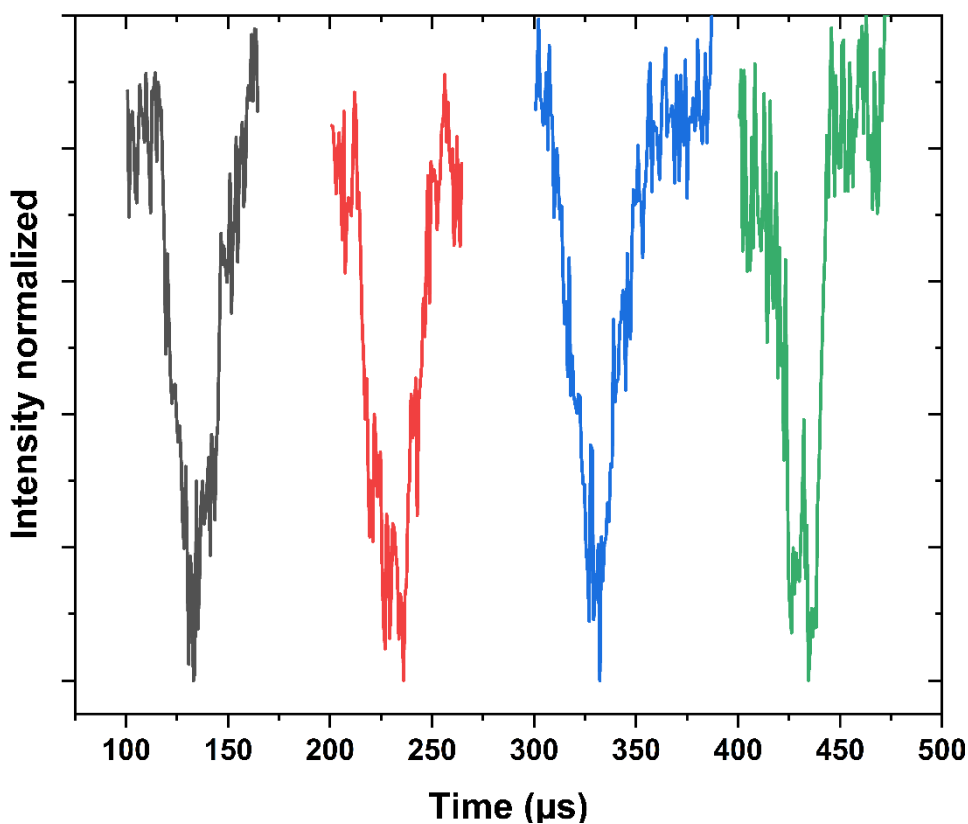


Figure IV-21. Observation of the nitrogen echo at different times T_2 times at $T = 5 \text{ K}$, $B = 1100 \text{ mT}$ and 23.1 MHz .

Then we attempted to construct the characteristic exponential decay curve, but the echo integration was complicated due to a noisy signal. If we had more time we could have obtained better resolved echo thus construct the characteristic exponential decay. Those experiment are difficult to achieve, only a few number of examples are described in the literature. [11] [12].

We observe an echo at $t = 0.4 \text{ ms}$, which means that there are molecules (well isolated) with $T_{2-N} > 0.4 \text{ ms}$. Ultimately, our goal is to study a diluted sample with only a limited number of well isolated molecules. We believe that in this situation the nuclear coherence time of the

CHAPTER IV: QUANTUM COHERENCE OF MONO- AND BINUCLEAR COMPLEXES BASED ON THE SALOPHEN LIGAND

proton will be at least equal to the one of the well isolated molecules at higher concentration.

A similar experiment was performed on the proton at 55 MHz (Figure IV-22), and here, due to a stronger signal, a very weak echo was observed for longer times $t = 0.56$ ms.

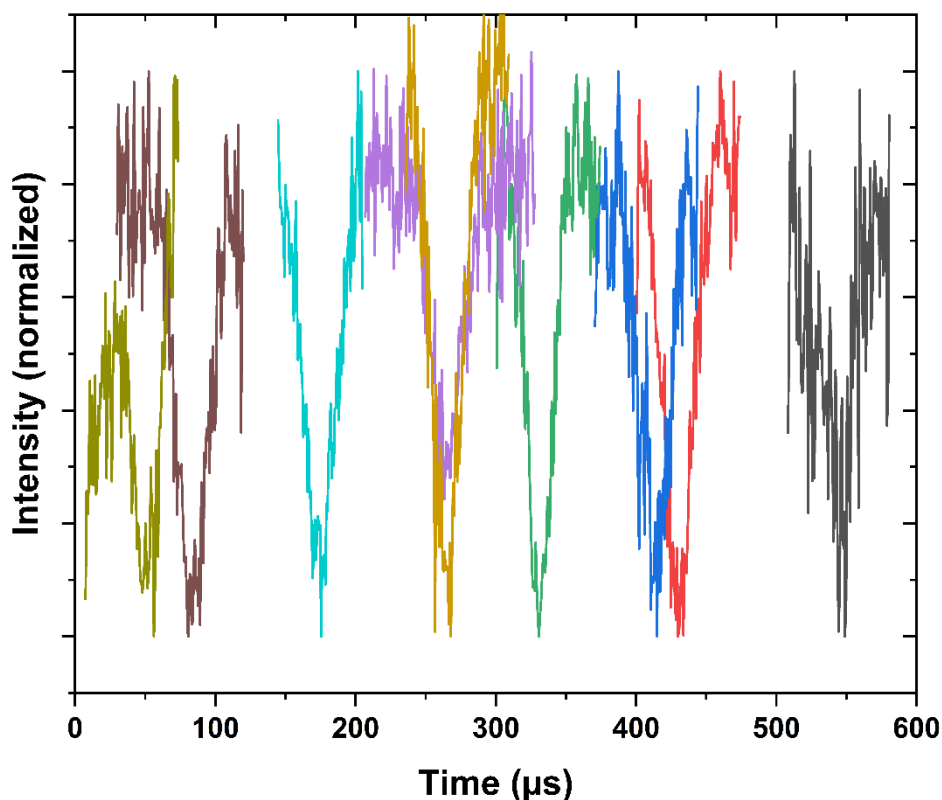


Figure IV-22. Observation of the proton echo at different T_2 times at $T = 5$ K, $B = 1100$ mT and 55MHz.

The concentration here is still very high (10^{-3} mol/L) and the only precaution was to work in a deuterated solvent. With higher dilutions, we expect to reach a coherence time up to the 1 ms proving that nuclear spins in molecules are as competitive as for other systems (cold atom, superconducting Josephson junctions etc.), despite the drawback of the magnetic fluctuation of the nuclear spin bath that induces decoherence. One may expect that addressing samples with 10^{15} spins/cm³ would lead to larger coherence times for the electronic and for the nuclear spins.

IV.3 [VO(SALOPHEN)]

The same type of experiment was conducted on the V(IV)O analogue. The comparison between V(IV) and Cu(II) is particularly interesting because both complexes exhibit spin $S = 1/2$. The compound was diluted in equimolar solution of $CD_2Cl_2/CDCl_3$ at 10^{-3} mol/L (10^{20} spins/cm³).

IV.3.a Preliminary experiment

The first experiment conducted was to determine the spin Hamiltonian parameters of the [VO(salophen)] using cw-EPR (Figure IV-23). Vanadium is known to possess numerous hyperfine resonances due to the value of its nuclear spin ($I = 7/2$). The spin Hamiltonian parameters g_{\perp} , g_{\parallel} , A_{\parallel} and A_{\perp} are reported in Table IV-3.

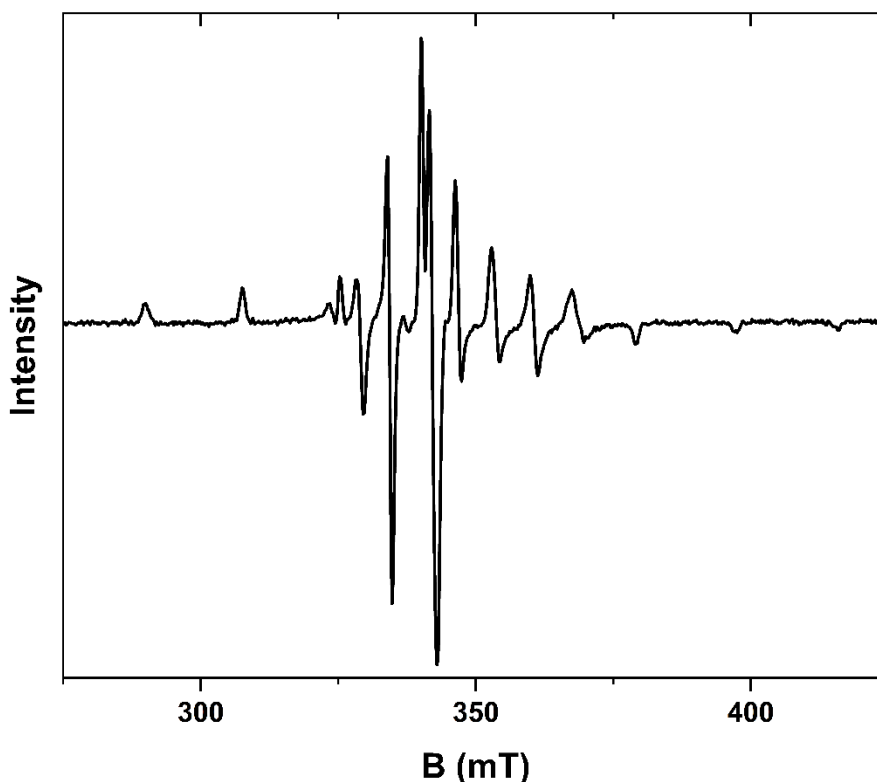


Figure IV-23. cw-EPR spectra of [VO(salophen)] at $T = 90$ K and 9.64 GHz.

The determined spin Hamiltonian parameters were reported Table IV-3.

Parameters	g_{\parallel}	g_{\perp}	A_{\parallel} (cm ⁻¹)	A_{\perp} (cm ⁻¹)
Value	1.945	1.989	0.0164 (461.6) ^a	0.0056 (168.1) ^a

Table IV-3. Spin Hamiltonian parameters of [VO(salophen)] determined from the cw-EPR spectrum. ^ain MHz

The EDFS spectra was recorded in Q band at 33.8 GHz (Figure IV-24). Table IV-4 gives the spin

CHAPTER IV: QUANTUM COHERENCE OF MONO- AND BINUCLEAR COMPLEXES BASED ON THE SALOPHEN LIGAND

Hamiltonian parameters of [VO(salophen)] determined from the EDFS spectrum. The determination of the g_{\perp} value was difficult due to the difficulty to identify all the bands associated.

Parameters	$g_{//}$	g_{\perp}	$A_{//}$ (cm ⁻¹)	A_{\perp} (cm ⁻¹)
Value	1.942	1.992	0.0151 (452.7) ^a	0.0084 (250,1) ^a

Table IV-4. Spin Hamiltonian parameters of [VO(salophen)] determined from the derivative of the EDFS spectrum. ^ain MHz

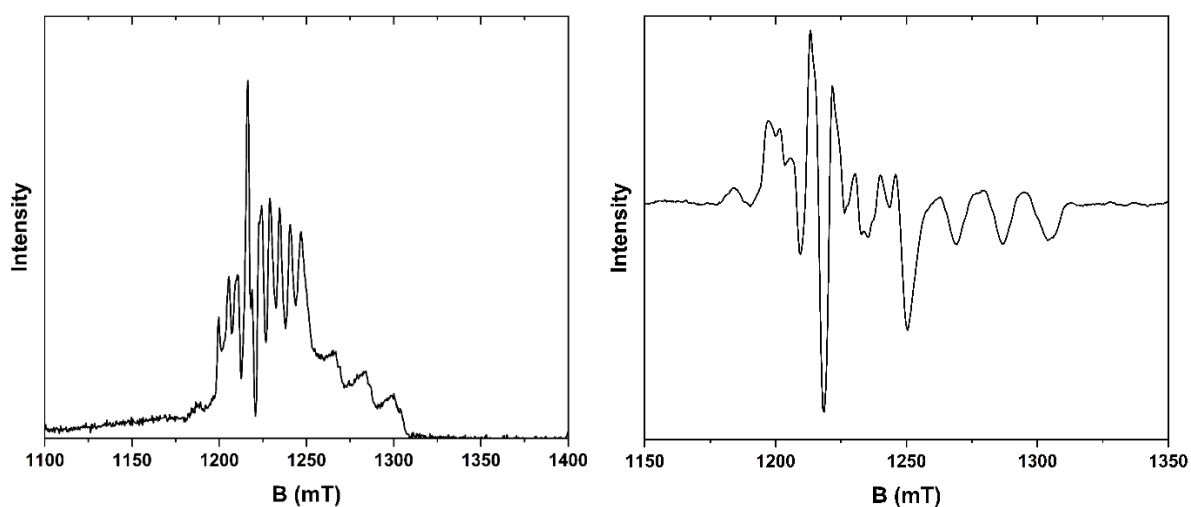


Figure IV-24. (Left) EDFS spectra of [VO(salophen)] recorded at $T = 15$ K and 33.8 GHz. (Right) Derivative of the EDFS spectra of [VO(salophen)] recorded at $T = 15$ K and 33.8 GHz

The spin-lattice relaxation time was first extracted from the inversion recovery experiment (Figure IV-25) that was carried out at different (three) values of the applied magnetic field corresponding to the parallel and perpendicular components of the g -tensor. The data were fitted using a stretched exponential model with $\alpha_s = 0.68$. Then the dependence of T_1 with temperature was measured for the three magnetic field values (Figure IV-26). The data were fitted leading to the following results:

$$T_{1-1206mT}(T) = (120 \pm 12) \times e^{\left(\frac{-T}{3.97 \pm 0.37}\right)}$$

$$T_{1-1218mT}(T) = (209 \pm 60) \times e^{\left(\frac{-T}{2.27 \pm 0.33}\right)}$$

$$T_{1-1283mT}(T) = (388 \pm 77) \times e^{\left(\frac{-T}{2.25 \pm 0.22}\right)}$$

CHAPTER IV: QUANTUM COHERENCE OF MONO- AND BINUCLEAR COMPLEXES BASED ON THE SALOPHEN LIGAND

It was noted that T_2 is not limited by T_1 within the range of our experiment, the mechanism previously described as T_1 -flip will be inoperant here.

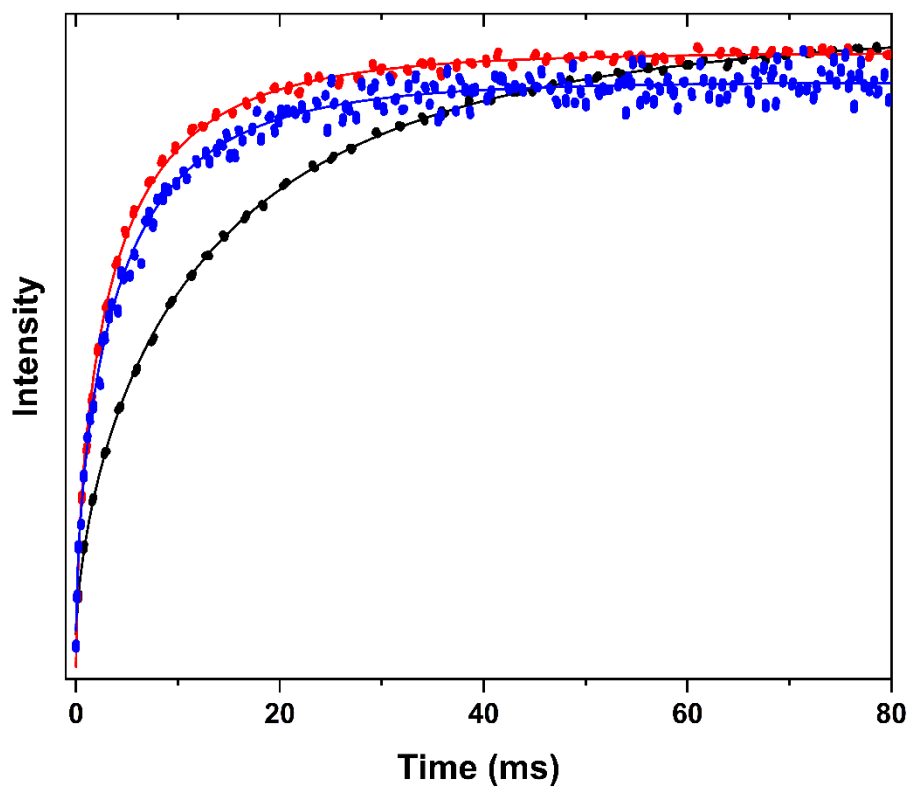


Figure IV-25. Spin-lattice relaxation time curves of [VO(salophen)] at $T = 10$ K, 33.72 GHz at $B = 1206$ mT (black), $B = 1218$ mT (red) and $B = 1283$ mT (blue).

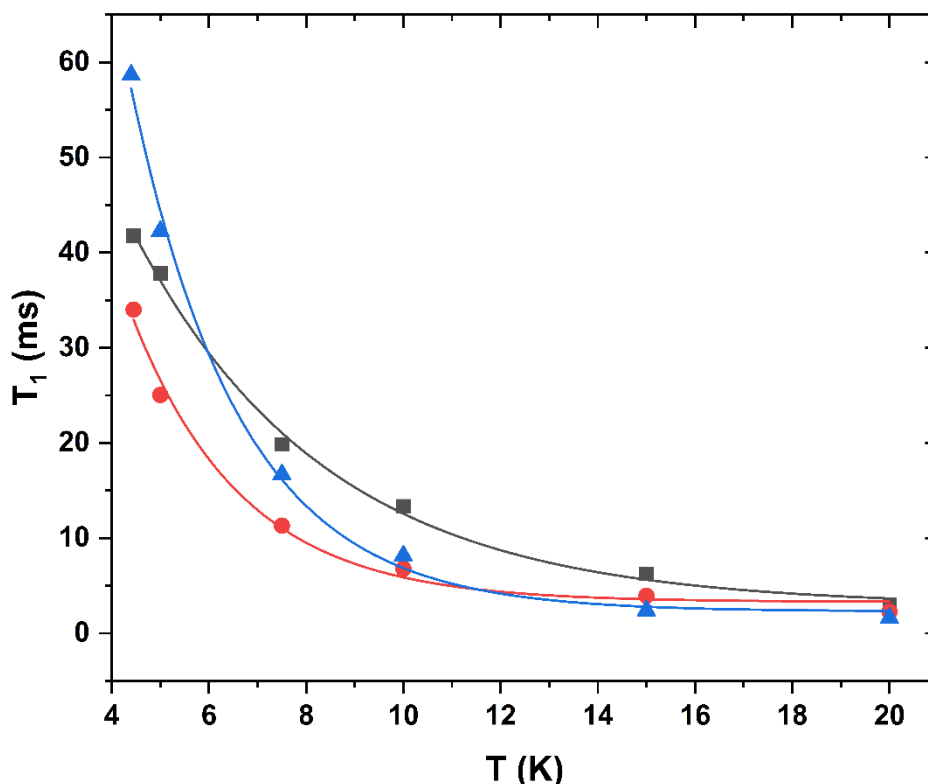


Figure IV-26. Variation of the spin-lattice relaxation time with temperature at 33.72 GHz, $B = 1206$ mT (black), $B = 1218$ mT (red) and $B = 1283$ mT (blue).

For the same reason mentioned previously one has to consider carefully those value. However here it is clear that T_1 is longer in the case of the $g_{//}$ transition than in the case of the g_{\perp} transition. The difference could be due to the fact that the interaction between the ligands and the d orbitals are more sensitive to the variation in the plane (where g_{\perp} is relevant) than along the z direction (where $g_{//}$ is relevant), the V=O bond is extremely rigid. Actually, such difference was already observed in the Cu(dithiocarbamate) complex. The reason invoked is the possible presence of vibrations modes that couple to spin degree of freedom via a mechanism involving spin-orbit coupling (SOC) in the plane that are absent in the apical position because Cu(II) (dithiocarbamate) does not possess apical ligands.[1] More precisely, it is well known that the shift of the g -value from g_e is due to spin-orbit coupling (SOC). In the axial direction, SOC is due to an excitation involving the d_{xy} (ground) and the $d_{x^2-y^2}$ (excited) orbitals that have the same quantum numbers. While for the perpendicular plane, SOC involves excitations between the d_{xy} and the d_{xz} and d_{yz} orbitals with different orbital quantum numbers. Since relaxation involves the absorption or emission of a phonon, it is prone to occur between states with different quantum numbers, therefore in the plane rather than for the axial direction. In summary, the presence of vibrational modes in the plane that can couple to the wavefunction

CHAPTER IV: QUANTUM COHERENCE OF MONO- AND BINUCLEAR COMPLEXES BASED ON THE SALOPHEN LIGAND

modified by the SOC may lead to faster relaxation than in the axial direction where the wavefunction modified by the SOC cannot couple to any vibration mode out of the plane. This mechanism invoked for a Cu(II) complex can be translated to the V(IV)O derivative, because the same orbitals are involved for the parallel and the perpendicular directions as for Cu(II). Considering this result, it is important to go back to the case of the Cu(salophen) discussed above. We assumed that the difference between the T_1 values for the parallel and perpendicular directions were not different enough globally. But if we look back at the T_1 values at $T = 5$ K, we find that T_1 is twice longer for the parallel than for the perpendicular direction as for the VO derivative, albeit T_1 is globally shorter for Cu(II).

It is possible to try to rationalize the longer T_1 for V(IV)O in comparison to Cu(II) that may be due to the nature of the orbital describing the unpaired electron for the two complexes. The unpaired electron is described by a d_{xy} for V(IV)O that points *between* the equatorial atoms of salophen, while for Cu(II) it is described by a $d_{x^2-y^2}$ orbital that points towards the equatorial atoms. The wave function is therefore much more sensitive to planar vibration modes for the Cu(II) complex than for the V(IV)O one. Finally, one may wonder why the presence of the apical oxygen atom in VO(salophen) does not make T_1 shorter. This is probably because the vibration mode in the parallel direction has high energy and as stated above, it cannot couple via SOC to the orbital that describes the unpaired electron.

Contrary to the case of Cu(II), in the range of temperature explored T_2 seems to exhibit a temperature dependence (Figure IV-27). However, this result is surprising because all curves reach 0 at the same value of t . If the coherence time were really longer with temperature, one could expect that the total relaxation of the system occurs at different times which is not the case here. The extremely strong ESEEM effect at higher temperature probably changes the shape of the exponential but not the coherence time. This hypothesis is supported by the variation of the stretched factor that goes from 1 to 1.6 meaning that we have some spin-diffusion (Figure IV-28). The same kind of behaviour is observed for each transition studied.

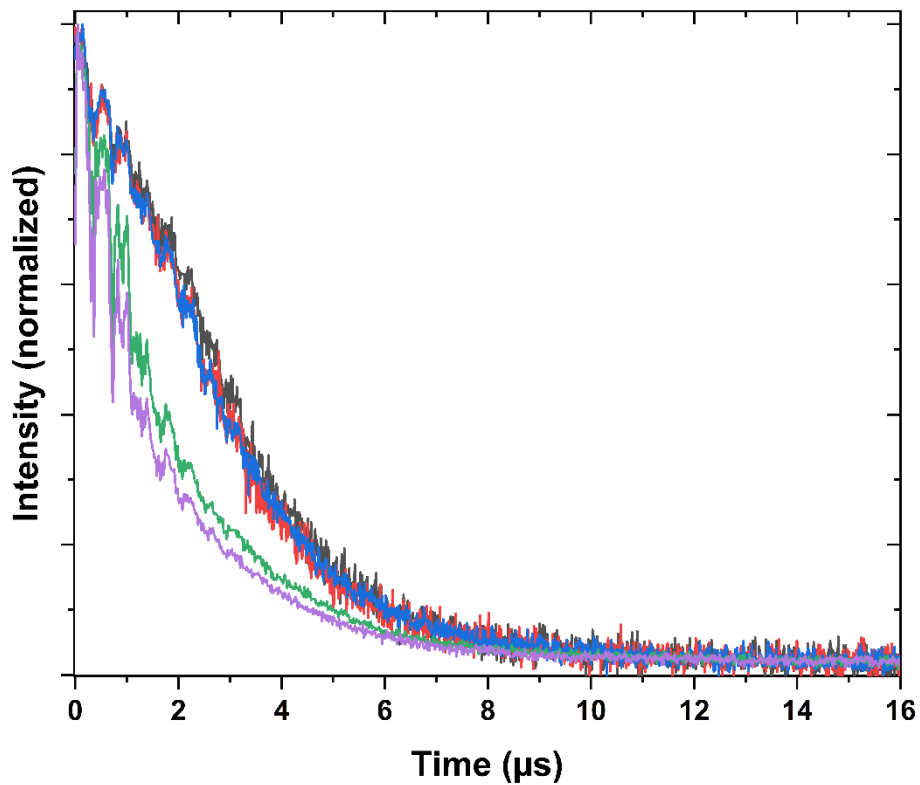


Figure IV-27. Spin-spin relaxation after a Hahn echo sequence at 33.72 GHz, $B = 1283$ mT and different applied temperature. $T = 4.5$ K (black), $T = 5$ K (red), $T = 7.5$ K (blue) $T = 10$ K (green) and $T = 15$ K (purple).

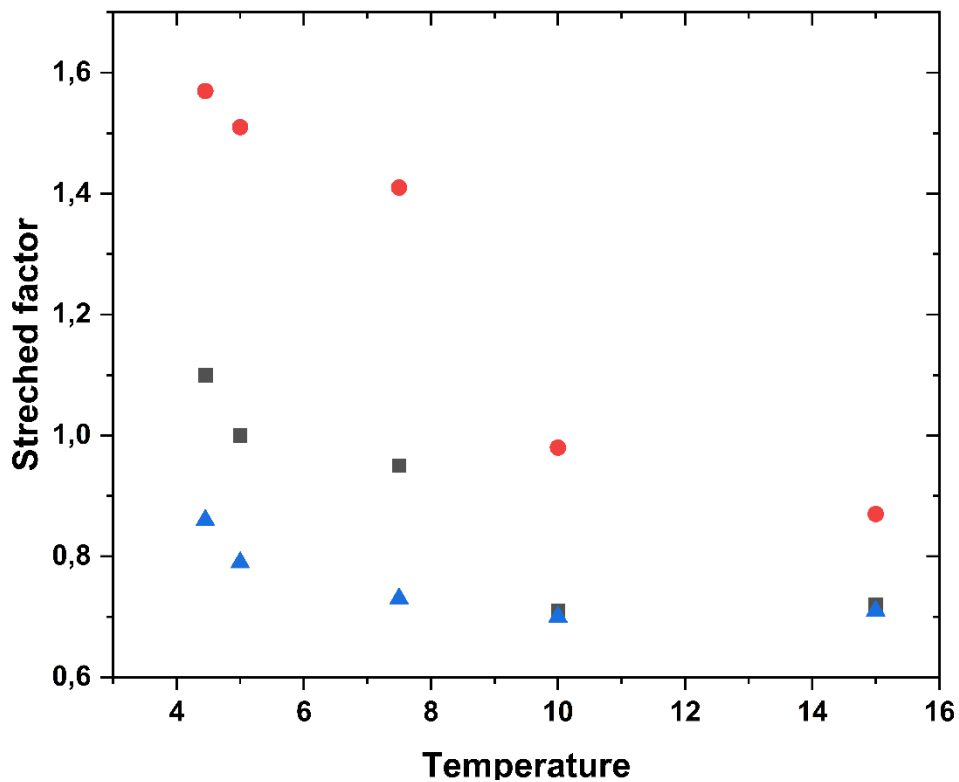


Figure IV-28. Variation of the stretched factor with applied temperature at 33.72 GHz, $B = 1205$ mT (black), $B = 1217$ mT (red) and $B = 1286$ mT (blue).

CHAPTER IV: QUANTUM COHERENCE OF MONO- AND BINUCLEAR COMPLEXES BASED ON THE SALOPHEN LIGAND

Here again the difference in the value of the stretched factor among the different magnetic field is probably due to difference in the ESEEM effect. If we compare the overall T_2 obtained using this model, we find important difference in T_2 (Figure IV-29), but if we compare the raw data (Figure IV-30) we observe again, a total relaxation of the system for the same time t . In conclusion we probably have different mechanisms involved but at the end the coherence time remains the same. From our data, it seems than the coherence times in V(IV) and Cu(II) are the same.

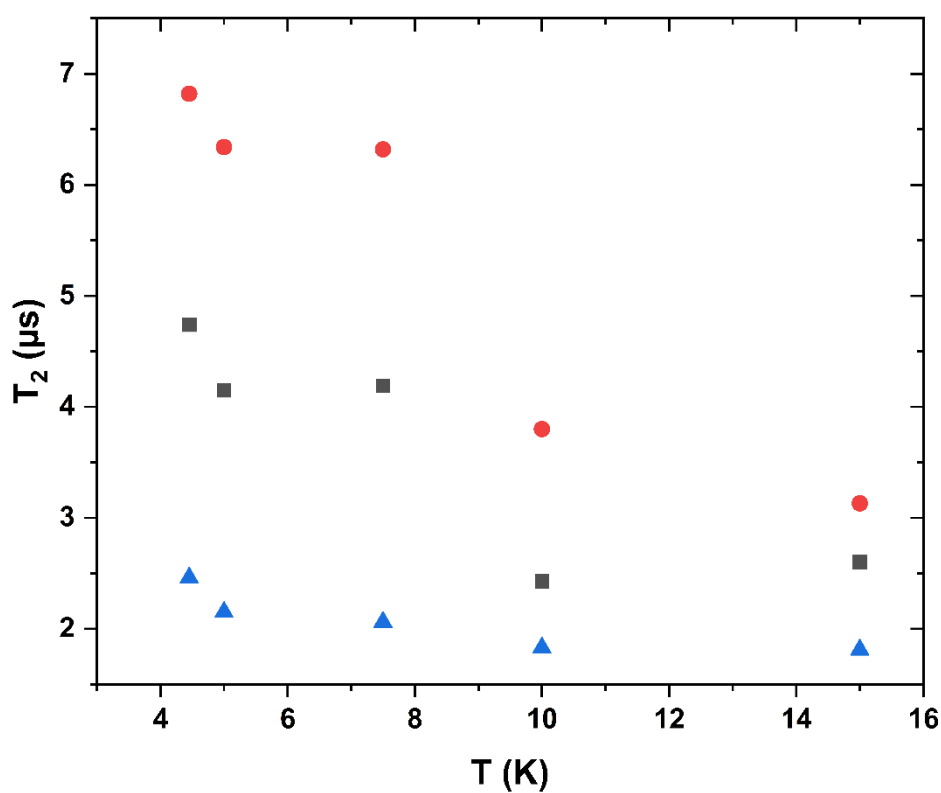


Figure IV-29. Variation of the coherence time with the applied temperature at 33.72 GHz and $B = 1205$ mT (black), $B = 1217$ mT (red) and $B = 1286$ mT (blue).

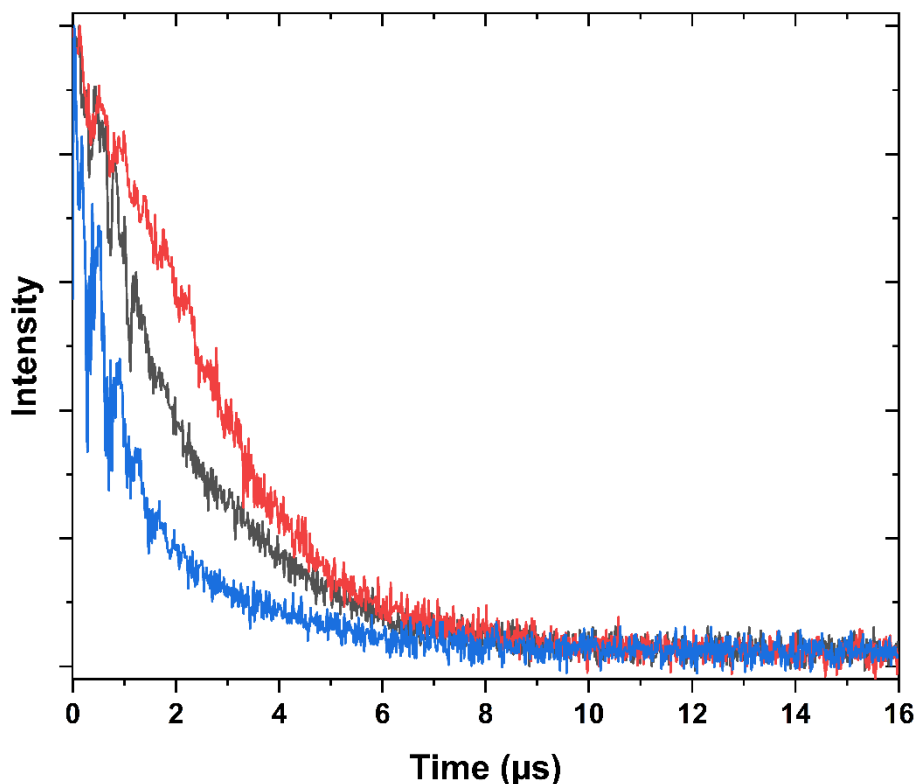


Figure IV-30. Spin-spin relaxation after a Hahn echo at $T = 5$ K, 33.72 GHz and $B = 1205$ mT (black), $B = 1217$ mT (red) and $B = 1286$ mT (blue).

IV.3.b ENDOR experiment

We attempted to perform the same type of ENDOR experiment as previously described. However, as shown in Figure IV-31, one very large band is observed. If this corresponds to one of the two expected bands that correspond to a coupling with a proton, the center of the bands should be at the Larmor frequency of the proton, which is not the case. It corresponds to the coupling the nuclear spin of the N atoms, the coupling would be very large, which is not possible because the unpaired electron of V(IV) is in a d_{xy} orbital that points between the N atoms, the coupling cannot be much larger than in the Cu(II) case. The very limited experimental time, did not allow us to perform any nutation or echo-detected experiments, in order to progress further.

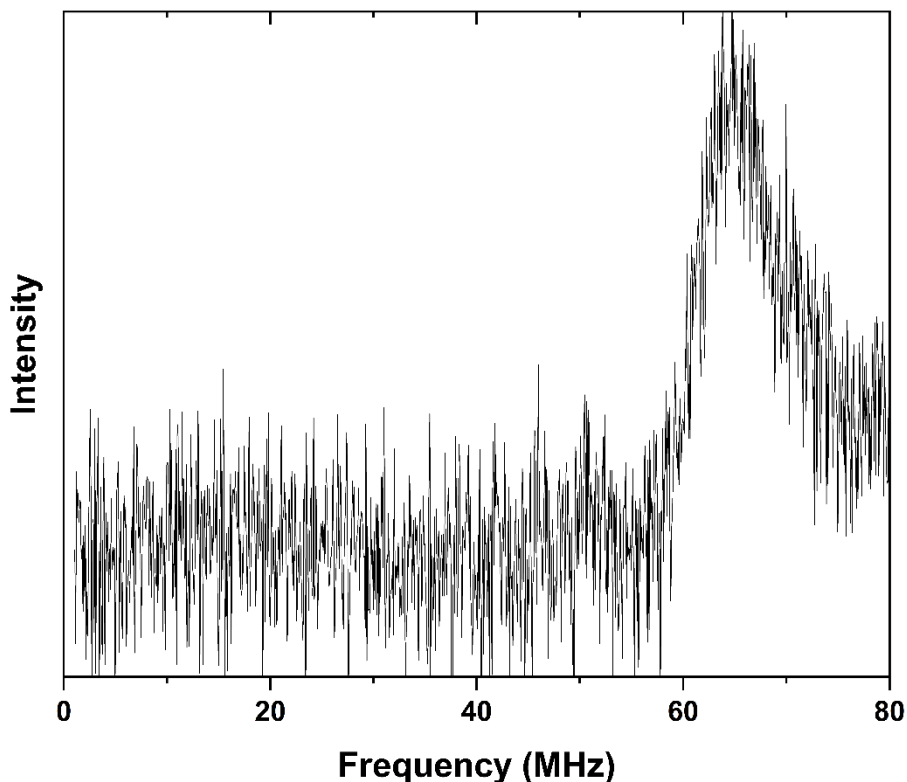


Figure IV-31. ENDOR spectra recorded at $T = 10$ K, 33721 GHz and $B = 1217$ mT.

IV.4 FROM MONONUCLEAR TO DINUCLEAR COMPLEXES

The encouraging results obtained for the Cu(II) mononuclear complex motivated us to synthesize the binuclear complexes presented in the introduction, using Cu(II), V(IV)O and Ni(II) that will play the role of the diamagnetic derivative (Ni(II) is diamagnetic in a square-planar geometry).

IV.4.a Synthesis

We started by preparing the complex with the longer M-M distance depicted in Figure IV-32. Two synthetic ways were considered. In the first strategy, we employed a synthetic procedure described in the literature,[13] to obtain the alkyne moiety. Then we tried to couple the benzene bridge with two salophen moieties. This was supposed to lead to the binuclear complex with M-M distance around 2.1 nm (Figure IV-32).

CHAPTER IV: QUANTUM COHERENCE OF MONO- AND BINUCLEAR COMPLEXES BASED ON THE SALOPHEN LIGAND

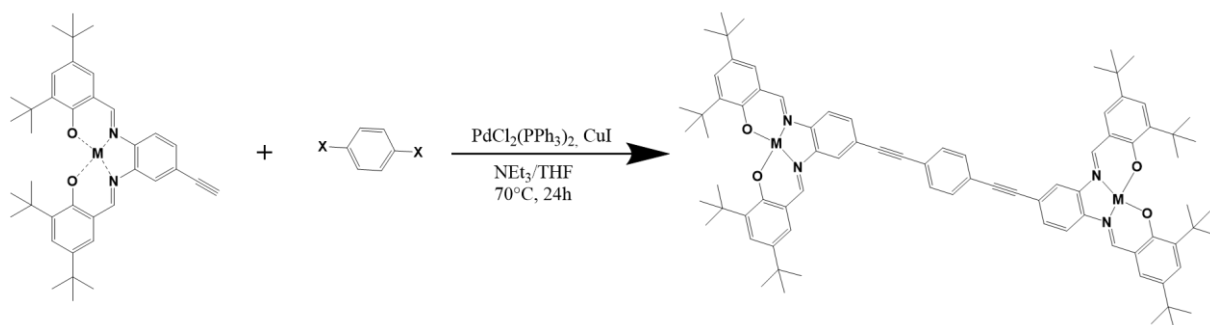


Figure IV-32. Synthetic procedure for the formation of the dimer. $X = Br, I$

Unfortunately, for the last step we had no evidence based on NMR (using Ni(II)) and IR that we obtained the desired compound. The only information we obtained was the disappearance of the alkyne H atom, evidencing it reacted (NMR pic at 3.17 ppm or IR band at 3100 cm^{-1} Figure IV-50, annexe). Unfortunately, it is difficult to check whether the benzene reactant is still present or not because its H atoms have chemical shifts close to the other aromatic rings present in the salophen moiety.

The solution left to crystallize gave a small amount of crystals that turned out to be the complex obtained from the direct coupling of the Ni(salophen) units (Table IV-5). This coupling reaction (Glaser coupling [14]) is well known and competes with the one we intended to carry out.

Space Group	$C 2/c$ (15)
Cell Lengths	a 51.379(10) b 12.041(2) c 27.275(5)
Cell Angles	α 90 β 113.423(6) γ 90
Cell Volume	15483.3
Z, Z'	Z : 12 Z' : 1.5

Table IV-5. Crystallographic data of $[Cu_2(salophen)_2(\mu\text{-bis-alkyne})]$

CHAPTER IV: QUANTUM COHERENCE OF MONO- AND BINUCLEAR COMPLEXES BASED ON THE SALOPHEN LIGAND

We tried to replace Br by I in order to increase the reactivity of the bridge moiety but this yields the same result. At the end, we probably have a mixture between the desired product and the one due to Glaser reaction. We do not expect any difference in the coordination sphere in both cases and even with the unwanted product the distance between the two copper is around 1.6 nm. Thus, the sample can be studied in pulsed EPR to confirm the independence of the two metallic centres.

We tried a second synthesis strategy in one step (Figure IV-33) without obtaining better results.

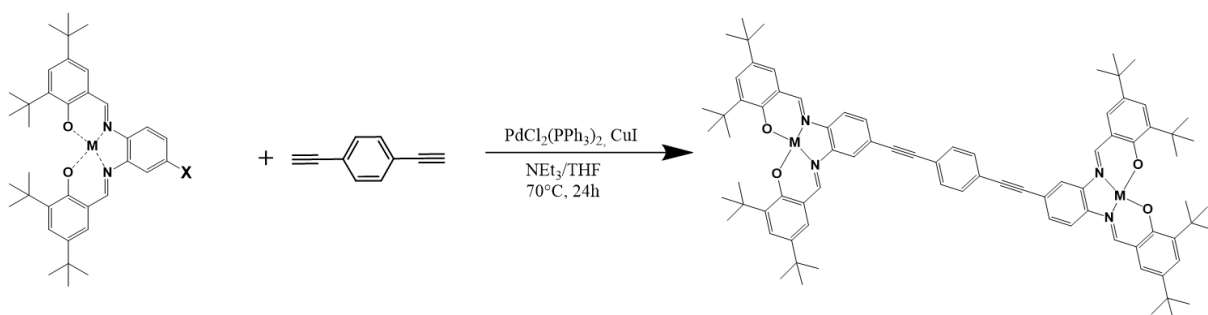


Figure IV-33. Synthetic procedure for the formation of $[M_2(\text{bis-salophen})]$ using one-step pathway. $X = \text{Br}, \text{I}$

The main problem faced is that all the molecules are very closed from a structural point of view rendering the purification and analysis of the result complicated. This is why we added OMe groups on the bridging moiety (Figure IV-34). We expected to obtain a signal around 3-4 ppm in NMR and a strong band in IR around 1200 cm^{-1} . We also decided to use $\text{Pd}(\text{PPh}_3)_4$ and to add dropwise the alkyne to maximize the Sonogashira coupling [15] instead of the Glaser one.

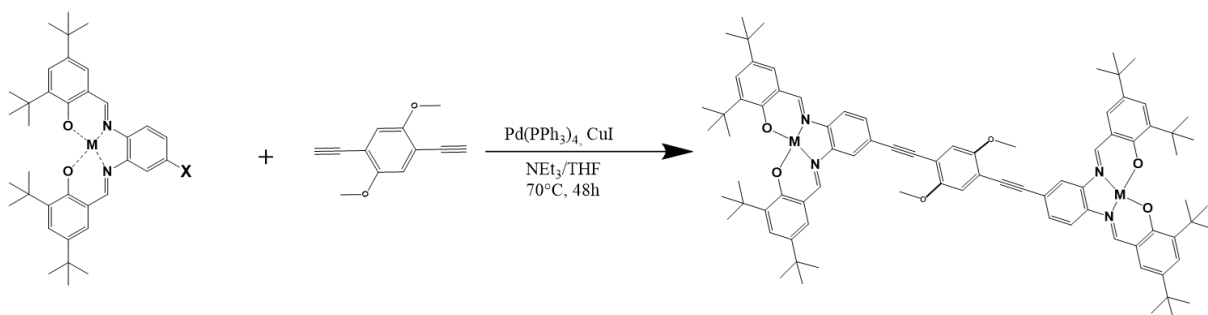


Figure IV-34. New synthetic procedure for the formation of $[M_2(\text{bis-salophen-OMe})]$.

With this new complex we found the conditions (THF/Hexane/DCM 10:10:1) to purify our mixture and isolated three fractions. The first one (most important fraction) corresponds to the unreacted monomer, but the second one could be our product since NMR show the presence of OMe (Figure IV-35). To be sure that we have formed the dimer we needed to compare the integration of the proton of the OMe with the one of the salophen group. Here, we see that

CHAPTER IV: QUANTUM COHERENCE OF MONO- AND BINUCLEAR COMPLEXES BASED ON THE SALOPHEN LIGAND

the integrations are in agreement with the expected ones because for 1 salophen proton we have 2.5 OMe proton. We need to continue the analysis (2D NMR) and start the recrystallization test on this fraction. It is worth mentioning that despite the presence of tertbutyls groups the solubility is very low.

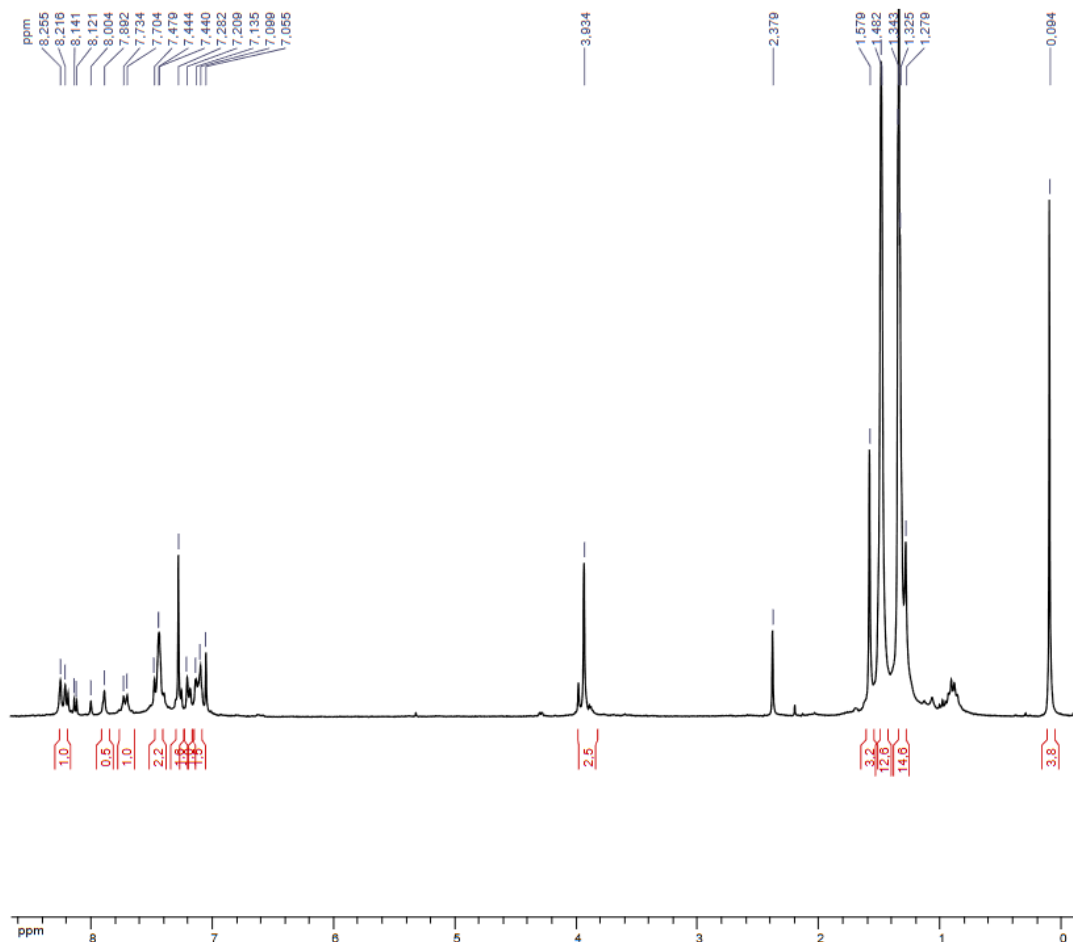


Figure IV-35. NMR spectra of the fraction 2 in $CDCl_3$.

IV.4.b Pulsed EPR experiment

We decided to study in pulsed-EPR the binuclear Cu(II) complex obtained with the indirect pathway because we assume that it is a dimer with paramagnetic centers separated by at least 1.7 nm. The compound was diluted at 10^{-3} mol/L in $CD_2Cl_2/CDCl_3$ mixture. The following section will present the preliminary result obtained on this compound.

The EDFS of the dimer (Figure IV-36) is exactly the same as the monomer. This is not surprising because the coordination spheres are the same in both cases.

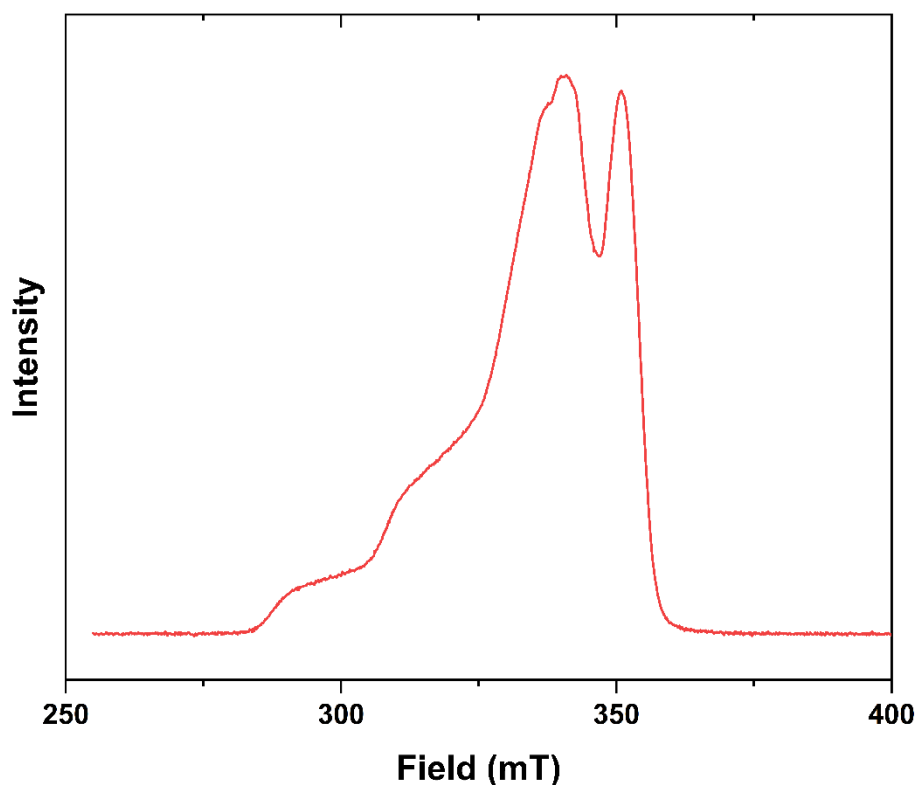


Figure IV-36. EDFS of $[Cu_2(\text{bis-salophen})]$ at $T = 20$ K and 33.8 GHz.

The variation of T_1 with temperature at 1100 mT is depicted in Figure IV-37. As we can see T_1 is around hundred times longer than for the Ni(II) compounds. The variation of T_1 with temperature can be described by a single-exponential model. The temperature dependence is given below:

$$T_1(T) = 54 \times e^{\frac{(-T)}{2.11}}$$

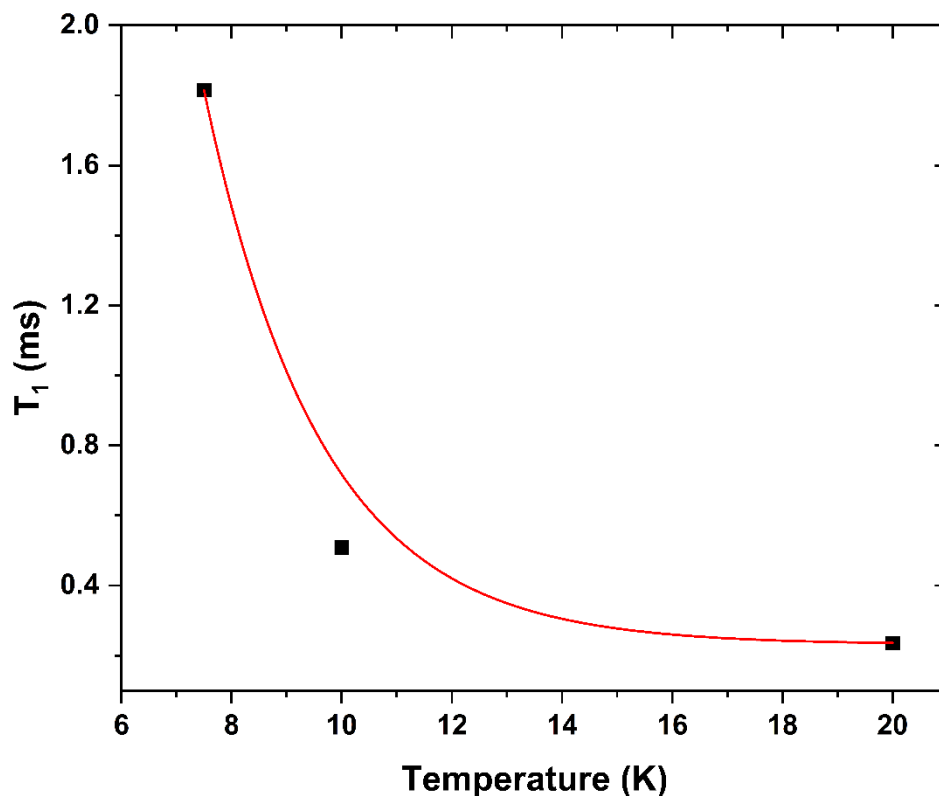


Figure IV-38. Variation of the spin-lattice relaxation time with temperature at $B = 1100$ mT and 33.72 GHz.

The spin-lattice relaxation time have been obtained by fitting the data using a stretched exponential model. The fitted curve, for $T = 10$ K (Figure IV-38), gives $\alpha_s = 0.72$. Such value lower than 1, indicates the presence of distributions of molecules, probably due to the high concentration in the frozen solution. We can see that T_1 remains long at $T = 10$ K and $B = 1100$

mT (red curve) but shorter than the mononuclear (blue curve) in the same condition.

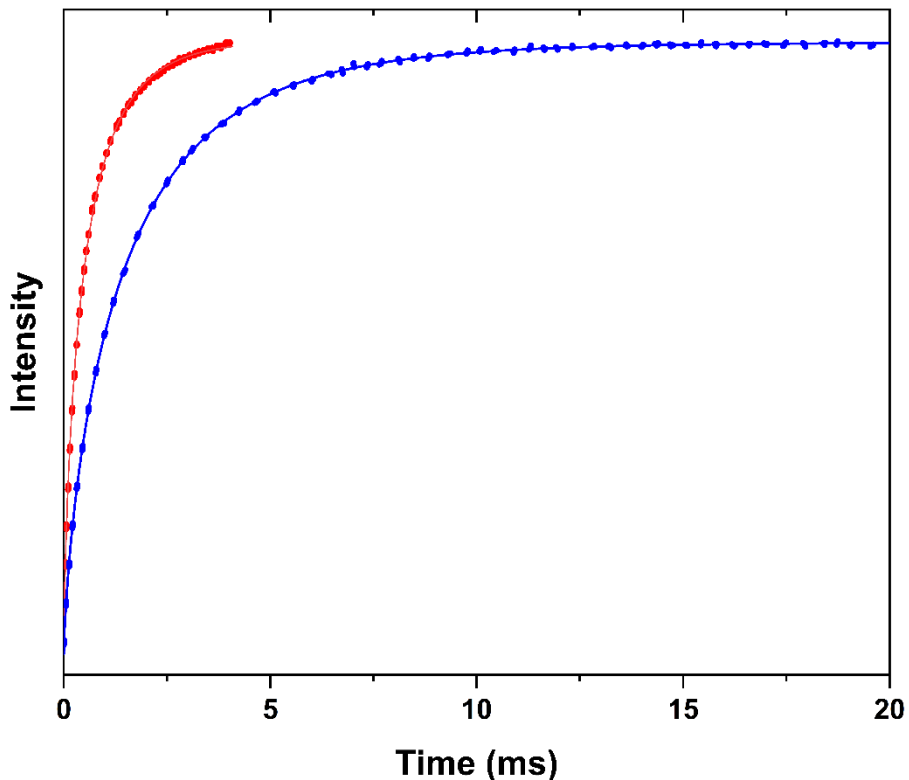


Figure IV-38. Spin-lattice relaxation time curves of $[Cu(salophen)]$ (blue) and $[Cu_2(bis-salophen)]$ (red) at $T = 10\text{ K}$, 33.72 GHz and $B = 1100\text{ mT}$.

We tried again to see any effect of the flip-flop process but here again, no influence was observed despite using power attenuation from 6 dB to 18 dB (Figure IV-39). The coherence time found $T_2 = 2.5\ \mu\text{s}$ is nearly the same as for the previously measured for the mononuclear complex.

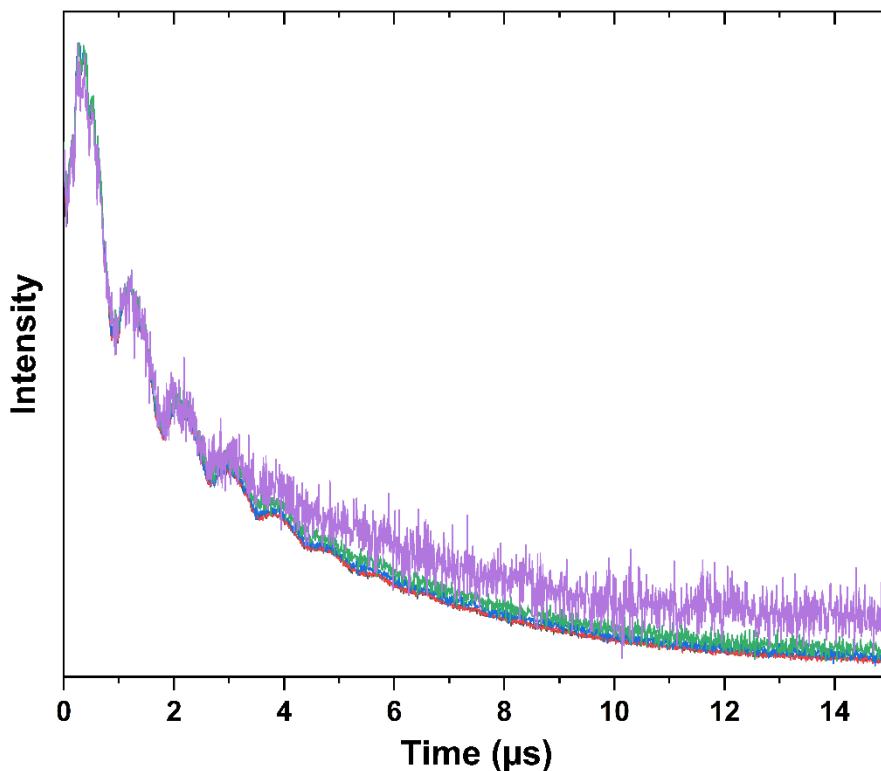


Figure IV-39. Spin-Spin relaxation after a Hahn echo sequence at 10^{20} spins/cm³ (top) and 10^{19} spins/cm³ (top) at $B = 1186$ mT at 6 dB (black) 9 dB (red) 12 dB (blue), 15 dB (purple) and 18 dB (purple).

V.4.c.i DEER experiment

Finally, we have reached the stage where we can try to measure the coupling between two copper atoms. Unfortunately, despite numerous attempts in both X and Q bands in order to discriminate between the modulation due to hyperfine coupling and the one due to the dipolar coupling. We failed to record a satisfactory spectrum (Figure IV-42). This can be explained by the following:

- (i) We applied our pulses at random frequencies, likely exciting only few molecules, which resulted in a poor signal-to-noise ratio.
- (ii) We observed periodic oscillations in the curve, of 14 MHz in X band which are due to proton coupling. The mathematical treatment of the data proposed in DEERANALYSIS [16] is not compatible with these periodic oscillations of constant intensity
- (iii) Both Cu(II) exhibit the same coherence time

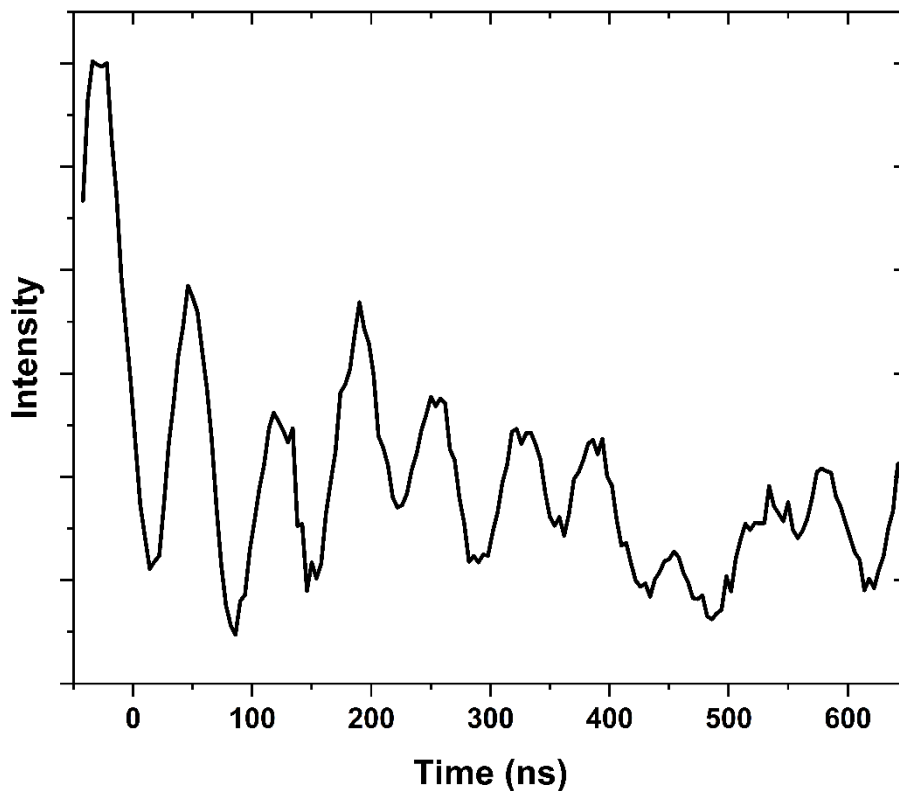


Figure IV-42. DEER curve obtained after applying baseline correction (asymmetric least squares smoothing) module of Origin software.

We observed a deformation of the signal at $t = 458$ ns, this supplementary modulation can be due the dipolar coupling between the two Cu(II). The associated coupling will be $J = 2.1$ MHz. However, we only observe one modulation rendering difficult to conclude if it corresponds to our dipolar coupling or not. Unfortunately, the spectra recorded at Q band is too noisy to extract any information.

IV.4.b.ii ENDOR

The ENDOR spectrum of the binuclear complex is identical to that of the mononuclear Cu(salophen) (Figure IV-43). Surprisingly, the signal in the binuclear sample was much more

intense compared to that of the mononuclear one.

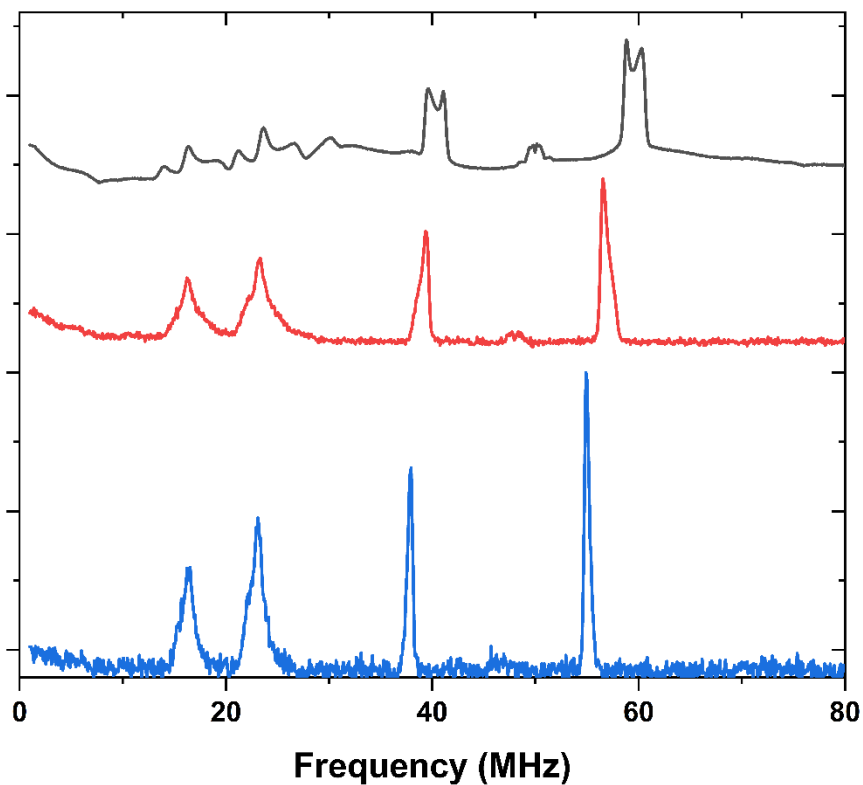


Figure IV-43. ENDOR spectra recorded at $T = 10$ K, 33.78 GHz and $B = 1100$ mT (blue), $B = 1137$ mT (red) and $B = 1186$ mT (black).

We want to go further and demonstrates the potential manipulation of those nuclear spins. This is why we performed nutation on the two nuclear spins (N and H). As we can see, in both cases we have modulation around $70 \mu\text{s}$ meaning that $T_2 > 70 \mu\text{s}$ and we can manipulate the spins for computation during at least this period without any loss of information.

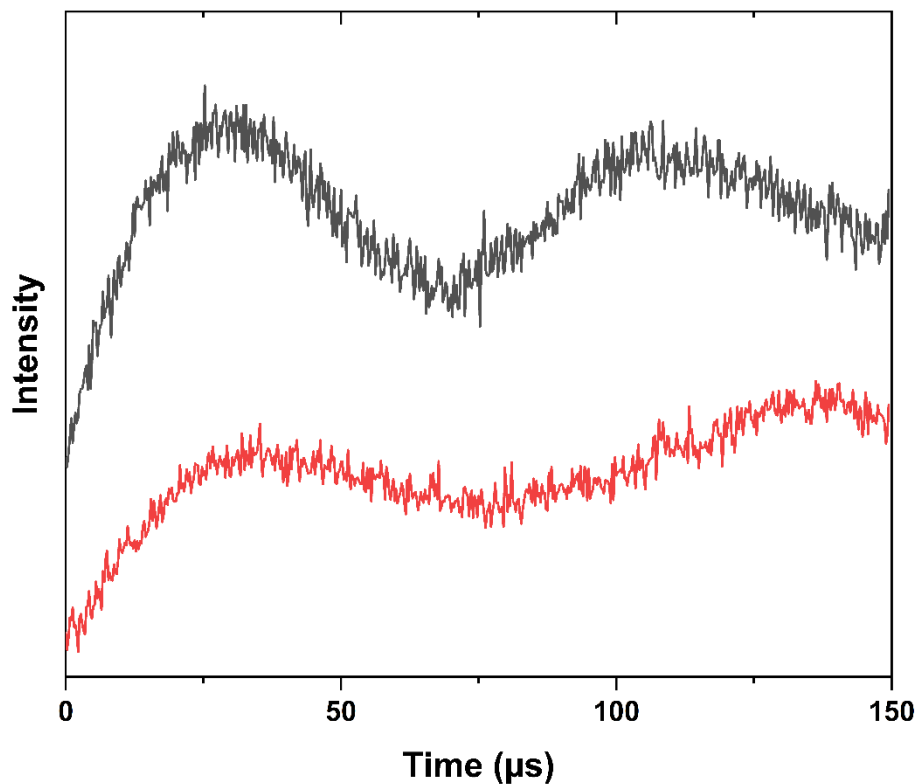


Figure IV-44. Nutation experiment at 23.24MHz (red) and 55MHz (black) at $T = 20\text{ K}$ and $B = 1100\text{ mT}$. Those frequencies correspond respectively to nitrogen and hydrogen.

Then we tried to estimate the coherence time of the nuclear spins especially the proton which possess the sharpest transition (Figure IV-45).

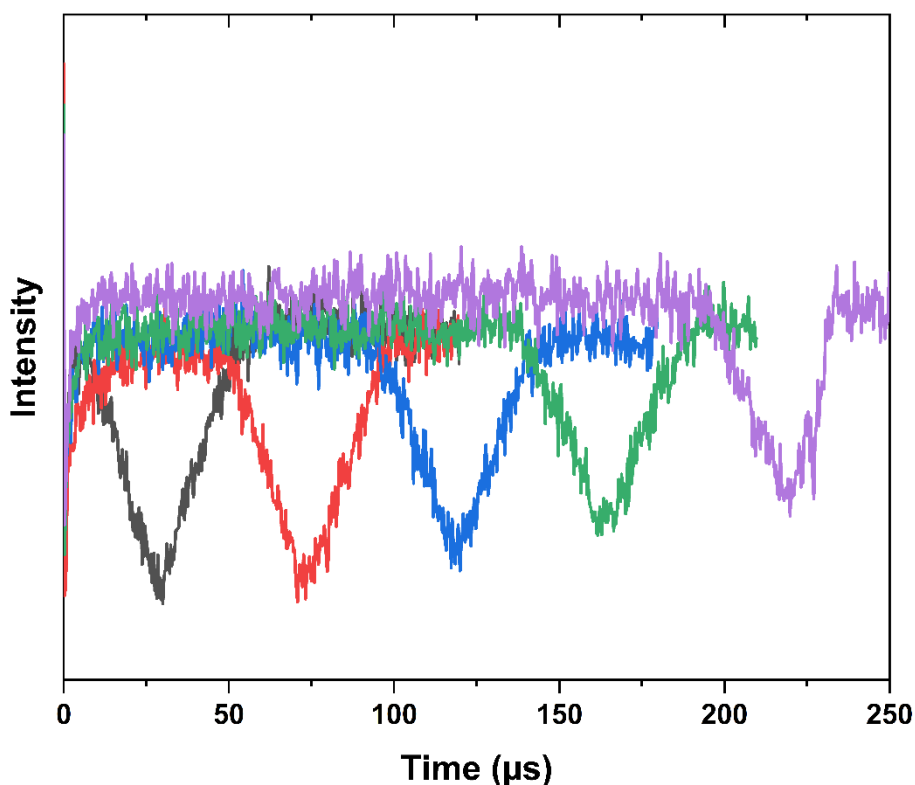


Figure IV-45. Observation of the proton echo at different T_2 times at $T = 10\text{ K}$, $B = 1100\text{ mT}$ and 55 MHz

We found the same result for the binuclear compound as for the mononuclear one. Due to a lack of time we could not detect an echo at longer times but we assumed that the coherence time of the proton will be the same as for the mononuclear complex. Additionally, the better signal quality could help us to build the exponential decay curve associated to determine the mechanisms responsible for the relaxation. We could not assess the coherence time of the nitrogen due to a lack of time but here again we expected a coherence time in the same range as for the mononuclear complex.

IV.5 CONCLUSION

In this chapter we have studied system possessing spin $S=1/2$ and recorded their relaxation time.

We found for the Cu(II) mononuclear complex $T_1 \approx 10$ ms at $T = 5$ K and $T_2 \approx 1.8$ μ s and for V(IV) $T_1 \approx 40$ ms at $T = 5$ K and $T_2 \approx 3$ μ s. In both cases the applied magnetic field seems not to have any effect while for the V(IV) a slight temperature dependence was observed. We performed ENDOR experiment on both compounds but the numerous hyperfine coupling in the V(IV) entity rendering the acquisition of an echo difficult while sharp transitions are found for the Cu(II). This allowed us to observe nuclear echo for nitrogen at time $t = 0.4$ ms and for proton at $t = 0.56$ ms. Those coherence times are in the same order of magnitude of the best system presented in the introduction.

We tried to go further by the study of a dimer but we faced synthesis difficulty notably on the purification of the compound. However the Cu(II) dimer studied seems to show the same kind of property than the Cu(II) monomer.

IV.6 EXPERIMENTAL PART

IR spectra were recorded on a Bruker TENSOR - 27 FT - IR spectrometer equipped with an attenuated total reflectance (ATR) sample holder in the 4000 - 250 cm^{-1} range.

NMR spectra were recorded on a Bruker Avance I (400 MHz), Bruker Avance I (360 MHz), Bruker Avance I (300 MHz).

X-ray diffraction data were collected by using a Bruker Kappa VENTURE PHOTON 100 diffractometer with graphite-monochromatic Mo $K\alpha$ radiation ($\lambda = 0.71073 \text{ \AA}$).

Reagents were purchased from commercial suppliers used without further purification and unless otherwise stated. Solvents have been purchased at Carlo Erba and VWR and distilled, if necessary, according to standard drying procedures (i.e. THF: Na / benzophenone; Et_2O : Na / benzophenone; CH_2Cl_2 : CaH_2 ; CH_3OH : Mg; CH_3CN : CaH_2).

[M₂(bis-salophen)]

Direct pathway

In a Schlenck, [M(salophen-X)] (2 eq), $\text{PdCl}_2(\text{PPh}_3)_2$ (8 mg, 0.012 mmol, 10%) and CuI (5 mg, 0.024 mmol, 20 %) was dried during 2h then distilled THF (8 mL) was added and the mixture was heated at 70°C. 1,4-Diethynylbenzene (113 mg, 0.45 mmol, 0.9 eq) was dissolved in a mixture of NEt_3 (6 mL) and distillate THF (12 mL). The mixture was degassed during 10 min then added dropwisely. The reaction was allowed to stirred at 70°C during 48h. After solvent evaporation under reduced pressure, CH_2Cl_2 and 10 drops of tris(2-aminoethyl)amine were added. The mixture was then washed with water, dried over MgSO_4 , filtrated, and evaporated. The crude product was purified by column chromatography (SiO_2 : CH_2Cl_2 / MeOH (0 – 10 %)).

Indirect pathway

In a Schlenck, 1,4- dibromobenzene (47 mg, 0.12 mmol, 1eq), [M(salophen)] (2 eq), $\text{PdCl}_2(\text{PPh}_3)_2$ (8 mg, 0.012 mmol, 10%) and CuI (5 mg, 0.024 mmol, 20 %) was dried during 2h. Then a mixture of NEt_3 (6 mL) and distillate THF (12 mL) was degassed during 10 min then added. The mixture was degassed at room temperature then heated at 70°C during 48h. After solvent evaporation under reduced pressure, CH_2Cl_2 and 10 drops of tris(2-aminoethyl)amine were

CHAPTER IV: QUANTUM COHERENCE OF MONO- AND BINUCLEAR COMPLEXES BASED ON THE SALOPHEN LIGAND

added. The mixture was then washed with water, dried over MgSO_4 , filtrated, and evaporated. The crude product was purified by column chromatography (SiO_2 : CH_2Cl_2 / MeOH (0 – 10 %)).

[M₂(bis-salophen-OMe)]

In a Schlenck, [M(salophen-I)] (2 eq), $\text{Pd}(\text{PPh}_3)_4$ (57 mg, 0.05 mmol, 5%), CuI (5 mg, 0.024 mmol, 20 %) and PPh_3 (5 mg, 0.02 mmol) was dried during 2h then distilled THF (12 mL) was added and the mixture was heated at 70°C. 1,4-Diethynyl-2,5-dimethoxybenzene (74 mg, 0.40 mmol, 0.8 eq) was dissolved in a mixture of NEt_3 (6 mL) and distillate THF (12 mL). The mixture was degassed during 10 min then added dropwisely over 30 min. The reaction was allowed to stirred at 70°C during 48h. After solvent evaporation under reduced pressure, CH_2Cl_2 and 10 drops of tris(2-aminoethyl)amine were added. The mixture was then washed with water, dried over MgSO_4 , filtrated, and evaporated. The crude product was purified by column chromatography (SiO_2 : THF/Hexane/DCM 10:10:1)

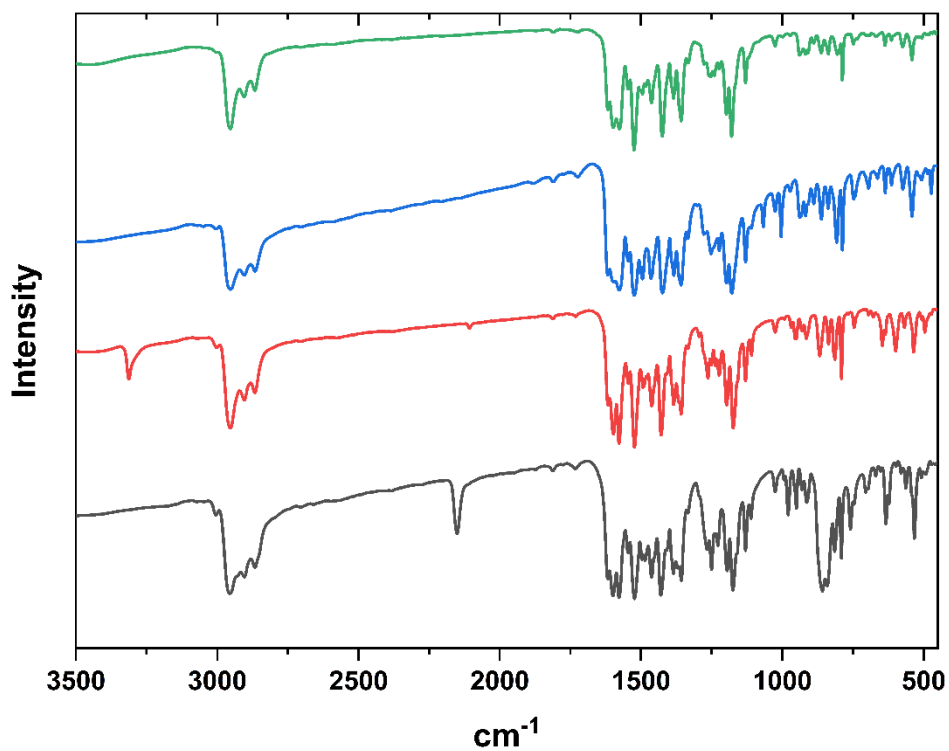


Figure IV-46. IR spectra of $[\text{Ni}(\text{salophen-alkyne-TMSA})]$ (black), $[\text{Ni}(\text{salophen-alkyne})]$ (red), $[\text{Ni}_2(\text{bis-salophen})]$ (blue) and $[\text{Ni}_2(\text{bis-salophen-alkyne})]$ (green) which correspond to the product obtain due to Glaser coupling.

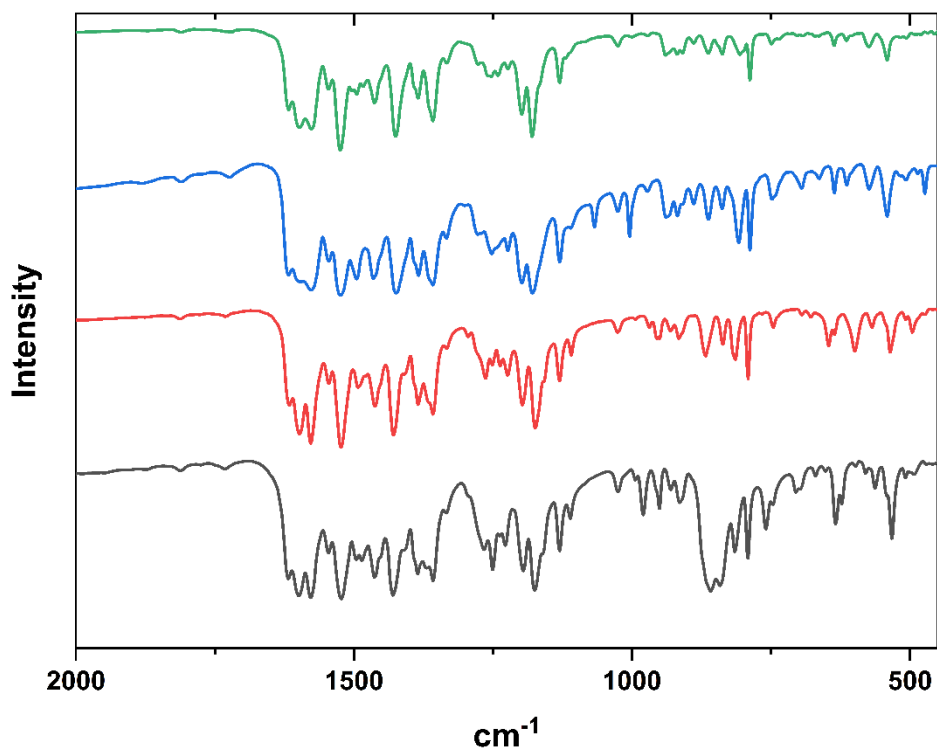


Figure IV-47. IR spectra (zoomed) of $[\text{Ni}(\text{salophen-alkyne-TMSA})]$ (black), $[\text{Ni}(\text{salophen-alkyne})]$ (red), $[\text{Ni}_2(\text{bis-salophen})]$ (blue) and $[\text{Ni}_2(\text{bis-salophen-alkyne})]$ (green) which correspond to the product obtain due to Glaser coupling.

CHAPTER IV: QUANTUM COHERENCE OF MONO- AND BINUCLEAR COMPLEXES BASED ON THE SALOPHEN LIGAND

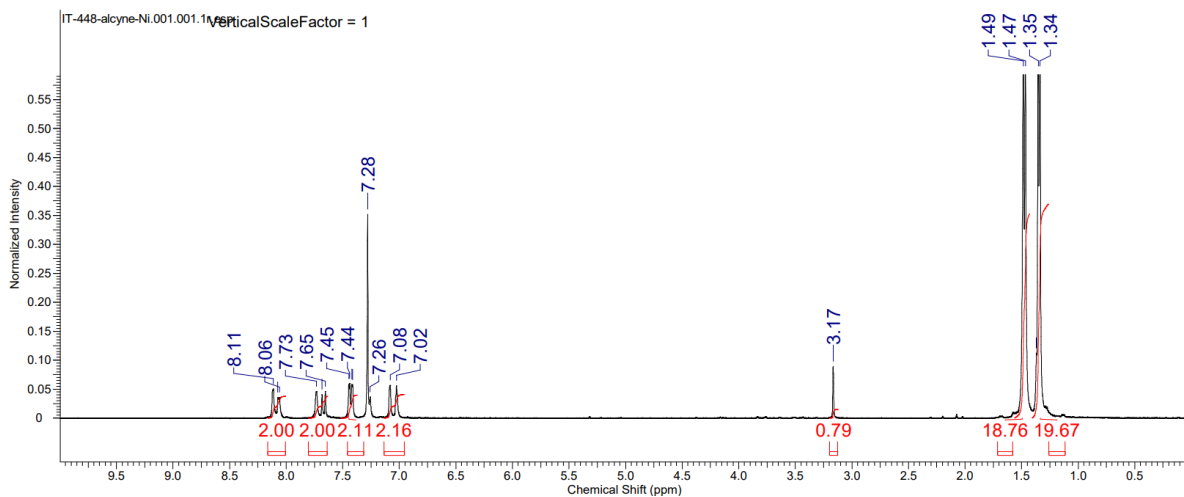


Figure IV-48. NMR spectra of $[Ni(salophen-alkyne)]$ in $CDCl_3$

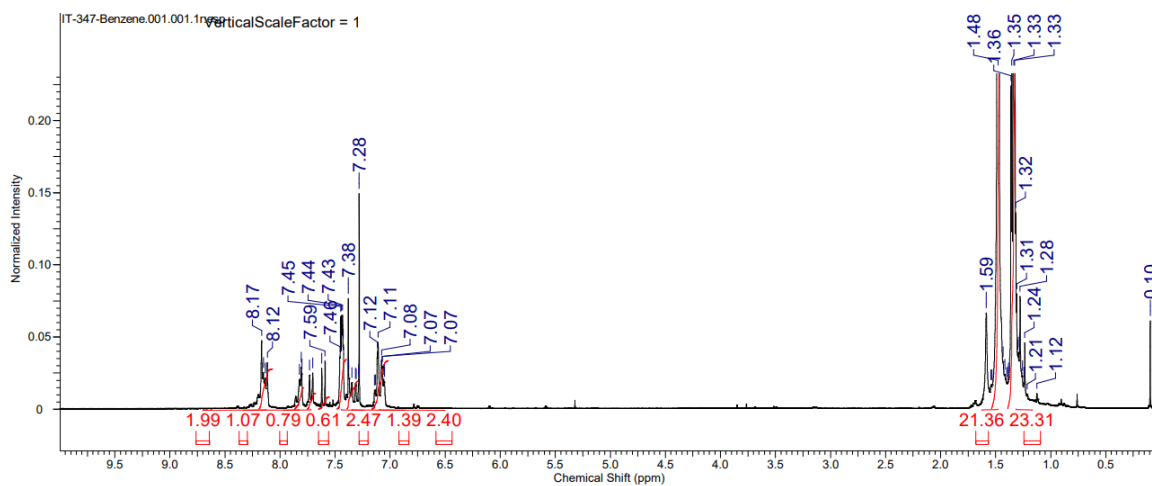


Figure IV-49. NMR spectra of $[Ni_2(bis-salophen)]$ in $CDCl_3$

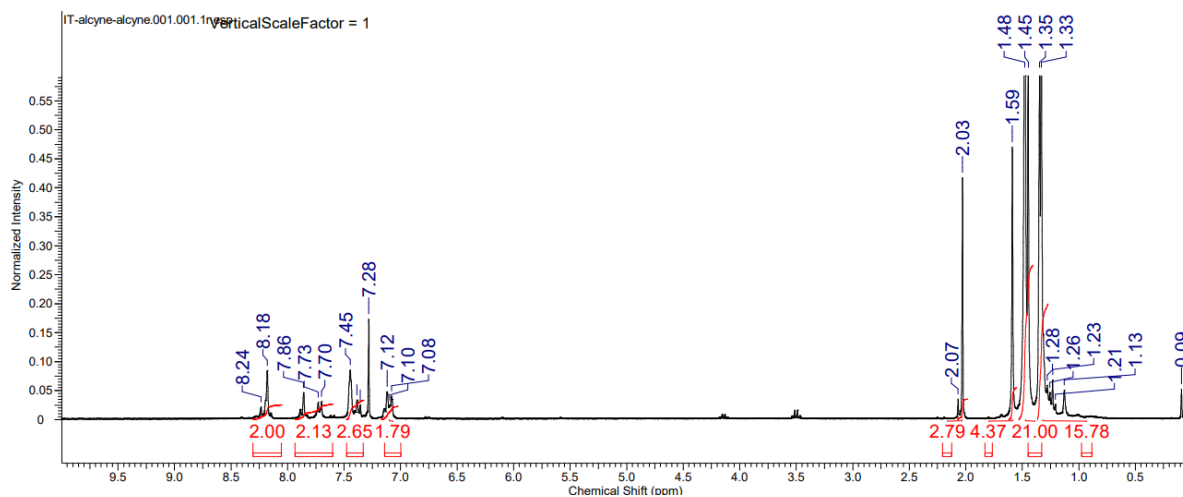


Figure IV-50. NMR spectra of $[Ni_2(bis-salophen-alkyne)]$ in $CDCl_3$

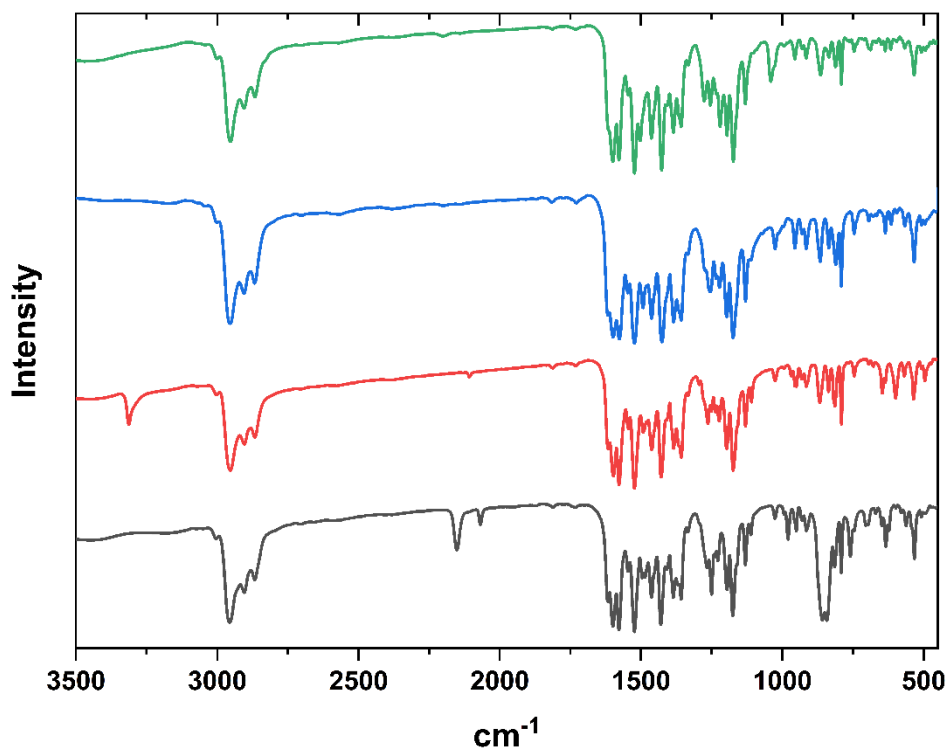


Figure IV-51. IR spectra of [Cu(salophen-alkyne-TMSA)] (black), [Cu(salophen-alkyne)] (red), [Cu₂(bis-salophen)] (blue) and [Cu₂(bis-salophen-OMe)] (green)

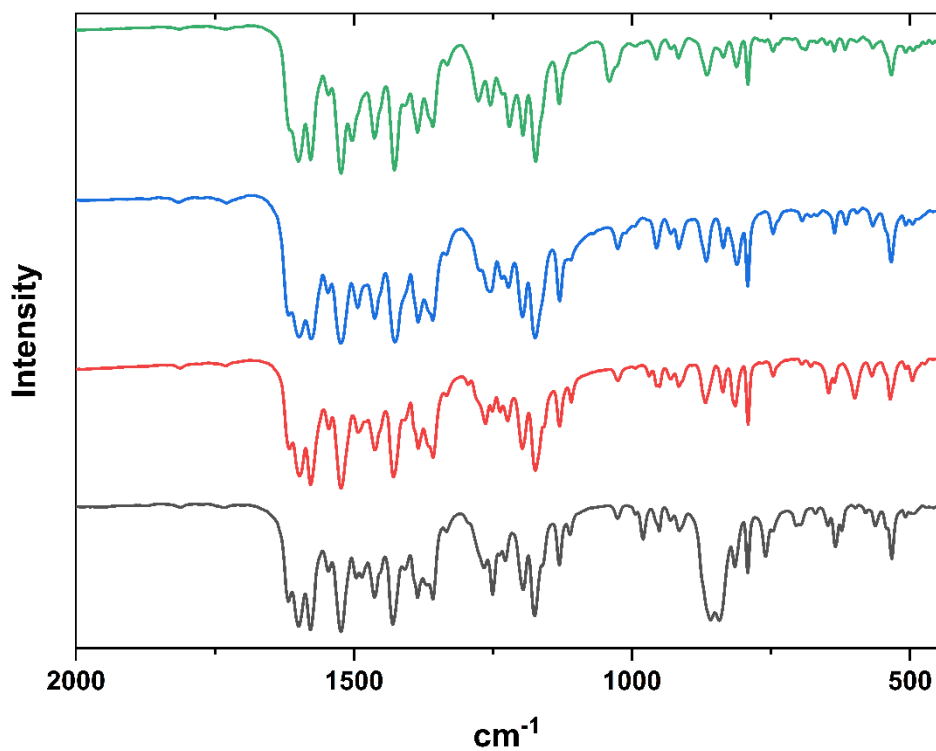


Figure IV-52. IR spectra (zoom) IR spectra of [Cu(salophen-alkyne-TMSA)] (black), [Cu(salophen-alkyne)] (red), [Cu₂(bis-salophen)] (blue) and), [Cu₂(bis-salophen-OMe).

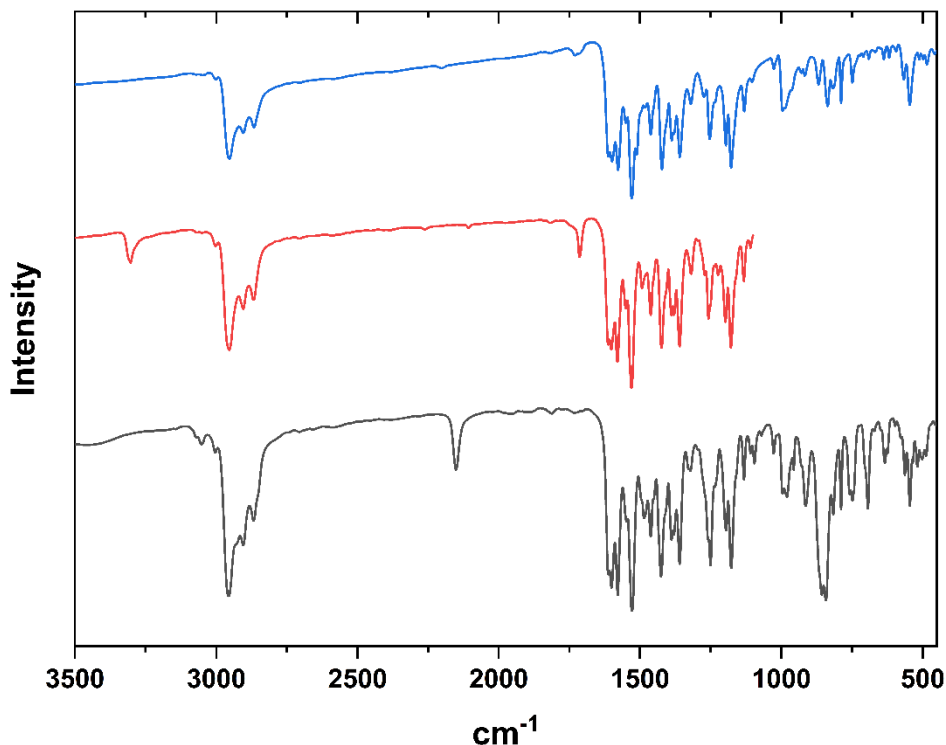


Figure IV-53. IR spectra of $[VO(\text{salophen-alkyne-TMSA})]$ (black), $[VO(\text{salophen-alkyne})]$ (red), $[VO_2(\text{bis-salophen})]$ (blue).

Pulsed EPR sequences

The experiments have been performed at 6 dB for the classical pulsed EPR sequences and 3 dB for the ENDOR experiments.

Echo-detected EPR. The echo-detected field-swept (EDFS) spectra were recorded with a two-pulse primary Hahn-echo sequence ($\pi/2 - t - \pi - t - \text{echo}$), with microwave pulse lengths of 16 and 32 ns respectively, a fixed delay time $t = 200$ ns for all samples and with the variation of the static B_0 magnetic field.

Hahn echo sequence. The spin-spin relaxation (T_2) spectra were recorded with a two-pulse primary Hahn-echo sequence ($\pi/2 - t - \pi - t - \text{echo}$), with microwave pulse lengths of 16 and 32 ns respectively, a fixed delay time $t = 200$ ns for all samples

Inversion recovery curves were collected by application of a three-pulse sequence ($\pi - T - \pi/2 - \tau - \pi - t - \text{echo}$), with microwave pulse lengths of 32, 16 and 32 ns respectively, pulse lengths and a fixed delay time $T = 4000$ ns and $t = 2000$ ns for all samples.

CHAPTER IV: QUANTUM COHERENCE OF MONO- AND BINUCLEAR COMPLEXES BASED ON THE SALOPHEN LIGAND

Davies ENDOR

The Endor spectra were recorded with a sequence ($\pi - T - \pi_{rf} - \pi/2 - t - \pi - t - \text{echo}$), with microwave pulse lengths of 32, 16 and 32 ns respectively, a fixed delay time $T = \mu\text{s}$ and $t = 200$ ns and radiofrequency pulse lengths of 10 μs for all samples.

Nuclear Hahn echo

The spin-spin relaxation (T_{2N}) spectra were recorded with the following sequence ($\pi - T - \pi_{rf}/2 - TT - \pi_{rf} - TT - \pi_{rf}/2 - T_3 - \pi/2 - t - \pi - t - \text{echo}$), with microwave pulse lengths of 32, 16 and 32 ns respectively, with radiofrequency pulse lengths of 12, 24 and 12 μs respectively and a fixed delay time $t = 200$ ns, $T_3 = 1$ ms and $TT = 26$ μs for all samples.

IV.7 REFERENCES

- [1] G. R. Eaton, S. S. Eaton, *Journal of Magnetic Resonance* **1999**, *136*, 63–68.
- [2] J.-L. Du, G. R. Eaton, S. S. Eaton, *Journal of Magnetic Resonance, Series A* **1995**, *117*, 67–72.
- [3] S. S. Eaton, G. R. Eaton, *Journal of Magnetic Resonance, Series A* **1995**, *117*, 62–66.
- [4] S. S. Eaton, J. Harbridge, G. A. Rinard, G. R. Eaton, R. T. Weber, *Appl. Magn. Reson.* **2001**, *20*, 151–157.
- [5] J. Peisach, W. E. Blumberg, *Archives of Biochemistry and Biophysics* **1974**, *165*, 691–708.
- [6] F. D. Breitgoff, K. Keller, M. Qi, D. Klose, M. Yulikov, A. Godt, G. Jeschke, *Journal of Magnetic Resonance* **2019**, *308*, 106560.
- [7] J. R. Harmer, in *eMagRes*, John Wiley & Sons, Ltd, **2016**, pp. 1493–1514.
- [8] O. Schiemann, C. A. Heubach, D. Abdullin, K. Ackermann, M. Azarkh, E. G. Bagryanskaya, M. Drescher, B. Endeward, J. H. Freed, L. Galazzo, D. Goldfarb, T. Hett, L. Esteban Hofer, L. Fábregas Ibáñez, E. J. Hustedt, S. Kucher, I. Kuprov, J. E. Lovett, A. Meyer, S. Ruthstein, S. Saxena, S. Stoll, C. R. Timmel, M. Di Valentin, H. S. Mchaourab, T. F. Prisner, B. E. Bode, E. Bordignon, M. Bennati, G. Jeschke, *J. Am. Chem. Soc.* **2021**, *143*, 17875–17890.
- [9] D. M. Murphy, R. D. Farley, *Chem. Soc. Rev.* **2006**, *35*, 249–268.
- [10] C.-J. Yu, M. J. Graham, J. M. Zadrozny, J. Niklas, M. D. Krzyaniak, M. R. Wasielewski, O. G. Poluektov, D. E. Freedman, *J. Am. Chem. Soc.* **2016**, *138*, 14678–14685.
- [11] J. J. L. Morton, A. M. Tyryshkin, R. M. Brown, S. Shankar, B. W. Lovett, A. Ardavan, T. Schenkel, E. E. Haller, J. W. Ager, S. A. Lyon, *Nature* **2008**, *455*, 1085–1088.
- [12] H. Morishita, S. Kobayashi, M. Fujiwara, H. Kato, T. Makino, S. Yamasaki, N. Mizuochi, *Sci Rep* **2020**, *10*, 792.
- [13] B. Doistau, L. Benda, J.-L. Cantin, L.-M. Chamoreau, E. Ruiz, V. Marvaud, B. Hasenknopf, G. Vives, *J. Am. Chem. Soc.* **2017**, *139*, 9213–9220.
- [14] K. S. Sindhu, G. Anilkumar, *RSC Advances* **2014**, *4*, 27867–27887.
- [15] M. Joshaghani, E. Faramarzi, E. Rafiee, M. Daryanavard, J. Xiao, C. Baillie, *Journal of Molecular Catalysis A: Chemical* **2006**, *259*, 35–40.
- [16] O. Dalmas, H. C. Hyde, R. E. Hulse, E. Perozo, *J. Am. Chem. Soc.* **2012**, *134*, 16360–16369.

CONCLUSION AND PERSPECTIVES

Conclusion and perspectives

In this dissertation, two main parts are presented.

The first part focuses on setting up a synthetic strategy for the design of $S = 1$ magnetic molecules that can play the role of quantum bits (qubits) and present a clock transition (CT) at zero applied magnetic field. To do so, we study the structural parameters (electronic and geometrical) of mononuclear Ni(II) complexes (d^8 , $S = 1$ spin) that influence the Zero-Field Splitting (ZFS) spin Hamiltonian parameters. We focus on complexes with distorted octahedral geometry (with pseudo tetragonal and trigonal axial symmetry). The objective was to obtain Ni(II) complexes with uniaxial anisotropy (negative D value, where D is the axial ZFS parameter) and rhombicity that lead to two low-lying levels allowing the complex to play the role of a qubit, with a qubit frequency ($2E$, where E is the rhombic ZFS parameter) in the range accessible by X- or Q-band EPR apparatus. This was done in four steps:

- (i) The explanation of the origin of ZFS parameters for an $S = 1$ spin
- (ii) The prediction of these parameters using wave function based theoretical calculations
- (iv) The confrontation of the calculated parameters with those extracted from High Field-High Frequency EPR (HF-HFEPR) spectroscopy study.

We have demonstrated that it is possible to predict and tune (to a certain extent) the axial ZFS parameter D and to tune the rhombic parameter E playing with different factors such as crystal packing and electronic effect in the case of the study of the $[\text{Ni}(\text{bpy})_3]^{2+}$ family. We succeeded to prepare complexes complying to all the criteria ($D < 0$ and $2E \approx 0.32 \text{ cm}^{-1}$) so that their relaxation time can be investigated by pulsed EPR. The pulsed EPR measurements have shown that it is possible to observe a transition at zero field even if the mean E value does not match exactly the frequency of the cavity. This is due to E -strain. In order to evidence the CT behavior, we used two approaches. The first straightforward approach consisted in measuring the coherence times as a function of the magnetic field. We demonstrated that the coherence time remains constant for applied magnetic fields lower than 2 mT (therefore near zero field) and then becomes shorter upon increasing the magnitude of the field consistent with negligible magnetic fluctuations at zero field which is the signature of a CT. The second more direct approach consisted in measuring performing the same experiment but on a sample where

Conclusion and perspectives

Co(II) derivative where embedded with the Ni(II) ones, that bring large magnetic fluctuation to the material. The experiments showed that the T_2 of the Ni(II) complexes remains insensitive to magnetic fluctuations at zero field, while that of the Co(II) complexes is highly reduced.

Complimentary investigations were focused on increasing the spin-lattice relaxation time T_1 . Several strategies have been employed, including using a matrix with a high Debye temperature, enhancing ligand rigidity, and optimizing the number of ligands. These approaches have enabled us to achieve longer T_1 times. We have seen that transposing mononuclear Ni(II) complexes into binuclear ones was particularly challenging notably due to the difficulties to predict the value of E . Most of the complexes synthesized were EPR silent. Additionally, even for the CT the relaxation time remains short rendering the pulsed EPR study difficult. We concluded that there are too many constraints and parameters to be mastered at once and decided to investigate half integer spin systems.

The second part focuses on the study of spin $S = 1/2$ systems, which necessarily exhibit a signal in EPR and have longer relaxation times, because the molecules are less sensitive to molecular vibrations responsible of the fluctuation of the qubit frequency. The design of the new complexes using $S = 1/2$ system was based of the important criteria that we have found when working on the binuclear complex of Ni(II):

- (i) The bridging ligand has to be chelating
- (ii) The bridging ligand has to be as modular as possible to easy tune the different parameters that influence the relaxation times

For the mononuclear Cu(II) based salophen complex, the relatively long relaxation times ($T_2 = 1 \mu\text{s}$ and $T_1(7.5\text{K}) = 1.8 \text{ ms}$) found in the monomeric unit remain unchanged in the binuclear complex. We tried to prepare several binuclear Cu(II) complexes with different Cu-Cu distances but unfortunately we were not able to measure any couplings in those complexes using the DEER sequence. However, we have shown using ENDOR that it is possible to use the interaction (superhyperfine coupling) between the electronic spin of the Cu(II) and the nuclear spin of the ligand to assess the coherence time of a nitrogen ($T_2(\text{N}) > 0.5 \text{ ms}$) and a proton ($T_2(\text{H}) > 0.57 \text{ ms}$). Those coherence time are compatible with the prerequisites for the quantum computing. Comparing results with another $S = 1/2$ spin, V(IV)O based salophen complex, we found that T_1 is longer ($T_1(7.5\text{K}) = 12 \text{ ms}$) for V(IV)O complexes. The superhyperfine interaction between

Conclusion and perspectives

V(IV)O and the nuclear spins were difficult to observed and the studied could not be further investigated in the time of the manuscript.

The long coherence times of the nuclear spin of the nitrogen and proton atoms open new perspectives for using molecular complexes as a genuine platform for quantum computing.

There is still a lot of work to achieve in the different projects presented in this manuscript. For the first one:

- (i) As mentioned in the introduction, the detection of the spin echo (electronic and nuclear) is particularly challenging. Some teams have developed home-made instruments with the possibility to detect a limited number of spins or with a tunable cavity frequency. The clock transition molecules presented in this manuscript have shown robustness to magnetic fluctuations and a relatively long T_2 with respect to dilution (10^{19} spin/cm³). Moving to a highly diluted system (10^{14} spin/cm³) could help us to reach coherence times longer than the one of other systems such as the superconducting qubit, and to get a better understanding of the relaxation mechanisms involved. This work is planned through a collaboration with A. Bienfait (École Normale Supérieure de Lyon) and P. Bertet (CEA, Univ. Paris-Saclay).
- (ii) Spin Electric Effect (SEC) has been demonstrated in some cases. The molecule can be coupled to an electric field and by doing so it is possible. This could be a strategy to shift the resonance frequency of the CT molecule in order to slightly modify E so it can match the frequency of the EPR cavity. In collaboration with J. Liu, and A. Ardavan (Clarendon laboratory, Univ. of Oxford) we will investigate the effect of electric field on the ZFS parameters of Ni(II) complexes in the form of single crystals.
- (iii) Computational study, neutron inelastic scattering or terahertz can help us to identify the vibrational mode responsible for the relaxation. Access to this information could help us to design new Ni(II) complexes with larger spin-lattice relaxation times.

For the second project involving polynuclear complex:

- (i) The synthesis of Salophen-based binuclear complexes has to be improved. New complexes with different Cu-Cu distances would be interesting in order to tune the

Conclusion and perspectives

magnetic coupling. New ligands allowing the formation of trinuclear complexes of Cu(II) and V(IV)O were in preparation (Figure VI-1). The synthesis and characterization of these molecules need to be completed.

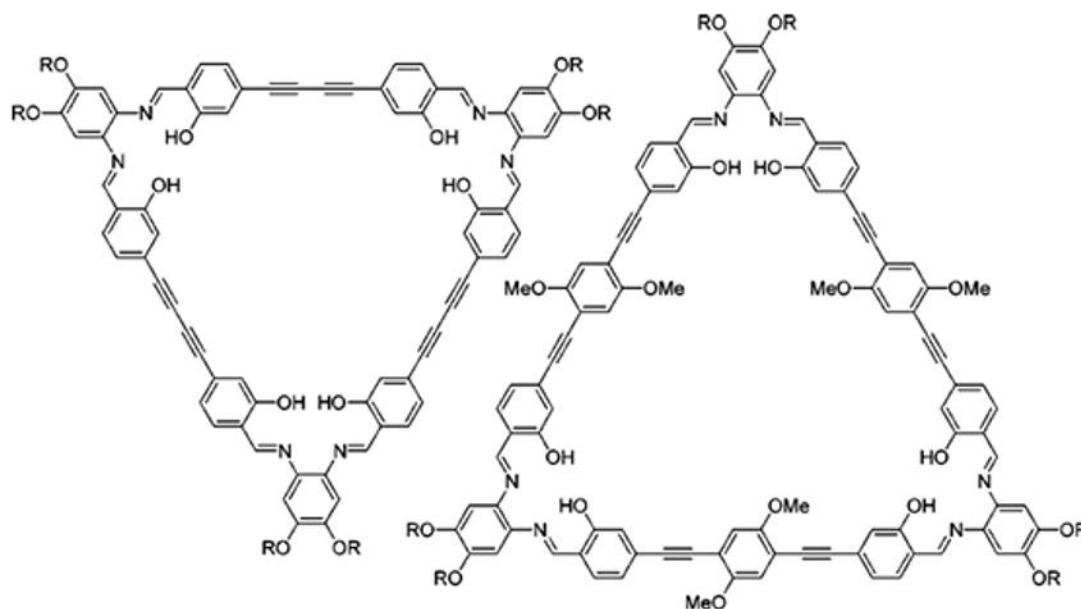


Figure VI-1. New ligands proposal for the obtention of trinuclear complex. $R = \text{Me}/\text{Et}$.

- (ii) Measuring the coupling between the different qubits in the polynuclear complexes may be carried out with pulsed EPR spectroscopy using specifically designed sequences, or perhaps inelastic neutron scattering.

RESUME EN FRANÇAIS

L'explosion des données générées chaque année pose des défis cruciaux en termes de stockage et de traitement. Les algorithmes classiques basés sur des bits ne sont pas adaptés à la gestion efficace de vastes ensembles de données, en particulier lorsque le temps de traitement devient prohibitif. En 1997, Grover a proposé une solution en utilisant des qubits, qui peuvent accélérer considérablement le traitement des données. Contrairement aux bits classiques, qui ne peuvent représenter que 0 ou 1, les qubits existent dans une superposition de ces deux états, permettant des calculs parallèles beaucoup plus rapides. Cependant, cette superposition d'états est fragile et ne dure qu'un certain temps, appelé temps de cohérence.

L'idée derrière l'informatique quantique est que des qubits avec un long temps de cohérence, s'ils sont enchevêtrés, peuvent simuler des calculs parallèles. Par exemple, un problème nécessitant 8 opérations pourrait être résolu beaucoup plus rapidement avec 3 qubits qu'avec 3 bits classiques grâce à cette capacité à traiter simultanément plusieurs états. Les qubits supraconducteurs, en particulier, sont très prometteurs grâce à leur long temps de cohérence et la possibilité de les coupler. Google a déjà réalisé des calculs quantiques avec cette technologie.

D'autres systèmes de qubits, notamment ceux basés sur le spin, sont également prometteurs. Par exemple, le centre NV dans le diamant présente un temps de cohérence très long, même à température ambiante. Le spin nucléaire d'une impureté donneuse dans le silicium a également montré des temps de cohérence impressionnants. Cependant, ces systèmes présentent encore une limite importante : il est difficile d'enchevêtrer les qubits, ce qui est essentiel pour l'informatique quantique.

Les molécules représentent une autre voie intéressante pour la création de qubits. Elles contiennent de nombreux spins électroniques et nucléaires, qui peuvent être couplés (couplage superhyperfin, couplage dipolaire) pour former des qubits avec un temps de cohérence prolongé. Grâce à l'effet Zeeman, en appliquant un champ magnétique, il est possible de lever la dégénérescence des niveaux de spin. Toutefois, les fluctuations magnétiques (dus à des interactions dipolaires) continuent de poser un problème majeur car elles détruisent la superposition d'états nécessaire au fonctionnement des qubits.

Pour atténuer ces effets, des systèmes appelés transitions d'horloge (TH) ont été étudiés, car ils sont insensibles aux fluctuations magnétiques. Des recherches ont montré que, dans ces systèmes, le temps de cohérence est considérablement plus long à l'intérieur de la transition d'horloge. Par exemple, dans des systèmes basés sur l'Holmium, le temps de cohérence est passé de 0,1 μs à 8 μs à l'intérieur de la transition. Toutefois, il reste beaucoup à découvrir sur les limites des transitions d'horloge.

La première partie se concentre sur la mise en place d'une stratégie synthétique pour la conception de molécules magnétiques $S = 1$ qui peuvent jouer le rôle de bits quantiques (qubits) et présenter une transition d'horloge (TH) à champ magnétique appliqué nul. Pour ce faire, nous étudions les paramètres structuraux (électroniques et géométriques) des complexes mononucléaires Ni(II) (d^8 , spin $S = 1$) qui influencent les paramètres de l'Hamiltonien de spin de séparation de champ nul (ZFS). Nous nous concentrons sur des complexes présentant une géométrie octaédrique déformée (avec une symétrie axiale pseudo-tétraogonale et trigonal). L'objectif était d'obtenir des complexes Ni(II) avec anisotropie uniaxiale (valeur D négative, où D est le paramètre ZFS axial) et rhombicité conduisant à deux niveaux d'énergie bas permettant au complexe de jouer le rôle de qubit, avec une fréquence de qubit ($2E$, où E est le paramètre ZFS rhombique) dans la plage accessible par les appareils EPR à bande X ou Q. Cela a été réalisé en quatre étapes : (i) L'explication de l'origine des paramètres ZFS pour un spin $S = 1$ (ii) La prédiction de ces paramètres à l'aide de calculs théoriques basés sur la fonction d'onde (iii) La confrontation des paramètres calculés avec ceux extraits d'études de spectroscopie EPR à haute fréquence et haute intensité (HF-HFEPR). Nous avons démontré qu'il est possible de prédire et de moduler (dans une certaine mesure) le paramètre ZFS axial D et de moduler le paramètre rhombique E en jouant avec différents facteurs tels que le *packing* et l'effet électronique dans le cas de l'étude d'analogie $[\text{Ni}(\text{bpy})_3]^{2+}$.

Nous avons testé la robustesse d'une transition d'horloge dans le composé de $[\text{Ni}(\text{HIM-2})_2(\text{NO}_3)](\text{NO}_3)$ face aux fluctuations magnétiques. Une série d'expériences a été réalisée avec des échantillons contenant différents pourcentages de cobalt, un élément paramagnétique. Le cobalt a été choisi car il possède à la fois un spin électronique et nucléaire, et son temps de relaxation rapide introduit des fluctuations magnétiques dans le système. Trois échantillons ont été préparés : un sans cobalt, un avec 5 % de cobalt et un autre avec 50 %.

- Échantillon sans cobalt : Le temps de cohérence de cet échantillon reste stable à l'intérieur de la transition d'horloge (TH), mais diminue en dehors de celle-ci en raison de l'apparition d'un nouveau mécanisme de relaxation causé par des fluctuations magnétiques externes.
- Échantillon avec 5 % de cobalt : Le comportement est similaire à celui de l'échantillon sans cobalt, montrant que l'introduction de cette petite quantité d'impureté n'a pas altéré le temps de cohérence du nickel. Cela signifie que les fluctuations magnétiques créées par ce faible pourcentage de cobalt ne suffisent pas à affecter la robustesse de la transition d'horloge.
- Échantillon avec 50 % de cobalt : Dans ce cas, la situation est différente. Le temps de cohérence devient plus court et n'est plus stable à l'intérieur du TH. Cela suggère que la transition d'horloge atteint ses limites et que la concentration élevée de cobalt perturbe la protection offerte par le TH.

Ces résultats montrent que la protection par la transition d'horloge est efficace contre les fluctuations magnétiques jusqu'à un certain seuil, représenté ici par l'échantillon contenant 50 % de cobalt. Cependant, une question reste ouverte : même dans l'échantillon sans cobalt, le temps de cohérence à l'intérieur du TH reste relativement court. Cela a conduit à l'hypothèse que le temps de relaxation T_1 (le temps nécessaire pour qu'un système retourne à son état fondamental après une excitation) limite le temps de cohérence T_2 . Une mesure à 5 K a révélé un temps de relaxation T_1 de 1,2 μ s, une valeur très courte qui limite T_2 . Ce phénomène est attribué aux vibrations moléculaires qui induisent des modifications structurales du système, affectant les paramètres du décalage de champ nul (ZFS) et détruisant ainsi la superposition d'états.

En parallèle de ce travail les spins nucléaires ont aussi été étudiés. Il a été observé que les spins nucléaires d'atomes isolés peuvent atteindre des valeurs de temps de cohérence T_2 très longues, mais leur manipulation est complexe en raison de la protection apportée par les spins électroniques. Cependant, dans un complexe, les spins nucléaires peuvent être adressés via l'interaction avec les spins électroniques, rendant les molécules magnétiques prometteuses pour l'informatique quantique. L'interaction superhyperfine entre les spins permet de coupler les spins nucléaires et électroniques, et la spectroscopie ENDOR a démontré la présence de spins nucléaires adressables dans les molécules. Pour le complexe de salophen à base de Cu(II)

mononucléaire, les temps de relaxation électronique ($T_2 = 1 \mu\text{s}$ et $T_1 (7,5 \text{ K}) = 1,8 \text{ ms}$) trouvés dans l'unité monomérique demeurent inchangés dans le complexe binucléaire. Nous avons tenté de préparer plusieurs complexes binucléaires de Cu(II) avec différentes distances Cu-Cu, mais nous n'avons malheureusement pas pu mesurer de couplages dans ces complexes en utilisant la séquence DEER. Cependant, grâce à l'ENDOR, nous avons montré qu'il est possible d'utiliser l'interaction (couplage superhyperfin) entre le spin électronique du Cu(II) et le spin nucléaire du ligand pour évaluer le temps de cohérence d'un atome d'azote ($T_2(\text{N}) > 0,5 \text{ ms}$) et d'un proton ($T_2(\text{H}) > 0,57 \text{ ms}$). Nous avons ainsi vu qu'au sein d'une molécule les spins nucléaires restent long même et qu'il est possible d'avoir plusieurs ressources accessibles au sein d'une unique molécule.

